Analysis and evaluation of Terrain Observation by Progressive Scans (TOPSAR) mode in Synthetic Aperture Radar

Final Year Project
by
Josep Ruiz Rodon

Universitat Politècnica de Catalunya

Escola Tècnica Superior d'Enginyeria de Telecomunicacions de Barcelona

Advisor: Antoni Broquetas Ibars

Acknowledgment

This project is the result of five years studying in the *Escola Tècnica Superior d'Enginyeria de Telecomunicacions de Barcelona* (ETSETB) in the *Universitat Politècnica de Catalunya* (UPC). During these years, I have learned a lot of technical question but, at the same time, they have been possible to live a new experience far from my town. This project would not have been possible without the academic and moral support of a large number of people.

First of all, I would like to express my gratitude to my advisor Toni Broquetas, who has always time for me when I was in trouble. His support has been really helpful to carry out this project. A special thank to all the people of the SAR group of UPC who help me when I needed their knowledge.

Thanks to my family for their support during these years of degree. I like to mention the colleagues that I met during in UPC and the long hours spent together studying the hardest subjects. Thanks to my friends of Valls who have been a great support when I came back to town at weekends.

Finally, my sincere thanks to EADS-CASA Espacio who let me work in the PAZ mission project. It has been a really gratifying experience which offers me the possibility to work with a project that will be a reality in a near future.

Table of Contents

List of Tables

List of Figures

List of Acronyms

AAP	Azimuth Antenna Pattern
AASR	Azimuth Ambiguity-to-Signal Ratio
AF	Array Factor
DTAR	Distributed Target Ambiguity Ratio
EM	ElectroMagnetic
FT	Fourier Transform
HS	High resolution Spotlight
ISLR	Integrated Side-Lobe Ratio
NESZ	Noise-Equivalent Sigma Zero
PRF	Pulse Repetition Frequency
PRI	Pulse Repetition Interval
PSLR	Peak Side-Lobe Ratio
RADAR	RAdio Detection and Ranging
RAR	Real Aperture Radar
RASR	Range Ambiguity-to-Signal Ratio
RCS	Radar Cross-Section
RFE	Radio Front-End
SAR	Synthetic Aperture Radar
SC	SCanSAR mode
SL	SpotLight mode
SM	StripMap mode
SM-S	StripMap Swath
SNR	Signal-to-noise ratio
SS	Sub-Swath
TBP	Time Band Product
TFD	Time/Frequency Domain
TOPSAR	Terrain Observation by Progressive Scans
TRM	Transmit/receive module

List of Symbols

P_{amb}	Ambiguous power
R_{amb}	Ambiguous range distances for RASR
$\Delta\phi$	Angle quantization step
θ_a	Antenna Azimuth beamwidth
θ_r	Antenna Elevation beamwidth
$a(x)$	Antenna field distribution
G	Antenna Gain
L_a	Antenna Length
ϕ_0	Antenna processing beamwidth
W	Antenna Width
θ_a	Azimuth angle between target and platform
T_B	Burst Time
T_R	Cycle time of TOPSAR scanning
P_d	Desired power
k_R	Doppler rate
f_d	Doppler Shift
d	Doppler track error
T_D	Dwell Time
Re	Earth Radius
T_0	Effective Temperature 290 K
v_e	Effective velocity on the ground
ξ	Footprint azimuth length
T_F	Footprint Time
$Frac(\ )$	Fractional portion of its argument
f	Frequency
Rg	Ground range
W_{ai}	Hamming reception window
θ_i	Incidence angle

$Int(\ )$	Integer portion of its argument
f_i	Intermediate frequency
θ_l	Look angle
A_e	Error quantization amplitude
$R_{\max}$	Maximum range reception
SNR_0	Minimum SNR in reception
h	Platform altitude
$\phi(\tau)$	Pointing angle evolution
T_p	Pulse repetition interval
α	Progressive phase of the antenna array
τ_P	Pulse duration
T_q	Quantization step time
ϕ_q	Quantized steering angle
σ	Radar cross-section
F	Receiver Noise Factor
B	Reception frequency bandwidth
X_a , ρ_{az}	SAR Azimuth resolution
X_b	SAR azimuth footprint length
R_0	Slant Middle Range
R	Slant range
c	Speed of light
k_ϕ	Steering angle rate
S	Swath width
A_{eff}	Target Effective Area
E_θ , E_ϕ	Theta and phi sub-array fields
τ_{RP}	Transmission/Reception guard time
P_t	Transmitted Power
λ	Wavelength radar operation
k_w	Windows correction factor

Chapter 1 Introduction

1.1 History and context of SAR remote imaging

Synthetic Aperture Radar (SAR) is a technique used in radar (RAdio Detection And Ranging) [1] systems to get high resolution images which are impossible to obtain with a conventional radar. This method allows us to acquire images from the surface of the Earth or other planets from large distances.

In SAR [2], a single antenna is used to get information of the targets, and the platform movement, where the antenna is fixed, is used to spread the Doppler history of received echoes improving the resolution of processed images.

Remote sensing is a wide area which studies different techniques to acquire information about targets situated at far distances. These techniques can be classified in two different areas according to their basic operation. The first group, called passive remote sensing [3] [4], uses passive sensors to acquire the energy radiated by the targets. This energy can come from an external source, such as Sun radiation, being reflected by the object or it can be emitted by the target itself. On the other hand, active remote sensing systems [4] emit pulses to illuminate the scanned area, providing their own energy. So, although it requires a more complex system, active sensing does not require an external source to operate which is an advantage when the conditions are not favourable.

SAR and other radar techniques are examples of active sensors, working at frequencies between 0.3 GHz and 300GHz. These systems send pulses towards the scanned area, the interaction of each pulse with the surface originates an echo which arrives to the receiver. This echo is originated by the energy backscattered by the objects in the scene and it will be dependant of the backscattering profile of the targets (radar cross-section) [5] [6]. The time delay and strength of power received as well as frequency properties of the returns are processed to determine the target locations and characteristics.

Synthetic aperture is similar to a conventional real aperture radar (RAR) antenna but it is achieved by signal processing. In a SAR, the antenna, installed in a moving platform, sends pulses to the scene and receives backscattered returns. The movement of the platform makes possible to illuminate the targets at different positions of the satellite trajectory, which is equivalent to have multiple antennas illuminating the scene at the same time.

Thus, SAR is a fairly recent acquisition method that has some advantages in comparison with other remote sensing techniques. The most significant are:

- Day/Night and all weather condition imaging since it does not depend on external power sources to detect the targets.
- Geometric resolution independent of altitude or wavelength.
- Signal data characteristic unique to the microwave region of EM spectrum which has suffers less deterioration in atmosphere propagation.

The SAR systems started with aero-transported missions and later, first space missions were sent. The SAR beginning dates back to 1951 when C. Wiley postulated the Doppler

beam-sharpening concept [7]. Highlights of SAR development can be seen in Table 1.1.

Date	Development
1951	Carl Wiley of Goodyear postulates the Doppler beam-sharpening concept.
1952	University of Illinois demonstrates the beam-sharpening concept.
1957	University of Michigan produces the first SAR imagery using an optical correlator.
1964	Analog electronic SAR correlation demonstrated in non-real time (U. Michigan).
1969	Digital electronic SAR correlation demonstrated in non-real time (Hughes, Goodyear, Westinghouse).
1972	Real-time digital SAR demonstrated with motion compensation (for aircraft systems)
1978	First space-borne SAR NASA/JPL SEASAT satellite [8]. Analog downlink; optical and non-real-time digital processing.
1981	Shuttle Imaging Radar series starts - SIR-A [9]. Non-real-time optical processing on ground.
1984	SIR-B digital downlink [10]; non-real-time digital processing on ground.
1986	Space-borne SAR Real-time processing demonstration using JPL Advanced Digital SAR processor (ADSP) [11]
1987	Soviet 1870 SAR is placed in Earth orbit.
1990	Magellan SAR images Venus [12]
1990	Evolution of SAR begins in space; Soviet ALMAZ (1991), European ERS-1 (1991) [13], Japanese JERS-1 (1992) [14], SIR-C (1994) [15], ERS-2 (1995) [16], Canadian RADARSAT-1 (1995) [17]
2000s	The last years the number of SAR missions increases significantly. Some examples are: SRTM (2000), ENVISAT (2002) [18], ALOS (2006), TerraSAR-X (2007) [19], RADARSAT-2 (2007) [20], SAR-LUPE (2007), SURVEYOR (2007)…

Table 1.1 Highlights in space-borne SAR history [21]

Annex A provides a summarized report of principal SAR mission and their operation characteristics.

A first approximation to SAR geometry is shown in Fig. 1.1. Azimuth direction is parallel to platform velocity, while range corresponds to the perpendicular direction. Look angle is defined as the angle between the nadir direction (perpendicular to the ground below the satellite) and the pointing direction. Incidence angle is defined as the angle between the illumination direction and the direction perpendicular to the surface in the scene. All parameters will be explained more accurately in Chapter 2.

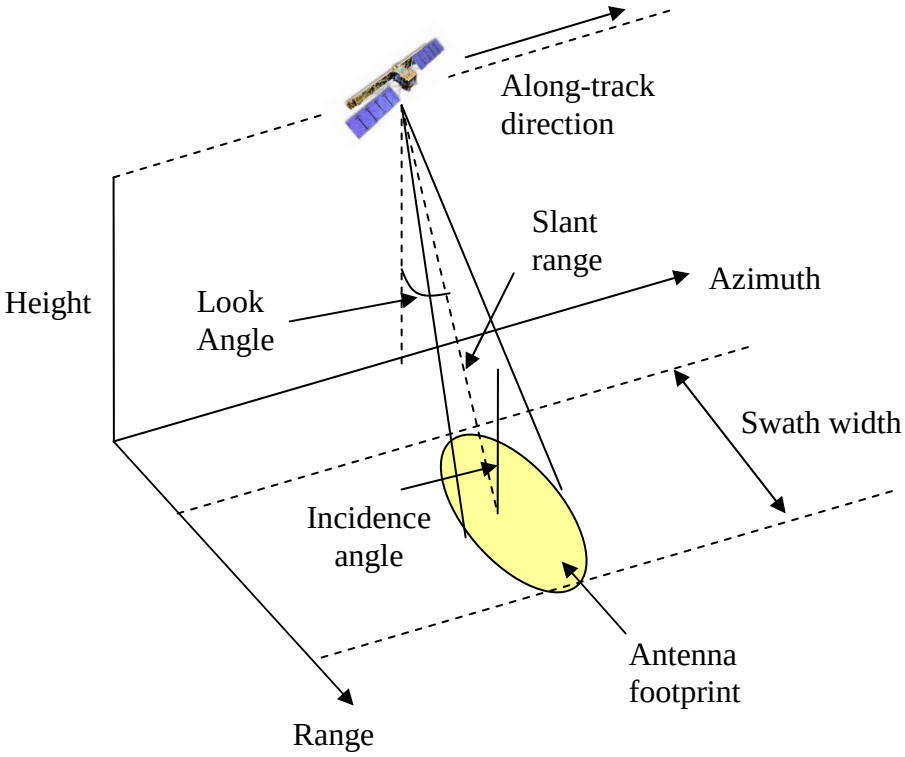

Fig. 1.1 Basic geometry and parameters for SAR

Nowadays, SAR investigations are still improving the imaging features. These research activities provide better resolution images with more versatility of scanning modes. The increase of SAR popularity is due to the commercialization of SAR technology, which in the first years only had military purposes. Among these new commercial possibilities, most notably could be sea surveillance and detection of boats, topographic mapping, forestry monitoring, natural disaster prevention and surveillance, etc. The increasing demand for SAR products is promoting the R&D of new SAR missions at international level with better Earth coverage and spatial resolution.

In this context, a first Spanish SAR satellite mission has been proposed based on the German mission TerraSAR-X. The Spanish satellite, called PAZ, will provide more than 200 images from earth surface every day. EADS-CASA is the main contractor of the PAZ spacecraft after specification of its subsystems will eventually integrate the satellite and carry out the functional tests. The Universitat Politècnica de Catalunya which has expertise in SAR techniques is assessing EADS-CASA in the PAZ satellite specification and

performance prediction. The present Final Year Project is part of the UPC study for the PAZ SAR mission addressing specifically a new acquisition mode (TOPSAR) designed to obtain wider coverage images compared to traditional SAR Stripmap operation.

1.2 Purpose of the project

Recently, several missions have been sent to the space in order to get high resolution images from Earth's surface and oceanic phenomena. TanDEM-X, RADARSAT-2, COSMO-SkyMed and TerraSAR-X are some examples. Nowadays, it is possible to obtain precise information with SAR technology but investigators are searching for advanced techniques that make possible to improve some system parameters.

In the context a Spanish SAR mission in X-Band has been proposed. This mission called PAZ belongs to the "*Programa Nacional de Observación de la Tierra por Satélite*", managed jointly by the Ministries of Defence and Industry, Trade and Tourism. EADS-CASA Espacio is the main contractor of the PAZ satellite. The Universitat Politècnica de Catalunya is supporting EADS CASA Espacio in the PAZ satellite performance assessment and to study some innovative SAR aspects. One of them is the possibility to incorporate a new operation mode called Terrain Observation by Progressive Scans (TOPSAR) which is the focus of the present Final Year Project.

One of the limitations imposed by the nature of spaceborne SAR is the impossibility to achieve high resolution and, at the same time, wide area coverage. For this reason, various scanning modes have been studied during the last years. Some of them are more adequate to get high resolution images as Spotlight or Stripmap mode. On the other hand, other modes, such as ScanSAR, provide wide coverage with a considerable loss of resolution.

In this project, the recently proposed mode TOPSAR [35] [36] will be studied and their performance features will be analysed. This scanning mode offers wide coverage avoiding some problems of ScanSAR mode, such as a ripple artefact in the image named scalloping that will be discussed later. Furthermore, it will be possible to optimize the azimuth resolution obtaining better results than in ScanSAR. On the other hand, other issues will appear and they must be studied to determine if they are really problematic for the correct radar performance.

TOPSAR moves the antenna main beam back to forward in the along track direction using the PAZ active antenna steering possibilities. With this steering, it is possible to illuminate all the points in the scene with the main beam of the antenna radar avoiding that some points are illuminated by edges of the beam.

The purpose of this report will be to study and determine the advantages and drawbacks of this mode. Parameters from TerraSAR-X will be used to make the analysis. TerraSAR-X parameters are used since it has similar configuration than PAZ satellite. Problems due to quantization of steering angle and ambiguities will be computed. Furthermore, an optimization of TOPSAR mode in terms of resolution will be done. Finally, a simple tool to compute basic TOPSAR parameters will be presented.

1.3 Structure of the document

This report is structured in 8 chapters. Firstly, in Chapter 2, the basic fundamentals of SAR technology are presented in order to clarify some concepts of SAR performance. The concepts defined in this section are fundamental to understand the next sections. SAR geometry, operation modes and other SAR features are described in this introductory section.

Once the key parameters has been defined, in Chapter 3 the TOPSAR mode is described in detail and its parameters are computed for PAZ system to get the first results that will be useful to compute other parameters in next chapters.

Chapter 4 studies one of the first problems that appear when TOPSAR mode is used to scan the scene. In fact due to the quantization of the steering angle, it is not possible to do a continuous sweep because of the limited storage capacity in the active antenna phased array programming. It will cause some ambiguity problems that must be discussed.

Continuing with TOPSAR analysis, in Chapter 5 azimuth and range ambiguities are computed. In this section a progressive study is shown, starting with basic modes such as Stripmap or ScanSAR and finally TOPSAR ambiguities computation. There is an analysis of sub-array antenna diagram and grating lobes which have most relevance when the antenna diagram is pointing laterally in squint directions.

Chapter 6 presents the optimization of TOPSAR in terms of resolution, and the parameters analysed in Chapters 4 and 5 are re-calculated to see if they are more critical with this new configuration.

Finally, in Chapter 7, a simple tool to compute the parameters exposed at this report is presented. It consists on a MATLAB program that provides a useful way to obtain TOPSAR parameters with no need to know this topic deeply.

Chapter 8 exposes the conclusions and future lines of study in TOPSAR mode.

Chapter 2 SAR fundamentals

In this section the basics of Synthetic Aperture Radar (SAR) are defined. The first part of this chapter reviews radar principles. After that, SAR scanning modes are briefly exposed and finally the chapter is centred to SAR basic performance: Doppler history vs. azimuth location of the targets, azimuth antenna pattern and other important parameters.

2.1 The radar equation

To understand the SAR system operation, it is necessary to explain the basic principles of radar. Initially, radar was created to detect the presence of voluminous targets such as aircraft and define their positions. The radar transmitter generates a high power pulse of radio electromagnetic energy which is radiated to the space with a directional antenna. Any perturbation along the propagation path due to the presence of dielectric or metallic objects originates an echo that will be backscattered to the radar antenna and detected by the radar receiver.

The reflected echoes arrive to the receiver in different times. The relative time delay τ between reception and pulse transmission is used to determine the range distance, which will be one of the coordinates to localize the targets (in the next section the basic SAR parameters are defined). The range distance can be easily computed as $R = c\tau / 2$ [22], where *c* is the speed of light.

The power of the received echo relative to the power transmitted in free space is proportional to $1/R^4$ [22] and, consequently, the received power will decrease considerably when the targets are far from the radar antenna. At range of interest, 100 to 1000 km in SAR systems, the received power can be of the order of microwatts, which can be problematic with in reception since the internal receiver noise can mask the signal reception.

The standard configuration of a radar system can be seen in Fig. 2.1. The transmitter generates the pulse and the antenna emits it to the space. The electromagnetic waves travel across the air and they are reflected by the targets. The echoes are captured by the antenna which sends these returns to the receptor. Data recorder and processor take these echoes and process them in order to show the target locations in the display.

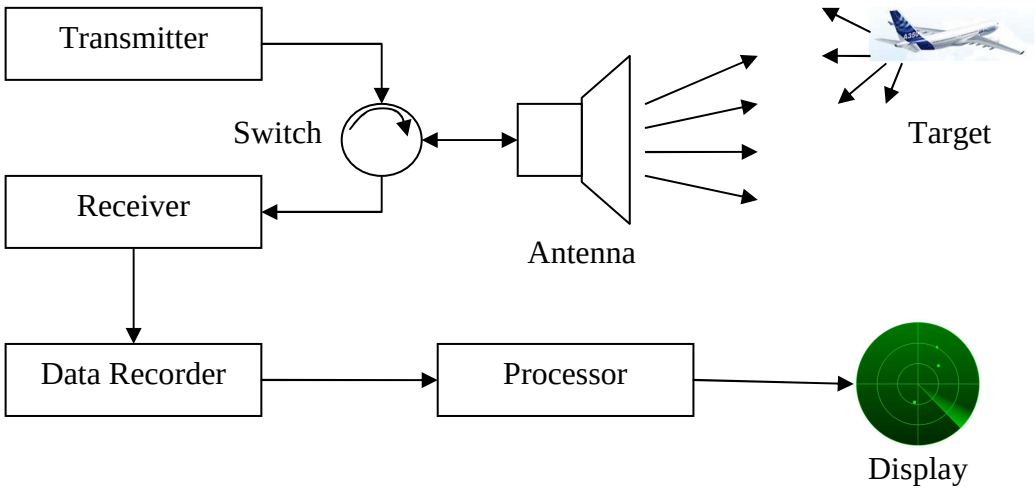

Fig. 2.1 Radar system basic modules

The probability of target detection will be determined by the relation between the power

received and the average noise power in reception. This ratio, called SNR (signal to noise ratio), has to reach a minimum level to achieve radar satisfactory performance. SNR will be determined by the target distance, target reflection characteristics, receiver parameters, etc. The SNR can be computed as [23]:

$$SNR = \frac{P_t G \sigma A_{eff}}{\left(4\pi R^2\right)^2 FkT_0 B} = \frac{P_t G^2 \sigma \lambda^2}{\left(4\pi\right)^3 R^4 FkT_0 B} \tag{2.1}$$

where *Pt* is the transmitted pulse power, G is the antenna gain, σ is the radar cross section, *Aeff* is the targets effective area. The receiver main parameters are the processed bandwidth (*B*) and the factor noise (*F*). T_0 is the reference temperature of 290 Kelvin. λ is the radar wavelength operation, while SNR_0 is the minimum signal to noise ratio to detect the targets correctly (radar sensibility). Defining the minimum value of the SNR for reliable detection as SNR_0, it is possible to determine the maximum range:

$$R_{\max} = \sqrt[4]{\frac{P_t G^2 \sigma \lambda^2}{\left(4\pi\right)^3 SNR_0 FkT_0 B}} \tag{2.2}$$

2.2 SAR principles and theory

SAR technique is a technology based on radar systems intended to obtain the highest possible target spatial resolution. In this section, the antenna properties and SAR geometry and parameters will be presented to introduce SAR most relevant information.

2.2.1 Antenna beam properties

The antenna is one of the most important parts of the radar systems. It is the responsible to emit the pulses and receive the echoes from the targets. The antenna pattern determines the lateral resolution of the radar. For these reasons, it is important to introduce the basic antenna principles to understand SAR operation.

Let us consider a one-dimensional line antenna of length *D* with a field distribution *a(x)* (Fig. 2.2), the far field at point *P* produced by an elementary section *dx* of this antenna is proportional to [24]:

$$dE \sim a(x) e^{jkx\sin\theta} dx \tag{2.3}$$

The term $kx\sin\theta$ represents the phase of the field due to element *dx*, situated at a generic point *x* relative to the centre of the antenna. Integrating all the *dx* elements along the antenna, the total far field at point P is proportional to:

$$E \sim \int_{-D/2}^{D/2} a(x) e^{jkx\sin\theta} dx \tag{2.4}$$

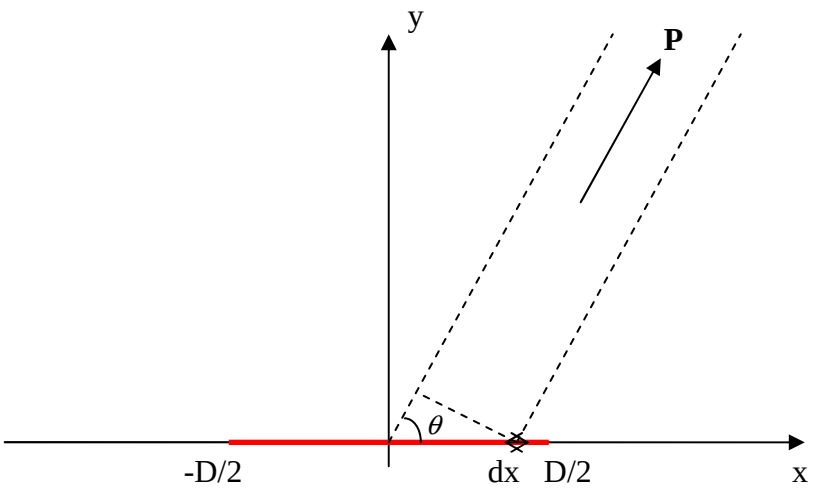

Fig. 2.2 One-dimensional antenna of length D

If a linear distribution $a(x)=a_0$ across the antenna aperture is considered, the equation (2.4) can be re-written as:

$$E \sim a_0 \int_{-D/2}^{D/2} e^{jkx\sin\theta} dx = a_0 D \frac{\sin\left(kD\sin\theta/2\right)}{\left(kD\sin\theta/2\right)} \tag{2.5}$$

This is the typical *sinc* pattern of a uniform aperture antenna represented in Fig. 2.3.

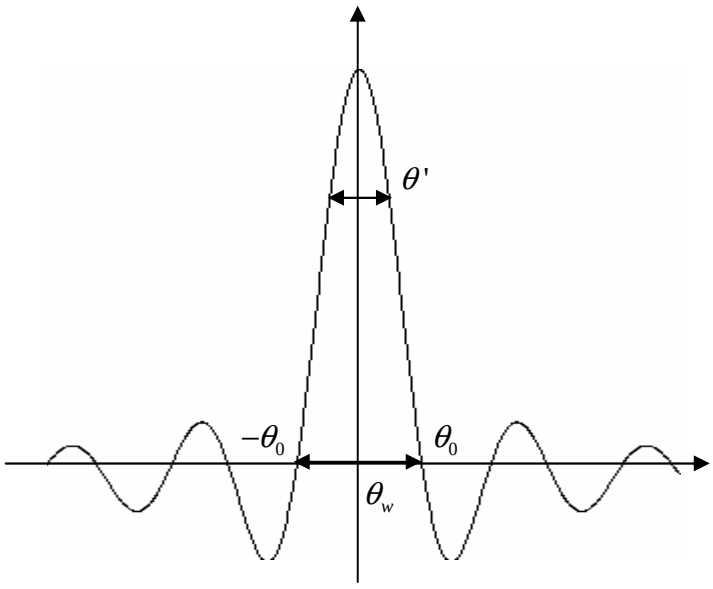

Fig. 2.3 Sinc behaviour of a one-dimensional antenna uniformly illuminated

The nulls of this function occur at:

$$kD\sin\theta/2 = m\pi \tag{2.6}$$

Which corresponds to θs:

$$\theta = \sin^{-1}\left(2m\pi/kD\right) = \sin^{-1}\left(m\lambda/D\right) \tag{2.7}$$

where m is an integer and $\lambda = 2\pi/k$ is the operating radar wavelength. The first null ($m=1$) occurs at:

$$\theta_0 = \sin^{-1}\left(\lambda/D\right) \approx \lambda/D \qquad \lambda \ll D \tag{2.8}$$

The distance between first nulls can be calculated as:

$$\theta_w = 2\lambda/D \tag{2.9}$$

Another angle of interest is θ' which can be observed in Fig. 2.3. θ' corresponds to the angle between half power points of the main beam. This angle can be obtained solving the next equation:

$$\left|\frac{\sin\left(kD\sin\theta/2\right)}{kD\sin\theta/2}\right|^2 = 0.5 \tag{2.10}$$

This equation provides a value for θ':

$$\theta' = 1.76\pi/kD = 0.88\lambda/D \tag{2.11}$$

The most powerful sidelobe has a relative peak power from the main beam 13.2 dB weaker. The power of these peaks can be reduced if a tapering in the antenna illumination is applied [25]. Some examples of these techniques are illustrated in Table 2.1.

Weighting	*a(x)*	Half power beam θ'	Level of first sidelobe (dB)
Uniform	1	$0.88\lambda/D$	-13.2
Linear	$1-2\lvert x\rvert/D$	$1.28\lambda/D$	-26.4
Square cosine	$\cos^2\left(\pi x/D\right)$	$1.45\lambda/D$	-32.0

Table 2.1 Antenna characteristics depending on the antenna illumination

Generally, the approximation λ/D is used for the value of the half-power beam width. These results obtained for a one dimensional linear antenna can be extrapolated to a 2D rectangular antenna considering the product of two *sinc* functions for the two antenna directions. In this document this approximation is used to compute the results for TOPSAR

mode. For SAR systems, the antenna is used both in transmission and reception. So, the sidelobe level is squared (doubled in dB) and the angle θ' is computed at 1/4 of the main beam maximum.

2.2.2 Antenna Array

The concept of array antenna consists of observing a point P with a large number of antennas which combine the returns to enhance the power received from this target. Taking a linear array of equally spaced antennas observing a target P, as in Fig. 2.4, the received signal from each element is carried via transmission line of electrical length l_n to central receiver. The receiver combines all these signals from antenna array elements.

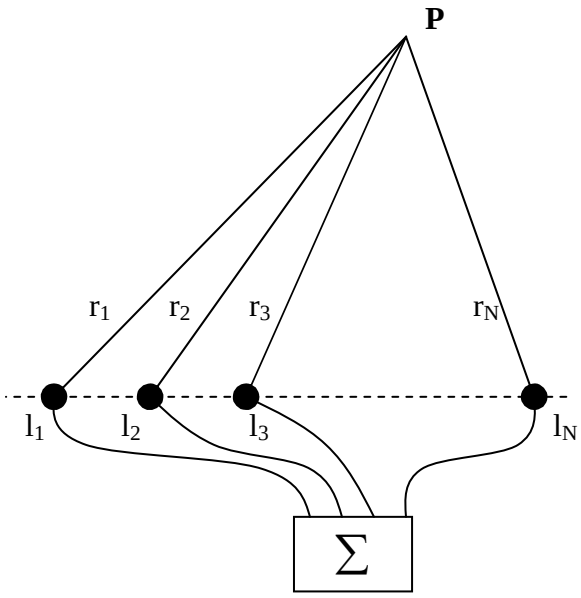

Fig. 2.4 Array of antennas

If the array transmission lines are selected such that the signal returns arrives at the same time to the receiver (2.12), the signals will add in phase and, then, the array is said to be focused at the target point P.

$$r_1 + l_1 = r_2 + l_2 = ... = r_N + l_N \tag{2.12}$$

If this array is used in a radar system, the transmitted signal is generated at the same point where the transmission lines are combined. If the transmission lines fulfil the equation (2.12), the echoes will still arrive in phase.

On the other hand, if the transmission lines have all the same length (l_1=l_2=...=l_n), the array is called unfocused, except for a target situated at infinity. Another possibility is that each element has its own receiver, and the summation of all the returns is done later time in a processor. Then the array focusing can be carried on if all the receivers have a common reference signal and echoes are combined after an appropriate phase shift is added to them. The signal V_n from the element A_n is shifted by a phase $\phi_n = 2kr_n$, so the total output signal is given by (2.13). This alternative configuration is shown in Fig. 2.5.

$$V = \sum_n V_n e^{-2\,jkr_n} \tag{2.13}$$

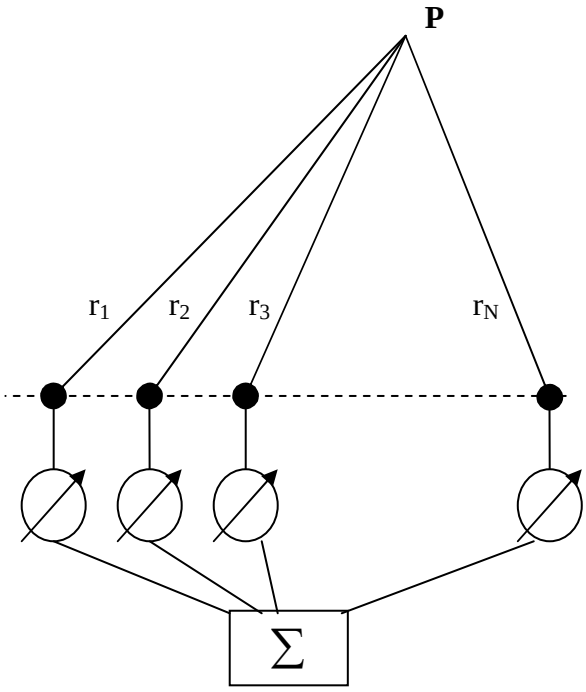

Fig. 2.5 Array focused at point P by using appropriate phase shifters

This scheme can be used to introduce the SAR systems. In synthetic aperture radar, a single antenna is moved along the array line and from each location a signal is transmitted and the echo received and coherently recorded to be added with other echoes. So, the antenna array is formed synthetically in a so-called SAR processor to generate the equivalent of a focused or unfocused array. This scheme is shown in Fig. 2.6.

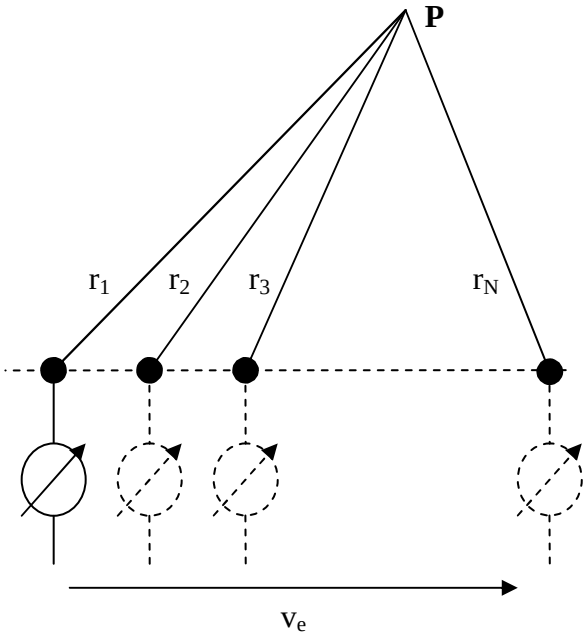

Fig. 2.6 A single antenna which is moved to synthesize an array

In the case of a linear array with a large number *N* of radiators and total length *L* focused at infinity, the contribution of the *n*th radiator in a direction θ can be written as [24] [26]:

$$E_n \sim a_n e^{j\phi_n} e^{-jkx_n \sin\theta} \tag{2.14}$$

And the total field radiated is proportional to:

$$E(\theta) \sim \sum_n a_n e^{j\phi_n} e^{-jkx_n \sin\theta} \tag{2.15}$$

where a_n and ϕ_n are the relative amplitude and phase of the radiator *n*. If all the radiators are identical and equally spaced (*d*), equation (2.15) can be re-written as:

$$E(\theta) \sim a e^{j\phi} \sum_n e^{-jknd \sin\theta} \tag{2.16}$$

This corresponds to a sum of N equal vectors shifted by a phase equal to $\psi = kd \sin\theta$. This sum is strongly dependant of the value of ψ, in particular, when ψ is such that $N\psi = 2\pi$ the sum is equal to zero. This corresponds to:

$$Nkd \sin\theta = kL \sin\theta = 2\pi \tag{2.17}$$

$$\theta = \sin^{-1}(2\pi / kL) = \sin^{-1}(\lambda / L) \approx \lambda / L \tag{2.18}$$

Which is equivalent to a single antenna of length *D=L*.

2.3 SAR basic operation

For imaging purposes, it is necessary to achieve a fine resolution to obtain images from Earth surface. The main objective of Synthetic Aperture Radar is to obtain high spatial resolution using a conventional antenna. Range resolution is dependant of the pulse bandwidth and it can be improved using spread spectrum pulses such as *chirp* [44]. On the other hand, azimuth resolution depends on the antenna geometry. In order to achieve an azimuth resolution of meters, in spaceborne satellites, an antenna of kilometres will be necessary, which is not feasible. The solution is to use a synthetic antenna array that combines the echoes received with a smaller antenna to get the desired azimuth resolution.

The main objective of SAR system is to improve the azimuth resolution, which in real aperture radar (RAR) is given by [28]:

$$X_a = \lambda h / L_a \cos\theta_l \tag{2.19}$$

For spaceborne SAR, the azimuth resolution is typically many hundreds of metres to many kilometres, because it is not possible to achieve an antenna length comparable with the platform altitude.

For a range distance of 800 Km which could be the case of space platforms and a ratio $L_a / \lambda = 200$, an azimuth resolution of 4 Km is obtained, which is totally unacceptable for imaging applications. To obtain a value of azimuth resolution of 1 Km, which is still insufficient, working at 800 km of slant range, a ratio L_a / λ of 800 will be required. This ratio is impractical for space platforms since it will require an antenna length of 25 meters working in X-band (wavelength of 0.031m).

To obtain a better azimuth resolution, a synthetic aperture technique is used. This method is based on the fact that the targets are in the radar main beam during a significant amount of time while the platform is moving across the sky. This provides information about the surface points from numerous locations along the satellite path.

The Synthetic Aperture Radar technique can be explained in two different ways: the synthetic array approach or Doppler synthesis approach.

2.3.1 Synthetic array approach

An array of antennas is equivalent to a single antenna moving along the array line if the received signals are coherently recorded and processed to perform the synthetic array. Let us consider a system with a sensor velocity *v* and antenna length *L*, the footprint of the antenna main beam in azimuth direction, considering a planar Earth model, is [22]:

$$\xi = 2\lambda h / L\cos\theta_l \tag{2.20}$$

As it can be seen in Fig. 2.7, while the sensor is moving, successive echoes are received at points x_1, x_2, x_3… x_N along the flight line. All these echoes are recorded and coherently processed in order to synthesize the linear array. From Fig. 2.7, we can determine that the maximum length for the synthetic aperture is equal to ξ, while the point P is in the main beam of the antenna.

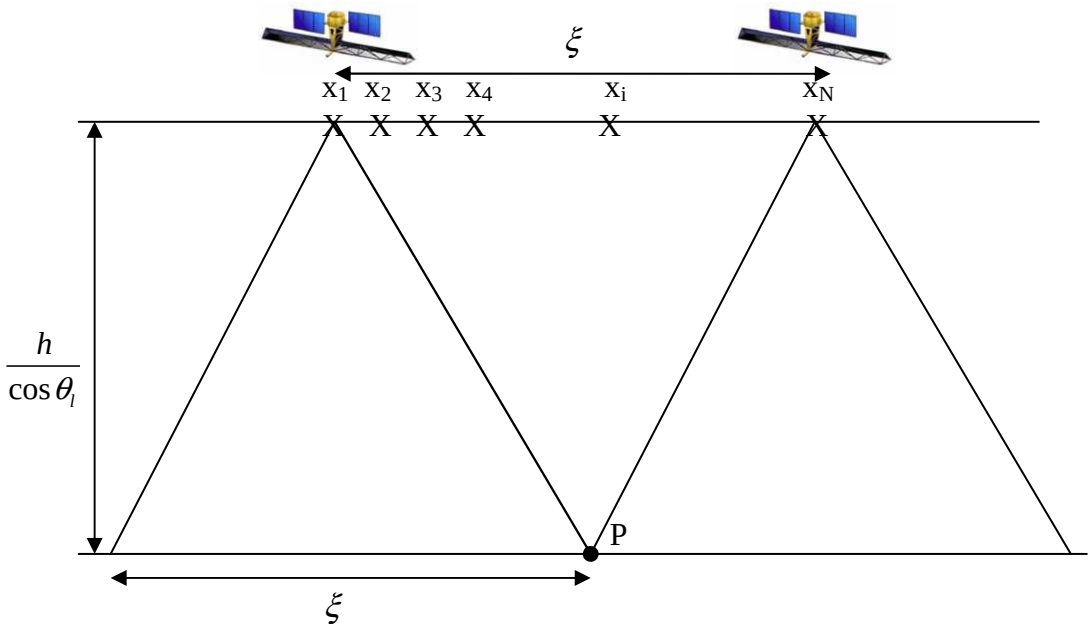

Fig. 2.7 Geometry of synthetic aperture array

From (2.18), the synthesized array beamwidth can be computed as:

$$\theta_s = \lambda / \xi = L \cos\theta_l / 2h \tag{2.21}$$

And the resulting array footprint on the ground is:

$$X_a = h\theta_s / \cos\theta_l = L / 2 \tag{2.22}$$

This corresponds to the finest resolution that can be obtained with the synthetic array. As it can be observed, the azimuth resolution is not dependant of the distance to the targets and the area being imaged. Besides, the azimuth resolution can be improved with a smaller antenna. Although it could seem incoherent, it can be explained in the following way:

- If the sensor is farther, then the footprint on the ground is larger, thus the synthetic array length increases. This leads to a finer synthetic beam which exactly counteracts the increase in distance.
- If the antenna length is smaller, the antenna footprint and, consequently, the synthetic array will be larger. This lead to a finer synthetic beam and a finer azimuth resolution.

2.3.2 Doppler Synthesis Approach

While the radar is moving across the sky, pointing to a stationary target P (Fig. 2.8), the evolution of Doppler shift of the echoes received from this target will first have a positive shift while the platform is moving to the target. This shift will decrease until the platform will be above the target, where the received echo will have no Doppler shift. Then it will become negative by the time P exits the beam. The spectrum of the echo from P covers the region $f_0 \pm f_d$, where f_0 is the operation radar frequency, and the Doppler shift f_d can be obtained as [29]:

$$f_d = \frac{2v}{\lambda} \sin\theta_a / 2 \simeq v\theta_a / \lambda = v / L \tag{2.23}$$

where θ_a is the angle between the position of the sensor and the target in the azimuth direction. The evolution of the Doppler shift can be observed in Fig. 2.8. If the Doppler history of a point P' separated *Xa* from P is analysed, the same evolution will be observed with a time delay of $t = X_a / v$. The shortest time displacement that can be measured after processing the signal with a spectrum bandwidth $B_d = 2 f_d$ is equal to [29]:

$$t_m = 1 / B_d = 1 / 2 f_d = L / 2v \tag{2.24}$$

which provides a finest possible resolution:

$$X_a = v t_m = L / 2 \tag{2.25}$$

Thus, it is demonstrated that this coincides with the finest azimuth resolution achieved with

synthetic array approach (2.22).

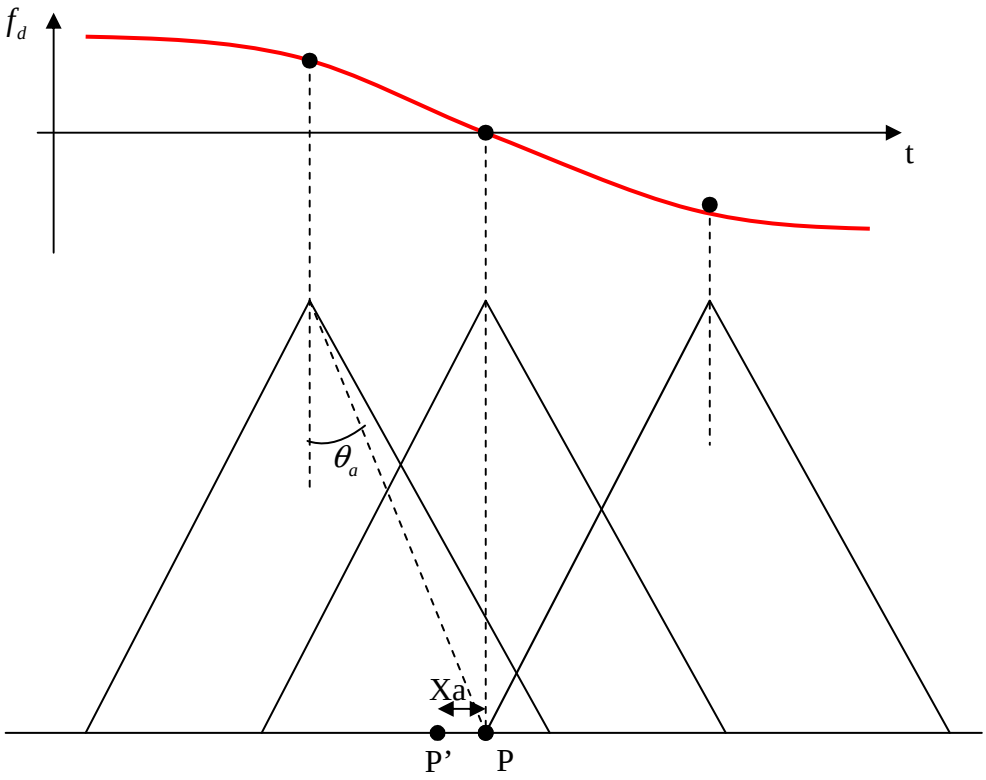

Fig. 2.8 Doppler shift history of the echoes received from point P

For an extended explanation about azimuth resolution consult *Annex B Azimuth resolution in SAR*, where a geometric analysis of the situation is presented to derive the azimuth resolution in SAR systems. Azimuth resolution has been considered as the key element of the SAR operation, hence the presence of this Annex.

2.3.3 SAR imaging coordinate system

Each positioning system has its own coordinate system to locate the targets in the scene. So, while the real aperture radars have an angle-time delay format, in Synthetic Aperture Radar, a Doppler-time delay format is used to locate the targets. The Doppler shift is produced by the relative movement between radar and the targets. So, a unique Doppler shift corresponds to each pointing direction which will make the target location possible. This can be observed in Fig. 2.9

If the configuration of Fig. 2.9 is considered, points which are located on a sphere centred at the radar location have their echoes received simultaneously. If these spheres are intersected with the surface plane where the targets are located, the result is a family of concentric circles, centred at the nadir point, defining lines of equidistance range to the sensor.

On the other hand, points located on coaxial cones, with the flight line as the axis and the

radar location as the apex [27] will produce echoes affected by the same Doppler shifts at the echoes received from them. Once again, if these cones are intersected with the surface plane, a collection of hyperbolas with the same Doppler shift is obtained.

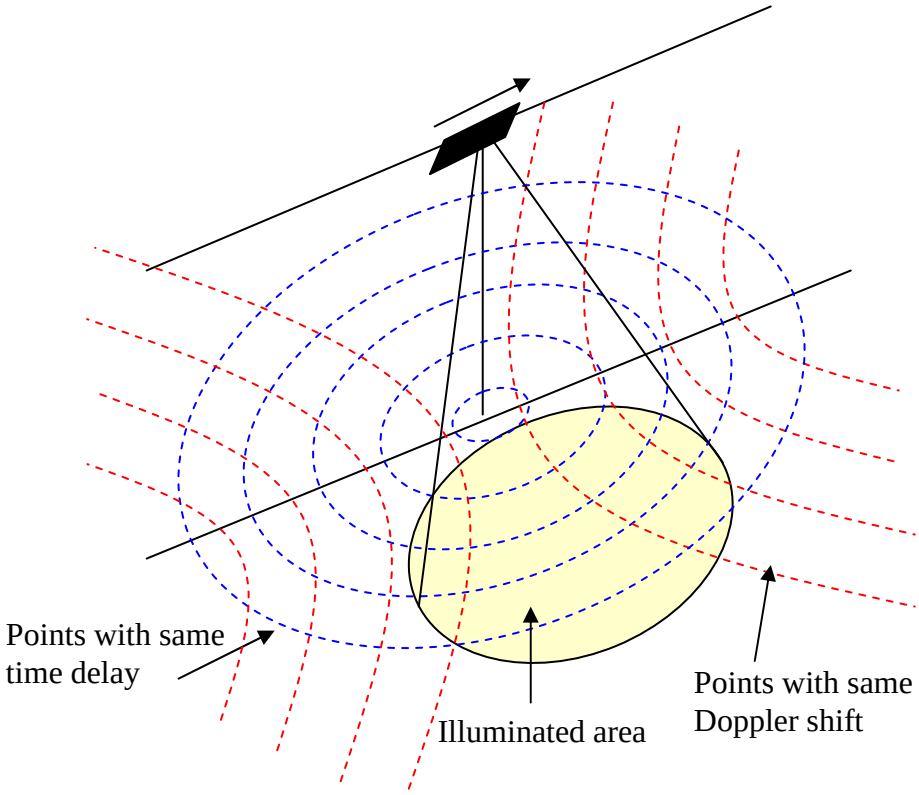

Fig. 2.9 SAR image coordinate system

As it is shown in Fig. 2.9, for a given time delay and Doppler frequency, there is a potential ambiguous point which the same Doppler and time delay than the desired target. It can be easily discriminated pointing the antenna to the desired target.

The brightness that is assigned to a specific pixel for imaging radar is proportional to the echo energy contained in the time delay bin and Doppler bin which correspond to the equivalent point on the surface scanned.

2.3.4 SAR parameters

Until now, SAR basics have been presented. In this section, the most relevant parameters of SAR geometry will be presented and defined. These parameters will be used along this document, so it is necessary to understand them to have a clear vision of SAR system operation.

From Fig. 2.10, Fig. 2.11 and Fig. 2.12, the most relevant parameters can be obtained. These figures show the geometry corresponding to a side looking imaging radar and the range and the azimuth plane cuts, respectively.

In Fig. 2.10, the basic SAR geometry can be observed. The orbital parameters such as altitude (h) and platform velocity (v_e) will define other geometric parameters of the system

that will be explained next. The radar antenna footprint illuminates a surface strip to one side of the nadir track. As the platform moves in its orbit, a continuous strip is mapped along the flight track.

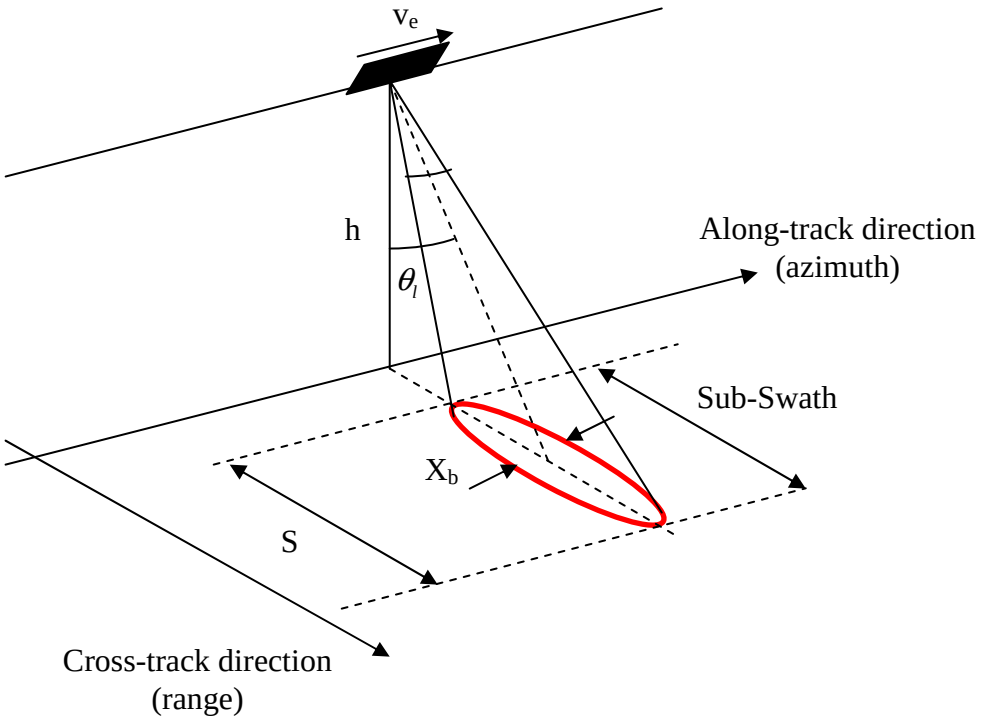

Fig. 2.10 SAR orbital and geometric parameters

Two perpendicular directions can be defined in SAR geometry. The along-track direction is parallel to the flight path of the satellite and it is usually called azimuth. On the other hand, the direction perpendicular to this one, cross-track direction, is called range.

The first parameter defined while the sensor is moving is the ground swath width. The strip width can be obtained from the parameters in Fig. 2.10 as:

$$S \simeq h\theta_r / \cos^2 \theta_l = \lambda h / W \cos^2 \theta_l \qquad (2.26)$$

where θ_r is the elevation beamwidth of the antenna, which can be approximated as $\theta_r = \lambda / W$, as it was explained in the previous section.

On the other hand, another important parameter in SAR geometry that appears in (2.26) is the look angle (θ_l). This corresponds to the angle between nadir and the directions where the antenna is pointing. Changing this angle, it is possible to switch between different sub-swaths illuminating in several range distances. The combination of some sub-swaths will provide high range coverage for some scanning modes.

The width in azimuth of the antenna footprint, defined as X_b in Fig. 2.10, will determine the observation time of the targets, and it will depends on the azimuth beamwidth of the antenna main beam.

In the range plane, the look angle and elevation beamwidth can be observed clearly. In this figure is possible to see the pulse duration τ_P and how it affects to the range resolution (*Xr*). The range resolution, as it will be demonstrated in *2.4 Range resolution*, can be computed as:

$$X_r = c\tau_P / 2\sin\theta_l \tag{2.27}$$

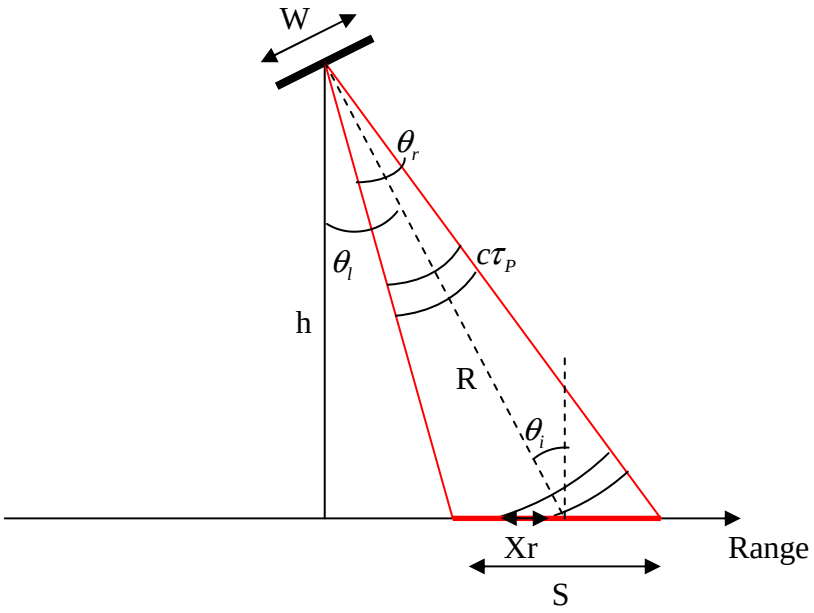

Fig. 2.11 Elevation plane geometry for SAR systems

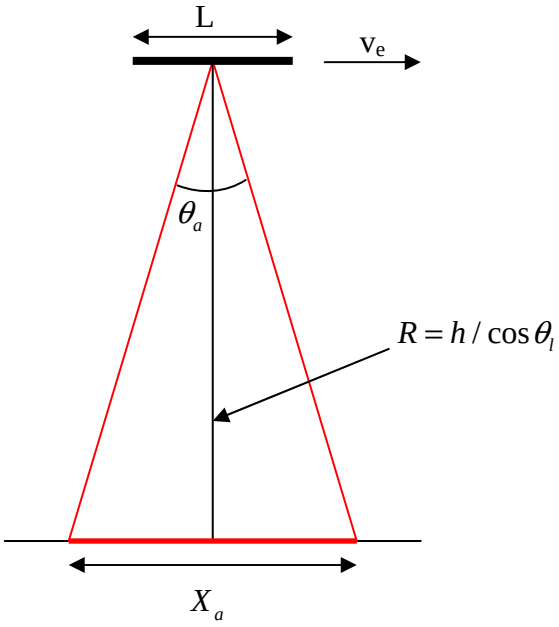

Fig. 2.12 Azimuth plane geometry for SAR systems

An important parameter that can be observed in Fig. 2.11 and which will be used along this document is the incidence angle, which corresponds to the angle between the pointing direction to the surface and the normal vector perpendicular to the incidence plane. Most of the results of this document are given in function of this angle.

Other important concepts in SAR geometry are the middle slant range, which is the distance between the platform and the middle of the swath. The ground range is the distance between the nadir point and the targets into the surface.

In Spaceborne Imaging Radar, a spherical Earth model is used since the planar model is not precise enough. In our case, a planet radius of 6378.15 Km and a platform height of 510 Km are used. A simple diagram of the model geometry is presented in Fig. 2.13. All the parameters in this figure are coherent with the previously explained. The distance between the target and the platform (R), the height of the platform (h) and the planet radius (R_e) are necessary parameters to know the location of the targets.

The distance between the platform and targets must be obtained using the cosine theorem. From parameters to the Fig. 2.13, (2.28) is obtained. The incidence angle (θi), and it can be found from look angle with (2.29). Finally, the distance to the target can be expressed as a function of the incidence angle (2.30).

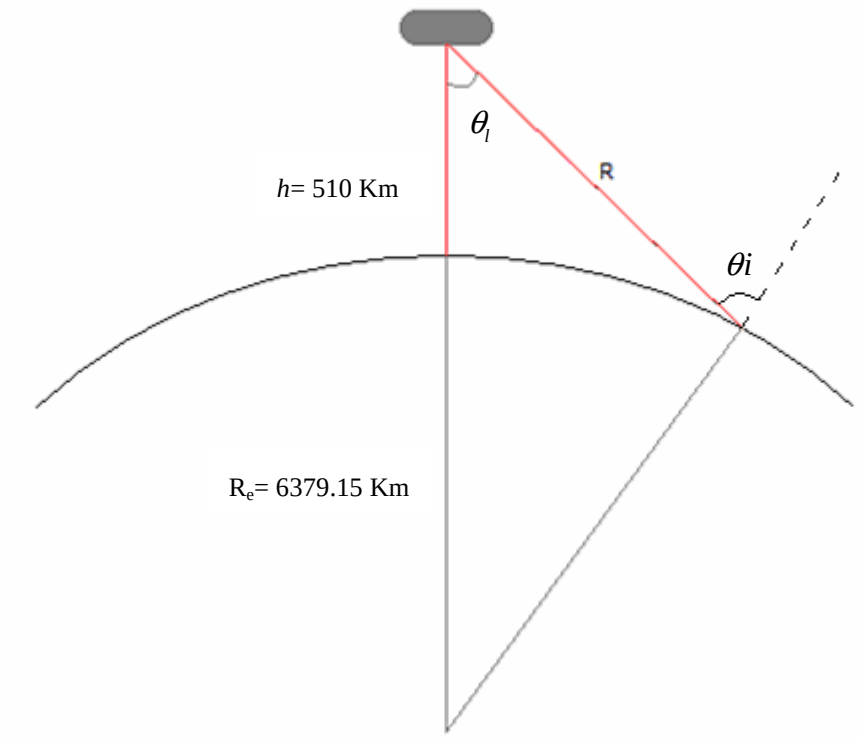

Fig. 2.13 Spherical Earth Model applied to SAR studies

$$R_0^2 = (R_0 + H)^2 + R^2 - 2R\left(R_0 + H\right)cos\theta_l \tag{2.28}$$

$$\theta_i = \sin^{-1}\left(\left(\frac{H + R_0}{R_0}\right)\sin\theta_l\right) \tag{2.29}$$

$$R_0^2 = (R_0 + H)^2 + R^2 - 2RR_0\sqrt{\left(\frac{H + R_0}{R_0}\right)^2 - \sin^2\theta_i} \tag{2.30}$$

Solving 2nd degree equation two solutions are obtained for target distance (*R*). The higher one must be dismissed since it does not represent a real solution in this case. In Table 2.2, there are some results applying (2.28) or (2.30) with different incident angle and the error resulting using planar Earth model instead of the spherical model.

Incident angle	Look Angle	Spherical model distance (Km)	Planar model distance (Km)	Planar model Error (Km)	Relative error
20,00	18,45	X1 = 12531 ;X2 =544	542	2	0.37%
25,00	23,02	X1 = 12124 ;X2 =563	558	5	0.89%
30,00	27,56	X1 = 11634 ;X2 =586	580	6	1.02%
35,00	32,06	X1 = 11066 ;X2 =616	606	10	1.62%
40,00	36,50	X1 = 10426 ;X2 =654	639	15	2.29%
45,00	40,87	X1 = 9722 ;X2 =702	680	22	3.13%

Table 2.2 Distance to the targets depending to the incident angle

2.4 Range resolution

The range resolution corresponds to the minimum ground distance between two points on the surface which can be discriminated and analysed as two point targets independently in range direction. If we take two points separated *Rg*, the returns will be received at the radar with a time separation Δt which can be obtained as:

$$\Delta t = \frac{2R_g}{c}\sin\theta_i \tag{2.31}$$

where θ_i is the incident angle which radar is pointing to the target. This equation can be easily demonstrated with Fig. 2.14.

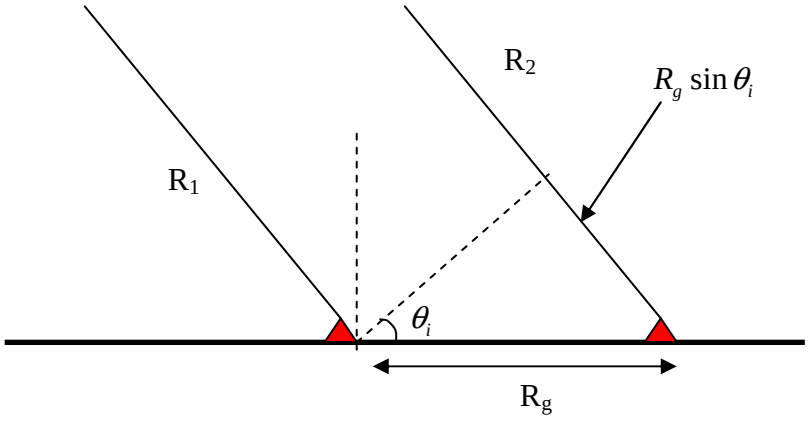

Fig. 2.14 Range resolution analysis for SAR

If we consider that the distance to the radar is much larger than the separation between targets, the antenna illumination beams can be considered parallel for both points. So, the distance R_2 can be expressed as the sum of R_1 and $R_g \sin\theta_i$. The relative range distance between both targets can be expressed as:

$$\Delta R = |R_1 - R_2| = |\cancel{R_1} - \cancel{R_1} - R_g \sin\theta_i| = R_g \sin\theta_i \tag{2.32}$$

Substituted in (2.33), the relationship between ground distance between targets and time difference in the receiver is obtained:

$$\Delta t = \frac{2\Delta R}{c} = \frac{2R_g}{c}\sin\theta_i \tag{2.33}$$

To get the range resolution for SAR system, it is necessary to determine the minimum time difference that receiver can discriminate two different targets. In SAR systems, two received echoes will be analysed separately if the time difference between them is larger than the pulse duration τ_P, which in general is defined as:

$$B = 1/\tau_P \tag{2.34}$$

Equation (2.34) corresponds to a rectangular pulse where the pulse bandwidth is the inverse of pulse duration. It is possible to use more sophisticate pulses, such as chirp, with pulse duration much larger than the inverse of the pulse bandwidth, but they can be compressed [30] to this value. So, the range resolution can be expressed for any pulse as:

$$R_g = \frac{c}{2\sin\theta_i}\Delta t = \frac{c}{2\sin\theta_i}\frac{1}{B} \tag{2.35}$$

2.5 PRF selection

The choice of the Pulse Repetition Frequency or PRF is constrained by a number of other factors. As we will see in ambiguity analysis, azimuth and range ambiguities are highly dependent of the PRF but, unfortunately, it has other restrictions that do not allow us to choose an arbitrary PRF.

A low value of PRF increase the azimuth ambiguity levels since spectral replicas that appear at multiples of PRF, will increase the aliasing of azimuth spectra. On the other hand, a high PRF will reduce the interpulse period and, as a result, the range ambiguities will be degraded since pulses are sent closely producing an overlap between consecutive received pulses in time. Ambiguities are widely explained in Chapter 5.

Besides, in SAR system the PRF selection has to fulfil other restrictions. SAR techniques use the same antenna for both transmit and receive, so time must be divided between transmission and reception. The transmit event must be interspersed between data reception. Furthermore, the values of the PRF must be selected such that the strong nadir returns from succeeding pulses do not arrive during the data reception window.

The first restriction, which we call the transmit interference, can be modelled with the next equations:

$$Frac\left(2R_1 PRF / c\right) / PRF > \tau_P + \tau_{RP} \tag{2.36}$$

$$Frac\left(2R_N PRF / c\right) / PRF > \frac{1}{PRF} - \tau_{RP} \tag{2.37}$$

and

$$Int\left(2R_N PRF / c\right) = Int\left(2R_1 PRF / c\right) \tag{2.38}$$

In these equations, R_1 is the slant range to the first data sample, R_N is the slant range to the last data sample in the recording window, τ_P is the duration of the pulse in transmission, and τ_{RP} is the protection time used in reception to avoid that emitted and received pulses present interferences. This value is, in most systems, about τ_P. Finally, the function *Frac* extracts the fractional portion of its argument, while the function *Int* takes the integer portion of the value. In order to illustrate these equations, Fig. 2.15 a) shows the timing diagram of the radar emission-reception.

The data window, as we can see in the figure, has to be between two consecutive pulse transmissions. This is imposed by equation (2.38) where the first and last data in one data reception are in the same inter-pulse time. Furthermore, equation (2.36) guarantees that the first data arrives after the protection time, while (2.37) adjusts the PRF such the last data taken arrives before the protection time of next emitted pulse.

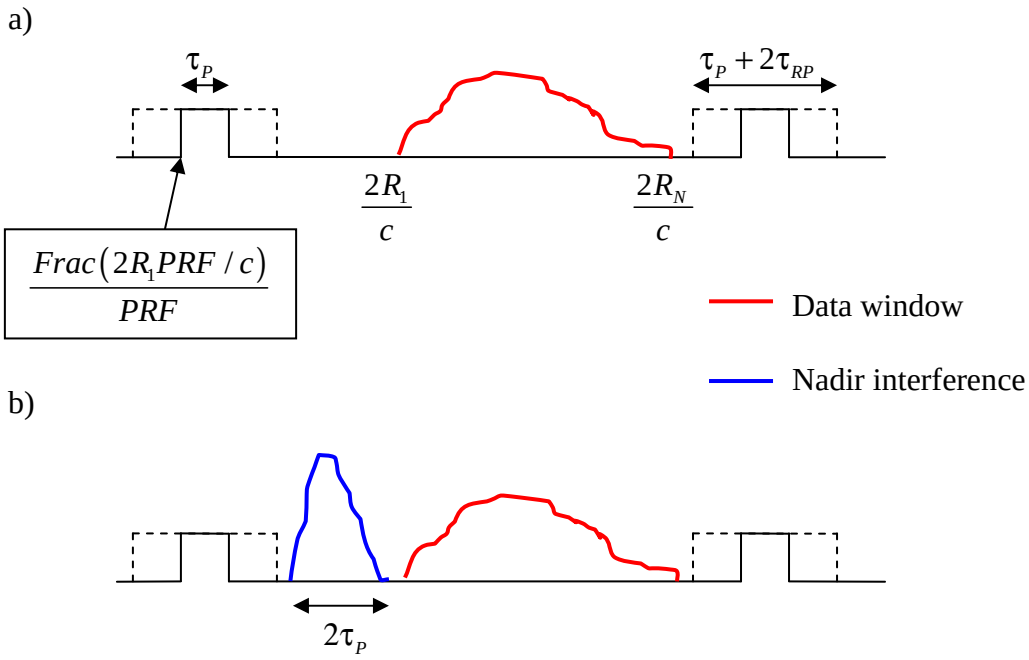

Fig. 2.15 Timing diagram for PRF constraints: a) transmit interference and b) nadir interference

On the other hand, we must be sure that the nadir return does not interfere to reception windows. For this reason, as it can be observed in Fig. 2.15 b), PRFs have to fulfil equations (2.39) and (2.40).

$$2h/c + j/PRF > 2R_N/c \qquad j = 0, \pm 1, \pm 2, ...\pm n_h \qquad (2.39)$$

$$2h/c + 2\tau_P + j/PRF < 2R_1/c \qquad j = 0, \pm 1, \pm 2, ...\pm n_h \qquad (2.40)$$

where h is the platform altitude above the surface nadir point. In this equation, the duration of nadir return is considered $2\tau_P$. Actually, the duration of nadir return depends on the terrain and its characteristics, but it is a good approximation for the case studied. Equation (2.39) adjusts the PRF such all the nadir returns of succeeding and preceding pulses (index j) arrive after the last data of recording window. On the other hand, and considering $2\tau_P$ as the duration of nadir echo, we must assure that these returns do not extend further than the next data reception window. This constraint is given by equation (2.40).

Rang of selectable PRFs will be established by the maximum acceptable range and azimuth ambiguity to signal ratios, as well as transmit and nadir interference explained previously. So, for a swath configuration of a SAR system, there will be some no acceptable PRFs depending on the incidence angle, which will restrict the PRF selection of each sub-swath.

For this purpose, the excluded zones are represented in a diamond diagram. In case of PAZ system, the diagrams of Fig. 2.16 and Fig. 2.17 are obtained, showing transmit and nadir interference constrictions and the range of selectable PRFs for each sub-swath in Stripmap

and ScanSAR modes respectively.

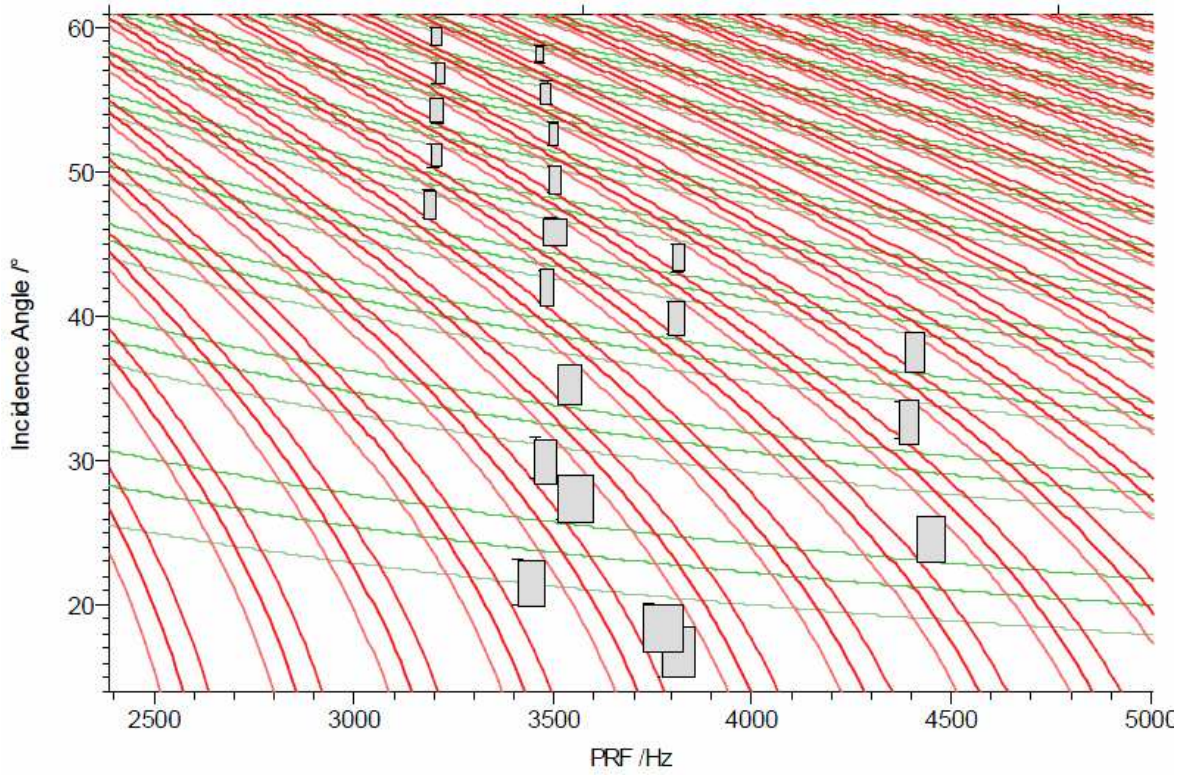

Fig. 2.16 Diamond diagram for Stripmap. In red are plotted the transmission interference while in green the nadir return problematic PRFs[34]

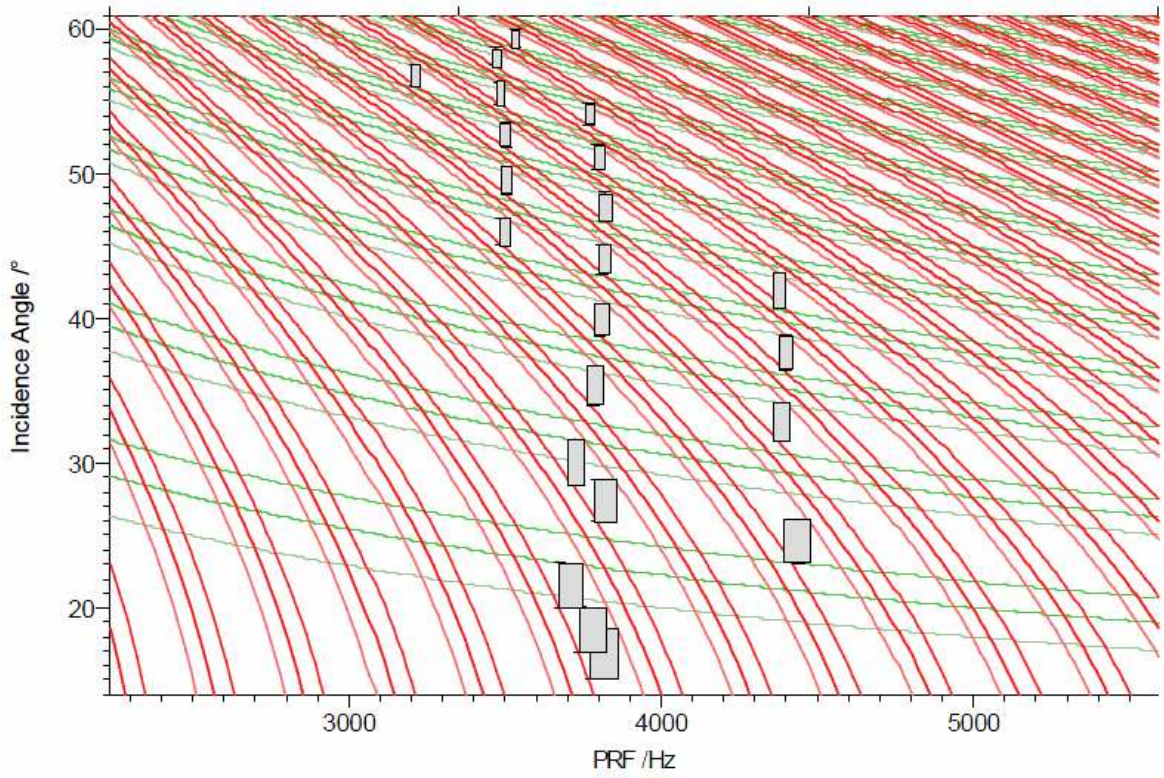

Fig. 2.17 Diamond diagram for Stripmap. In red are plotted the transmission interference while in green the nadir return problematic PRFs[34]

In diamond diagrams presented, red lines indicate the problematic zones due to transmit interference while green zones indicate problems with nadir interference. In design of SAR system, the PRF of each sub-swath must be chosen such that they will be in grey zones of the diagrams. So, for example, in sub-swath 1 in Stripmap mode, we could select a PRF from 3.75 KHz to 3.85 KHz. On the other hand, in some sub-swaths, such as SS3 in Stripmap, it is no possible to select a PRF that fulfil all the requirements and, in these cases, the most undesirable effect is the transmit interference, so we will select a PRF that will not satisfy nadir interference constraints completely.

2.6 System design consideration

When a SAR imaging system is designed, a large number of parameters have to be chosen in order to fulfil the desired requirements. The end-to-end design involves tradeoffs between these parameters which are interrelated. The final design is the result of the system designers, the hardware engineers, the platform engineers and scientific users' interactions. Consequently, it is necessary to do a large number of iterations to obtain the final configuration for the SAR system.

There is not a fixed way to proceed when a SAR system is designed. The process of defining and choosing all the parameters depends on the input parameters given. These input parameters are fixed by platform orbital characteristics (v and h) or radar operation values (λ). In this example, swath width will be taken as an input parameter too. Azimuth resolution is another key design parameter that user sets in the system definition. With these first parameters we can obtain some of the design parameters of the antenna:

$$S = \lambda h / W \cos^2 \theta_l \tag{2.41}$$

where S is the swath width, h the platform altitude, λ the radar wavelength, W the antenna width and θ_l is the look angle. This relationship can be derived from Fig. 2.18 where all these parameters are shown.

With the equation (2.41) is easy to obtain the antenna width that provides the desired swath width:

$$W = \frac{\lambda h}{S \cos^2 \theta_l} \tag{2.42}$$

On the other hand, the antenna length will be determined by the desired azimuth resolution (X_a). In SAR system, as it has been demonstrated in Chapter 2, the azimuth resolution is computed as $L_a/2$. With this equation we obtain the antenna length:

$$L = 2X_a \tag{2.43}$$

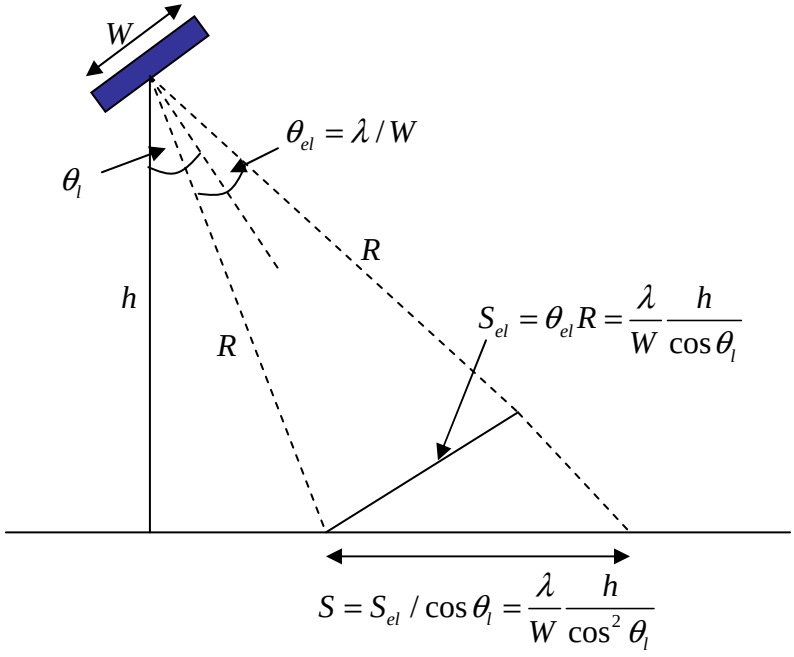

Fig. 2.18 Swath width definition

Similarly as swath width, the azimuth footprint can be determined. Considering the azimuth beamwidth $\theta_{az} = \lambda / L$, and the distance to the target $R = h / \cos\theta_l$, the azimuth footprint length can be computed:

$$X_b = \theta_{az} R = \frac{\lambda h}{L \cos\theta_l} \tag{2.44}$$

this provides an integration time equal to:

$$T_i = X_b / v \tag{2.45}$$

The backscatter cross section which provides a SNR=1, called thermal noise equivalent backscatter (σ_n), now can be already determined [32]:

$$\sigma_n = \frac{8\pi k T B^2 \lambda h^3}{P_t G W^2 L c} \frac{\sin\theta_l}{\cos^4\theta_l} \tag{2.46}$$

From thermal noise equivalent backscatter, $SNR(thermal) = \sigma / \sigma_n$ is defined. A value of 5 or more is usually desired in system design.

Until now, only antenna parameters and quality ratios have been obtained. Besides, radar basic parameters must be defined to assure a correct operation. One of the most important parameters is the PRF which will be really important in ambiguity analysis and echoes reception. On one hand, a PRF that fulfils Nyquist criterion has to be chosen (2.47) but, moreover, the PRF has to avoid the overlap of successive echoes (2.48) [29]:

$$PRF > 2v / L \tag{2.47}$$

$$PRF < \frac{cW\cos^2\theta_l}{2\lambda h\sin\theta_l} = \frac{c}{2S\sin\theta_l} \tag{2.48}$$

These two equations give another constraint in the antenna physical parameters. To satisfy the above two inequalities, next one must be fulfilled:

$$WL > \frac{4\lambda hv\sin\theta_l}{c\cos^2\theta_l} \tag{2.49}$$

Furthermore, the PRF has to be chosen in order to avoid the coincidence between the data reception and the return from nadir and transmission time. From Fig. 2.15 in section *2.5 PRF selection*, the time while we are receiving is:

$$t = \frac{2h}{c\cos\theta_l} \text{ to } t = \frac{2h}{c\cos\theta_l} + 2\frac{S}{c}\sin\theta_l + \tau' \tag{2.50}$$

To avoid the nadir returns, this time has not to coincide with:

$$t = \frac{2h}{c} + \frac{n}{PRF} \text{ to } t = \frac{2h}{c} + \frac{n}{PRF} + \tau' \tag{2.51}$$

The transmission time has not to coincide with echoes in order not to lose signal returns. This imposes that the reception temporal windows neither should coincide with:

$$t = \frac{n'}{PRF} \text{ to } t = \frac{n'}{PRF} + \tau' \tag{2.52}$$

These are the most relevant parameters that we need to consider when a SAR system is designed. However, once these parameters are chosen, azimuth and range ambiguities, antenna integrated noise, total system noise… must be computed. If one of them is under the minimum values to assure the right operation of the radar, some of the computed parameters should be modified and recalculated again.

In Fig. 2.19, the flow diagram of the process presented above is shown. As we can see the input parameters (λ, θ, *h*, *S*, *v*, and *Xa*) are in boxes. From these parameters, the other key values of the system are defined.

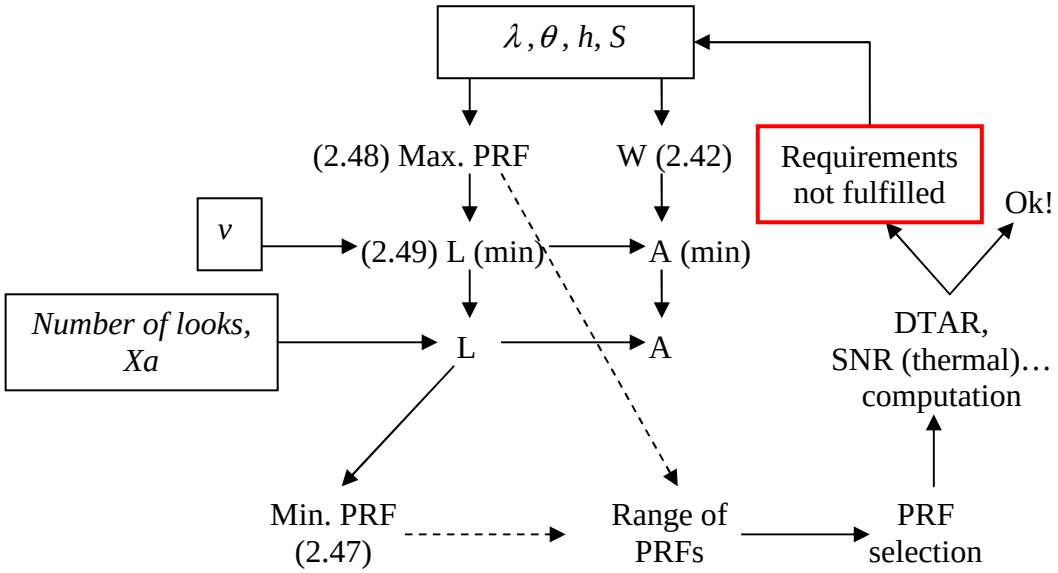

Fig. 2.19 SAR parameters flow diagram

2.7 SAR scanning modes

As SAR technologies have been developing, different scanning modes have been defined in order to fulfil the requirements of each mission. The main operating mode is Stripmap, but nowadays other modes can be programmed in the radar. So, the most common alternative modes are Spotlight and ScanSAR, which will be described next.

On the other hand, another mode has been proposed recently. The study and evaluation of this mode, called TOPSAR mode, is the main topic of this project and it will be explained and analysed in Chapter 3. In this section, Stripmap, Spotlight and ScanSAR mode characteristics will be presented in order to have an approximation to the Synthetic Aperture Radar scanning options.

2.7.1 Stripmap mode

Stripmap mode is the basic SAR imaging mode. The antenna points to a fixed direction in range and azimuth. The points in the surface are illuminated by the main-beam of the antenna while the satellite flies over the scene. The platform movement makes possible to illuminate all the points with the complete scanning beam which provides an image with constant quality in azimuth. The main geometry of Stripmap mode can be observed in Fig. 2.20.

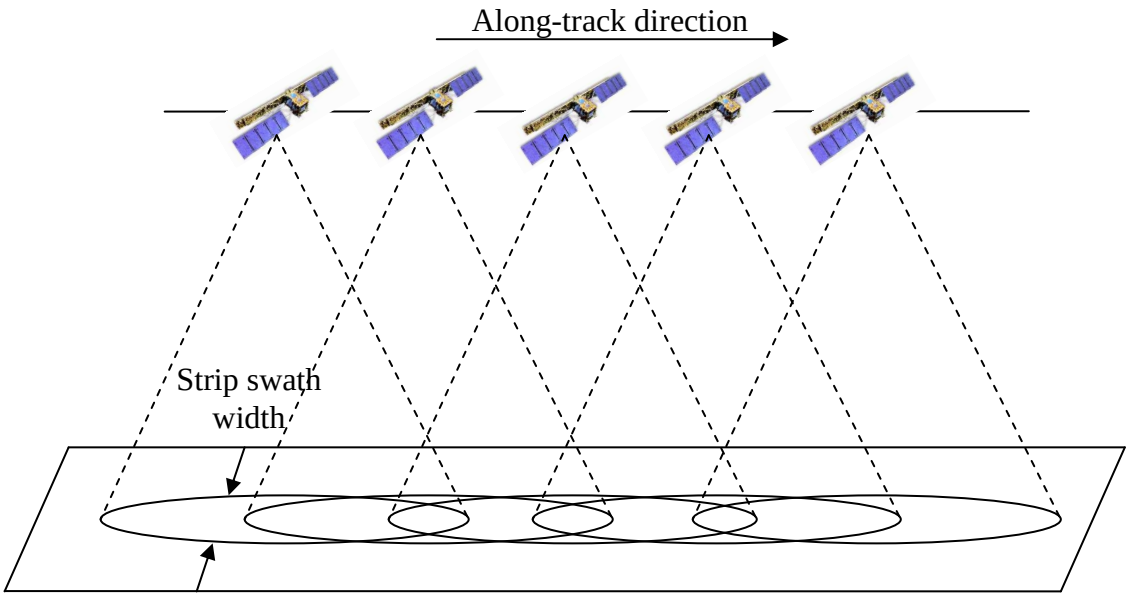

Fig. 2.20 Stripmap mode geometry

As we can see, the pointing direction of the antenna is fixed, and it is the satellite movement that allows us to scan all the points in azimuth. Furthermore, each point in azimuth is seen by the antenna in different relative positions which is equivalent to a antenna array if the returns are processed at the receiver. This mode provides high azimuth resolution with low range coverage. The particular parameters for TerraSAR-X working in Stripmap mode can be observed in Table 2.3 [33].

Parameter	Value
Scene Extension (azimuth)	50 Km. Standard Max. 1650 Km
Swath width (ground range)	30 Km (single polarization) 15 Km (double polarization)
Data access incidence angle range	15º - 60º
Full performance incidence angle range	20º - 45º
Number of elevation beams	27
Azimuth resolution	3 meters at 150 and 300 MHz
Ground range resolution	1.55 – 3.21 meters @ 45º - 20º incidence angle
Polarization	Singe pol. (HH, VV) Dual pol. (HH/VV, HH/HV, VV/VH)

Table 2.3 Characteristics for Stripmap mode in TerraSAR-X

2.7.2 Spotlight mode

Spotlight mode uses an azimuth steering of the antenna main beam to increase the illumination time of the targets or, equivalently, the size of synthetic aperture. With this feature, it is possible to improve the azimuth resolution but, on the other hand, we will lose azimuth scene size. If we consider that the steering counteracts the platform movement, the antenna footprint will remain on the scene and, consequently, the azimuth scene size will correspond to the azimuth footprint size.

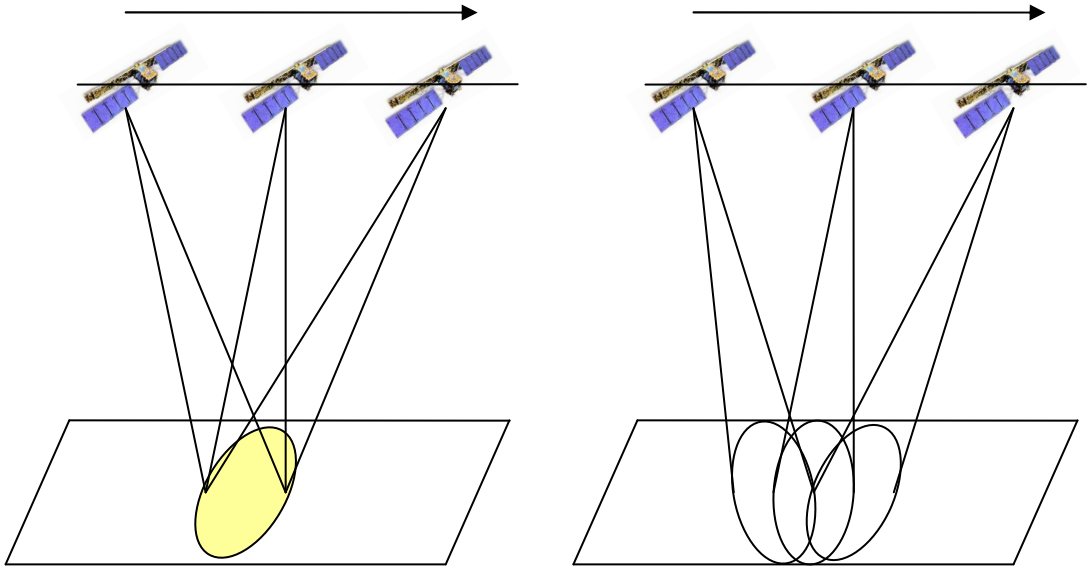

Fig. 2.21 Spotlight and High Resolution Spotlight modes geometries

Parameter	Value
Scene Extension (azimuth)	5 Km. SL 10 Km. HS
Swath width (ground range)	10 Km
Data access incidence angle range	15º - 60º
Full performance incidence angle range	20º - 55º
Number of elevation beams	249
Azimuth resolution	1 m and 2 m (single pol) 2 m and 4 m (dual pol)
Ground range resolution	1.34 – 3.21 meters
Polarization	Singe pol (HH, VV) Dual pol (HH/VV)

Table 2.4 Characteristics for Spotlight modes in TerraSAR-X

We have two variants of Spotlight mode which will provide different azimuth resolutions and scene size. The Spotlight Mode (SL) steers the antenna beam in a way that the platform movement is compensated. As a result, the footprint is illuminating the same surface zone while the antenna crosses the sky. The other variation, called High Resolution Spotlight (HS), presents an azimuth steering that does not compensate completely the along-track movement, providing worse azimuth resolution but higher azimuth scene size. A simple diagram to understand both alternatives is presented in Fig. 2.21. The main characteristics for these modes in TerraSAR-X are described in Table 2.4 [33].

2.7.3 ScanSAR mode

In ScanSAR mode the antenna beam steering is in range direction. This elevation steering is used to divide the scanning time to different incidence angle corresponding to different sub-swaths. Thus, it is possible to obtain a swath width of more than 100 Km, higher than in Stripmap or Spotlight modes (25 Km.). On the other hand, due to the alternation between beams, only bursts of SAR echoes are received from each swath, resulting in a reduced azimuth resolution. There is no azimuth steering in this mode.

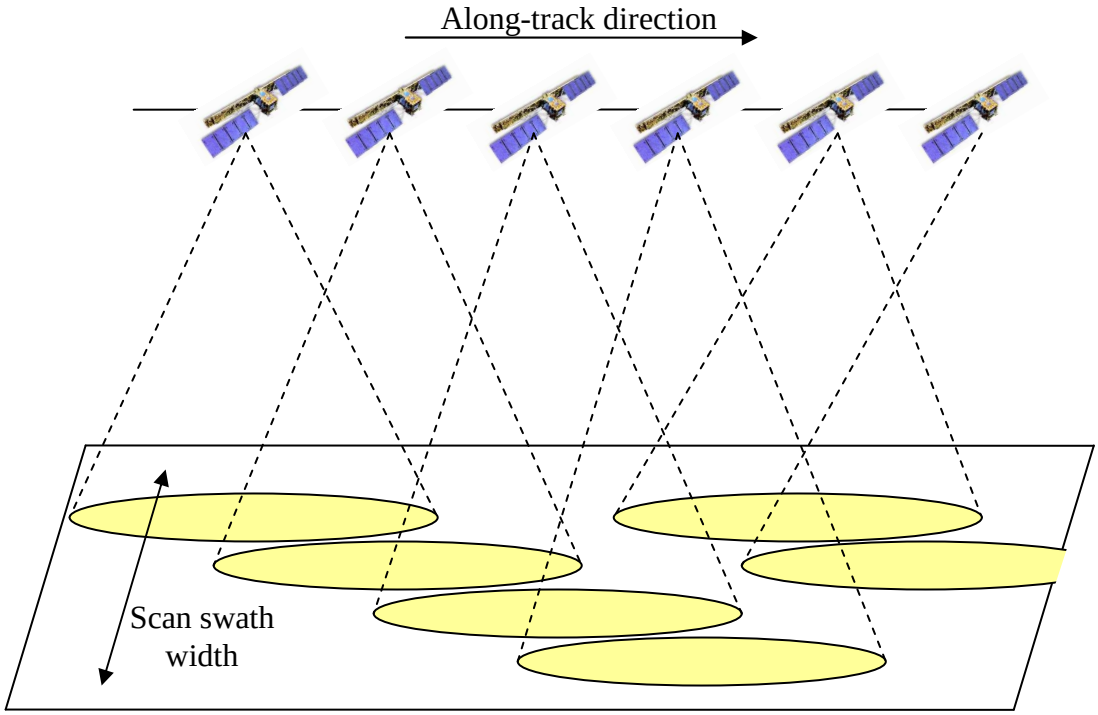

Fig. 2.22 ScanSAR mode geometry

Parameter	Value
Standard scene extension	150 Km (azimuth) x 100 Km (ground range)
Number of sub-swaths	4
Swath width (ground range)	100 Km
Max. acquisition length	Ca. 1650 Km
Data access incidence angle range	15º - 60º
Full performance incidence angle range	20º - 55º
Number of elevation beams	27
Azimuth resolution	16 m
Ground range resolution	1.55 – 3.21 meters @ 45º - 20º incidence angle

Table 2.5 Characteristics for ScanSAR mode in TerraSAR-X

The number of looks of each target is equal to the lower integer of the ratio T_F/T_R, being T_F the footprint time and T_R the time between two consecutive explorations of the same swath.

Fig. 2.23 shows the number of looks of different targets considering a footprint time more than four times longer than inter-burst time. Each target along the track is illuminated four times before the footprint crosses the space. The figure shows the azimuth movement of the footprint in one sub-swath and how many times it sees the targets located in azimuth positions 1 and 2.

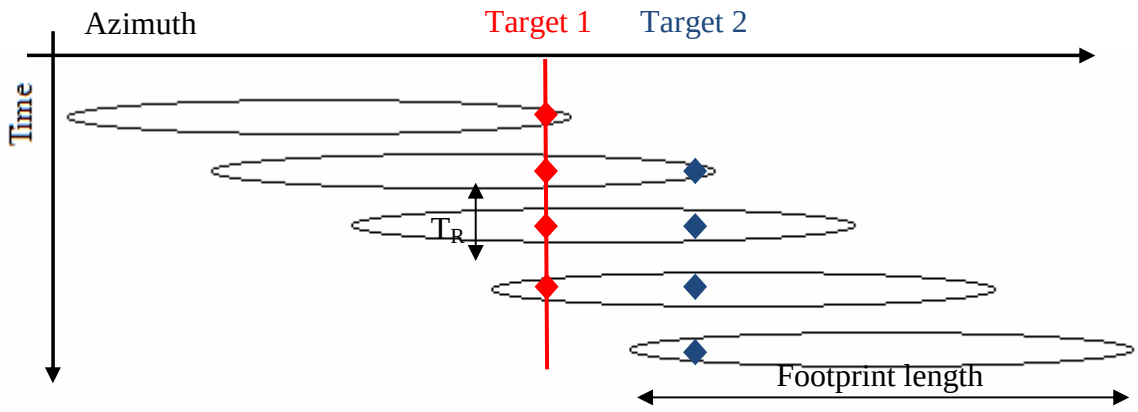

Fig. 2.23 Footprint movement along-track direction

ScanSAR system provides a wide-coverage with only one pass of the satellite making it really interesting for imaging applications. However, ScanSAR mode has some disadvantages due to its acquisition scheme. In Fig. 2.24, these drawbacks can be observed when the radar is illuminating three targets in different azimuth location. Each target presents different response to the radar illumination because of the non-uniform antenna gain. That's why not all the points in the image have the same received power.

ScanSAR mode will be really interesting to analyse the new scanning mode called TOPSAR since it combines the azimuth and elevation steering to solve some of the ScanSAR problems. The most important drawback of ScanSAR that can be avoided with TOPSAR is the azimuth non-uniformity of received echoes. Some targets in the scene can be seen only by the edge of the main beam, producing lower returns than other points that can be illuminated by the centre of the antenna beam. This undesired effect will cause a problem in reception that is called scalloping, which we try to solve with the TOPSAR mode. This unavoidable effect is presented in Fig. 2.25. The geometry and parameters of TerraSAR-X working with ScanSAR mode are presented in Fig. 2.22 and Table 2.5 respectively [33].

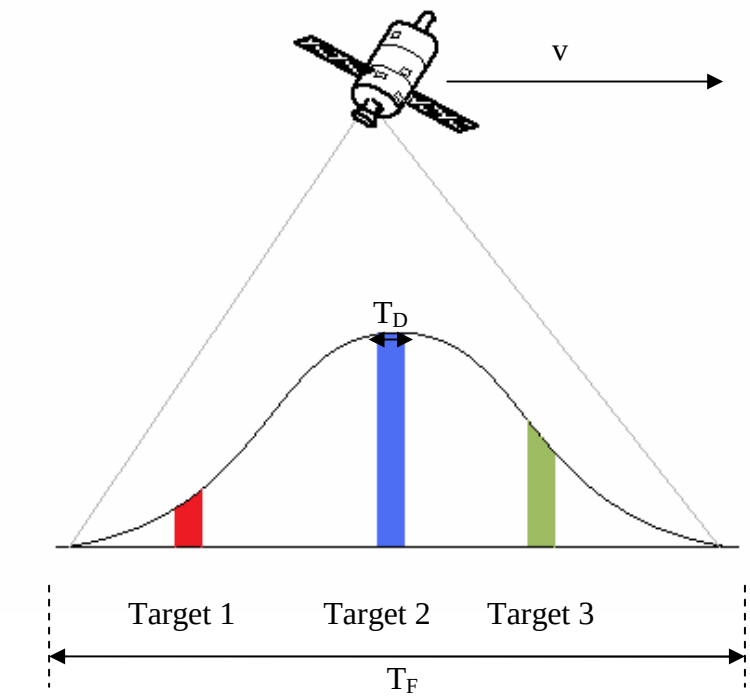

Fig. 2.24 Azimuth dependant problems in ScanSAR acquisition mode

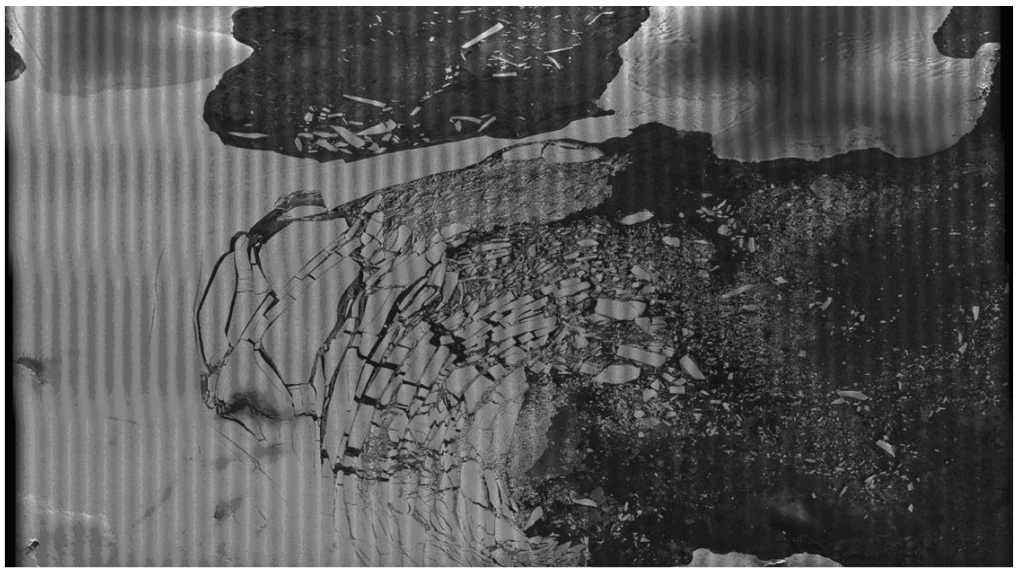

Fig. 2.25 Scalloping effect in ScanSAR mode

2.8 Doppler history and azimuth dependency

In SAR systems the Doppler frequency of received echoes is connected to the satellite platform relative movement to ground targets. The Doppler frequency can be expressed in terms of the azimuth displacement or slow time τ as:

$$f_D(\tau) = k_R \tau \tag{2.53}$$

where the burst centre has been chosen as the time origin, so the zero-Doppler correspond to the azimuth direction where the antenna beam points perpendicularly to the swath; and K_R is the Doppler rate which in the rectilinear geometry can be calculated as [35]:

$$k_R = \frac{1}{2\pi}\frac{\partial^2 R(\tau)}{\partial \tau^2} = -\frac{2v_e{}^2}{\lambda R_0} \tag{2.54}$$

where R_0 is the closest approach distance (slant middle range) and v_e is the effective antenna spot velocity on the ground. From (2.54), with an observation time per target T_D (dwell time), the Doppler Bandwidth of each target can be compute as follows:

$$B_a = |k_R| T_D \tag{2.55}$$

Assuming the parameters of the TerraSAR-X system, similar to PAZ parameters, the values of Table 2.6 are obtained. For this example a T_D of 0.08 seconds has been used. Twelve sub-swath parameters have been computed using an effective velocity of 7043.08 m/s and a satellite height of 510 Km.

2.9 The azimuth antenna pattern (AAP)

The Azimuth Antenna Pattern (AAP) corresponds to the antenna main beam pointing evolution of the targets while the platform is moving across the sky. The AAP shape has more importance in ScanSAR mode, where not all the targets in the image are illuminated by the same part of the antenna beam. Consequently, the power of the echoes will not be uniform although the surface presents constant reflectivity. To study TOPSAR mode, the AAP will be modelled as a $sinc^2$ function as in (2.56). The shape depends on the antenna length, the radar operation wavelength and finally the angle ϕ between the target illumination direction and the perpendicular direction to the ground.

$$G_a(\phi(\tau)) \approx G_0 sinc^2\left(\frac{L}{\lambda}\phi(\tau)\right) \tag{2.56}$$

The variation of the angle ϕ is produced by the sensor movement, target displacement is considered zero because the surface usually remains static in the few seconds elapsed for each point in Synthetic Aperture acquisition. In Fig. 2.26, the variation of the angle is shown while the platform is moving across the space. The azimuth relative position between the target and the radar changes due to platform movement and the distance to the ground is given by slant middle range (R_0).

Swath Name	Slant middle range	k_R (Hz/s)	Ba (Hz)	Max. Fd (Hz)
SM-S_1	530.654	-6032.2	482.5750	±241.2875
SM-S_1	535.591	-5976.6	478.1267	±239.0633
SM-S_3	545.367	-5869.4	469.5560	±234.7780
SM-S_4	556.535	-5751.7	460.1334	±230.0667
SM-S_5	569.041	-5625.3	450.0209	±225.0104
SM-S_6	582.777	-5492.7	439.4139	±219.7070
SM-S_7	597.665	-5355.9	428.4680	±214.2340
SM-S_8	613.620	-5216.6	417.3272	±208.6636
SM-S_9	630.549	-5076.5	406.1228	±203.0614
SM-S_10	648.385	-4936.9	394.9511	±197.4755
SM-S_11	667.109	-4798.3	383.8658	±191.9329
SM-S_12	686.570	-4662.3	372.9850	±186.4925
SM-S_13	706.747	-4529.2	362.3366	±181.1683
SM-S_14	727.518	-4399.9	351.9918	±175.9959
SM-S_15	748.938	-4152.7	341.9246	±170.9623
SM-S_16	770.825	-4274.1	332.2159	±166.1080
SM-S_17	793.259	-4035.3	322.8206	±161.4103
SM-S_18	816.207	-3921.8	313.7444	±156.8722
SM-S_19	839.471	-3813.1	305.0497	±152.5248
SM-S_20	863.089	-3708.8	296.7021	±148.3511
SM-S_21	887.235	-3607.8	288.6274	±144.3137
SM-S_22	911.614	-3511.4	280.9087	±140.4544

Table 2.6 Doppler characteristics of each sub-swath

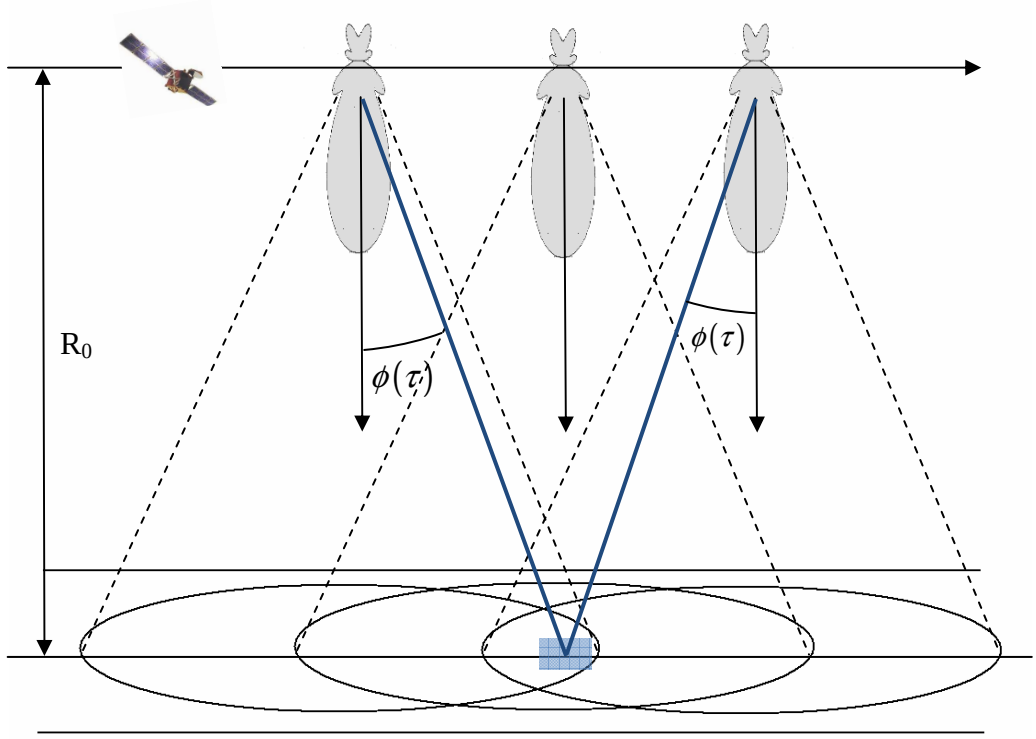

Fig. 2.26 Variation of the antenna azimuth pointing angle due to his own movement

The ground distance between the azimuth target location and the azimuth point perpendicular to the platform is dependant to the slow time and the platform velocity. If we take τ = 0 when the platform pass over the target (plot as a blue square in Fig. 2.26), then the azimuth ground distance can be expressed as $v_e\tau$. The product $v_e\tau$, usually, is much lower than R_0, so it is possible to approximate angle tangent for its argument (2.57). Finally, using (2.57) in (2.58), we get a useful approximation of the AAP in function of the slow time τ which is clearly related to the relative azimuth position between the target and the radar sensor.

$$\tan\left(\phi(\tau)\right) = \frac{v_e\tau}{R_0} \approx \phi(\tau) \qquad \left(R_0 \gg v_e\tau\right) \tag{2.57}$$

$$G_a\left(\phi(\tau)\right) \approx G_0 sinc^2\left(\frac{L}{\lambda}\frac{v_e\tau}{R_0}\right) \tag{2.58}$$

With TerraSAR-X parameters, and taking as an example the sub-swath SS6 (R_0=600.9 Km) the results in Table 2.7 are obtained. Fig. 2.27 shows the azimuth antenna pattern in dB in function of the slow time or displacement of the platform, with a platform velocity of 7605.92 m/s and R_0 of the SS1, SS6 and SS12. The main lobe of the antenna has a -3 dB bandwidth of approximately $\Delta\tau$ = 0.406, which corresponds to $\Delta\phi$ of 0.33 degrees. With these results, a target will be seen by the main lobe of the antenna with an amplitude loss lower than 3 dB while the azimuth displacement between the pointing direction and the target azimuth position would be lower than 1.712 Km.

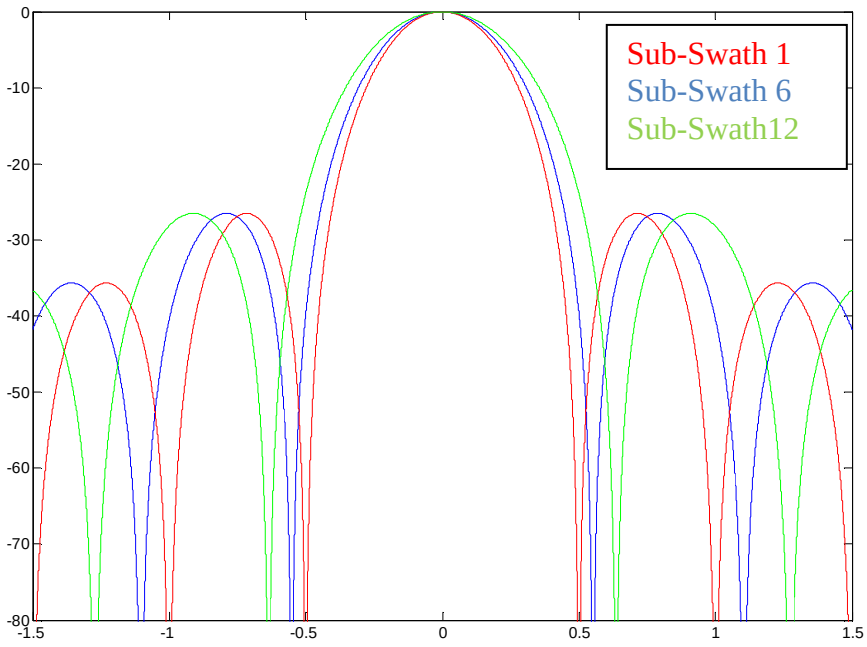

Fig. 2.27 Azimuth antenna pattern in SS1, SS6 and SS12

τ	Ga (sinc)	$\|Ga\|^2$	$\|Ga\|^2$ (dB)
-0,5	0,1020	0.0104	-39,63
-0,45	0,2135	0.0456	-26,82
-0,4	0,3338	0.1114	-19,06
-0,35	0,4576	0,2094	-13,58
-0,3	0,5794	0,3357	-9,47
-0,25	0,6951	0,4831	-6,32
-0,2	0,7976	0,6361	-3,93
-0,15	0,8826	0,7789	-2,17
-0,1	0,9468	0,8964	-0,95
-0,05	0,9862	0,9727	-0,24
0	1	1	0
0,05	0,9862	0,9727	-0,24
0,1	0,9468	0,8964	-0,95
0,15	0,8826	0,7789	-2,17
0,2	0,7976	0,6361	-3,93
0,25	0,6951	0,4831	-6,32
0,3	0,5794	0,3357	-9,47
0,35	0,4576	0,2094	-13,58
0,4	0,3338	0,1114	-19,06
0,45	0,2135	0,0456	-26,82
0,5	0,1020	0,0104	-39,63

Table 2.7 Gain parameters of the antenna in SS6

Chapter 3 Terrain Observation by Progressive Scans (TOPSAR) mode

In this section the basic operation of this recently proposed mode, called TOPSAR, will be explained. Firstly, the basic parameters of analysed system and swath definition are introduced since they will be the input values to compute TOPSAR parameters at the end of this chapter. Before the computation of TOPSAR parameters, they will be defined and explained, and the TOPSAR requirements and equations will be introduced to understand its basic operation.

This section reports the necessary modifications of PAZ ScanSAR Mode parameters in order to operate in TOPSAR acquisition mode. TOPSAR, unlike the ScanSAR Mode, uses an azimuth steering of the antenna providing wide swath coverage with a uniform signal to noise ratio. Differently from SpotLight Mode, the antenna beam is steered back to forward in the along-track direction. Thus, all targets are illuminated by whole antenna beam avoiding image distortions like scalloping.

3.1 PAZ system parameters. Sub-swath characterization

In order to compute the necessary parameters for TOPSAR, first of all we need to know the basic parameters of PAZ system. Since PAZ operating parameters are still under discussion and subject to confidentiality restrictions, TerraSAR-X parameters will be used because they are similar to PAZ. With these parameters we are going to obtain some representative results for PAZ system.

In Table 3.1, Table 3.2 and Table 3.3, the flight parameters, operating frequency and antenna configuration of the system are presented. The most interesting parameters that will be used in further analysis are the platform height of 510 Km and the velocity, which will be key parameters in all calculations. TerraSAR-X, such as PAZ, works in X-band with a radar frequency of 9.65 GHz, which provides a wavelength of 31 mm. The antenna length is 4.794 m and the antenna width 0.7 m.

Flight Parameters	
Planet Radius	6378.15 Km
Planet Mass	5.9742 x10^{24} Kg
Satellite Altitude	510 Km
Platform Velocity	7605.92 m/s
Orbital Period	94.82 minutes

Table 3.1 Flight Parameters

Antenna Configuration	
Number of Azimuth Phase Centres	12
Radiators per Azimuth Phase Centre	16
Number of radiators (Azimuth)	192
Radiating Element Spacing (Azimuth)	0.8022 wavelengths
Antenna Length	4.794 m
Number of Elevation Phase Centres	32
Radiators per Elevation Phase Centre	1
Number of radiators (Elevation)	32
Radiating Element Spacing (Elevation)	0.7077 wavelengths
Antenna Width	0.700 m
Total number of phase centres	384
Antenna Boresight Look Angle	33.8º

Table 3.2 Antenna Configuration

Operating Frequency	
Radar Centre Frequency	9.650 GHz
Radar Operating Band	X-Band
Radar Wavelength	0.031 m
Max Tx Pulse Bandwidth	300.0 MHz
Guard Time before and after pulse transmission	5 microseconds

Table 3.3 Operating Frequency

The basic structure of the PAZ antenna is shown in Fig. 3.1. The antenna consists of a Radio Front End (RFE) which divides the signal through the hybrid and signal splitter. These electromagnetic pulses arrives to the transmit/receive modules (TRMs). The antenna consists of 12 panels in azimuth direction each one with 32 elevation TRMs. The transmission-reception scheme is shown in Fig. 3.2. As it can be seen, the signal crosses each sub-system two times in the transmission-reception line.

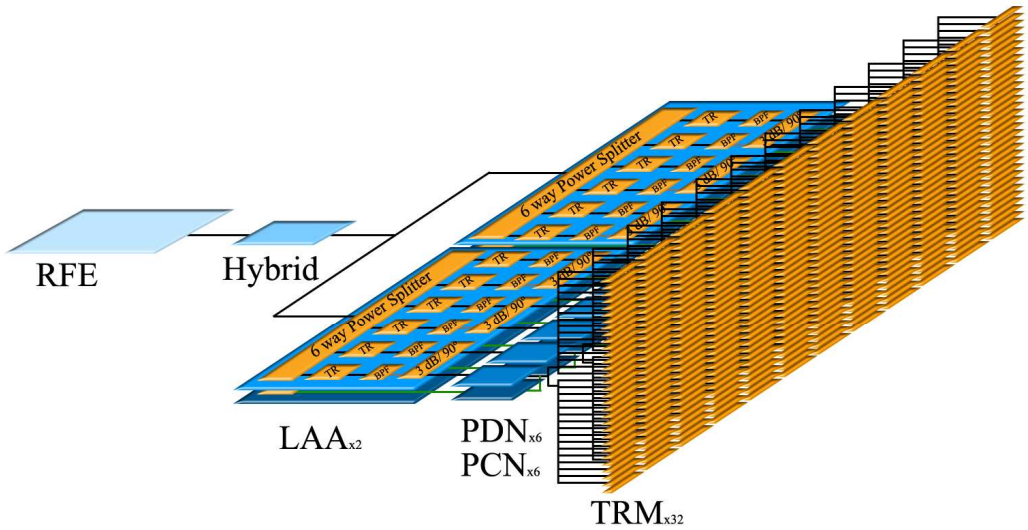

Fig. 3.1 Antenna configuration scheme [45]

As it was commented previously, TOPSAR mode has similar features to ScanSAR. Both modes divide their scanning times in different sub-swaths to achieve higher range coverage. For this reason, it is interesting to present the ScanSAR parameters in order to adapt them to TOPSAR operation.

ScanSAR mode in PAZ works with a swath width of 100Km (an alternative configuration using 3 sub-swaths with range coverage of 75 Km will be proposed in this section for TOPSAR operation). In order to get such width, the antenna switches the elevation beam pointing to several directions. In PAZ, this elevation steering enables four sub-swaths in

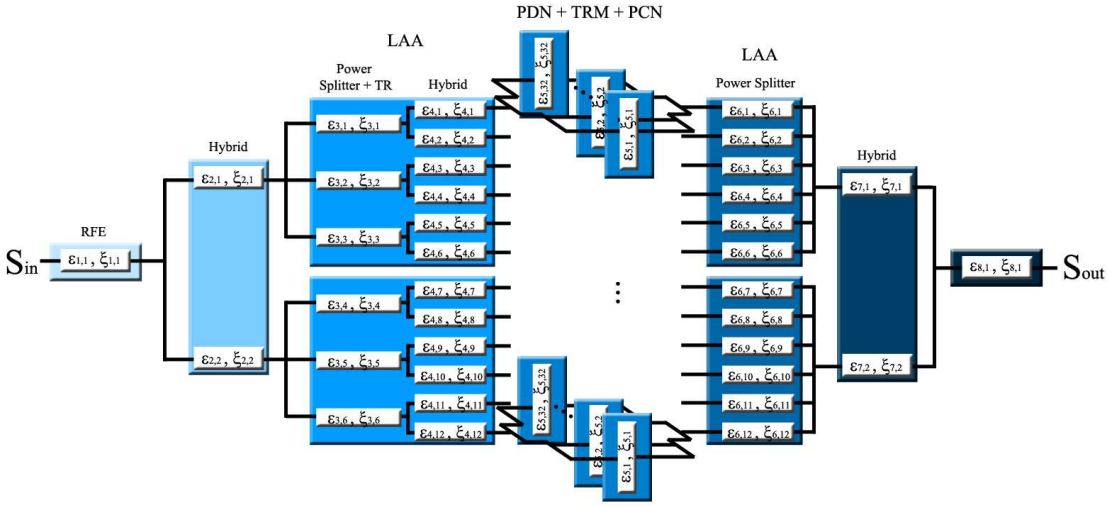

Fig. 3.2 Transmission-reception antenna sub-systems [45]

one pass of the antenna. Each sub-swath has a swath width of 30 Km with, approximately, 1.5 Km of overlap, providing a total swath width larger than 100 Km.

Table 3.4 shows the basic parameters of ScanSAR mode. The most relevant parameter is the azimuth resolution, which is 18 meters. It will be used as a goal in the TOPSAR analysis at the end of this section. Ambiguities, called Distributed Target Ambiguity Ratio (DTAR), it will be another key parameters to the correct performance of our system and they will be accurately studied in Chapter 5.

Parameter	Requirement
Polarization	HH, VV
Full performance angle range	20º - 45º
Data collection angle range	15º - 60º
Azimuth resolution	≤ 18 m (@ 1 along look)
Range resolution	≤ 6 m (@ a across looks)
Swath	≥ 100 Km
Minimum swath overlap	≥ 5%
Pixel Localization	= 8.5 m (1σ)
PSLR	≤ -20 dB
ISLR	≤ -13 dB
DTAR	≤ -17 dB (goal: ≤ -20 dB)
Nominal NESZ	≤ -21 dB
Worst Case NESZ	≤ -19 dB
Dynamic Range (distributed targets)	NESZ-3 dB to NESZ+39 dB
Dynamic Range (point targets)	=54 dB
Radiometric stability	= 0.5 dB (1σ)
Absolute Radiometric Accuracy	= 1.5 dB (1σ)
Relative Radiometric Accuracy	= 0.5 dB (1σ)

Table 3.4 ScanSAR Parameters for PAZ system

Finally, the sub-swaths must be defined in order to compute the parameters for all of them. From incident angles of sub-swaths it is possible to compute other important geometric parameters of the system, which will be useful for TOPSAR analysis. In Table 3.5, Table 3.6 and Table 3.7, the parameters for 22 sub-swaths are computed.

Look angles can be obtained from the incidence angles with (2.29). Elevation beamwidths, in degrees, are computed directly from look angles (look angle far – look angle near). Slant ranges are computed with (2.30), using the incidence angles. Ground range can be obtained with the next equation:

$$R_G = \sqrt{h^2 + R^2 - 2hR\cos(\theta_l)} \tag{3.1}$$

where R_G is the ground range, h is the satellite altitude, R is the slant range and θ_l is the look angle. Once we get the ground ranges, the swath width can be computed as the difference between the far ground range and near ground range. Similarly, swath overlap is calculated as the difference between the far ground range of one sub-swath and the near ground range of the next one. Slant middle range, a parameter that will be used in most of computations in this document, is computed with (2.28) using the middle look angle.

Swath Name	PRF (Hz)	Incident angle (near)	Incident angle (far)	Look angle (near)	Look Angle (far)
SM-S_1	3781,00	15.000	18.370	13.866	16.967
SM-S_2	3741,40	16.850	20.160	15.569	18.610
SM-S_3	3675,00	20.000	23.200	18.463	21.394
SM-S_4	4440,20	23.040	26.120	21.247	24.058
SM-S_5	3796,30	25.970	28.920	23.921	26.602
SM-S_6	3732,10	28.780	31.590	26.475	29.016
SM-S_7	4377,00	31.460	34.140	28.899	31.310
SM-S_8	3782,00	34.010	36.570	31.193	33.483
SM-S_9	4400,70	36.440	38.870	33.367	35.527
SM-S_10	3805,00	38.750	41.050	35.421	37.452
SM-S_11	4388,20	40.940	43.130	37.355	39.275
SM-S_12	3816,00	43.020	45.090	39.179	40.979
SM-S_13	3496,80	44.990	46.950	40.892	42.583
SM-S_14	3187,70	46.850	48.710	42.497	44.087
SM-S_15	3504,10	48.620	50.380	44.010	45.501
SM-S_16	3200,90	50.290	51.960	45.425	46.825
SM-S_17	3504,10	51.880	53.460	46.758	48.069
SM-S_18	3214,00	53.390	54.890	48.012	49.243
SM-S_19	3484,30	54.820	56.240	49.185	50.338
SM-S_20	3214,00	56.170	57.530	50.281	51.371
SM-S_21	3471,10	57.470	58.760	51.323	52.344
SM-S_22	3207,00	58.700	59.930	52.297	53.258

Table 3.5 Sub-swath definition and features (a)

Swath Name	Elevation Beamwidth	Slant Range (near)	Slant Range (far)	Ground Range (near)	Ground Range (far)
SM-S_1	3.101	526.595	535.208	126.208	156.195
SM-S_2	3.041	531.080	540.600	142.554	172.535
SM-S_3	2.930	540.094	551.145	171.062	201.069
SM-S_4	2.810	550.545	563.039	199.540	229.564
SM-S_5	2.680	562.384	576.218	228.071	258.074
SM-S_6	2.541	575.516	590.560	256.617	286.525
SM-S_7	2.411	589.819	606.037	285.108	315.032
SM-S_8	2.290	605.203	622.571	313.544	343.592
SM-S_9	2.160	621.640	639.994	342.026	372.053
SM-S_10	2.031	639.039	658.264	370.531	400.484
SM-S_11	1.920	657.299	677.458	399.013	429.099
SM-S_12	1.800	676.397	697.279	427.547	457.556
SM-S_13	1.690	696.224	717.804	456.067	486.057
SM-S_14	1.590	716.655	738.915	484.485	514.516
SM-S_15	1.490	737.793	760.613	513.023	543.005
SM-S_16	1.400	759.399	782.776	541.431	571.427
SM-S_17	1.311	781.614	805.423	569.952	599.862
SM-S_18	1.231	804.330	828.599	598.502	628.411
SM-S_19	1.152	827.427	852.022	626.979	656.772
SM-S_20	1.090	850.768	875.920	655.266	685.264
SM-S_21	1.021	874.773	900.197	683.907	713.803
SM-S_22	0.961	898.978	924.748	712.378	742.294

Table 3.6 Sub-swath definition and features (b)

Swath Name	Swath width	Swath Overlap	Middle Look Angle	Slant Middle range
SM-S_1	29.987	13.641	15.417	530.654
SM-S_2	29.981	1.474	17.090	535.591
SM-S_3	30.007	1.529	19.928	545.367
SM-S_4	30.024	1.493	22.653	556.535
SM-S_5	30.003	1.456	25.261	569.041
SM-S_6	29.907	1.417	27.745	582.777
SM-S_7	29.924	1.488	30.104	597.665
SM-S_8	30.048	1.565	32.338	613.620
SM-S_9	30.027	1.522	34.447	630.549
SM-S_10	29.953	1.471	36.436	648.385
SM-S_11	30.087	1.553	38.315	667.109
SM-S_12	30.009	1.490	40.079	686.570
SM-S_13	29.990	1.572	41.737	706.747
SM-S_14	30.032	1.493	43.292	727.518
SM-S_15	29.982	1.575	44.755	748.938
SM-S_16	29.997	1.476	46.125	770.825
SM-S_17	29.910	1.360	47.414	793.259
SM-S_18	29.910	1.432	48.627	816.207
SM-S_19	29.793	1.506	49.762	839.471
SM-S_20	29.998	1.357	50.826	863.089
SM-S_21	29.896	1.425	51.834	887.235
SM-S_22	29.916	-	52.778	911.614

Table 3.7 Sub-swath definition and parameters (c)

3.2 TOPSAR mode

In TOPSAR mode, the scanning time is divided into different sub-swath and the antenna points to different strips periodically. The major difference between ScanSAR and TOPSAR modes is the azimuth steering that the second one introduces. In this new operation mode the antenna rotates during the acquisition time from back to forward in along-track direction. This mode is called Terrain Observation with Progressive Scans (TOPSAR). It is important to note that the azimuth antenna rotation is in the opposite direction of the SPOT (SAR) and, therefore, in TOPSAR mode worse azimuth resolution will be obtained. This resolution loss, due to the antenna steering in azimuth direction in movement way, is compensated by a longer burst which can cover all the azimuth land without any holes.

In TOPSAR, the antenna rotation is added to the natural angle variation due to the platform movement. In Fig. 3.3, we can see how the evolution of the azimuth pointing angle changes in comparison with StripMap or ScanSAR modes. The resulting pointing angle is the addition of the angle variation due to the platform movement and the azimuth antenna rotation. The steering angle in along-track direction can be expressed in terms of the steering angle rate k_ϕ (rad/s) as:

$$\phi_{TOPS} = k_\phi \tau \qquad k_\phi < 0 \tag{3.2}$$

$$\phi(\tau) = \phi_{vel}(\tau) + \phi_{TOPS}(\tau) = \frac{v_e \tau}{R_0} + |k_\phi| \tau \tag{3.3}$$

k_ϕ has been taken negative, anti-SPOT. With (3.3) in (2.56), expression (3.4) is obtained for the azimuth antenna pattern in TOPSAR operation [36].

$$\begin{aligned} G_{a,TOPS}(\psi(\tau)) &\approx G_0 sinc^2\left(\frac{L}{\lambda}\left(\frac{v_e \tau}{R_0} + |k_\phi| \tau\right)\right) \\ &= G_0 sinc^2\left(\frac{L}{\lambda}\frac{v_e \tau}{R_0}\left(1 + \frac{R_0 |k_\phi|}{v_e}\right)\right) \end{aligned} \tag{3.4}$$

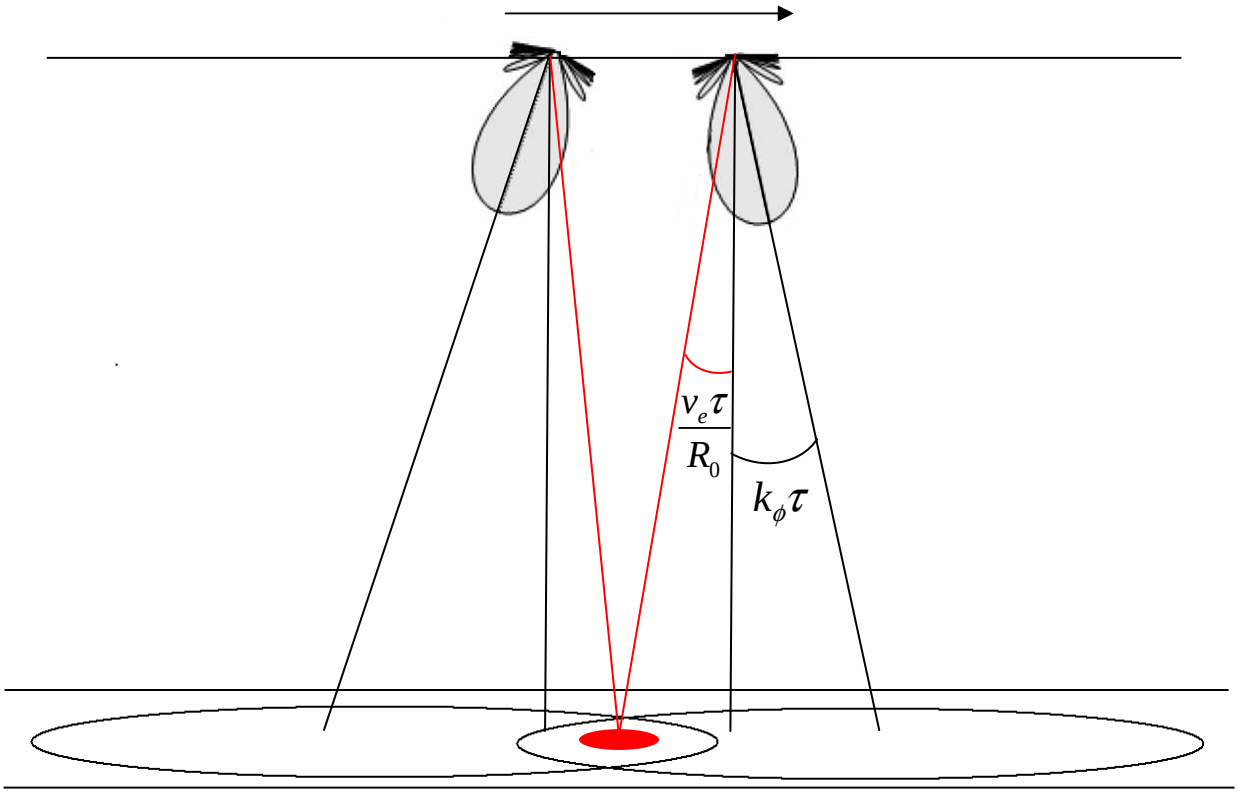

Fig. 3.3 Azimuth pointing angle evolution in TOPSAR Mode

The resulting azimuth antenna pattern (AAP) is equivalent to the antenna in ScanSAR mode but shrunk by a factor α (3.5). The AAP is equivalent to a Stripmap mode working with an antenna length of $L = \alpha \cdot L_{strip}$. This feature causes an α times worse azimuth resolution than Stripmap case since the azimuth resolution is proportional to the antenna length in SAR acquisition systems ($\rho_{az} \approx \alpha L/2$).

$$\alpha = 1 + \frac{R_0 \left| k_\phi \right|}{v_e} \tag{3.5}$$

Fig. 3.4 exemplifies the azimuth beamwidth reduction in function of the slow time or platform movement and, consequently, the resolution loss. A k_ϕ of 0.05 rad/s has been taken. The AAP in TOPSAR mode has got narrower compared with the original StripMap or ScanSAR azimuth antenna pattern. However, the steering azimuth rotation permits to illuminate all the targets in the sub-swath with the same AAP weighting. Thus, ambiguities become stationary in azimuth as well signal-to-noise ratio (SNR), avoiding the scalloping effects observed in ScanSAR.

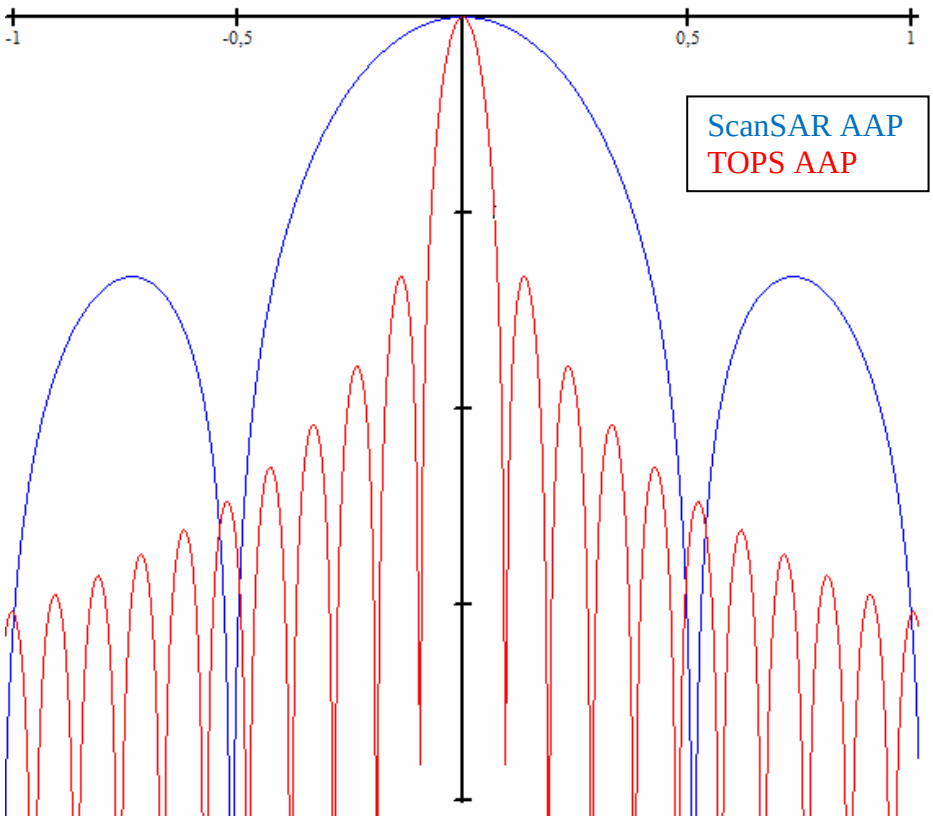

Fig. 3.4 AAP in TOPSAR mode compared with the APP in ScanSAR

3.3 TOPSAR acquisition

It is important to see the differences between ScanSAR and TOPSAR acquisition modes. In Fig. 3.5, the time/frequency domain (TFD) is presented for both modes. Four targets (P1-P4) are located in their zero-Doppler time. That means the location in azimuth where they would be perpendicular to the platform with a null Doppler displacement.

The Doppler evolution of each target is drawn by a line with negative slope. This slope is

equal to the Doppler rate k_R calculated in (2.54). Naturally, the Doppler frequency increases in module when sensor moves away from the zero-Doppler position.

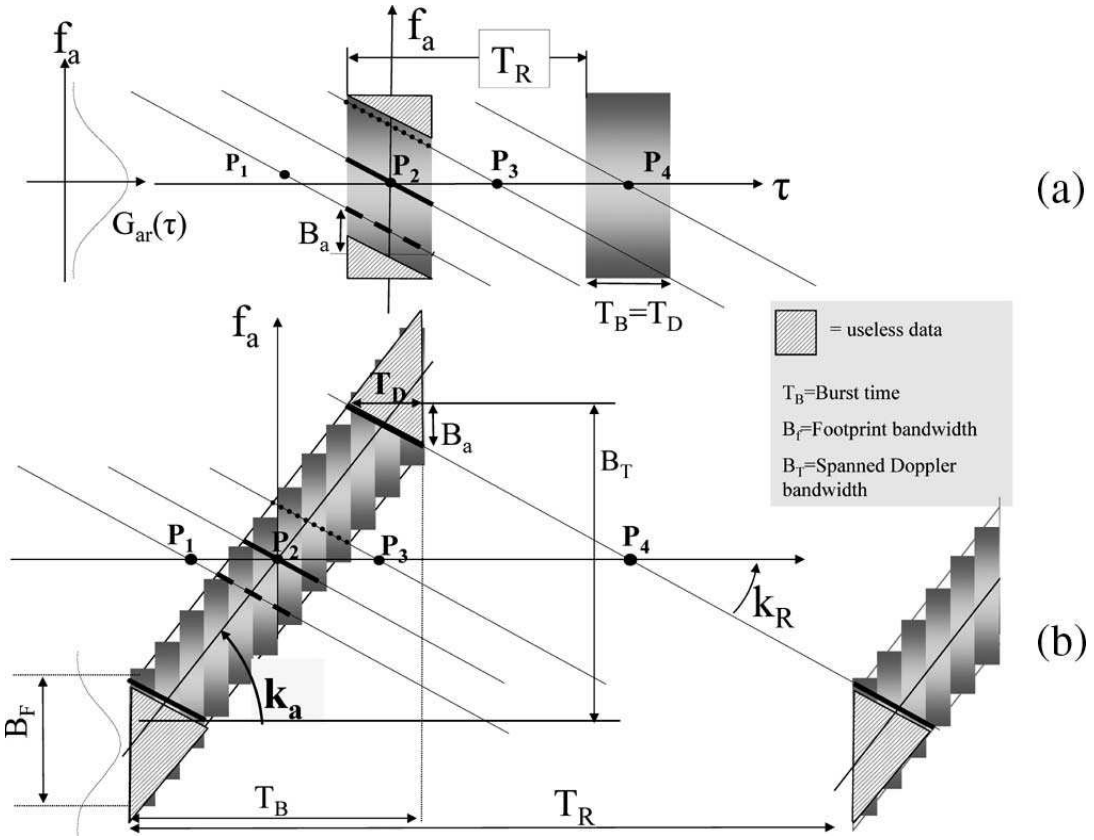

Fig. 3.5 Time frequency domain (TFD) representation in case of ScanSAR acquisition. (a) ScanSAR and TOPSAR acquisition (b) [35]

In the figure, the grey zones represent the Doppler frequencies supported by the azimuth antenna pattern during the scan time of one sub-swath. The antenna weigthing is shown at the left side of the picture as well as a colour grating in the shaded region (white for maximum response and black to worse response). The AAP evolution is the main difference between both modes. In ScanSAR mode the AAP is fixed and, as a result, there is a rectangular TFD support for collected data. In TOPSAR mode, the antenna pointing sweeps along time and, consequently, target with different Doppler frequency can be illuminated with whole antenna beam (for example target P3). The displacement of the pointing angle is known as Doppler centroid rate [35] and it can be obtained as:

$$k_a = \frac{\delta\left(-\frac{2v_s}{\lambda}\sin\left(\phi_{TOPS}(\tau)\right)\right)}{\delta\tau} \approx -\frac{2vs}{\lambda}k_\phi \tag{3.6}$$

With this new feature, it is possible to point at all targets in the azimuth direction with whole antenna beam, avoiding the dependant azimuth SNR in ScanSAR. As we can see in the figure, in ScanSAR mode the target number 3 is seen by one of the edges of the antenna beam, hence target 3 will present a lower echo power although it has a similar

RCS that target number 2 or 4, which are illuminated by the centre of the antenna beam producing a powerful echo in reception. On the other hand, the TOPSAR mode solves this problem with the antenna steering in azimuth. Thus, all the targets can be illuminated by whole antenna beam during the scanning. It solves the weighting AAP problem and the different targets keep having different Doppler displacement in reception to determine their azimuth position.

Another important difference is the burst time duration, which is longer in TOPSAR mode and it does not coincide with the dwell time as in ScanSAR mode. The dwell time (T_D), time while a point target is in the antenna footprint, is chosen according to the desired azimuth resolution (ρ_{az}). Considering the azimuth time band product (TBP) [35] is large, we obtain:

$$TBP = B_a T_D = \frac{B_a^{\,2}}{|k_R|} \tag{3.7}$$

$$\rho_{az} = v_e \frac{k_w}{B_a} = v_e \frac{k_w}{|k_R| T_D} \tag{3.8}$$

Where k_w is a correction factor that depends on the superimposed window [35] and usually it is close to one.

One problem that appears in TOPSAR mode, which will be exposed later, is the quantization of the steering angle of the antenna. This quantization is caused by the limited memory in radar, hence only some antenna direction can be stored. This fact could cause some problems but they will be discussed accurately in Chapter 4.

Finally, we must determine the steering rate in order to get a complete coverage of all azimuth points without any holes. For this purpose, we need that a target situated in the middle of the inter-burst interval is seen by the previous and posterior burst antenna scanning. This is the case of target 4 in Fig. 3.5 (b). In order to scan completely this target, the restriction showed at (3.9) must be fulfilled.

$$B_T = k_a (T_B - T_D) \geq |k_R| (T_R - T_B + T_D) \tag{3.9}$$

3.4 TOPSAR parameters

When a TOPSAR system is being designed, first we have to compute the parameters that achieve the requirements of that mode. So, k_ϕ, burst time of each sub-swath and the total cycle time have to be chosen to assure the desired resolution of the system and cover all the azimuth terrain with no holes. The process of selection is, basically, divided in three phases. Firstly, we have to set the part of the antenna beam that will be used for focusing the targets in the scanning sub-swaths. After that, and knowing the required azimuth resolution, the steering angle rate of each sub-swath must be chosen. Finally, we must set the basic scan timeline for the whole system to reach all the points in the scene.

1. The choice of the azimuth angle to be exploited for focusing is a trade-off between

the desired resolution, which means a large angle to improve the azimuth viewing of the targets in the image; and the necessity of ambiguity suppression. A different beamwidth for each sub-swath can be chosen depending on the desired requirements.

2. When the azimuth resolution is already fixed, it is time to select the appropriate k_ϕ for each sub-swath. According to (3.4),

$$\rho_{az} = \left(1 + \frac{R_0^{(n)} \left| k_\phi^{(n)} \right|}{v_e}\right) \frac{\lambda}{2\phi_0^{(n)}} \tag{3.10}$$

And then:

$$k_\phi^{(n)} = -\left(\frac{2\rho_{az}\phi_0^{(n)}}{\lambda} - 1\right) \frac{v_e}{R_0^{(n)}} \tag{3.11}$$

3. To cover all the points in along-track direction for all the sub-swath, the follow equations must be accomplished:

$$\left(\left|k_\phi^{(n)}\right| T_B^{(n)} - \phi_0^{(n)}\right) R_0^{(n)} + v_e T_B^{(n)} = v_e T_R \tag{3.12}$$

It is simple to understand why the linear system (3.12) must be fulfilled observing Fig. 3.6. Initially, the satellite is pointing to the azimuth point x_0 in the time t_0. The antenna is scanning this sub-swath during the burst time (T_B), so at the end of this period the antenna is pointing to the position x_1 in azimuth. Considering a distance to the target R_0 and taking x_0 the reference azimuth position, x_1 can be obtained as:

$$x_1 = x_0 + v_e T_B + k_\phi T_B R_0 \tag{3.13}$$

The azimuth direction where the antenna points after T_B depends on two factors. The first one is the displacement of the platform along the sky, which directly corresponds to a ground displacement of $v_e \cdot T_B$. The second factor that affects the azimuth pointing at the end of the burst is the steering angle rate. During the time T_B the antenna sweeps the main beam in along-track direction. The resulting angle variation in the burst is equal to $k_\phi T_B$ which corresponds to an azimuth ground displacement of $k_\phi T_B R_0$.

However, the interesting azimuth point is, actually, x_2 which is the last point illuminated by the whole antenna main beam exploited for focusing (the part of main beam contained between $[-\phi_0/2,\ \phi_0/2]$). The azimuth location of x_2 is calculated as:

$$x_2 = x_1 - \frac{\phi_0}{2} R_0 = x_0 + v_e T_B + k_\phi T_B R_0 - \frac{\phi_0}{2} R_0 \tag{3.14}$$

In order to scan all the points with no holes in the along-track direction, the time line must be set so that the antenna illuminates the next point that had not been processed in the previous burst when it scans again the same sub-swath.

The satellite will scan the sub-swath again after T_R, consequently the azimuth point x_2 must be illuminated again after T_R:

$$x_2 = x_0 + v_e T_R + \frac{\phi_0}{2} R_0 \tag{3.15}$$

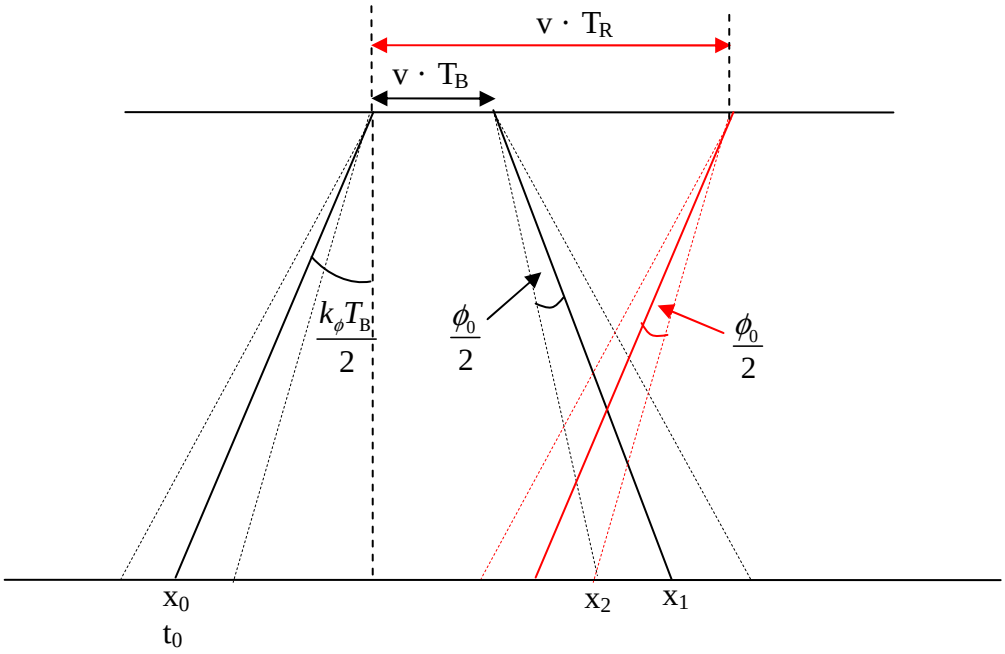

Fig. 3.6 Timeline in TOPSAR Mode to cover all points

Finally, taking the results from (3.14) and (3.15) the equation (3.18) is obtained for each sub-swath:

$$x_0 + v_e T_B + k_\phi T_B R_0 - \frac{\phi_0}{2} R_0 = x_0 + v_e T_R + \frac{\phi_0}{2} R_0 \tag{3.16}$$

$$v_e T_B + k_\phi T_B R_0 - \phi_0 R_0 = v_e T_R \tag{3.17}$$

$$\left(k_\phi T_B - \phi_0\right) R_0 + v_e T_B = v_e T_R \tag{3.18}$$

3.5 Results and parameters for TOPSAR mode in PAZ satellite

In order to decide the most appropriate configuration for PAZ working in TOPSAR mode, in this section two alternatives have been analysed. Both of them work with the PAZ system parameters defined in section 3.1 for flight parameters, antenna configuration and operating frequency. Moreover, both configurations use the parameters of ScanSAR Mode in order to adapt them to TOPSAR operation. The main difference between these alternatives is the number of sub-swaths used to cover scanned region.

First configuration uses three sub-swaths providing range coverage of 75 km and it was a new proposal for PAZ system in TOPSAR mode. The second alternative for TOPSAR mode uses four sub-swath, as in ScanSAR configuration, so this mode provides wider range coverage (100 Km approximately).

First of all, and following the steps defined in section 3.4, the part of the antenna main beam used in the scanning must be chosen. Although in this section a constant angular interval (ϕ_0) has been chosen for all sub-swaths, it is possible to select a different angular interval for each sub-swath in order to assure a desired suppression of the ambiguities in reception. For this analysis the angular interval used in scanning has been set to 0.33 degrees.

Sub-swath name	Slant middle range (Km)	Steering angle rate (rad/s)	Steering angle rate (deg/s)
SM-S_1	530.654	7.821e-002	4.4810
SM-S_2	535.591	7.749e-002	4.4397
SM-S_3	545.367	7.610e-002	4.3601
SM-S_4	556.535	7.457e-002	4.2726
SM-S_5	569.041	7.293e-002	4.1787
SM-S_6	582.777	7.121e-002	4.0802
SM-S_7	597.665	6.944e-002	3.9786
SM-S_8	613.620	6.763e-002	3.8751
SM-S_9	630.549	6.582e-002	3.7711
SM-S_10	648.385	6.401e-002	3.6673
SM-S_11	667.109	6.221e-002	3.5644
SM-S_12	686.570	6.045e-002	3.4634
SM-S_13	706.747	5.872e-002	3.3645
SM-S_14	727.518	5.705e-002	3.2684
SM-S_15	748.938	5.541e-002	3.1750
SM-S_16	770.825	5.384e-002	3.0848
SM-S_17	793.259	5.232e-002	2.9976
SM-S_18	816.207	5.085e-002	2.9133
SM-S_19	839.471	4.944e-002	2.8326
SM-S_20	863.089	4.808e-002	2.7550
SM-S_21	887.235	4.678e-002	2.6801
SM-S_22	911.614	4.553e-002	2.6084

Table 3.8 Steering angle rates for each sub-swath in PAZ

Once the angular interval is chosen, the steering angle rate of each sub-swath can be determined in order to assure the desired azimuth resolution (18 m in PAZ system for ScanSAR Mode). The steering angle rate of each sub-swath is not dependant of the number of sub-swath used in scanning and neither of which sub-swaths are chosen. So, using the geometric parameters defined for ScanSAR, the resulting steering angle rates obtained from (3.11) are shown in Table 3.8.

When the steering angle rates are known, it is the moment to select the number of sub-swaths that will be used for scanning. That choice, as it is shown in the next section, is a trade-off between range coverage and the error committed due to limited storage capacity and the ambiguity levels. Once the number of sub-swaths are chosen, it must be decided which ones are used depending on the desired scanned area. From now on, as an example, sub-swaths 5-6-7 will be taken when 3 sub-swaths are used for lower range coverage alternative, and sub-swaths 5-6-7-8 in the case of wider range coverage. Solving the linear system (3.18) the timelines of both alternatives are given in Table 3.9 and Table 3.10.

Sub-swath name	Steering angle rate (rad/s)	Steering angle rate (deg/s)	Doppler rate (Hz/s)	Burst time	Dwell time	Doppler BW	Max. steering angle
SS5	0.07292	4.1781	-6056.027	0.12337	0.07600	460	± 0.2578
SS6	0.07120	4.0796	-5913.292	0.12500	0.07784	460	± 0.2550
SS7	0.06943	3.9780	-5765.993	0.12675	0.07983	460	± 0.2521

Table 3.9 Timeline for PAZ system using 3 sub-swaths for range coverage

Sub-swath name	Steering angle rate (rad/s)	Steering angle rate (deg/s)	Doppler rate (Hz/s)	Burst time	Dwell time	Doppler BW	Max. steering angle
SS5	0.07292	4.1781	-6056.027	0.17158	0.07600	460	± 0.3584
SS6	0.07120	4.0796	-5913.292	0.17320	0.07784	460	± 0.3533
SS7	0.06943	3.9780	-5765.993	0.17496	0.07983	460	± 0.3480
SS8	0.06762	3.8746	-5616.065	0.17684	0.08196	460	± 0.3426

Table 3.10 Timeline for PAZ system using 4 sub-swaths for range coverage

As it was explained before, some parameters of TOPSAR mode do not depend on the number of sub-swaths used for scanning the surface. Steering angle rates remain constant as well as the Doppler rates for both alternatives. These parameters are obtained from equations (3.11) and (2.54) respectively, calculated from flight parameters of the sensor (velocity, range, frequency…) and ScanSAR requirements, such as azimuth resolution.

On the other hand, burst time and, consequently, maximum steering angle change in both situations. The burst time is the period while the antenna is illuminating each sub-swath and the cycle time (T_R) can be obtained as the sum of the burst time of all sub-swaths, and it corresponds with the time that sensor takes to illuminate each sub-swath from one burst to the next one. In the example analysed T_R, the interburst periods, are equal to 0.37512 seconds in the first case and 0.69568 seconds in the second one.

The main disadvantage using 4 sub-swaths is the longer burst time that the system needs to

cover all the points in the scene. A longer burst time means a higher maximum steering angle and, consequently, the antenna needs to steer the main beam in a higher number of azimuth direction. As it is explained in the next section, the limited storage capacity will result in a higher steering angle quantization step and a worse response of the TOPSAR mode.

In conclusion, the results obtained for TOPSAR mode using both alternatives are achievable with the PAZ antenna characteristics. Even so, more specific analysis of ambiguities must be done in order to assure the correct operation of the radar using this mode. Next chapters introduce the concept of ambiguities in this kind of applications and compute them for the system analysed.

Chapter 4 Steering angle quantization analysis for TOPSAR mode

As it was commented in previous section, the storage capacity of the PAZ system is not unlimited. In the particular case of the TOPSAR operation mode, it is essential to store the different azimuth antenna angles where the antenna needs to point in order to set the necessary azimuth steering to cover all points of each sub-swath. Due to the limited capacity, it is not possible to have a continuous steering in along track direction so a quantization of the steering angle will appear in the azimuth antenna pattern, causing a quantization error that will be studied to analyse its impact to the received data.

In this chapter, the error due to quantization of the steering angle will be evaluated and its influence in Doppler reception will be discussed. As it will be exposed, this error will produce azimuth ambiguities which must be evaluated to have a correct imaging of targets in the scene.

4.1 Limited storage capacity in radar

PAZ, like other radar systems, has a limited capacity to store the positions where the antenna will point. This feature will cause that the steering in azimuth will not be continuous and, therefore, there will be a quantization of azimuth angle variation. This steering angle quantization can be described as in (4.1). The angle quantization step ($\Delta\phi$) will be directly related to the storage system capacity and the azimuth swept necessary to reach all the points. The resulting angle has the shape showing in Fig. 4.1, where one can see the step evolution of the quantized angle.

$$\phi_q = \phi - \mathrm{mod}(\phi, \Delta\phi) + \frac{\Delta\phi}{2} \tag{4.1}$$

Such quantization of the steering angle causes some imperfections in the AAP response in TOPSAR mode. When quantized angle (4.1) is inserted in the AAP equation (2.56) the resulting quantized AAP in Fig. 4.2 is obtained. The first observable problems can be seen in Fig. 4.2. These graphics correspond to the AAP of the sub-swaths 5-6-7-8 when 4 sub-swaths are used to scan the scene. Fig. 4.3 shows the AAP for sub-swath 5 scaled to see the quantized problems with more detail. In the graphics, the blue AAP represents the ideal response of the antenna using a continuous steering angle, while the red one is the quantized AAP.

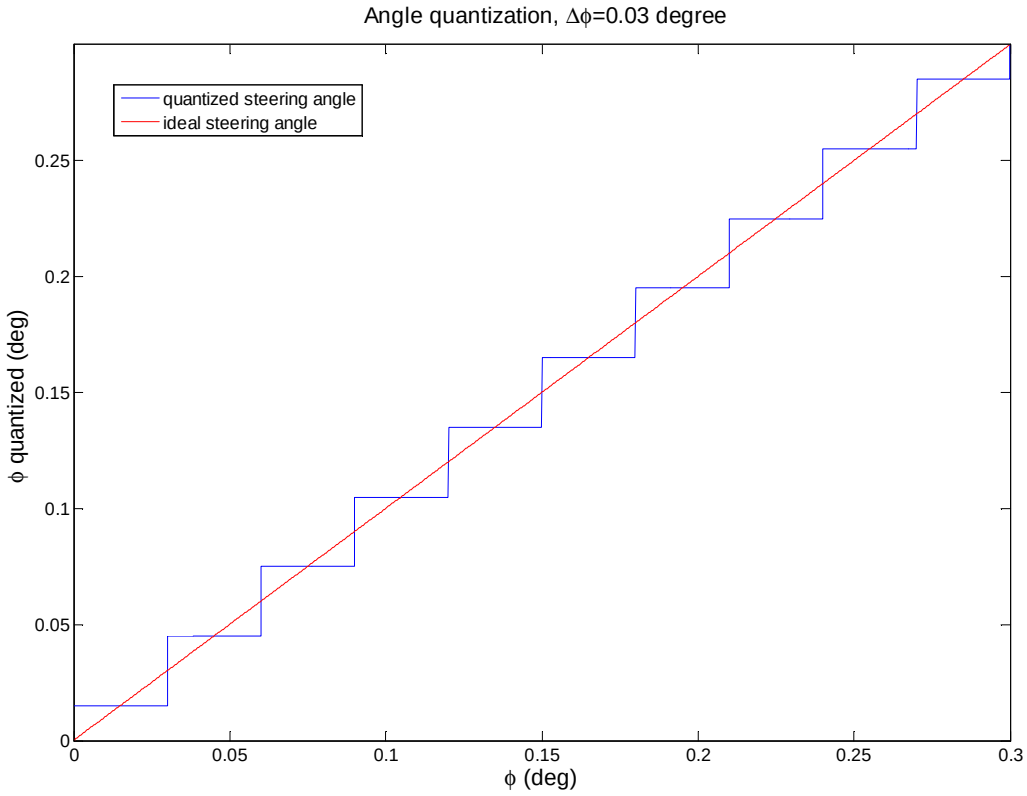

Fig. 4.1 Steering angle quantization

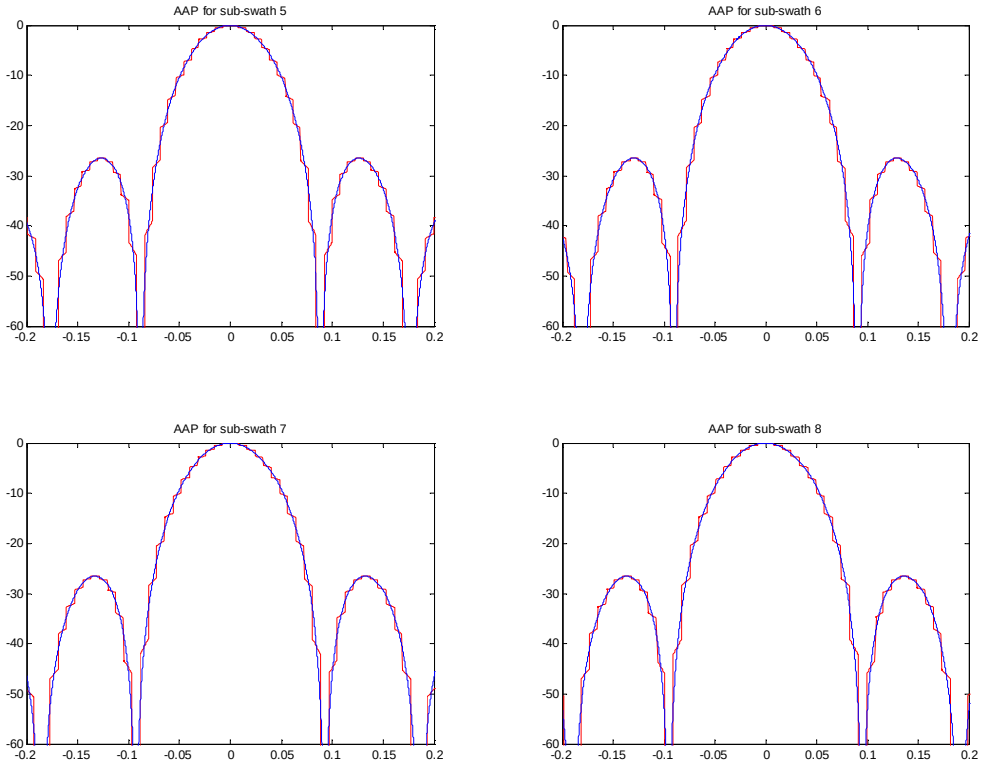

Fig. 4.2 Ideal AAP and AAP with quantized steering angle

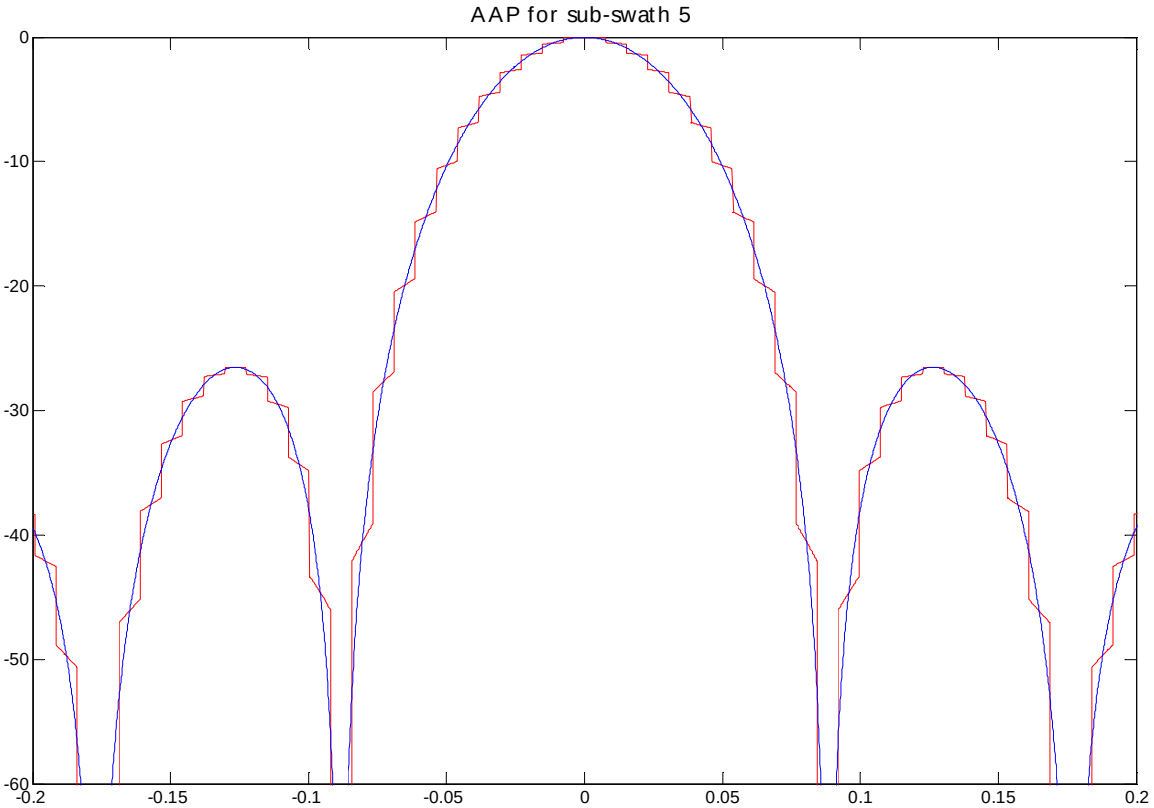

Fig. 4.3 AAP in sub-swath 5 and quantization effects

As it is shown in Fig. 4.3, the angle quantization causes that the antenna diagram in TOPSAR mode suffers some anomalies. So, a fixed pointing angle stored in the radar memory is set to the antenna, and therefore the AAP evolution is slower because the azimuth pointing angle only changes due to the platform movement. Taking equation (3.3), it means that only the first term evolves while the antenna keeps the same pointing angle. After some time, the radar switches to the next stored pointing angle, and then a step is observed in the AAP evolution.

4.2 Angle quantization step

Once the first approximation to the AAP quantization problems is shown, it is time to determine the effects of the quantization in target detection. As it was done in previous section, the same two alternatives are analysed and compared. First of all, the angle quantization step of both alternatives must be calculated. Certainly, the best results will be obtained using three sub-swaths because a smaller azimuth steering sweep is needed. However, the main purpose of this study is to compare the TOPSAR acquisition performance using three or four sub-swaths in the scanning. To calculate the quantization step, the maximum steering angle in Table 3.9 and Table 3.10 are needed. Furthermore, PAZ system memory allows 126 storing slots. As a result, the equation (4.2) will determine the angle quantization step:

$$\Delta\phi = \frac{\sum_i K_{\phi i} T_{Bi}}{126} \tag{4.2}$$

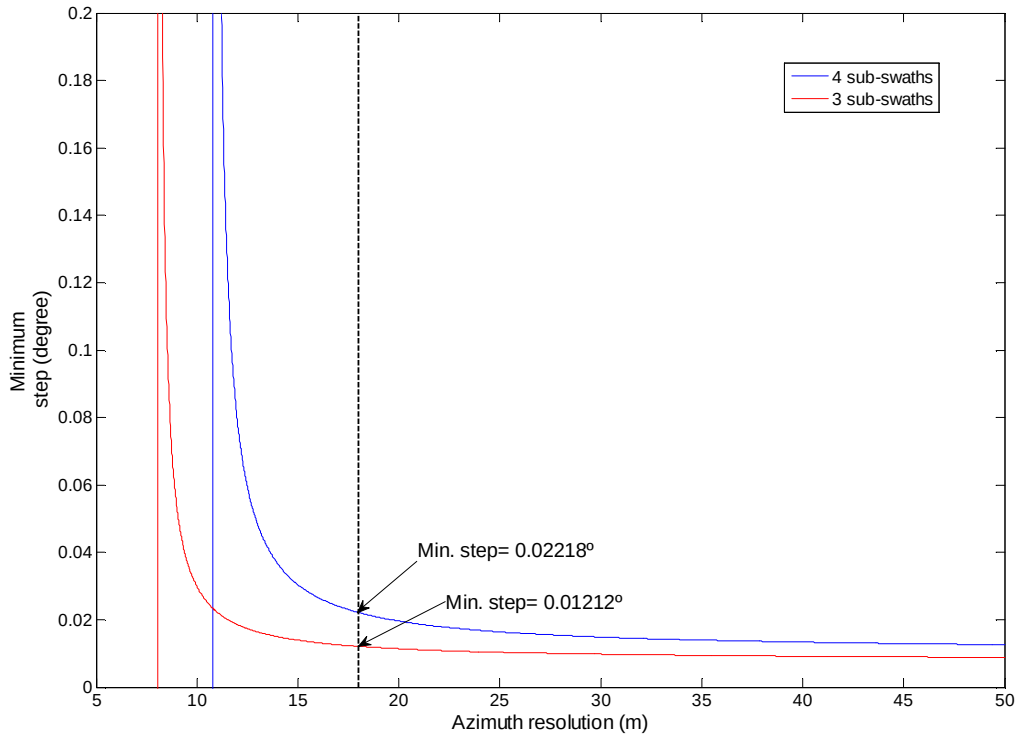

Fig. 4.4 Angle quantization step vs. Azimuth resolution using 3 or 4 sub-swaths

$K_{\phi i}T_{Bi}$ is the total steering swept of the sub-swath *i*, and the summation represents the sub-swaths used during the scanning process. In the particular cases studied, equation (4.2) provides an angle quantization step of 0.01212 degrees using three sub-swaths and 0.02218 degrees using for sub-swaths. Fig. 4.4 shows the evolution of angle quantization step depending on the desired azimuth resolution and the number of sub-swaths used. The more sub-swaths we use, less fine quantization step we will get. Also, if the desired resolution is too demanding, the quantization step will increase causing a worse response.

These are the minimum steps to get the desired azimuth resolution, but it is not possible to choose an arbitrary step. In the radar memory there are save some positions for Spotlight mode, and we have to take them for TOPSAR. The possible steps that we can use to do the steering in azimuth are multiples of the minimum step 0.008º. This provides an azimuth quantization steep of **0.016º** for the first case and **0.024º** when we work with four sub-swaths.

4.3 Analysis of error due to azimuth steering angle quantization

Now that the angle quantization steps are known for both cases, it is time to analyse the error due to such quantization. In a first approximation to characterize this error, the difference between the ideal and quantized AAP was plotted in Fig. 4.5. Fig. 4.5 a) shows the quantization error in the sub-swath 7 using three sub-swaths while b) shows the error in the same sub-swaths but using 4 sub-swaths. These errors are calculated using the linear antenna response, not the logarithmic. How it was predicted before, case a) presents better response in terms of error.

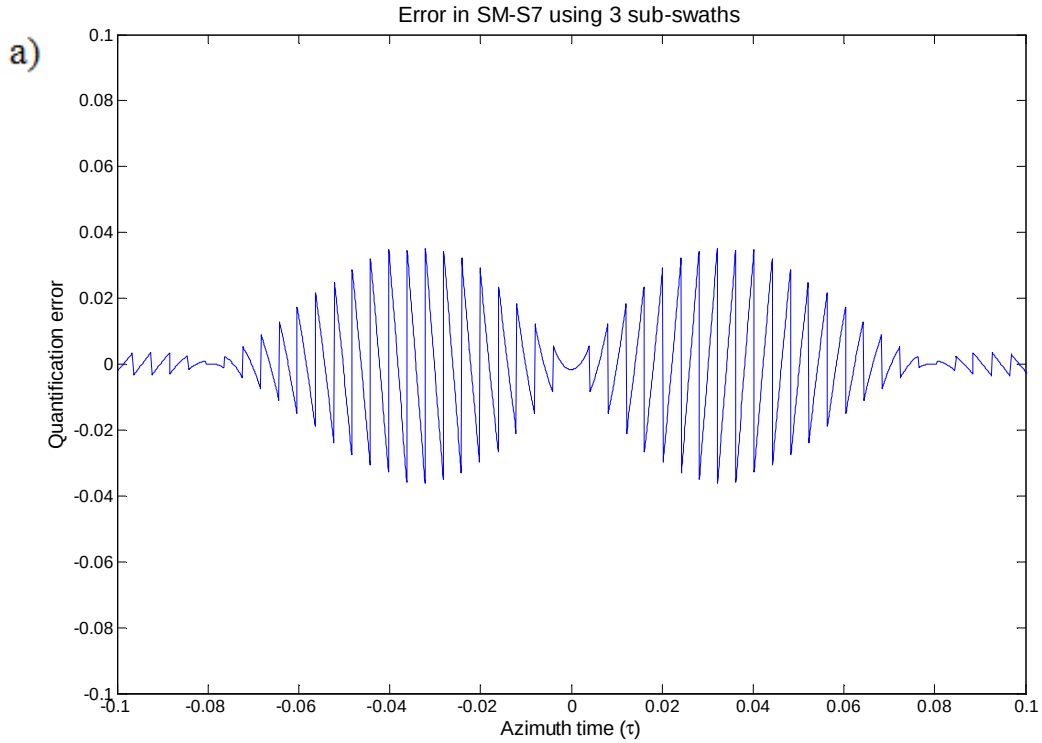

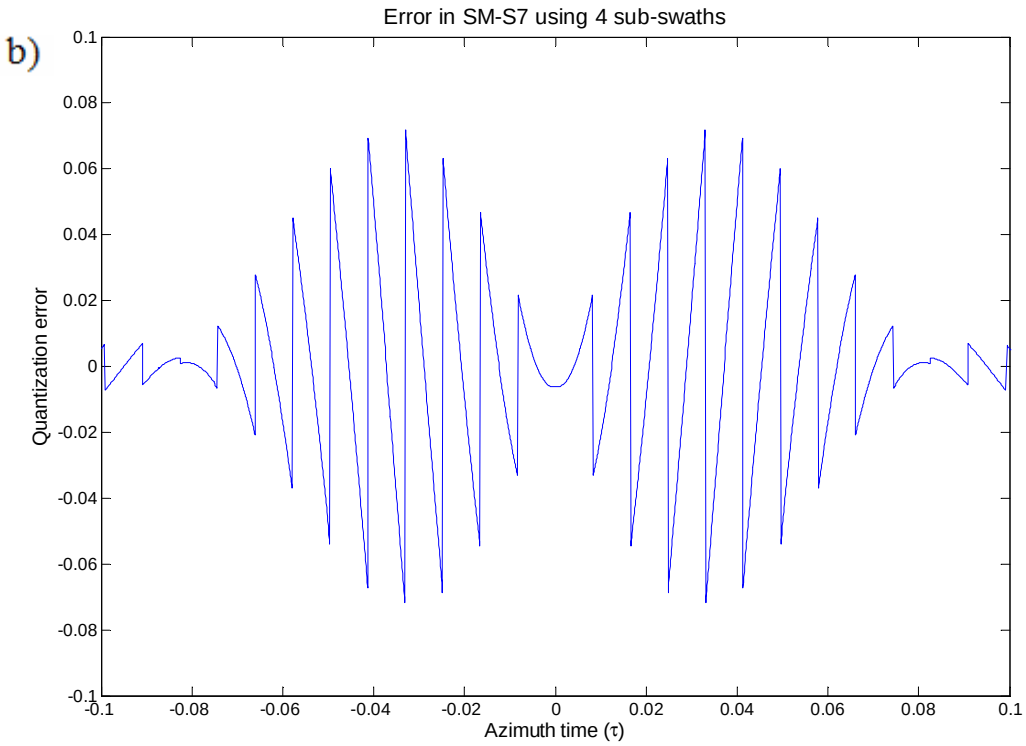

Fig. 4.5 Error due to quantization using a) 3 sub-swaths b) 4 sub-swaths

In order to do an analytical study of the errors, it is necessary to model them. The quantization of the AAP will generate a periodic amplitude modulation in the azimuth response. This modulation of the amplitude response will generate undesirable spurious peaks, producing spatial azimuth ambiguities. The error plotted in Fig. 4.5 can be approximated as a sawtooth signal [36]:

$$x_{err}(\tau) = A_e \sum_n rect\left(\frac{\tau - nT_q}{T_q}\right)\left(\tau - nT_q\right) \tag{4.3}$$

To have a complete model of the error, the parameters A_e and T_q must be defined and calculated. A_e will be taken as the maximum amplitude of the quantization error. As it is plotted in Fig. 4.5, this error has a shape similar to a sawtooth signal, but the signal amplitude is not constant. However, to do the analysis, a worst case has been taken and a sawtooth signal with constant amplitude equal to the maximum error has been chosen.

This maximum value of the error can be calculated approximately in the point of the *sinc*^{2} with maximum slope and where the quantization error will be the highest [36]. As it is shown in Fig. 4.6, the sinc^2 function has a maximum slope approximately in the *sinc*^{2}*(1/2)* point. So the value A_e can be approximated as [36]:

$$A_e = \text{sinc}^2\left(\frac{1}{2}\right) - \text{sinc}^2\left(\frac{1}{2} - \frac{\Delta\phi}{2\phi_{3dB}}\right) \tag{4.4}$$

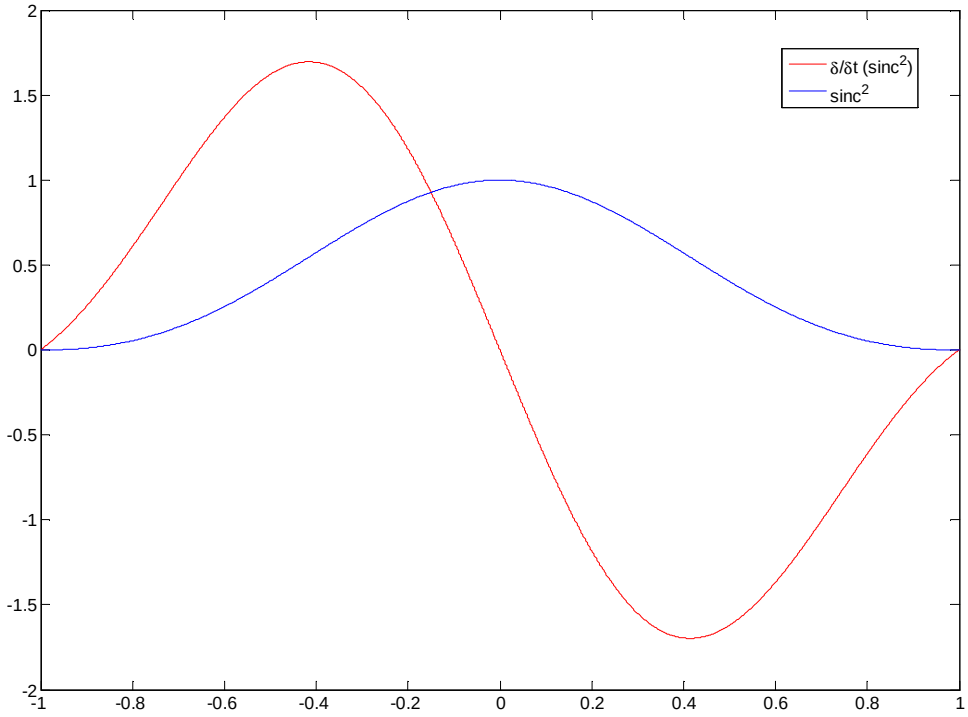

Fig. 4.6 Maximum slope of a sinc function

On the other hand, the period T_q is the time while the radar does not change the antenna pointing angle, and corresponds with the period of the sawtooth error signal. The radar scans a total angle of $K_\phi T_B$ in each sub-swath. This swept must be equal than the angle quantization step multiplied by the number of steps (N) in the sub-swath. At the same time, the burst time T_B has to be equal than the number of steps in the swath multiplied by the period of each step T_q. These condition lead to the equation (4.6):

$$\Delta\phi N = K_\phi T_B = K_\phi N T_q \tag{4.5}$$

$$T_q = \frac{\Delta\phi}{K_\phi} \tag{4.6}$$

Once the error is characterized, we are going to compare this approximation with the real error. Fig. 4.7 shows the error in blue and the sawtooth approximation defined in (4.3) with the parameters obtained in (4.4) and (4.6) in red. As it can be seen, the error is higher in *sinc(1/2)* while the approximated error is a pessimist prediction that matches up with the real error in that point.

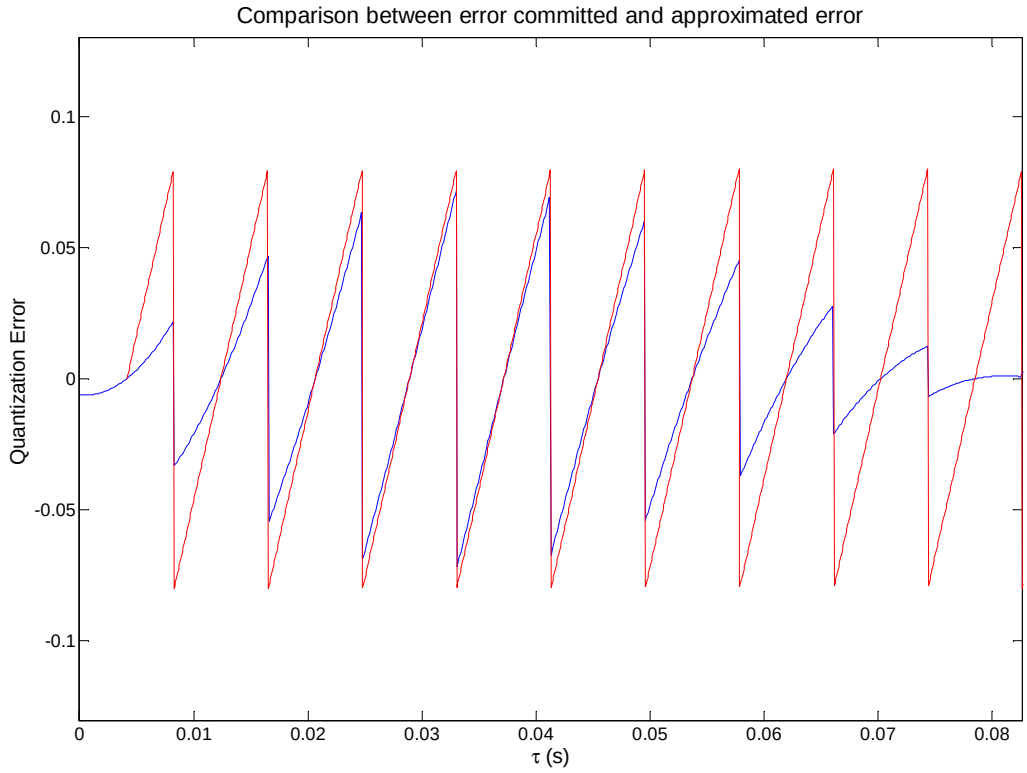

Fig. 4.7 Error due to quantization vs. error approximation

4.4 Fourier transform of quantization error. Azimuth ambiguity problems

Using the error approximation, it is easy to calculate the Fourier transform in order to determine the frequency response of the quantization errors. The Fourier transform can be solved from the Fourier series. In the case of a sawtooth periodic signal with amplitude $[-A_e, A_e]$ and period T_q, the Fourier series is defined in (4.7) [37] [38]:

$$x_{err}(\tau) = \frac{2A_e}{\pi} \sum_{k=1}^{\infty} \frac{\sin\left(2\pi k \frac{1}{T_q}\tau\right)}{k} \tag{4.7}$$

Once the Fourier series is defined, it is easy to find the Fourier transform to determine the frequency components of the error and the power of the resulting spurious peaks. These peaks will be interpreted as false targets situated at positions which provide the correspondent Doppler shift. The Fourier transform of the error signal is:

$$X_{err}(f) = F.T.\{x_{err}(\tau)\} = F.T.\left\{\frac{2A_e}{\pi} \sum_{k=1}^{\infty} \frac{\sin\left(2\pi k \frac{1}{T_q}\tau\right)}{k}\right\} \tag{4.8}$$

$$X_{err}(f)=\int\frac{2A_e}{\pi}\sum_{k=1}^{\infty}\frac{\sin\left(2\pi k\frac{1}{T_q}\tau\right)}{k}e^{-j2\pi ft}df=\frac{2A_e}{\pi}\sum_{k=1}^{\infty}\frac{1}{k}\int\sin\left(2\pi k\frac{1}{T_q}\tau\right)e^{-j2\pi f\tau}d\tau \quad (4.9)$$

$$X_{err}(f)=\frac{2A_e}{\pi}\sum_{k=1}^{\infty}\frac{1}{k}F.T.\left\{\sin\left(2\pi k\frac{1}{T_q}\tau\right)\right\}=\frac{2A_e}{\pi}\sum_{k=1}^{\infty}\frac{1}{k}\frac{1}{2}\left(\delta\left(f-\frac{k}{T_q}\right)-\delta\left(f+\frac{k}{T_q}\right)\right) \quad (4.10)$$

In the case studied, the most interesting part of the Fourier Transform is its amplitude in order to find the power and frequency location of spurious peaks that will appear due to quantization. Thus, taking the module of the Fourier transform calculated in (4.10):

$$\left|X_{err}(f)\right|=\left|\frac{2A_e}{\pi}\sum_{k=1}^{\infty}\frac{1}{k}\frac{1}{2}\left(\delta\left(f-\frac{k}{T_q}\right)-\delta\left(f+\frac{k}{T_q}\right)\right)\right|=\frac{A_e}{\pi}\sum_{k\neq 0}\frac{1}{|k|}\delta\left(f-\frac{k}{T_q}\right) \quad (4.11)$$

Finally, it is possible to change $|k|$ for $|fT_q|$ since the delta function is only different to zero for values k/T_q. So, the equation (4.12) can be rewritten as:

$$\left|X_{err}(f)\right|=\frac{A_e}{\pi|fT_q|}\sum_{k\neq 0}\delta\left(f-\frac{k}{T_q}\right) \quad (4.12)$$

Equation (4.12) reveals the presence of harmonics in multiples of $1/T_q$. However, the amplitude of spurious peaks decreases as the frequency increases. The resulting Fourier transform module and the analytical bound present in the first part of equation (4.12) are plotted in Fig. 4.8.

This figure shows the evolution of the Fourier transform relative to the azimuth position. This means that the receiver will interpret the spurious peaks in frequency as targets displaced in azimuth that provide a Doppler frequency equal to the error harmonics. False target detections in azimuth will be placed at points:

$$fd=\frac{2v_e^{\,2}}{\lambda R_0}\tau=\frac{2v_e^{\,2}}{\lambda R_0}\frac{x}{v_e}=\frac{k}{T_q} \quad (4.13)$$

$$x_k=\frac{k}{T_q}\frac{\lambda R_0}{2v_e} \quad (4.14)$$

a)

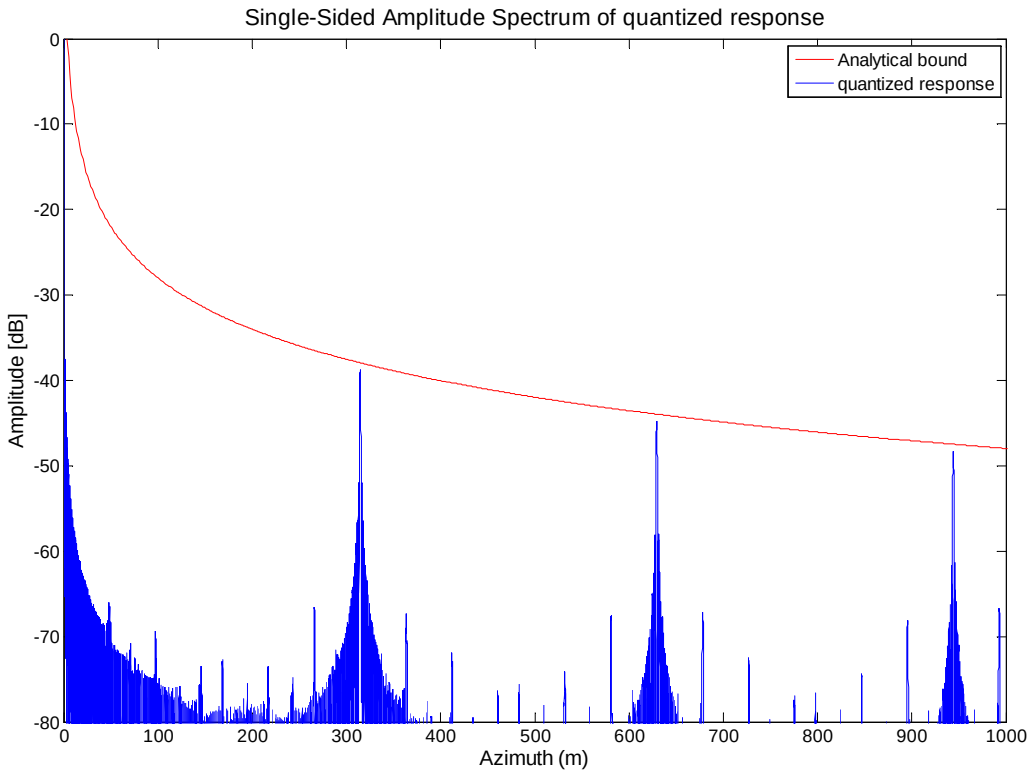

b)

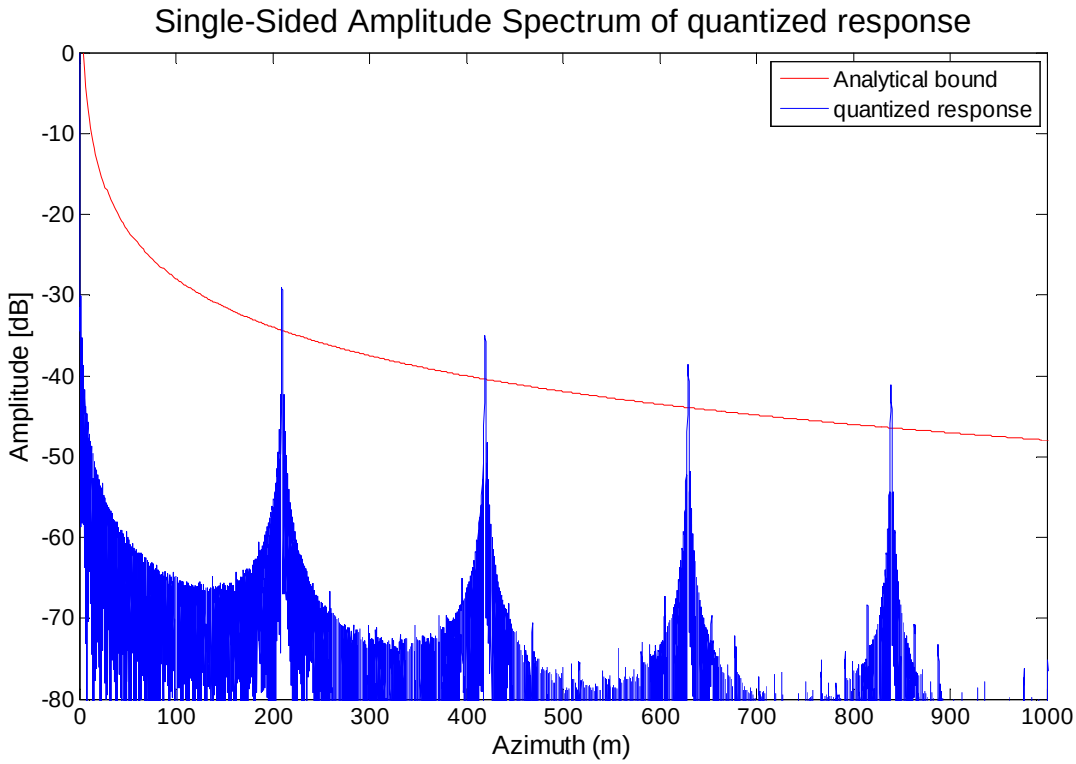

Fig. 4.8 Fourier transform of the approximated error a) 3 sub-swaths b) 4 sub-swaths

Working with 3 sub-swaths, as shows Fig. 4.8 a), better results are obtained. Spurious peaks appear further from the zero azimuth displacement and, consequently, the power of the higher harmonic is lower than the first spurious peak using four sub-swaths for the scanning. Furthermore, using a higher quantization step means to have the spurious peaks closer and worse results.

However, as it can see in Fig. 4.8, the powers of first spurious peak are 38 and 34 dB below the response of a target centred in the zero azimuth displacement. To obtain the level of the first spurious peak, we must evaluate the equation (4.12) in $f = 1/T_q$. The power of the first spurious peak is A_e/π and its evolution with angle quantization step can be seen in Fig. 4.9.

The conclusion about the steering angle quantization problems is that, although a frequency modulation appears in the response of the radar, the level of the spurious peaks are more than 30 dB below the main response for angle quantization step used. Using smaller quantization steps, better results would be obtained. However, using four sub-swaths, the modulation effects due to quantization will be negligible too, getting a wider coverage with a similar image quality.

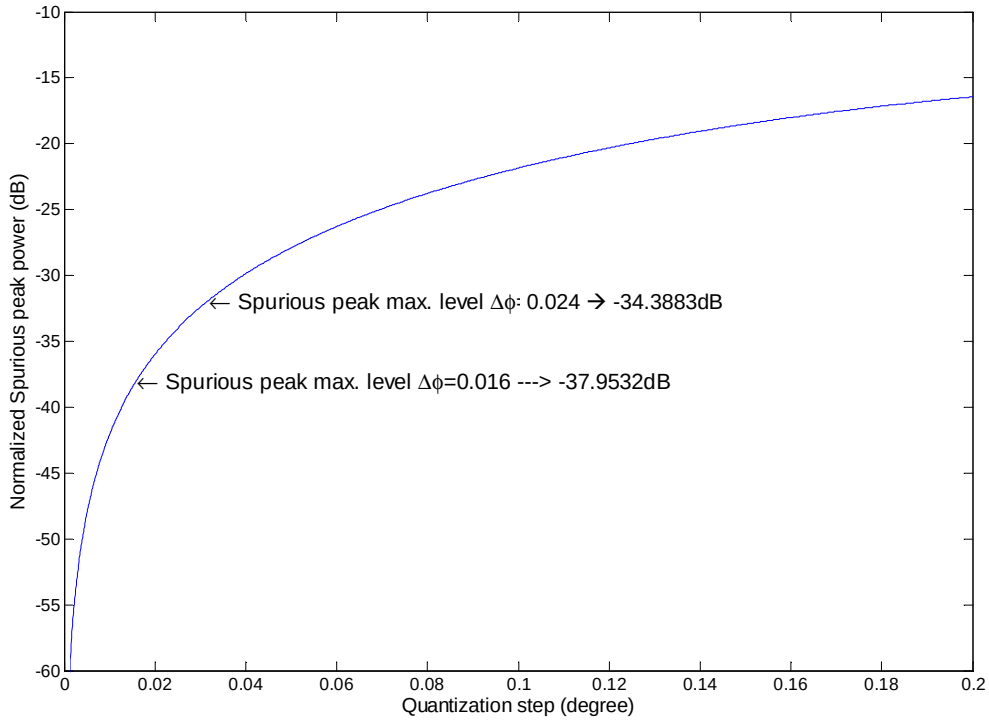

Fig. 4.9 Max. Spurious peak using three or four sub-swaths

Chapter 5 Ambiguity analysis for SAR systems

In this section the ambiguities are studied and analysed for Stripmap, ScanSAR and TOPSAR operation modes. Ambiguities are one of the key elements to the correct performance of the radar system and they are extremely related to the antenna shape and dimensions, the processed Doppler bandwidth and other design parameters of the radar such as the PRF.

It is considered ambiguous signal the power returns that do not correspond to the echoes from the illuminated area by the antenna footprint. The ambiguous echoes can cause image artefacts and misplaced replicas of bright targets. These ambiguities are classified in two categories depending on their origin. On one hand, azimuth ambiguities arise from the finite sampling of the Doppler spectrum at intervals of the PRF [39]. On the other hand, range ambiguities appear when the echoes from preceding and succeeding pulses arrive at he same time that the return of the desired pulse [39]. The level of these ambiguities will determine the azimuth ambiguity to signal ratio (AASR) and the range ambiguity to signal ratio (RASR) of our system.

At the end of this chapter, a more accurate analysis for ambiguities in TOPSAR are done considering sub-array diagram and grating lobes which have more influence when the antenna is not pointing perpendicularly to the swath. This analysis will be done with the help of AMOR (Antenna MOdelleR), a MATLAB tool created by UPC professor José María González Arbesú, which provides the real antenna diagram for the cases studied.

5.1 Ambiguities in SAR systems

In order to improve the ambiguity to desired signal ratio, the antenna pattern as well as the PRF must be chosen to fulfil the system requirements. So, for a given range and azimuth antenna pattern, it is necessary to select the right PRFs such that the power of the desired signal will be higher than the total ambiguous power. On the other hand, for a given range of PRFs, it will be necessary to determine the dimensions and weighting of the antenna in order to get an antenna pattern cuts that minimize ambiguity to signal ratio for all sub-swaths.

In a first approximation the ambiguous power received can be computed as [22]:

$$P_{amb} = \sum_{\substack{m,n=-\infty \\ m,n\neq 0}}^{\infty} G^2\left(f_0 + mPRF, \tau_0 + \frac{n}{PRF} \right) \cdot \sigma^0 \left(f_0 + mPRF, \tau_0 + \frac{n}{PRF} \right) \qquad (5.1)$$

From above, the dependency of the ambiguous power with the PRF can be observed. The power received from one point, determined by its Doppler frequency (f_0) and the time delay of the received echo (τ_0), is calculated multiplying the two way power antenna pattern (G^2) by the surface reflectivity (σ^0) [5] [6] of the analysed point. So, the total ambiguous power received for a given Doppler frequency and a time delay point will be calculated as the summation of the echoes from preceding and succeeding pulses, represented in (5.1) with the *n*-index ($\frac{n}{PRF}$); and the power of the replicas of the Doppler spectrum, which correspond to the *m*-index of the summation ($m \cdot PRF$), that disguise the desired part of the spectrum. Obviously, the summation indexes *m,n=0* must be ignored because they correspond to the desired signal power.

So, using (5.1), the integrated ambiguity to signal ratio (ASR) for a given processed Doppler bandwidth (B_p) can be computed with (5.2):

$$ASR(\tau) = \frac{P_{amb}}{P_u} = \frac{\sum_{\substack{m,n=-\infty \\ m,n\neq 0}}^{\infty} \int_{-Bp/2}^{Bp/2} G^2\left(f_0 + mPRF, \tau_0 + \frac{n}{PRF} \right) \cdot \sigma^0 \left(f_0 + mPRF, \tau_0 + \frac{n}{PRF} \right) df}{\int_{-Bp/2}^{Bp/2} G^2(f,\tau) \cdot \sigma^0(f,\tau)\, df} \qquad (5.2)$$

Unfortunately, the equation (5.2) is not useful for spaceborne SAR imaging since it requires the knowledge of the azimuth-range antenna pattern while most specifications of the antenna are given by their azimuth or range cuts separately. For this reason, to facilitate the computation of the ASR, it is possible to separate the ambiguities in azimuth and range, calculating them independently. In the following sections the effects of azimuth and range ambiguities will be analysed to see their impact in the radar operation.

5.2 Azimuth ambiguities

As it has been briefly explained in previous section, azimuth ambiguities appear due to the finite sampling of the azimuth antenna pattern every T seconds. That is easy to understand if the problem is defined in time domain. Every T seconds the radar sends a pulse to the scanned area (being T the inverse of the PRF) which is reflected by the ground surface and returns to the radar antenna. This fact causes that each point in the illuminated surface is seen by the antenna as a collection of discrete points as in Fig. 5.1.

In this figure, the radar is flying left to right illuminating a point target. The satellite movement is continuous, but in the figure there are only drawn the positions every 1/PRF. In each of these points, the radar sends a finite pulse that illuminates the point with the correspondent weighting of the antenna diagram. For this reason, in the bottom of the picture, we can see the azimuth antenna diagram sampled in time since the radar only receives information about the target every 1/PRF.

Once the origin of the azimuth ambiguities has been explained, now it is time to study them analytically and determine how these ambiguities affect to the radar operation. To calculate the contamination of the ambiguous signal to the desired return, it will be useful to work in frequency domain. In order to obtain the spectrum of the received signal, it is necessary to compute the Fourier transform of the sampled azimuth antenna pattern. First of all, the power received from a point target in function of time can be expressed as:

$$P(\tau) = P_0 \sum_n G^2(\tau) \cdot \sigma^0(\tau)\, \delta\left(\tau \pm \frac{n}{PRF}\right) \tag{5.3}$$

where P_0 is the maximum power received in the centre of the antenna main beam, $G^2(\tau)$ is the two way azimuth antenna pattern and $\sum_n \delta\left(\tau \pm \frac{n}{PRF}\right)$ is an impulse train that simulates the sampling of the AAP. It is possible to approximate the returns as *Dirac's delta* function since the duration of the pulses, in the order of microseconds, is much shorter than the interpulse period, in the order of milliseconds. $\sigma^0(\tau)$ is the target reflectivity. From now, in this analysis we will assume a uniform backscattering model for the targets in azimuth and range cuts, so $\sigma^0(\tau)$ becomes constant and it will not have interest in the ratios computation. To calculate the Fourier Transform of equation (5.3) it is necessary to know the Fourier Transform of the impulse train [41]:

$$F.T.\left\{\sum_n \delta\left(\tau \pm \frac{n}{PRF}\right)\right\} = \sum_k \delta(f \pm k \cdot PRF) \tag{5.4}$$

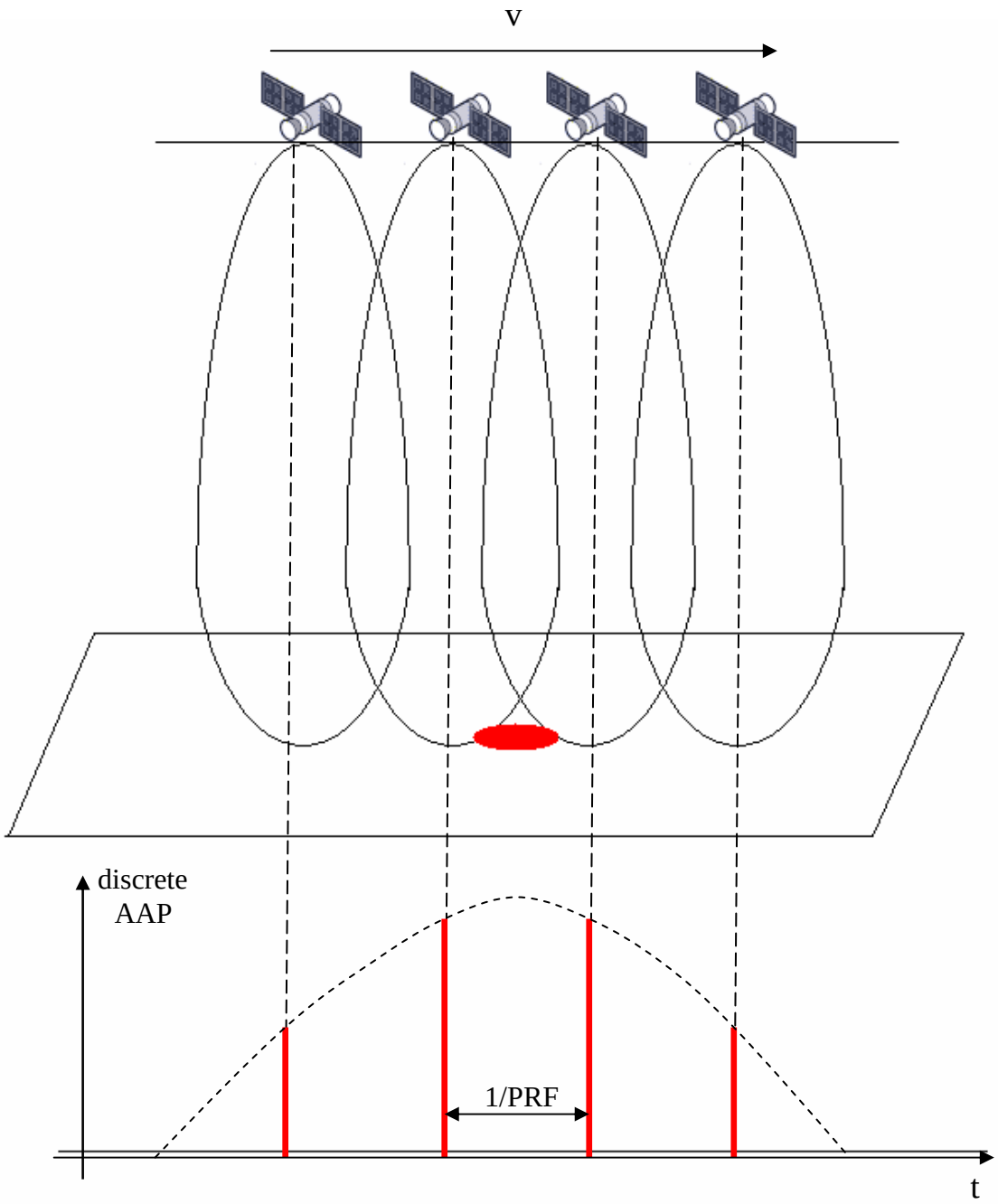

Fig. 5.1 AAP quantization due to discrete pulse emission

Then, from (5.4) the spectrum of the discrete AAP can be obtained (5.5):

$$\begin{aligned} &F.T.\{P(\tau)\} = F.T.\left\{P_0 \sum_n G^2(\tau)\cdot\delta\left(\tau \pm \frac{n}{PRF}\right)\right\} = P_0 \sum_n F.T.\left\{G^2(\tau)\delta\left(\tau \pm \frac{n}{PRF}\right)\right\} = \\ &= P_0 \sum_n F.T.\{G^2(\tau)\} * F.T.\left\{\delta\left(\tau \pm \frac{n}{PRF}\right)\right\} = P_0 '\, G^2(f) * \sum_n \delta(f + n\cdot PRF) = \\ &= P_0 ' \sum_n G^2(f + n\cdot PRF) \end{aligned} \qquad (5.5)$$

Finally, to get the spectrum of the received signal the AAP must be defined in function of the Doppler frequency. From equations (2.53) and (2.54), the one-to-one relationship between azimuth time and Doppler frequency is obtained:

$$f_d = \frac{2v_e{}^2\tau}{\lambda R_0} \tag{5.6}$$

The shape of the azimuth spectrum will be the same than the two-way power antenna pattern in time since the one-to-one lineal relationship between azimuth slow time and Doppler frequency. It is important to remember that a uniform backscattering model is used. If not, the spectrum could be calculated as the convolution between the two-way azimuth antenna pattern and the backscattering model taken [42]. So, the azimuth antenna pattern can be written in terms of the Doppler frequency (using a uniform aperture approximation) as [22]:

$$G^2(f_d) = G_0 \cdot \mathrm{sinc}^4\left(\frac{Lf_d}{2v_e}\right) \tag{5.7}$$

Once we have defined how the spectrum of the received signal is; now it is possible to compute the azimuth ambiguities. As it was defined in previous section, the azimuth ambiguity to signal ratio (AASR) is the relation between the desired power divided by the ambiguous one in the processed Doppler bandwidth.

The desired power in the receiver can be expressed as in (5.8), where B_p is the processed Doppler bandwidth, $W_{ai}(f)$ is the processing window in the receiver and G_{2az} is the azimuth two-way antenna pattern.

$$P_d = \int_{-Bp/2}^{Bp/2} W^2{}_{ai}(f_d)\frac{G_{2az}(f_d)}{G_{2azMAX}}df_d \tag{5.8}$$

On the other hand, the ambiguous signal that interferes in the processed bandwidth can be obtained as:

$$P_{amb} = \sum_{m\neq 0}\int_{-Bp/2}^{Bp/2} W^2{}_{ai}(f_d)\frac{G_{2az}(f_d + mPRF)}{G_{2azMAX}}df_d \tag{5.9}$$

Finally, using (5.8) and (5.9) the AASR is calculated as the ratio between them:

$$AASR = 10\log_{10}\left(\frac{P_{amb}}{P_d}\right) = 10\log_{10}\left(\frac{\sum_{m\neq 0}\int_{-Bp/2}^{Bp/2} W^2{}_{ai}(f_d)\frac{G_{2az}(f_d + mPRF)}{G_{2azMAX}}df_d}{\int_{-Bp/2}^{Bp/2} W^2{}_{ai}(f_d)\frac{G_{2az}(f_d)}{G_{2azMAX}}df_d}\right) \tag{5.10}$$

This is the theoretical way to compute the AASR. Fortunately, the number of critical ambiguities, represented by index *m*, is not infinite because the AAP decays to negligible values when the Doppler frequency increases sufficiently. In practise, we will analyse the

ambiguities for a finite number of ambiguities, which is a reasonable approximation to the real result for azimuth ambiguities. In the next section we are going to compute the AASR for different SAR operation modes. Stripmap and ScanSAR are analysed previously to get some basics results that will be useful to compute the ambiguities of this new operation mode, TOPSAR.

5.2.1 AASR for Stripmap

Stripmap mode is the basic operation mode for SAR systems. In this mode the radar overflies the observed surface with the antenna pointing to the ground with neither azimuth nor elevation steering. In order to get the azimuth ambiguities for Stripmap, the parameters of equation (5.10) are necessary.

One of the most critical parameters is the PRF. The PRF is chosen to avoid the returns in nadir direction and receive the desired pulses between two consecutive pulses avoiding they will be masked. AASR and RASR are extremely dependant on the PRF, so this will be an important parameter in the ambiguity analysis. For the case studied, the values of PRF for 22 sub-swaths defined for PAZ are in Table 5.1.

Sub-swath name	PRF (Hz)	Sub-swath name	PRF (Hz)
SM-S_1	3781,00	SM-S_12	3816,00
SM-S_2	3741,40	SM-S_13	3496,80
SM-S_3	3411,80	SM-S_14	3187,70
SM-S_4	4440,20	SM-S_15	3504,10
SM-S_5	3524,00	SM-S_16	3200,90
SM-S_6	3458,00	SM-S_17	3504,10
SM-S_7	4377,00	SM-S_18	3214,00
SM-S_8	3556,80	SM-S_19	3484,30
SM-S_9	4400,70	SM-S_20	3214,00
SM-S_10	3805,00	SM-S_21	3471,10
SM-S_11	3477,70	SM-S_22	3207,00

Table 5.1 PRFs in Stripmap

The two-way azimuth antenna pattern has been modelled as a $sinc^4$ function (5.7). W_{ai}, the processing window in reception, has been taken as a Hamming window with the expression:

$$W_{ai}(f_d) = \alpha + (1-\alpha)\cos\left(\frac{2\pi\left[f_d - \left(\frac{f_i^u}{2} + \frac{f_i^l}{2}\right)\right]}{B_p}\right) \tag{5.11}$$

Expression (5.11) shows the general expression for a Hamming window. In the case analysed a value of 0.75 is taken for α (specified by EADS-CASA Espacio), and the values

f_i^u and f_i^l has been set to $\frac{B_P}{2}$ and $-\frac{B_P}{2}$. The Hamming window is centred to the zero Doppler frequency in Stripmap mode.

Finally the Doppler processed bandwidth must be determined. As it has been explained, the Doppler processed bandwidth is related to the azimuth resolution desired. With equation (3.8) the necessary Doppler bandwidth to get the desired resolution can be written as:

$$B_P = 0.886 v_e \frac{k_w}{\rho_{az}} \tag{5.12}$$

where v_e is the effective velocity and k_w is a correction factor due to the bandwidth reduction caused by the window. Using the equation (5.12), the values of Table 5.2 are obtained for an azimuth resolution of 3 meters in Stripmap and a correction factor of 1.132, considering another factor of 0.886 for calculating the *Bp* in the -3dB. Fig. 5.2 justifies this value for a $sinc^2$ antenna pattern computing the processed bandwidth at -3dB point (equivalent to the half-power point in the lineal AAP). As it is shown, the Doppler processed bandwidth at -3dB point is shrunk by a 0.886 factor.

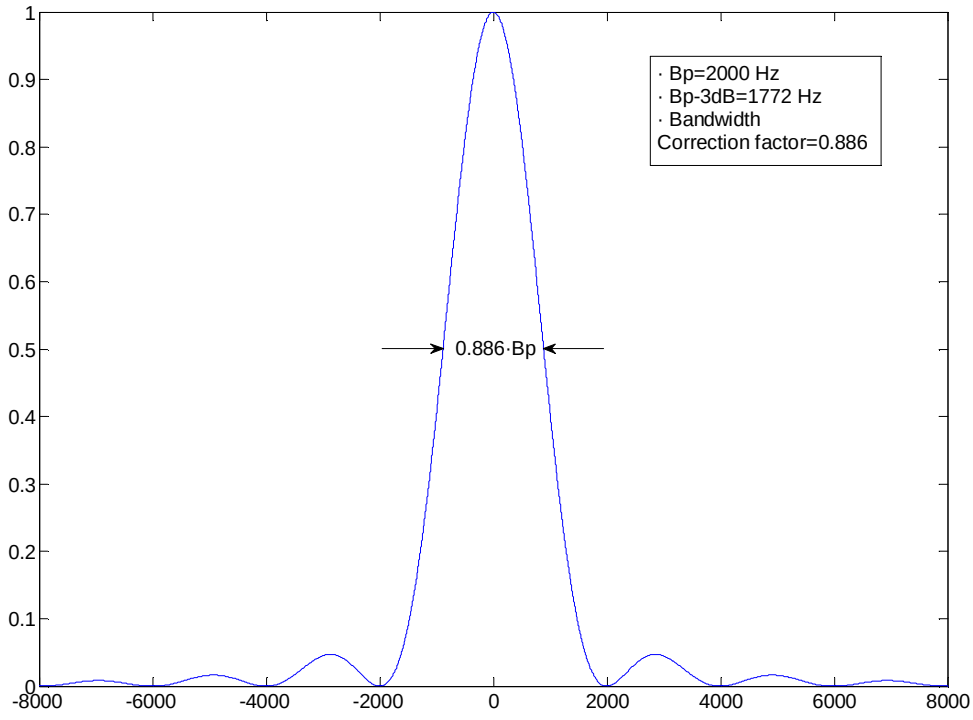

Fig. 5.2 Bandwidth correction using -3dB criteria for processed bandwidth

Sub-swath name	Bp (Hz)	Sub-swath name	Bp (Hz)
SM-S_1	2446,71	SM-S_12	2444,20
SM-S_2	2446,65	SM-S_13	2443,82
SM-S_3	2446,51	SM-S_14	2443,42
SM-S_4	2446,35	SM-S_15	2442,99
SM-S_5	2446,17	SM-S_16	2442,54
SM-S_6	2445,96	SM-S_17	2442,06
SM-S_7	2445,73	SM-S_18	2441,56
SM-S_8	2445,47	SM-S_19	2441,03
SM-S_9	2445,19	SM-S_20	2440,48
SM-S_10	2444,88	SM-S_21	2439,91
SM-S_11	2444,55	SM-S_22	2439,31

Table 5.2 Doppler processed bandwidth

With these values and using the equation (5.10) with a number of ambiguities of 12 (m=-6, 6), Fig. 5.3 and Table 5.3 show the AASR values for Stripmap mode.

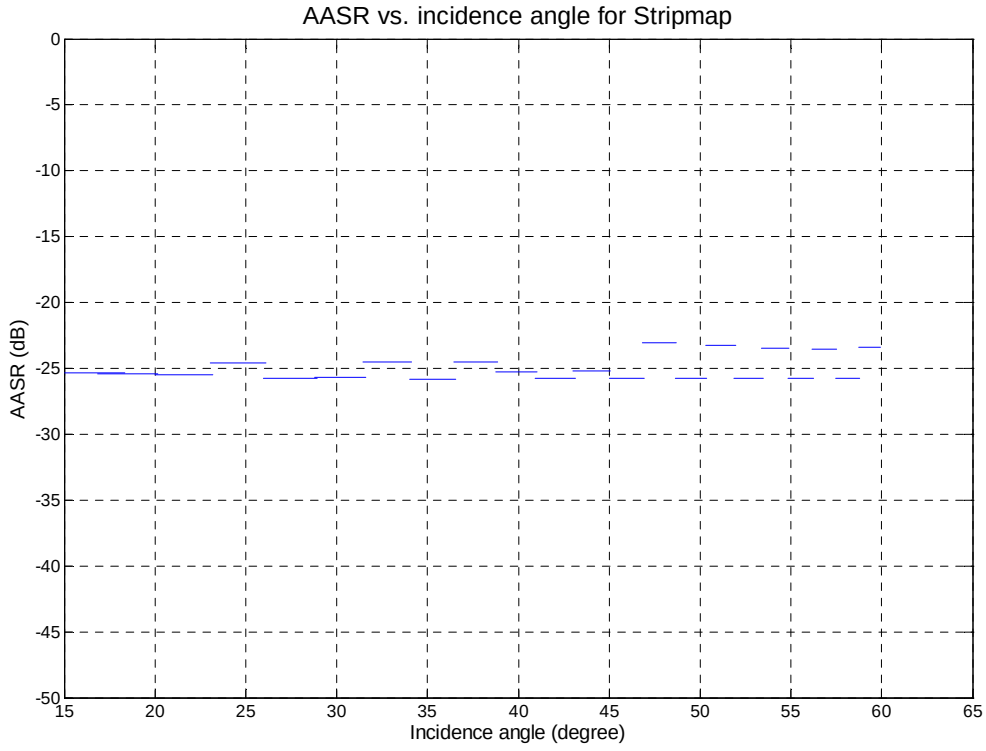

Fig. 5.3 AASR vs. Incident angle in Stripmap Mode

Sub-swath name	AASR(dB)	Sub-swath name	AASR (dB)
SM-S_1	-25.333	SM-S_12	-25.237
SM-S_2	-25.443	SM-S_13	-25.780
SM-S_3	-25.484	SM-S_14	-23.086
SM-S_4	-24.569	SM-S_15	-25.792
SM-S_5	-25.798	SM-S_16	-23.294
SM-S_6	-25.681	SM-S_17	-25.794
SM-S_7	-24.533	SM-S_18	-23.498
SM-S_8	-25.804	SM-S_19	-25.767
SM-S_9	-24.544	SM-S_20	-23.510
SM-S_10	-25.267	SM-S_21	-25.744
SM-S_11	-25.739	SM-S_22	-23.414

Table 5.3 AASR for Stripmap

The values of the AASR for Stripmap are around of -25 dB, and therefore they do not cause problems to the radar operation. Even so, targets with high reflectivity could cause some azimuth anomalies masking other targets, but it will not be significant while the undesired return is less than 25 dB higher than the desired target.

5.2.2 AASR for ScanSAR

The way to compute the azimuth ambiguities for the ScanSAR mode is similar to the Stripmap with some extra considerations. As it was explained, in ScanSAR the radar divides its scanning time to different sub-swaths in order to cover a wider total swath. For this reason, azimuth point targets will be illuminated by different portions of the antenna main beam. The swath switching causes that parts of the terrain will have less powerful returns than others that will be illuminated by the centre of the beam.

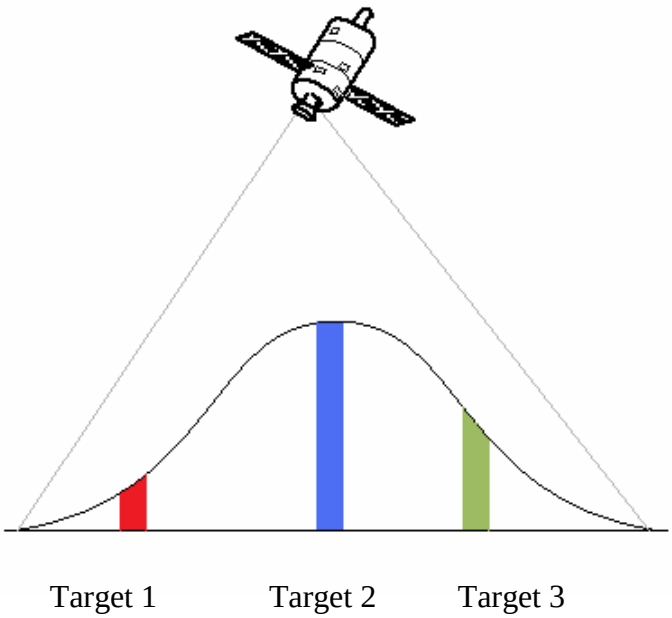

Fig. 5.4 Non-uniformity of received desired echoes

The displacement of the processed Doppler frequency affects to the equations (5.8)-(5.10). To consider the shift introduced in the Doppler spectrum, an extra variable must be inserted in the azimuth antenna pattern.

The new factor, called intermediate frequency (f_i), can take values from –Bp/2 to Bp/2. In order to calculate the AASR for each sub-swath, ten different f_i's will be taken (from -35 Hz to 1065 with 100 Hz step). The new function to compute the AASR will be:

$$AASR = 10\log_{10}\left(\frac{P_{amb}}{P_d}\right) = 10\log_{10}\left(\frac{\sum_{m\neq 0}\int_{-Bp/2}^{Bp/2} W^2{}_{ai}(f_d)\frac{G_{2az}(f_d + mPRF + f_i)}{G_{2azMAX}}df_d}{\int_{-Bp/2}^{Bp/2} W^2{}_{ai}(f_d)\frac{G_{2az}(f_d + f_i)}{G_{2azMAX}}df_d}\right) \quad (5.13)$$

The processing window is, as in Stripmap case, a Hamming window with coefficient 0.75 defined in equation (5.11). The two-way azimuth antenna pattern is still a $sinc^4$ function (5.7).

Finally, the processed Doppler bandwidth changes in comparison with Stripmap. In this case, using the equation (5.12), with the same factor 0.886, and 18 meters for the azimuth resolution, the Doppler bandwidths in Table 5.4 are obtained:

Sub-swath name	Bp (Hz)	Sub-swath name	Bp(Hz)
SM-S_1	407,79	SM-S_12	407,37
SM-S_2	407,77	SM-S_13	407,30
SM-S_3	407,75	SM-S_14	407,24
SM-S_4	407,73	SM-S_15	407,17
SM-S_5	407,70	SM-S_16	407,09
SM-S_6	407,66	SM-S_17	407,01
SM-S_7	407,62	SM-S_18	406,93
SM-S_8	407,58	SM-S_19	406,84
SM-S_9	407,53	SM-S_20	406,75
SM-S_10	407,48	SM-S_21	406,65
SM-S_11	407,43	SM-S_22	406,55

Table 5.4 Doppler bandwidth processed in 22 sub-swaths for ScanSAR with azimuth resolution of 18 meters

ScanSAR PRFs in PAZ are similar to the Stripmap PRFs. Only some of the sub-swaths change their PRFs. In order to compute the AASR for ScanSAR the same PRFs as Stripmap have been used, changing the values of the swaths 3, 5, 6, 8 and 11. The new values are:

Sub-swath name	PRF (Hz)	Sub-swath name	PRF (Hz)
SM-S_1	3781,00	SM-S_12	3816,00
SM-S_2	3741,40	SM-S_13	3496,80
SM-S_3	3675,00	SM-S_14	3187,70
SM-S_4	4440,20	SM-S_15	3504,10
SM-S_5	3796,30	SM-S_16	3200,90
SM-S_6	3732,10	SM-S_17	3504,10
SM-S_7	4377,00	SM-S_18	3214,00
SM-S_8	3782,00	SM-S_19	3484,30
SM-S_9	4400,70	SM-S_20	3214,00
SM-S_10	3805,00	SM-S_21	3471,10
SM-S_11	4388,20	SM-S_22	3207,00

Table 5.5 PRFs for ScanSAR mode

With these input parameters, the results of AASR for ScanSAR are shown in Fig. 5.5. As we can see, 10 results are obtained for each sub-swath. To make the results clearer, Fig. 5.6 shows the worst AASR case for each sub-swath which it is considered the appropriate value for AASR assessment. Table 5.6 presents the values of AASR in ScanSAR mode.

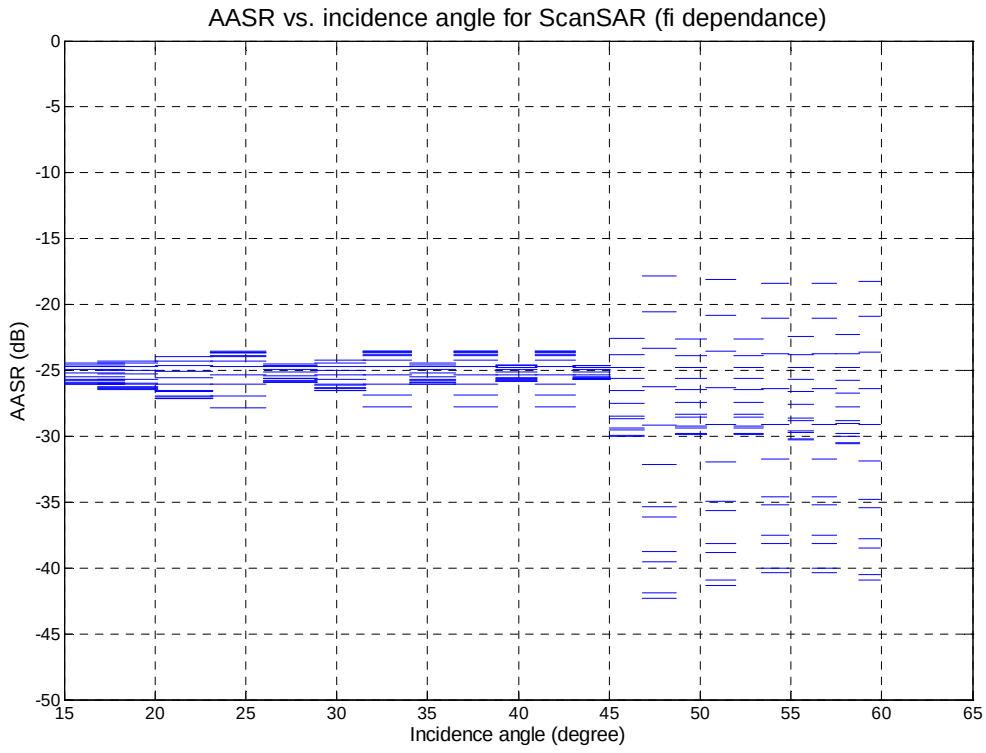

Fig. 5.5 AASR vs. Incident angle in ScanSAR Mode

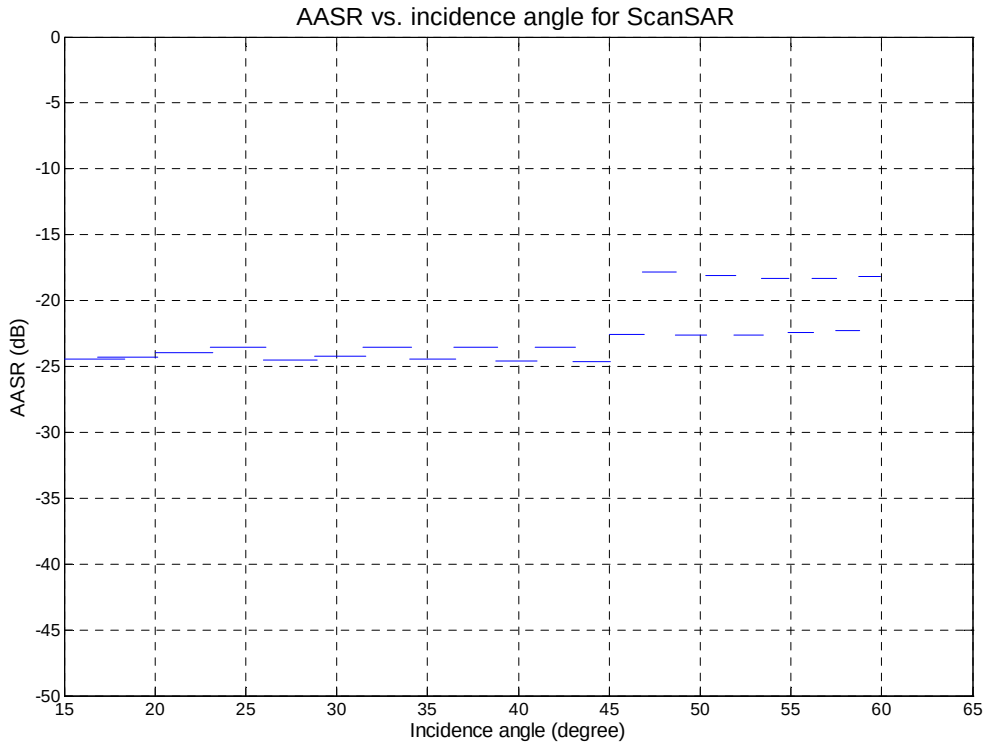

Fig. 5.6 AASR vs. Incident angle in ScanSAR Mode (worst case)

Sub-swath name	AASR(dB)	Sub-swath name	AASR (dB)
SM-S_1	-24.472	SM-S_12	-24.640
SM-S_2	-24.279	SM-S_13	-22.580
SM-S_3	-23.931	SM-S_14	-17.858
SM-S_4	-23.570	SM-S_15	-22.654
SM-S_5	-24.546	SM-S_16	-18.105
SM-S_6	-24.233	SM-S_17	-22.654
SM-S_7	-23.527	SM-S_18	-18.348
SM-S_8	-24.477	SM-S_19	-22.449
SM-S_9	-23.536	SM-S_20	-18.348
SM-S_10	-24.588	SM-S_21	-22.305
SM-S_11	-23.530	SM-S_22	-18.219

Table 5.6 AASR for ScanSAR

As in Stripmap, the azimuth ambiguities in ScanSAR will not be critical to radar operation. For higher incidence angle, the AASR is worst but still remains below -18 dB (-17 dB was considered the worst acceptable ambiguity ratio in Table 3.4). Once the azimuth ambiguities are studied for Stripmap and ScanSAR modes, it is time to consider TOPSAR mode which has an operation similar to the ScanSAR but with some modifications.

5.2.3 AASR for TOPSAR

To compute the azimuth ambiguities in TOPSAR mode, the steering in azimuth must be taken into account because it will change the Doppler history of desired targets as well as the Doppler reception of the ambiguous zones.

The way used to calculate the AASR is the same that in Stripmap and ScanSAR, but the parameters in equations (5.8), (5.9) and (5.10) will change. In particular, the azimuth antenna pattern in function of Doppler frequency will not be the same due to the squint angle introduced by the antenna steering in azimuth [40]. So, while in Stripmap and ScanSAR the evolution of the azimuth angle between the radar and the target only changed due to the platform velocity; in TOPSAR, the steering in azimuth must be added to the natural movement of the satellite. This new feature, as it was explained in section 3.2, causes that the temporal AAP shrinks as well as the reduction of the Doppler bandwidth received from each target.

In Fig. 5.7 we can see the evolution of the received echoes from both modes, Stripmap and TOPSAR. As we can see in the scanning, the step between two consecutives echoes in Stripmap is smaller than in TOPSAR since the evolution of the AAP only varies due to platform movement and, consequently, more pulses will be received from one target using the Stripmap mode.

Fig. 5.8 shows the temporal evolution of the received echoes in both modes. Assuming that the same PRF is used for Strip and TOPSAR, the interpulse period will be the same, so the returns from the target are equally spaced. Consequently, the antenna is illuminating a single target during less time in TOPSAR than in Stripmap, producing a reduction of processed Doppler bandwidth for each point.

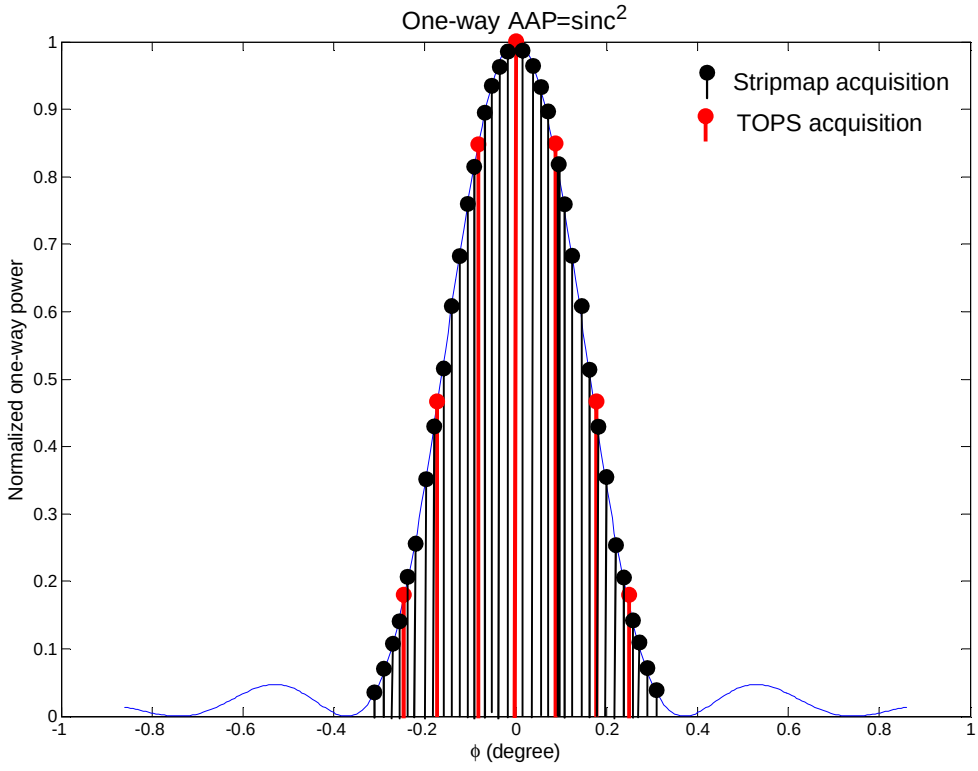

Fig. 5.7 AAP sampling for Strip and TOPSAR

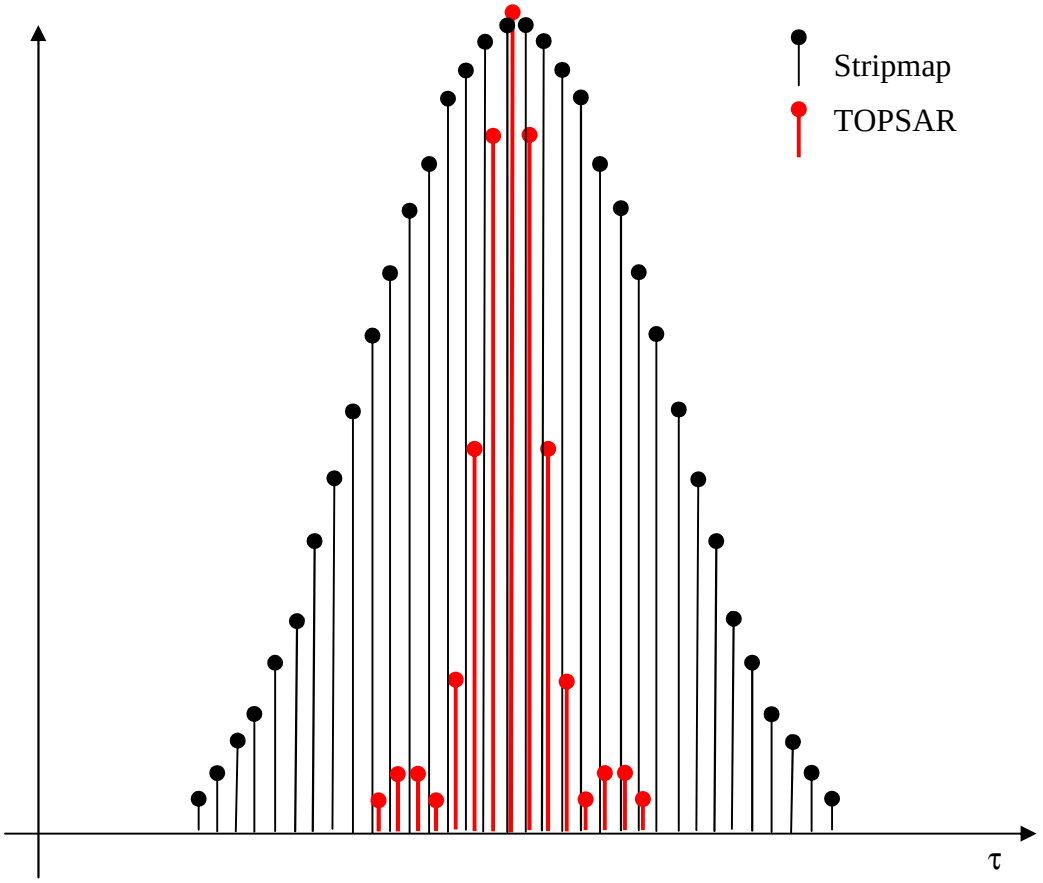

Fig. 5.8 Target echoes evolution due to antenna illumination. Samples are spaced T=1/PRF

The equivalent antenna diagram in function of Doppler frequency will shrink too. Fig. 5.9 shows the antenna pattern versus Doppler frequency for both modes. The equivalent AAP used to represent the Doppler history of a target in TOPSAR mode is described by equation (5.14), where the steering in azimuth causes the contraction of the AAP. This will be the antenna diagram used to compute de desired power received from one target, but it will be necessary to study how the azimuth steering affects to the ambiguous returns in azimuth.

$$G_{2az}\left(\phi\left(f_d\right)\right) = G_0 \mathrm{sinc}^4\left(\frac{L}{2v_e} f_d \left(1+\frac{R_0 K_\phi}{v_e}\right)\right) \tag{5.14}$$

To understand how to compute the ambiguous power received in TOPSAR mode, it is interesting to get back to Stripmap case. In Stripmap, the antenna illuminates the surface with no steering in azimuth. Consequently, all the targets in azimuth will have the same Doppler history, but not at the same time. In Fig. 5.10, the Doppler response of the antenna to a point target is shown. The spectrum processed as desired power is shaded in blue, while the ambiguous power will be computed from the red zones, which are situated at multiples of the PRF (considered around the 3500 Hz for this example). These zones will be indistinguishable from the desired returns.

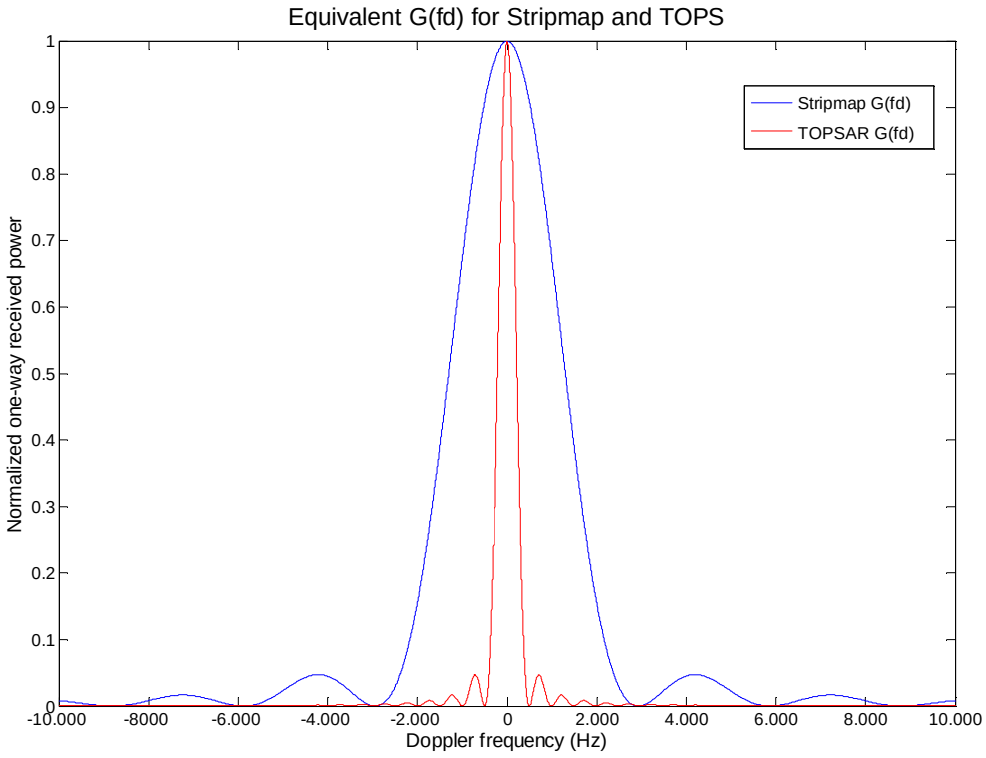

Fig. 5.9 AAP vs. Doppler frequency for Stripmap and TOPSAR

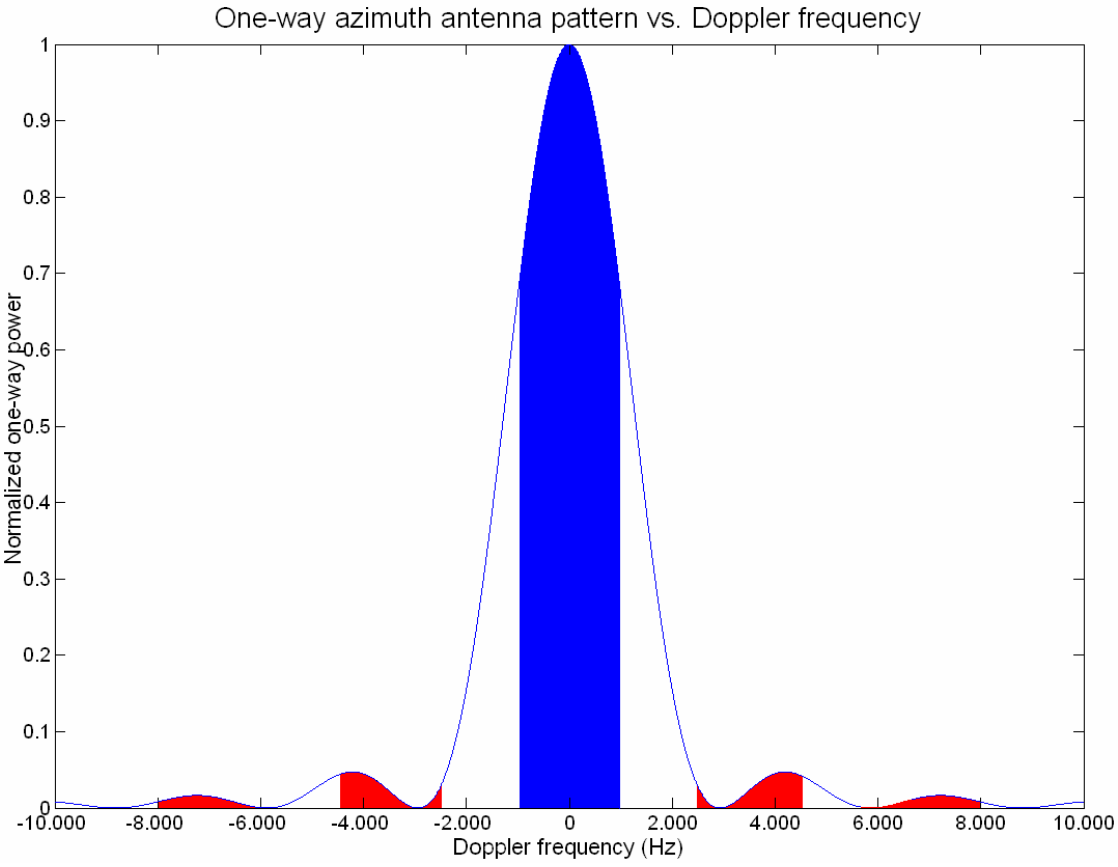

Fig. 5.10 Desired power and ambiguous zones for Stripmap

The ambiguous power for Stripmap mode can be calculated integrating all the ambiguous zones of the spectrum situated at multiples of the PRF. However, to make the computation easier, the AAP can be shifted to multiples of the PRF to centre the ambiguous zones to the processing bandwidth (from *–Bp/2* to *Bp/2*). The resulting diagrams are plotted in Fig. 5.11. As we can see, the Doppler shift of the AAP produces that the ambiguous zones are in the processing window while, at the multiples of the PRF, will appear the main beam of the AAP, but with no physical meaning.

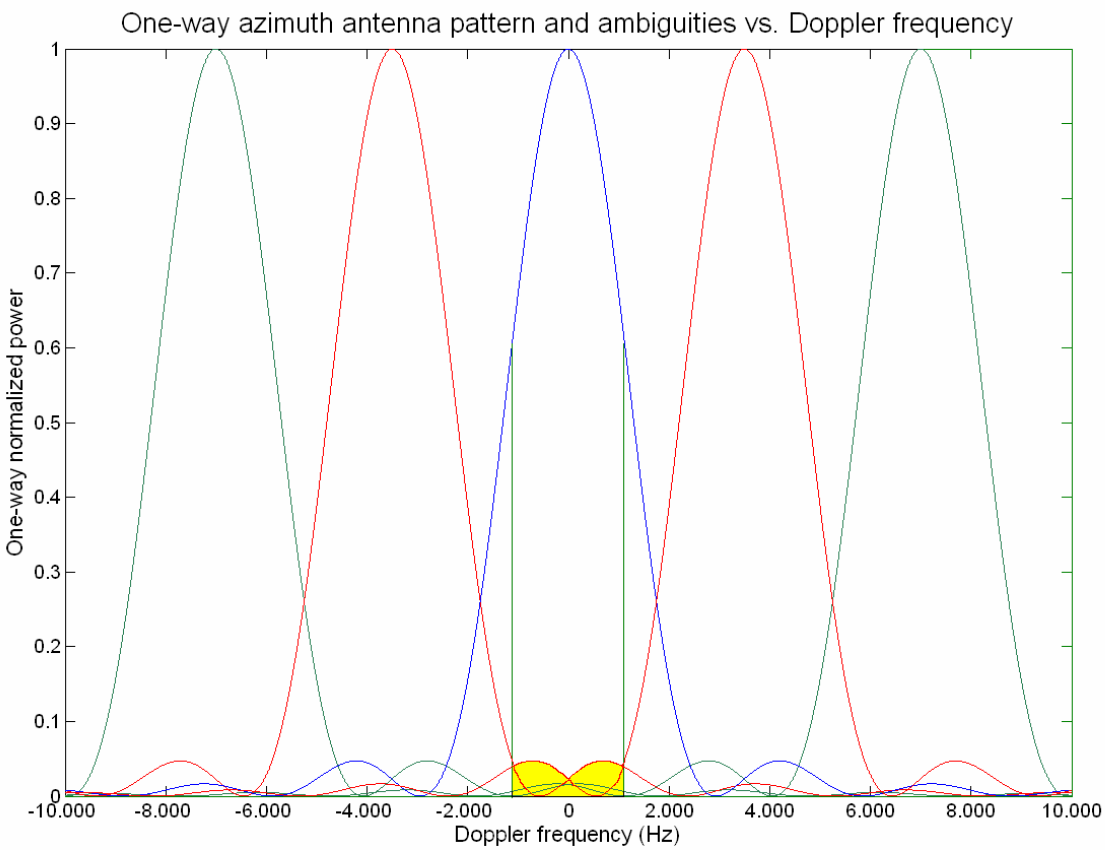

Fig. 5.11 Ambiguous zones shifted to the processing windows at [Bp/2, Bp/2]

To obtain the ambiguous power for TOPSAR mode, a similar study than in Stripmap will be done, but considering the changes introduced by the steering in azimuth. In Fig. 5.12, we can see the temporal evolution of desired and ambiguous signals.

In the top of the figure, the azimuth antenna diagram is plotted in blue, and we can see that the ambiguous zones are illuminated by one of the lateral lobes at this moment. So, in t_0, the antenna is pointing directly to the target with the centre of the main beam, while at the same time, the ambiguous zone is illuminated by the second lateral lobe. The steering in azimuth causes the compression of the temporal evolution for all the points and, consequently, desired and ambiguous zones will have a shorter observation time.

The steering in azimuth will affect the Doppler history of all the points in the scene. Now, unlike the Stripmap mode, not all the points in azimuth will have the same Doppler history. Firstly, the azimuth steering will cause that the desired target does not always have the maximum response at zero Doppler. Moreover, ambiguous zones will have a different Doppler history than in Stripmap, where all the points had maximum of the AAP in zero

Doppler when the antenna crossed over the target.

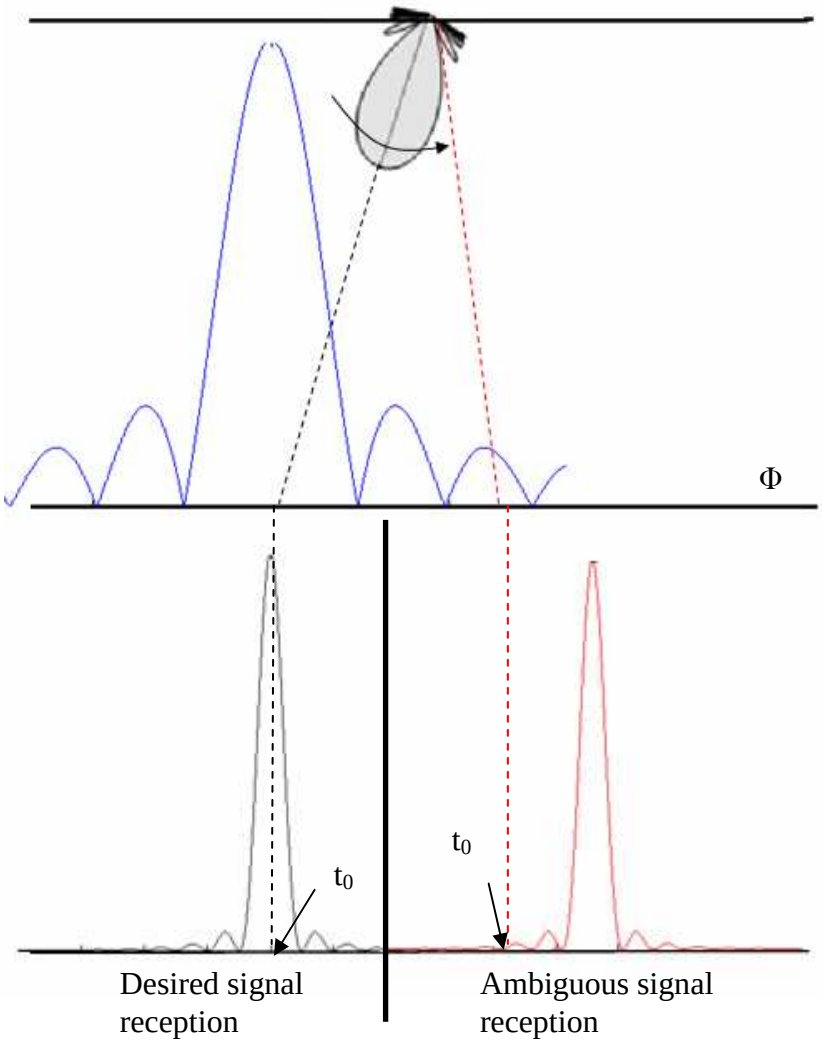

Fig. 5.12 Temporal responses of desired and ambiguous zones

Fig. 5.13 shows the Doppler history of the target and ambiguous zones analysed in the previous picture. The desired target is pointed by the antenna main beam when the radar has already crossed azimuth position of the target. Consequently, a maximum of the AAP is obtained at negative Doppler frequency. On the other hand, the evolution of Doppler for the ambiguous zone, situated at 3500 Hz from the maximum of the desired target, is not the same.

Considering the first ambiguity, that was pointed by the secondary lobe of the antenna, the frequency response will shrink. In the figure, we have marked the azimuth antenna diagram in grey (this is not function of the frequency but it is useful to see where the antenna is pointing in t_0).

Thus, the Doppler response of the desired target suffers the contraction around the -500 Hz, where the antenna points. On the other hand, for the ambiguous zone situated at 3000 Hz (-500 Hz + PRF), the Doppler response will suffer the contraction from this point

(approximately at the beginning of the secondary lobe). As a result, we obtain the same contraction for all of azimuth points but not at the same position and, therefore, not all the points will have the same response in Doppler history.

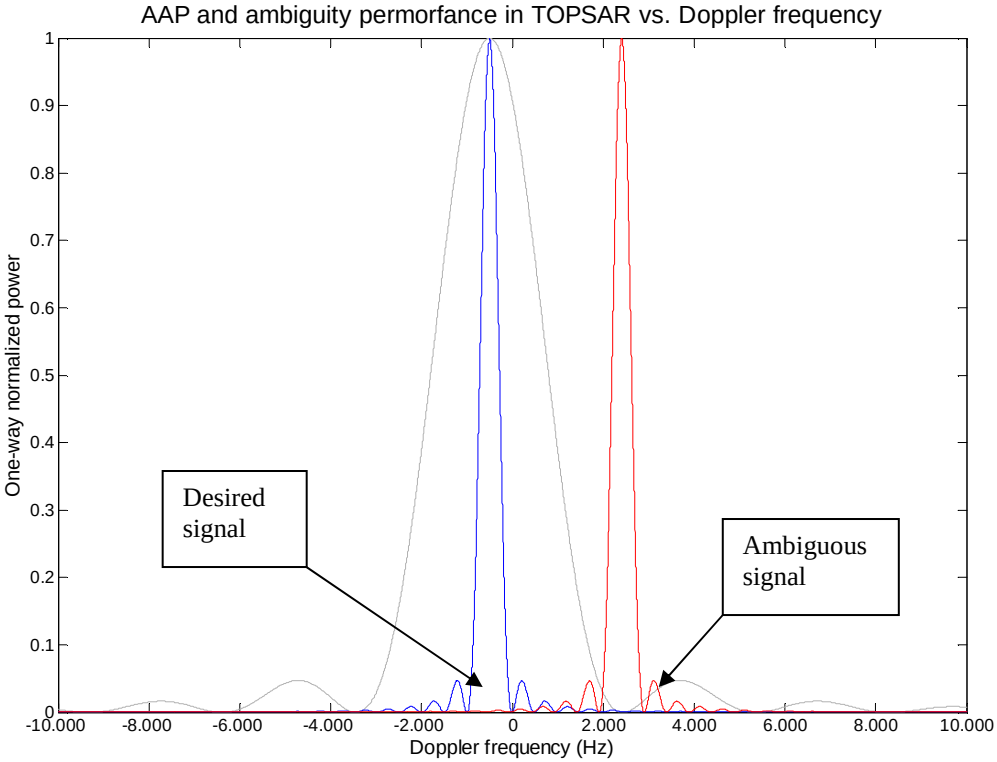

Fig. 5.13 Desired and ambiguous return Doppler histories

Continuing with the azimuth ambiguities analysis, now it is time to integrate all the ambiguous parts of the spectrum that will not be differentiated by the receiver. These ambiguous frequencies, as in Stripmap, will correspond to the frequencies separated at multiples of the PRF from the desired frequencies. To compute the ambiguous power, the parts of the spectrum which correspond to the ambiguous zones must be integrated considering the shift at multiples of the PRF and the shrunk of the AAP characteristic of TOPSAR mode.

Alternatively, it is possible to follow the same procedure used in Stripmap in order to simplify the computation. This will consist on moving the frequency diagrams of ambiguous returns at multiples to the PRF. Doing this, it will be possible to integrate the ambiguities inside the processing window.

Fig. 5.14 shows what it is happening in the azimuth ambiguity analysis for TOPSAR. The lateral lobe processed to compute the ambiguities is the same that in Stripmap since the Doppler shift of ambiguous zones will depend on the PRF. On the other hand, in the TOPSAR case these lobules will shrink due to the azimuth steering.

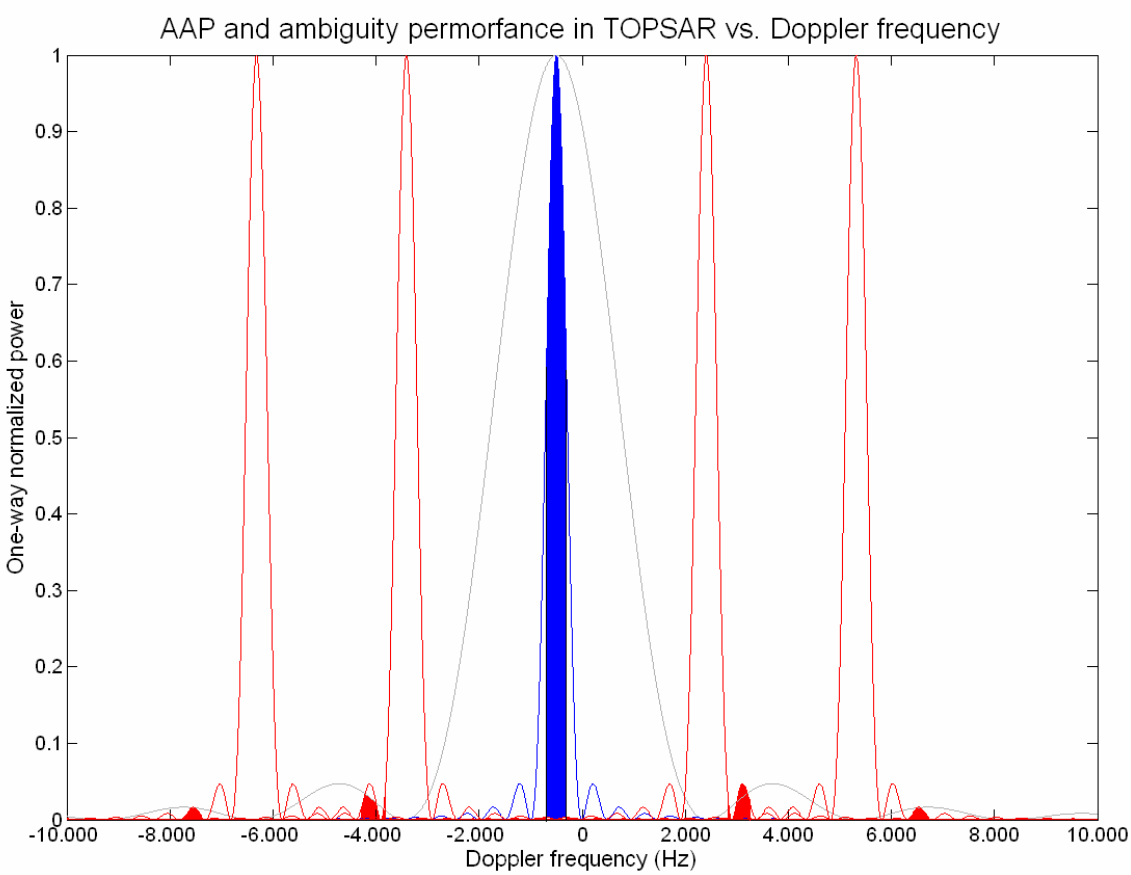

Fig. 5.14 Desired power and ambiguous zones for TOPSAR

The equations to compute the AASR in TOPSAR mode will change significantly due to the modifications that we have explained previously. These equations have to include the steering rates in azimuth as well as the Doppler shift where the ambiguous zones are located. The new equations will be:

$$P_t = \int_{-Bp/2}^{Bp/2} \left[W_{ai}{}^2 (f_d + f_i) \frac{G_{2az}\left(\phi(f_d + f_i + d)\right)}{G_{2az\,MAX}} \right] df_d \tag{5.15}$$

$$G_{2az}\left(\phi(f_d + f_i + d)\right) = G_0 \mathrm{sinc}^4 \left(\frac{L}{2v_e} (f_d + f_i + d) \left(1 + \frac{R_0 K_\phi}{v_e} \right) \right) \tag{5.16}$$

$$P_{amb} = \sum_{m \neq 0} \int_{-Bp/2}^{Bp/2} \left[W_{ai}{}^2 (f_d + fi) \frac{G_{2az}\left(\phi(f_d + mPRF + f_i + d)\right)}{G_{2az\,MAX}} \right] df_d \tag{5.17}$$

$$G_{2az}\left(\phi(f_d)\right) = G_0 \mathrm{sinc}^4 \left(\frac{L}{2v_e} \left[(f_d + f_i + d) \left(1 + \frac{R_0 K_\phi}{v_e} \right) + mPRF \right] \right) \tag{5.18}$$

The way to compute the desired and ambiguous power is the same considering that now the processing window will present a Doppler shift depending on the Doppler centroid of processed target.

The AAP used to compute the ambiguities in TOPSAR must consider the azimuth steering, which involves a Doppler response contraction, and the PRF shift of each ambiguous zone. The processed Doppler bandwidth will be smaller than in Stripmap. Specifically, to obtain an azimuth resolution of 18 meters as in ScanSAR, the Doppler bandwidth using (5.12) will be 400 Hz approximately. With equations from (5.15) to (5.18) and the PRF from ScanSAR Mode (Table 5.5) the results of the next table are obtained for the AASR in TOPSAR:

Sub-swath name	AASR(dB)	Sub-swath name	AASR (dB)
SM-S_1	-25.202	SM-S_12	-25.146
SM-S_2	-25.256	SM-S_13	-24.925
SM-S_3	-25.306	SM-S_14	-21.466
SM-S_4	-24.647	SM-S_15	-24.961
SM-S_5	-25.179	SM-S_16	-21.674
SM-S_6	-25.267	SM-S_17	-24.963
SM-S_7	-24.611	SM-S_18	-21.875
SM-S_8	-25.201	SM-S_19	-24.856
SM-S_9	-24.622	SM-S_20	-21.875
SM-S_10	-25.165	SM-S_21	-24.779
SM-S_11	-24.616	SM-S_22	-21.767

Table 5.7 AASR for TOPSAR

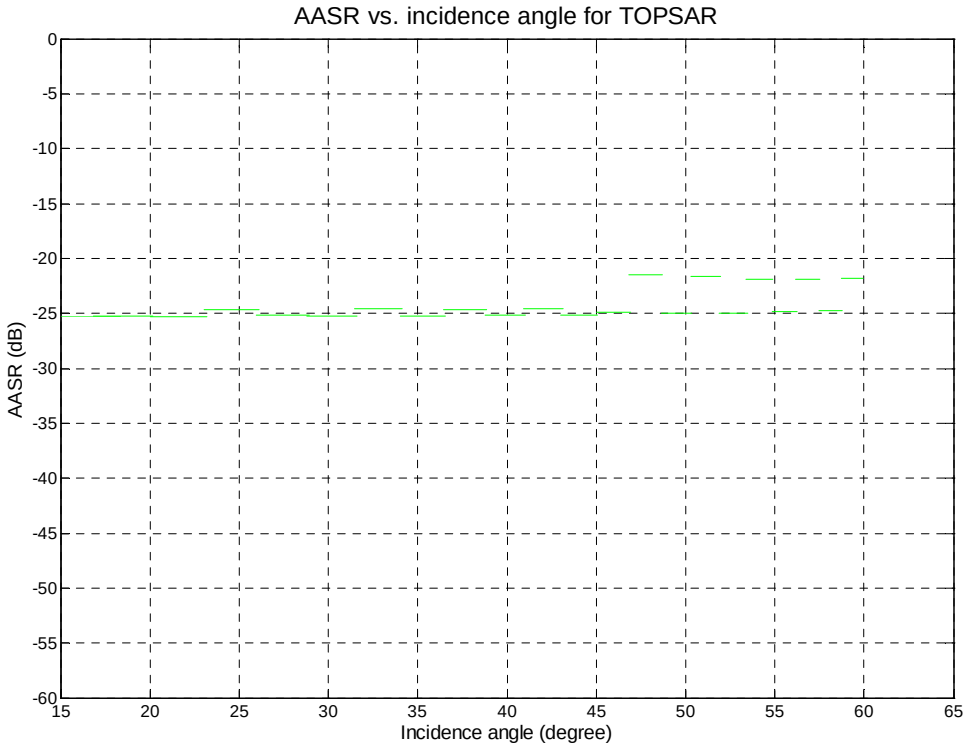

Fig. 5.15 AASR vs. incidence angle for TOPSAR

Once again, the results of the AASR for TOPSAR are better than -20 dB, goal defined in Table 3.4 for ScanSAR, so the results are in the admissible limits. The results of the AASR are plotted in Fig. 5.15 in function of the incidence angle. Finally, Fig. 5.16 shows the differences in AASR of Stripmap, ScanSAR and TOPSAR. As it was expected, ScanSAR has a worst performance since the target can be illuminated by the edge of the main beam. Besides, the results from Stripmap and TOPSAR are similar except from those swaths with different PRFs. These results state the better performance of the TOPSAR mode vs. ScanSAR. Once again, TOPSAR shows better results, so it must be consider as an interesting alternative in imaging radar for wide range coverage purposes. Furthermore, with TOPSAR, the AASR azimuth dependency of ScanSAR has been solved.

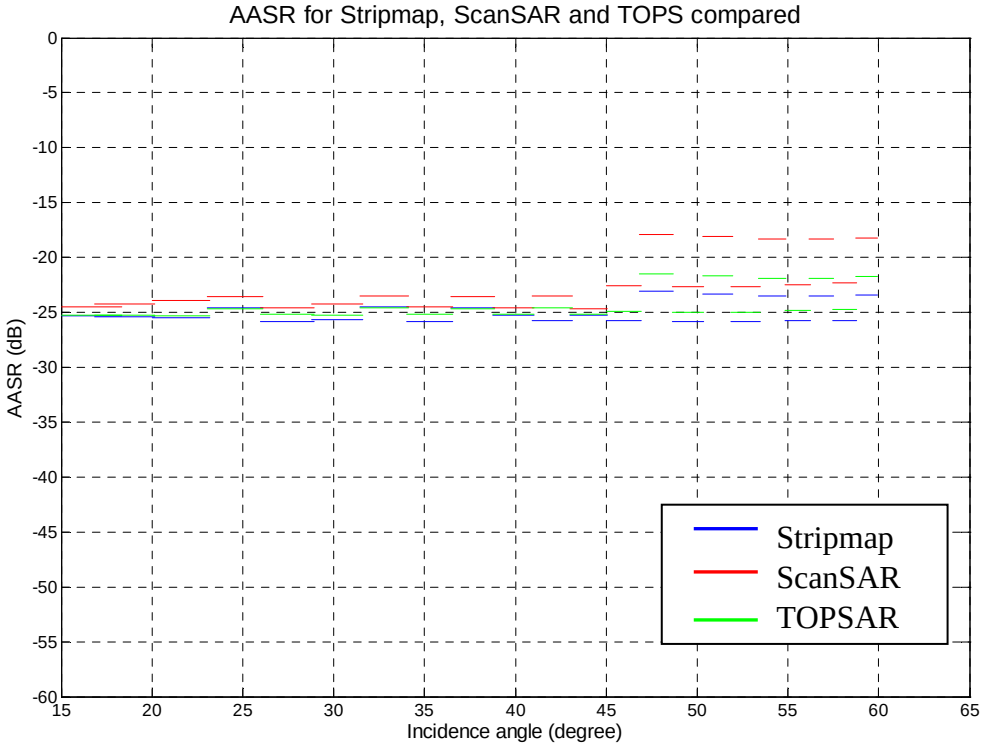

Fig. 5.16 AASR in Stripmap, ScanSAR and TOPSAR

5.3 Range ambiguities

As it was explained, range ambiguities are the result of echoes from preceding and succeeding pulses that arrive at the same time that desired return at the antenna. Range ambiguities to signal ratio (RASR) will be computed as the quotient between the total power received from preceding and succeeding pulses and the power of the desired pulse [22].

In Fig. 5.17, a simple diagram illustrates the origin of range ambiguities. In the figure, swath is identified as a yellow strip on the ground. The antenna illuminates the swath but the sidelobes can receive echoes from further or nearer range distances. The antenna pattern in range is plotted in blue in the figure. As it can be seen, the main beam points to the centre of the swath, but the side lobes are illuminating undesired range distances.

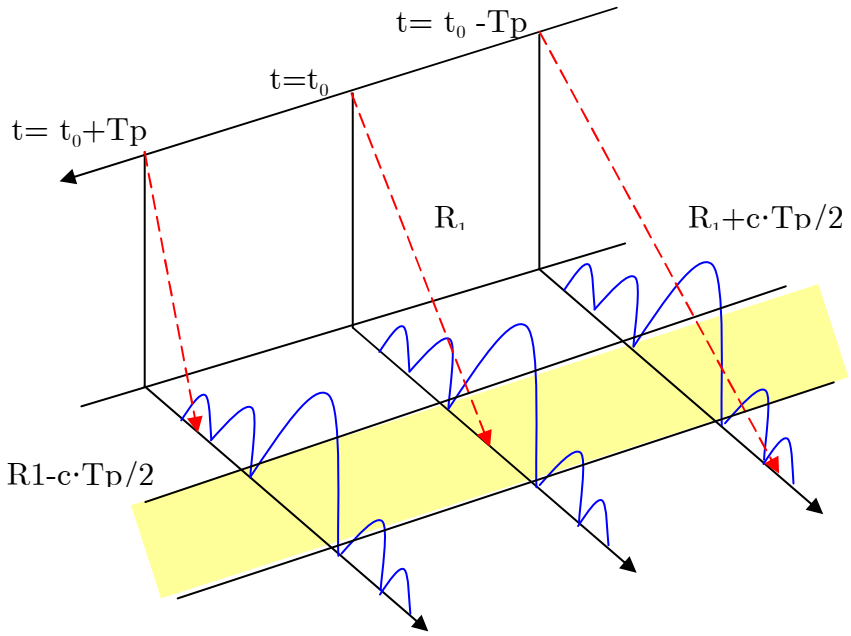

Fig. 5.17 Origin of range ambiguities in SAR systems

In Fig. 5.17, the desired pulse is send at t_0, so the echo will arrive to the antenna at $t_1 = t_0 + \frac{2R_1}{c}$, where R_1 is the distance to the middle of the swath. The pulses that will cause higher ambiguous returns are sent at times $t_0 - T_p$ and $t_0 + T_p$, where T_p is the inverse of the PRF. The desired returns of these pulses, will arrive at $t_0 + \frac{2R_1}{c} - T_p$ and $t_0 + \frac{2R_1}{c} + T_p$, so these returns would not affect to the desired echo. However, radar illuminates more than the desired swath. So, for the previous emitted pulse, the receiver will receive the return of a target situated at $R_2 = R_1 + \frac{cT_p}{2}$ at:

$$t_2 = t_0 - T_P + \frac{2R_2}{c} = t_0 - T_P + \frac{2\left(R_1 + \frac{cT_p}{2}\right)}{c} = t_0 + \frac{2R_1}{c} \qquad (5.19)$$

Consequently, the echo of this point will arrive at the same time that the desired pulse since $t_2 = t_1$ and it will be considered as an ambiguous return. With a similar reasoning, the ambiguous distances for succeeding pulses can be determined. Considering a target situated at distance $R_3 = R_1 - \frac{cT_p}{2}$ and knowing that the pulse has been sent at $t_0 + T_p$, in (5.20) is demonstrated that it will be an ambiguous zone:

$$t_3 = t_0 + T_P + \frac{2R_2}{c} = t_0 + T_P + \frac{2\left(R_1 - \frac{cT_p}{2}\right)}{c} = t_0 + \frac{2R_1}{c} \tag{5.20}$$

However, not only the adjacent pulses will cause ambiguous returns. It is necessary to consider further pulses to do a complete analysis of range ambiguities. In order to generalise the ambiguous ranges of a general point situated at R_1, the ambiguous distances will be obtained as:

$$R_{amb} = R_1 \pm n\frac{cT_p}{2} \qquad n = \pm 1, \pm 2 \ldots n_h \tag{5.21}$$

Where *n* is an integer that represents the pulse number (0 for desired pulse, negative for succeeding pulses and positive for previous ones) and n_h is the number of pulses considered in RASR computation. Theoretically the number of pulses is infinite, but in practise when *n* increases the distance increases and the illumination of these points by the antenna pattern decreases, so the receive power will be insignificant for great *n's*.

Once the ambiguous distances are determined, the RASR can be calculated from the radar equation (5.22), where the constant values will not have interest when we compute the RASR because they will be in the numerator and denominator of the ratio. So, finally, the required parameters to compute the range ambiguities will be the incidence angle and the backscattering coefficient of the illuminated surface, as well the ambiguous distances of these pulses determined by (5.21). Also, the weighting of the antenna diagram in range will be necessary to compute the total RASR.

$$P_r = \frac{P_t G_{TX} G_{RX} \sigma^0 S \lambda^2}{(4\pi)^3 R^4 L} = \left(\frac{P_t G_{TX} G_{RX} \sigma^0 \lambda^2}{(4\pi)^3 R^4 L}\right)\left(R_0 \theta_H\right)\left(\frac{c\tau_0}{2\sin\theta_i}\right) = K\frac{G_{TX} G_{RX} \sigma^0}{R^3 \sin\theta_i} \tag{5.22}$$

Then, the RASR for each point can be determined by taking the power of all ambiguous returns, which include the previous and succeeding echoes, and the desired power. Taking the ratio between these powers the RASR will be:

$$RASR = 10\log_{10}\left(\frac{P_{amb}}{P_d}\right) \tag{5.23}$$

The desired power (P_d) received at the radar is obtained from (5.22) taking the variable parameters, which will not be cancelled at the ratio (5.23). The total ambiguous power (P_{amb}) will be obtained as the summation of the powers received from preceding and succeeding pulses. Equations (5.24) and (5.25) are used to compute the desired and ambiguous powers respectively.

$$P_d = \frac{\sigma^0(\theta_i) G_{TX} G_{RX}}{R^3 \sin(\theta_i)} \tag{5.24}$$

$$P_{amb} = \sum_{\substack{n=-n_h \\ n\neq 0}}^{n_h} P_{amb}^{+} \sum_{n=-n_h}^{n_h} P_{amb}^{-} = \sum_{\substack{n=-n_h \\ n\neq 0}}^{n_h} \frac{\sigma^0(\theta_{ian}) G_{TXn}^{+} G_{RXn}^{+}}{R_{amb_n}{}^3 \sin(\theta_{ian})} + \sum_{\substack{n=-n_h \\ n\neq 0}}^{n_h} \frac{\sigma^0(\theta_{ian}) G_{TXn}^{-} G_{RXn}^{-}}{R_{amb_n}{}^3 \sin(\theta_{ian})} \quad (5.25)$$

Where $\sigma^0(\theta_{ian})$ is the backscattering coefficient for each point, G_{TX}, G_{RX} are the antenna pattern in transmission and reception and θ_i is the incidence angle of the desired return while θ_{ian} is the incidence angle for the *n*th ambiguous pulse. Finally, the terms P_{amb}^{+} and P_{amb}^{-} mean the total ambiguous power in look direction and the opposite direction from the desired target.

As with azimuth ambiguities, the range ambiguities will be computed for Stripmap and ScanSAR to get some preliminary results in order to compute the range ambiguities for the TOPSAR mode.

5.3.1 RASR for Stripmap

In order to determine the range ambiguities for Stripmap mode, the values of equations (5.24) and (5.25) are needed to get the desired and the ambiguous powers. First of all, the antenna pattern in range must be defined. For this study a *sinc*^{2} pattern (5.26) will be use.

$$G_{TX} = G_{RX} = G_0 \mathrm{sinc}^2\left(\frac{W}{\lambda}\phi\right) \quad (5.26)$$

ϕ is the difference between the look angle where the antenna is pointing with the main beam centre and the look angle of the point that we are analysing. To calculate this angle, the next expression is used:

$$\phi = |\theta_{l0} - \theta_l| = \left|\cos^{-1}\left(\frac{(R_e+h)^2 + R_0{}^2 - R_e{}^2}{2(R_e+h)R_0}\right) - \cos^{-1}\left(\frac{(R_e+h)^2 + R^2 - R_e{}^2}{2(R_e+h)R}\right)\right| \quad (5.27)$$

In equation (5.27), R_0 is the distance to the middle of the swath where the antenna is pointing, R is the slant range to the point that is being analysed, R_e is the earth radius and h is the platform height.

Another necessary parameter is the PRF of each sub-swath in order to know where the ambiguous points are. Using the PRFs of Table 5.1, the values of ambiguous distances ca be obtained. The backscattering model used to compute the ambiguities, as in AASR, is a uniform model. Finally, the number of ambiguous pulses considered (n_h) has been set to 6.

With these parameters the results of Fig. 5.18 are obtained. As it can be observed, the range ambiguities are below -20 dB except for the last four sub-swaths where we get a worse performance. Then, a correct operation of the radar can be guaranteed for incidence

angle from 15 to 50 degrees. For higher incidence angles, some problems due to ambiguous signals could appear for points with little reflectivity and situated at the edges of these sub-swaths.

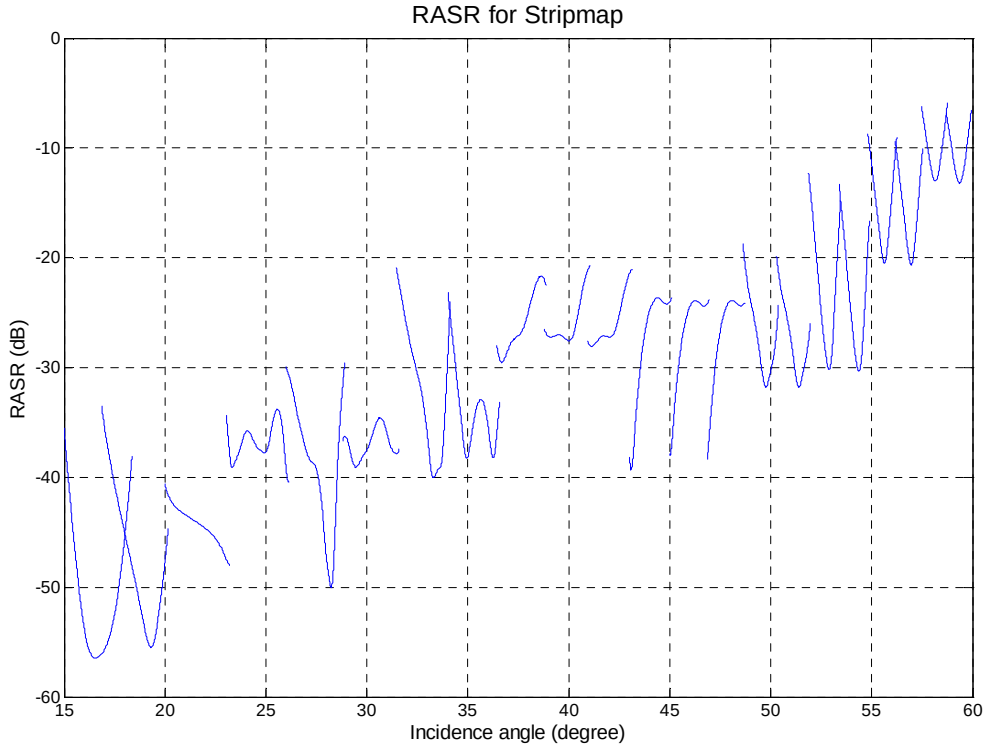

Fig. 5.18 RASR vs. Incident angle in Stripmap Mode

5.3.2 RASR for ScanSAR

Since the Doppler processed bandwidth and the sub-swath commutation do not affect to the computation of the range ambiguities, the differences between the results obtained in Stripmap mode and ScanSAR will be caused by the changes on the PRFs of some sub-swaths.

Using the same equations (5.24) and (5.25) to get the desired and ambiguous powers and taking the PRFs from Table 5.5, the results obtained for range ambiguities are plot in Fig. 5.19.

Once again, the results for range ambiguities are not worrying except those corresponding to the furthest sub-swaths, where the RASR raises above -20 dB as in Stripmap mode. The most critical zones are in the edges of last sub-swaths where the ambiguity ratio can deteriorate the radar image reception.

As it was commented, these results are an approximation of real values of RASR since we are using a *sinc* shape to calculate the ambiguities. This approximation is good enough for far distances, but in section 5.4, the RASR will be computed with real antenna range patterns. There will be checked that the approximation for near range is not precise enough and the results will vary slightly.

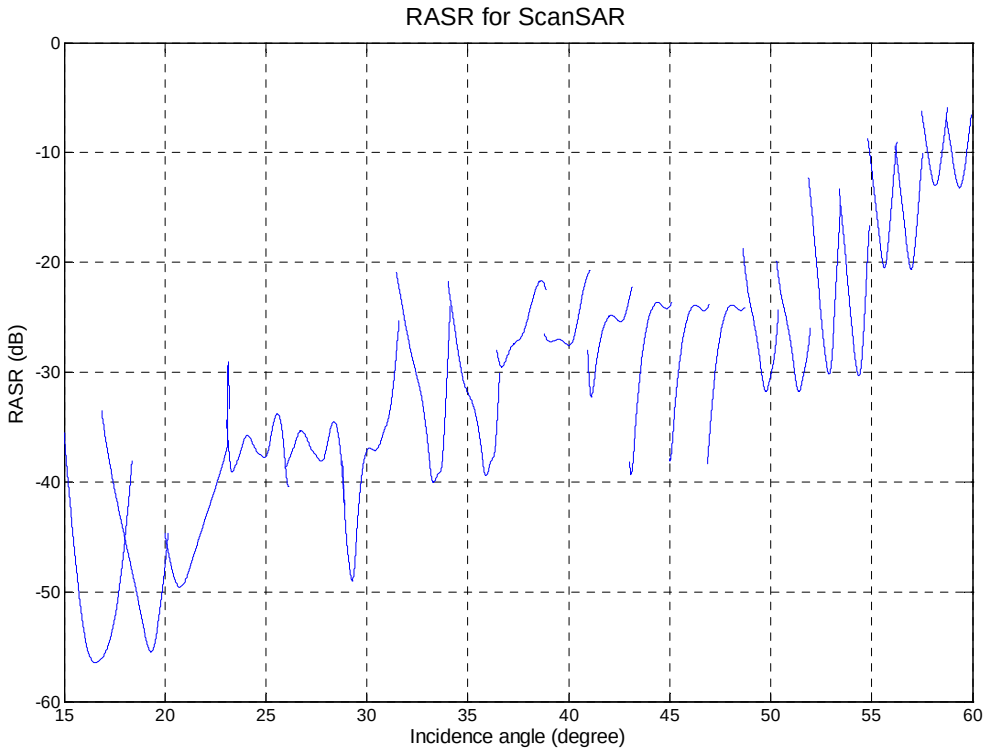

Fig. 5.19 RASR vs. Incident angle in ScanSAR Mode

5.3.3 RASR for TOPSAR

TOPSAR mode introduces an azimuth steering of the antenna that can affect to the range ambiguities. For each slant range, the antenna can point perpendicularly to the fly direction or with a little squint due to the azimuth steering. The azimuth change in the antenna pointing direction can cause variations to the RASR. Fig. 5.20 shows this new feature and explains how it affects the ambiguous distances where the RASR is computed. In the picture two different pointing directions are plotted in the same sub-swath scanning. In point P1, the antenna is perpendicularly pointing to the swath at a general distance R_1. On the other hand, in point P2, the antenna modifies its azimuth pointing, due to the azimuth steering of the antenna, changing the distance to the pointed target for the same slant range. Now, the target which was situated at slant range R_1, will be at $\frac{R_1}{\cos\phi}$, being ϕ the azimuth steering angle.

To understand better what is happening, in Fig. 5.21 the same situation as in Fig. 5.20 is plotted but in a top view, considering only azimuth and range directions. As we can see, the distance to the middle of the sub-swath has increase, and now the distance to the targets is $\frac{R_1}{\cos\phi}$. Furthermore, the distance that can cause ambiguous returns has also changed.

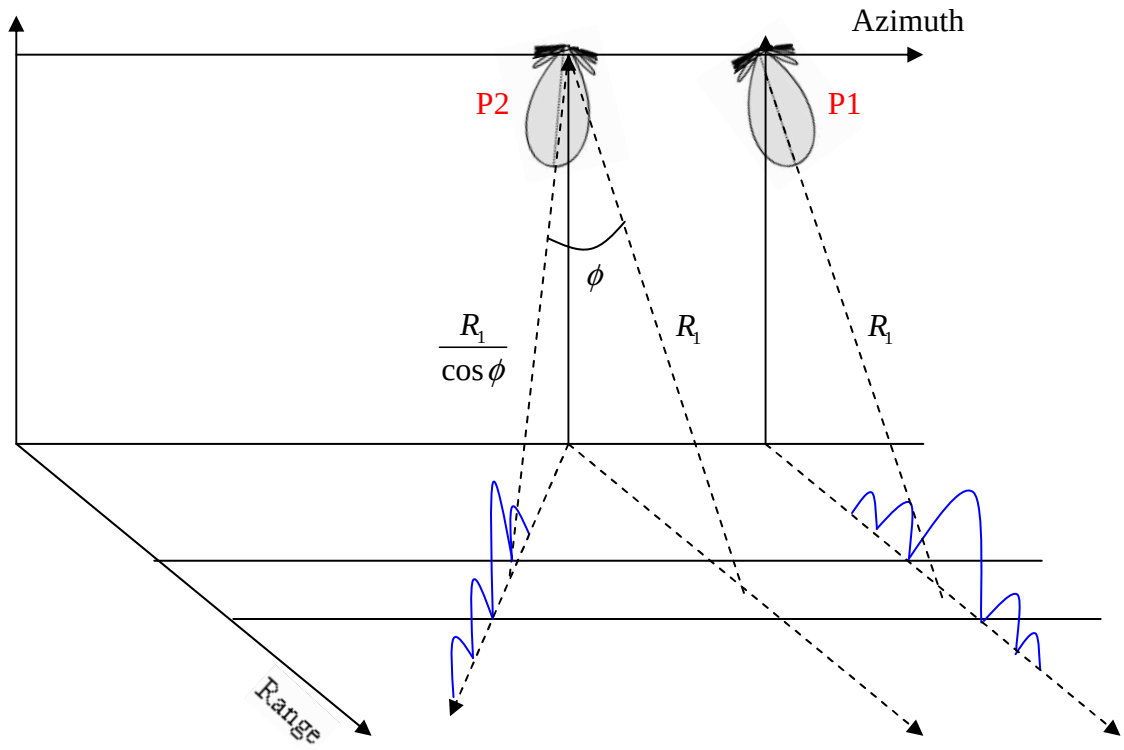

Fig. 5.20 RASR variation due to azimuth pointing variation in TOPSAR

The ambiguous returns will come from distances $R_{amb} = \frac{R_1}{\cos\phi} \pm n\frac{cT_p}{2}$ as it is demonstrated in following equations. The desired echo will arrive at the receiver at $t_1 = t_0 + \frac{2R_1/\cos\phi}{c}$. On the other hand, the returns from preceding and succeeding pulses send at $t_0 - T_p$ and $t_0 + T_p$ respectively, will arrive, considering the distances of the Fig. 5.21, at:

$$t_2 = t_0 - T_P + \frac{2R_2}{c} = t_0 - T_P + \frac{2\left(\frac{R_1}{\cos\phi} + \frac{cT_p}{2}\right)}{c} = t_0 + \frac{2R_1/\cos\phi}{c} = t_1 \qquad (5.28)$$

$$t_3 = t_0 + T_P + \frac{2R_2}{c} = t_0 + T_P + \frac{2\left(\frac{R_1}{\cos\phi} - \frac{cT_p}{2}\right)}{c} = t_0 + \frac{2R_1/\cos\phi}{c} = t_1 \qquad (5.29)$$

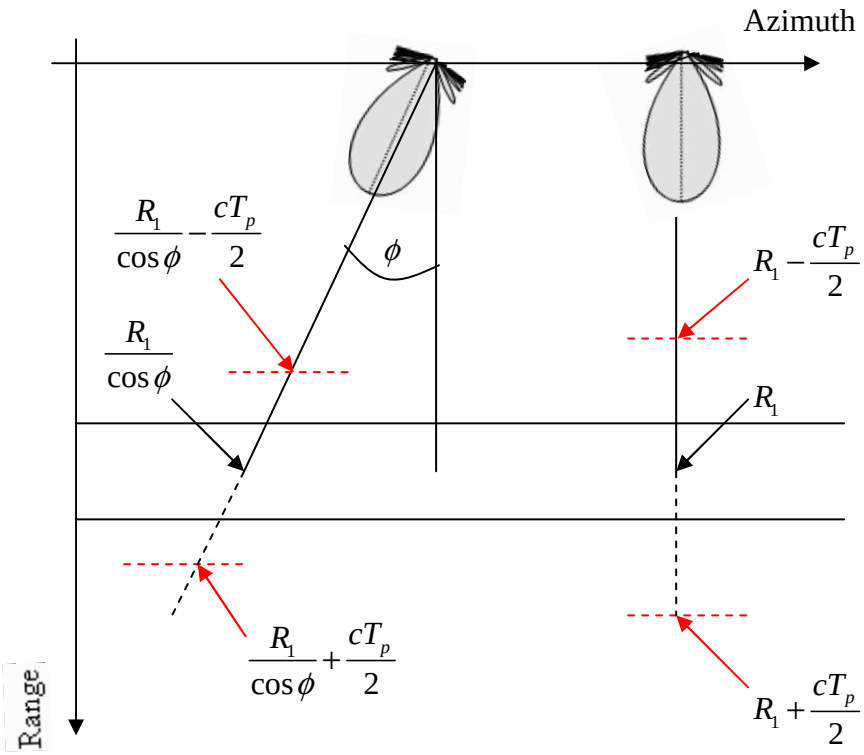

Fig. 5.21 2D top view of RASR ambiguities in TOPSAR mode

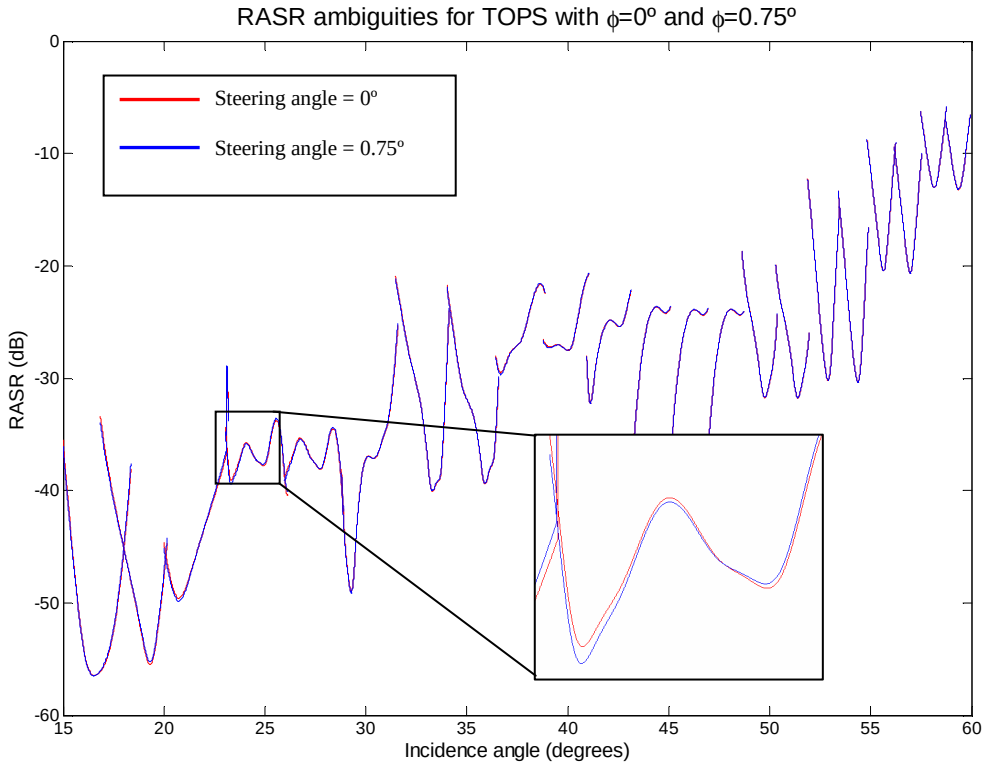

Fig. 5.22 RASR vs. incidence angle in TOPSAR

Considering the azimuth steering angle characteristic of TOPSAR mode the RASR results will change slightly. The steering angle in azimuth will not be larger than 0.4º, when an azimuth resolution of 18 meters is required, but we will consider an extreme case using the maximum deviation in azimuth allowed in PAZ system (0.75º).

With this parameter, the new results for RASR in TOPSAR are plotted in Fig. 5.22. The differences introduced due to the steering in azimuth are negligible since the azimuth steering angle is small. If we zoom in the ambiguities in one sub-swath, it is possible to distinguish the differences between both azimuth steering angles, but they are tenths of a dB and, consequently, they can be considered negligible.

Once again, it is an approximated result. We need to consider other factors that can affect to the RASR when the antenna is steered in azimuth (sub-array diagram, grating lobes…). For this reason, next section presents the results for ambiguities computed with real antenna diagrams obtained with Antenna MOdelleR for PAZ (AMOR).

5.4 Ambiguity computation with non-approximated antenna patterns

Until now, a theoretical model for antenna pattern has been used to compute the range and azimuth ambiguities. It was a good approximation for Stripmap or ScanSAR, but in TOPSAR, grating lobes rise significantly and sub-array diagram has more influence due to the steering in azimuth. In this section, real antenna pattern computed using AMOR will be used to obtain more exact results for RASR and AASR.

First of all, we are going to introduce the concept of sub-array diagram and grating lobes. After that, a brief introduction to AMOR interface will be exposed. However, this document does not pretend to be a user guide for AMOR, so it will only be an explanation of how we have obtained the antenna pattern cuts. Finally, range and azimuth ambiguities will be computed again to see how the new antenna patterns affect to the RASR and AASR

5.4.1 Sub-array diagram and grating lobes influence

The antenna in our system consists of 3 leaves, with 4 panels each in the azimuth direction. Each panel has 32 sub-arrays of 16 slotted rings in the elevation direction. Separation between sub-arrays is 0.8 lambda in x-axis and 0.7 lambda in y-axis. The sub-array of the antenna can be modelled as follows [43]:

$$E_\theta = \frac{jke^{jkr}}{2\pi r}\frac{\sin\left(\frac{kl}{2}\sin\theta\cos\phi\right)}{\frac{kl}{2}\sin\theta\cos\phi}\cos\left(\frac{kl}{2}\sin\theta\cos\phi\right)\frac{\sin\left(8kd_x\sin\theta\cos\phi\right)}{\sin\left(0.5kd_x\sin\theta\cos\phi\right)}\sin\phi \qquad (5.30)$$

$$E_\phi = \frac{jke^{jkr}}{2\pi r}\frac{\sin\left(\frac{kl}{2}\sin\theta\cos\phi\right)}{\frac{kl}{2}\sin\theta\cos\phi}\cos\left(\frac{kl}{2}\sin\theta\cos\phi\right)\frac{\sin\left(8kd_x\sin\theta\cos\phi\right)}{\sin\left(0.5kd_x\sin\theta\cos\phi\right)}\cos\theta\cos\phi \qquad (5.31)$$

where k is the wave number, (r, θ, ϕ) are the spherical coordinates of the point in space where the fields are to be computed, l is the square element size and d_x is the separation between elements.

The sub-array diagram will affect to the reception of echoes since the pattern of the antenna is the combination of array factor multiplied by sub-array diagram. For this reason, when the antenna is steered in azimuth, the power received from desired target can suffer some degradation and, at the same time, some ambiguous return can be seen more powerful. In Fig. 5.23, the sub-array diagram in θ cut can be observed. If an azimuth steering of 1 degree is set to the antenna, the desired signal could suffer a degradation of 2 dB due to sub-array diagram. Using the patterns cuts computed with AMOR, the effect of sub-array diagram will be considered and we must study how it will degrade the signal reception.

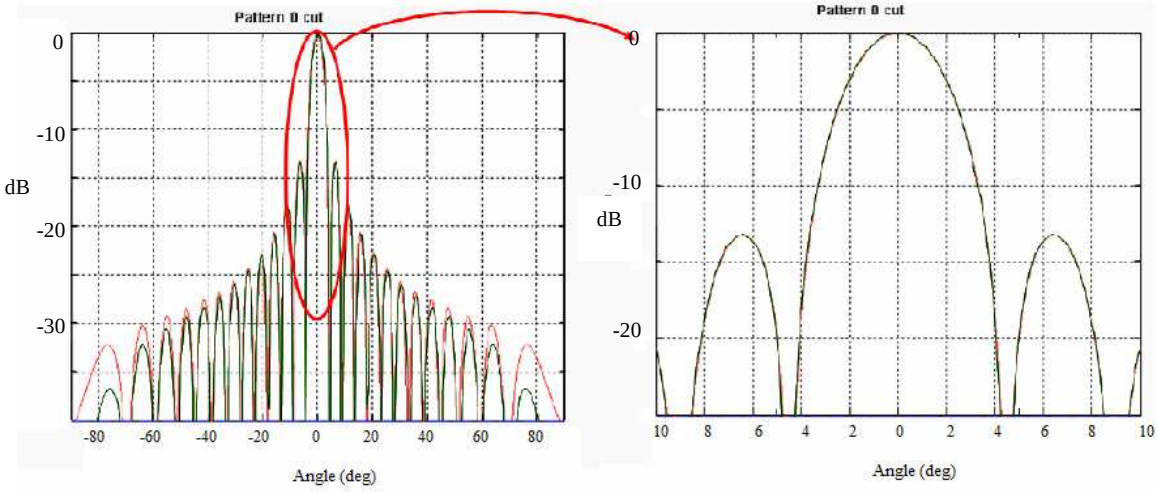

Fig. 5.23 Sub-array diagram in θ cut. The sub-array attenuation can be significantly when a higher steering angle in azimuth is set

On the other hand, the influence of grating lobes must be considered. When an azimuth steering is applied to the antenna diagram, grating lobes can increase significantly. In order to determine the origin of grating lobes, a short explanation about array antennas is presented next.

Let us to consider a 1-dimensional array with all the elements with same separation for this study. Although the antenna in SAR consists of a 2-dimensional sub-array, this explanation will be really useful to understand why the grating lobes appear at the antenna diagram.

Considering the linear array of Fig. 5.24, the electrical field radiated by the sub-array can be obtained from [26]:

$$\vec{E}(\vec{r}) = \vec{E}_0(\vec{r}) \sum_{n=0}^{N-1} a_n e^{jn(kd\cos\theta+\alpha)} \tag{5.32}$$

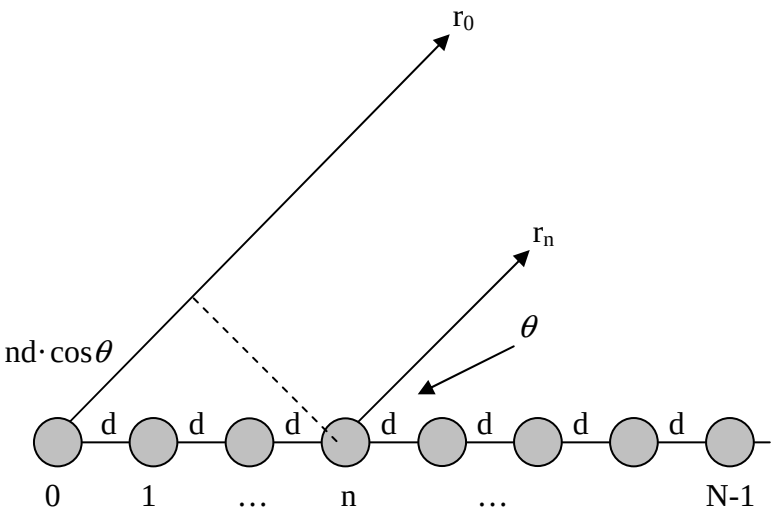

Fig. 5.24 Radiated fields from an antenna array

In equation (5.32), term $kd\cos\theta+\alpha$ is called ψ and it represents the phase difference between contributions in far field of two consecutives elements of the array. This difference is equal to the change of phase due to the difference of the ways ($kd\cos\theta$) and the progressive phase α of each element. a_n represents the excitation current of *n*th element and $\vec{E}_0$ is the radiated field by the basic element with unitary excitation. From this equation we can obtain the array factor (AF) which is defined as:

$$AF(\psi)=\sum_{n=0}^{N-1}a_n e^{jn\psi} \tag{5.33}$$

The AF for one-dimensional array presents the following properties:

- It is a periodic function of ψ angle, with 2π period, whose Fourier coefficients correspond to excitation coefficients a_n. The AF is a Fourier transform of the discreet sequence of these coefficients.
- If a_n coefficients are real and positive, the array factor is maximum at the origin (ψ=0).
- θ angle, which shows the radiation direction, only takes real values from 0 to π, which correspond to an interval of ψ compressed between:

$$\psi\in[-kd+\alpha, kd+\alpha] \tag{5.34}$$

  This interval is called visible margin. The length of visible margin is *2kd* and it is centred to $\psi=\alpha$.
- With a_n real and positives, if the visible margin includes the origin ψ=0, the maximum in the real radiation diagram will be in:

$$\theta_{\max} = \arccos\left(-\frac{\alpha}{kd}\right), \quad |\alpha| \le kd \tag{5.35}$$

As we can see, the maximum direction can be easily changed modifying the value of progressive phase between elements. It is what we use in radar to do the steering in azimuth for TOPSAR mode (in SAR the antenna is a two-dimensional array but the operation is similar).

- If the maximum is in $\psi_{\max}$, periodical maximums will appear at integer multiples of 2π due to the periodicity of array factor, at $\psi = 2m\pi + \psi_{\max}$. If these maximums are in the visible margin, that means $kd + \alpha \ge 2\pi$ or $-kd + \alpha \le 2\pi$, multiple radiation maxima will appear in the real space which are called grating lobes. These grating lobes, deserve particular attention in our SAR ambiguities assessment since can alter significantly azimuth ambiguity values obtained previously using an approximated antenna pattern. The grating lobes of the antenna will be weighted by the sub-array (array element) diagram and become of particular relevance when the steering in azimuth increases.

The last characteristic in the list is the most interesting for the case studied. In Fig. 5.25, it is shown how we can pass from AF(ψ) in Cartesian coordinates to array factor in real space, as a function of θ angle. As we can see, the visible margin determines the grating lobes. In this example, the visible margin is not long enough to include the first grating lobes, but on our system it is not true. Working with an element spacing of 0.7λ, when $\alpha \ge 2\pi - kd = 2\pi - \frac{2\pi \cdot 0.7\lambda}{\lambda} = 0.3 \cdot 2\pi$ (108º) or $\alpha \le 2\pi + kd = 2\pi + \frac{2\pi \cdot 0.7\lambda}{\lambda} = 1.7 \cdot 2\pi$ (252º), grating lobes will appear in the visible margin. These values of α correspond to a steering in θ between 115º and 180º (the same that consider a steering between 0 and 65º). Considering that the steering in TOPSAR will be always between 0 and 1º, the grating lobes will be present on this mode and can not be ignored.

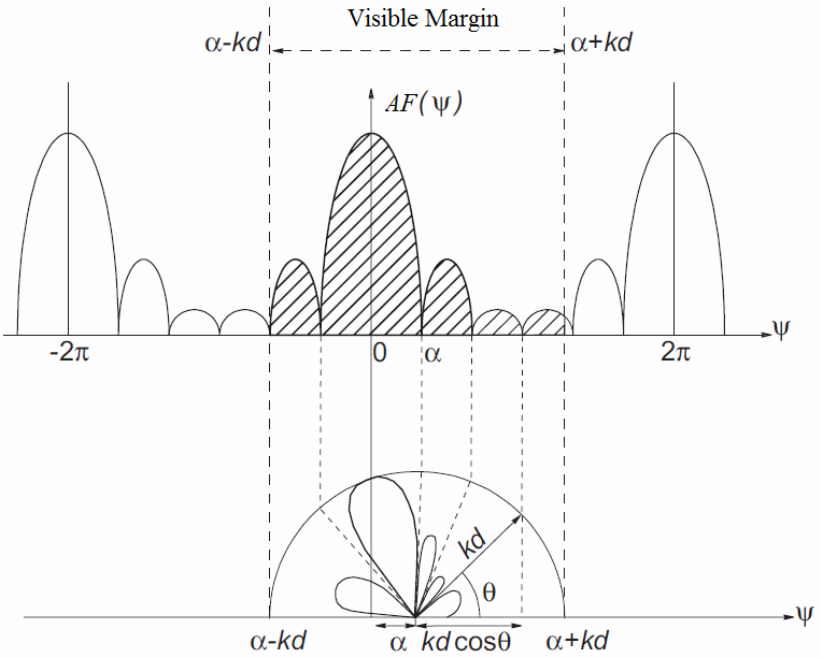

Fig. 5.25 Array factor in real space

This introduction has been a useful way to understand why grating lobes appear in our system. Next figures which have been computed using AMOR, show the situation and relative power of the grating lobes when the steering in azimuth increases.

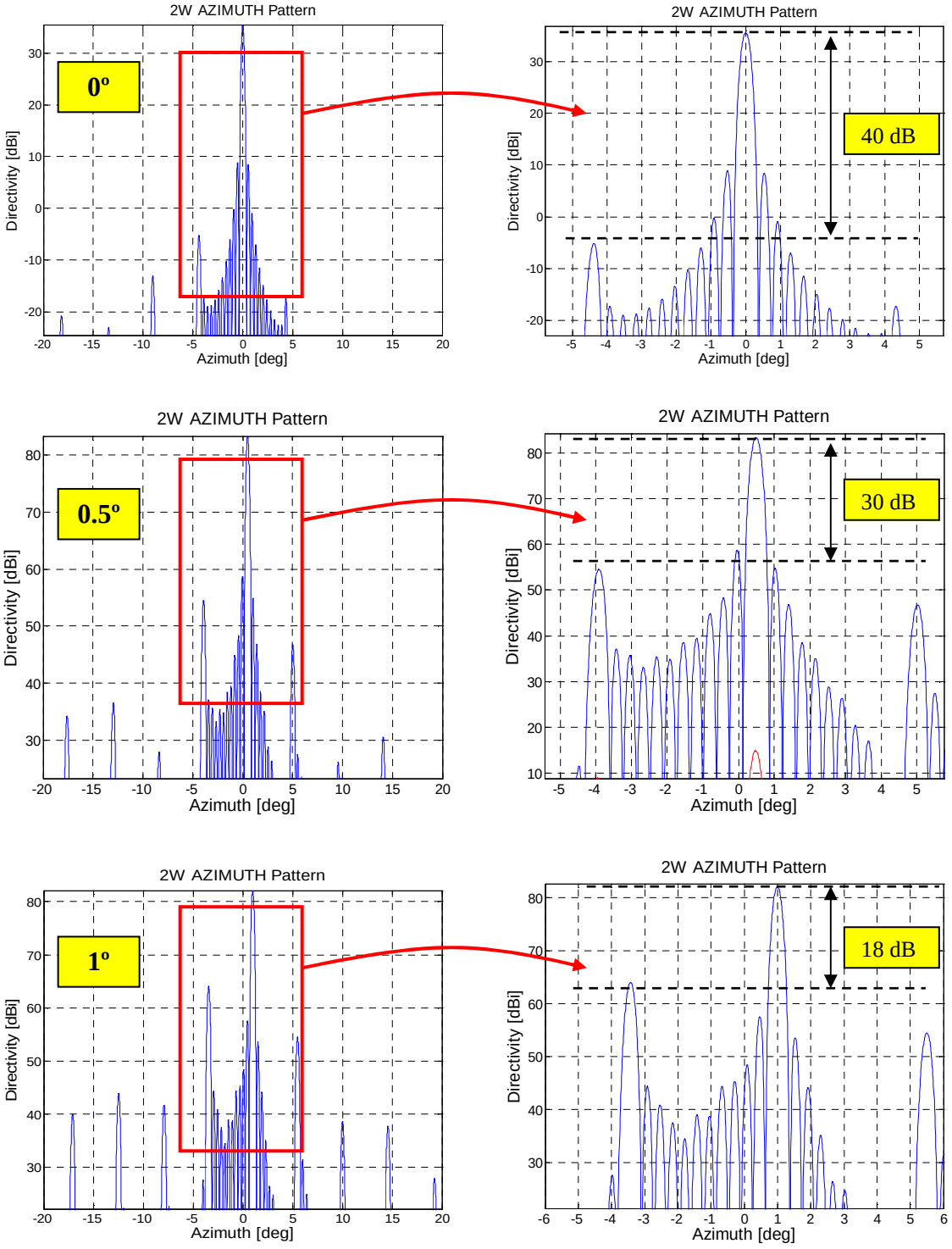

Fig. 5.26 Grating lobes in PAZ antenna with steering angles of 0º, 0.5º and 1º in SS2. The right side is a zoom of the pattern within the red box in the left side.

As we can see in Fig. 5.26, grating lobes levels increase when the azimuth steering increases. In this example, antenna diagram of sub-swath 2 has been chosen for the analysis. When the steering in azimuth is null, the ratio between main beam and highest grating lobes is approximately of 40 dB. When the steering is about 0.5 degrees, a steering angle that fulfil the requirements for TOPSAR with a desired resolution equal to ScanSAR, the grating lobes are 30 dB below the main beam. Finally, if we repeat the calculation for a steering angle of 1 degree, the results are worse, only 18 dB of difference. Fortunately, as we can see in next section, when we optimize the azimuth resolution for TOPSAR, a steering angle of 1 degree will be not necessary.

5.4.2 Using AMOR to compute the antenna patterns

In this section we are going to explain how the antenna patterns cuts in azimuth and range can be obtained using AMOR. AMOR is a useful tool developed by UPC which provides antenna information for SAR missions. So, it is possible to synthesize an antenna diagram from user requirements or analyse antenna radiation patterns from the weightings of the sub-array elements. In Fig. 5.27, AMOR interface is presented.

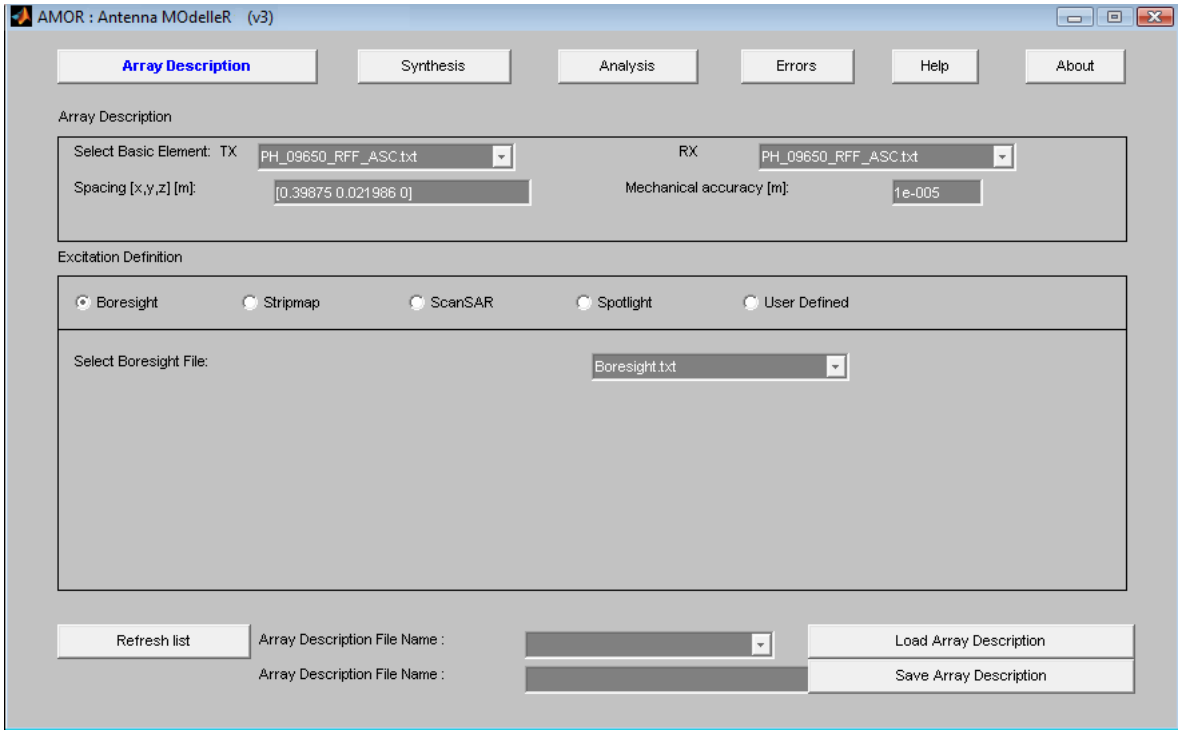

Fig. 5.27 Antenna MOdelleR (AMOR) interface

The option that we will use to get the azimuth and range cuts of the antenna will be *Array Description*, *Synthesis* and *Analysis*. The first one is used to define the weightings of the antenna that will be analysed. The weightings of the sub-array elements are read from an excitation file which can be selected by user in the pop-up menu *Select File* in *Excitation Definition*. Here we can choose which mode we want to analyse: Boresight, Stripmap, ScanSAR, Spotlight or User Defined. TOPSAR mode is not an option, but it can be studied from Spotlight since both modes use the steering in azimuth as a main feature.

In order to obtain the antenna pattern cuts, the next procedure will be followed. First of all, we are going to enter in *Synthesis* options. In this section, we can generate the beam-form that we desire. In our case, we want to generate the coefficients for a Spotlight since it will be useful for TOPSAR analysis. Fig. 5.28 shows the panel that allows us to select the sub-swath and the azimuth steering for our analysis. As it can be seen, we can choose the reference Stripmap file, which correspond to the sub-swaths where the steering in azimuth will be done. The steering angle in azimuth can be selected in the second text-box. Finally, the antenna weightings will be stored at the output file that user provides.

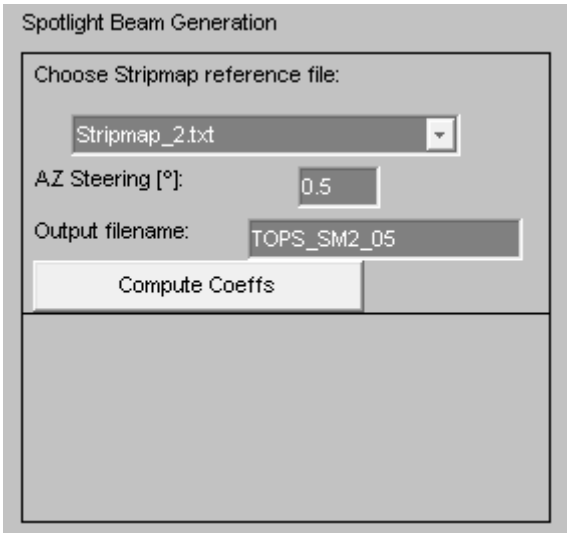

Fig. 5.28 Synthesis of antenna beam-form with AMOR

When the *Compute Coeffs* button is clicked the routine starts the sub-array coefficients computation. After some iterations searching the progressive phase that must be applied to obtain the desired steering in azimuth, the program shows the results in antenna diagrams. One of them, shown in Fig. 5.29, gives information about footprint location. In the right figure in red, the main footprint before the steering is plotted, while in blue, we can see the footprint steered in azimuth.

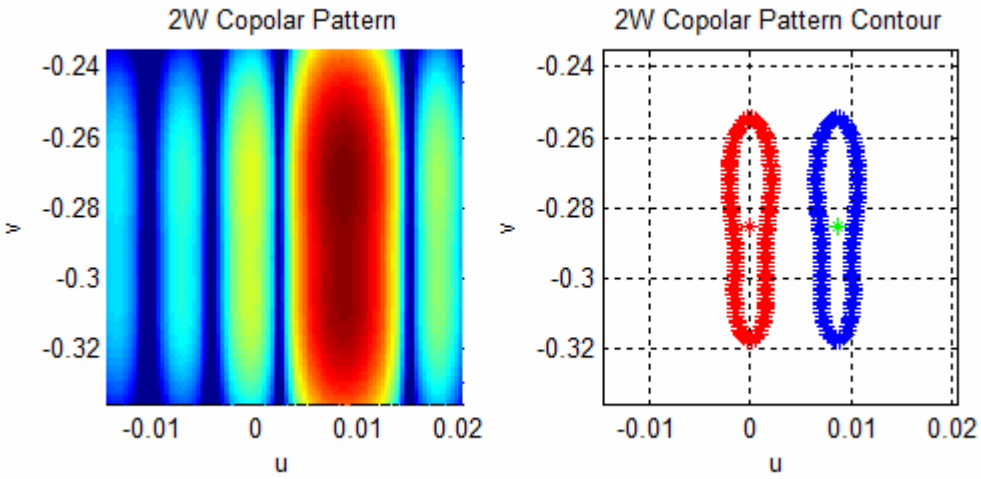

Fig. 5.29 Antenna footprint steered in azimuth

Besides, the program will generate a *.txt file* with the necessary weightings to obtain the desired beam-form with the steering in azimuth selected. This file contains the module and phase of 32x12 sub-array elements in transmission and reception. The file format can be seen in Fig. 5.30.

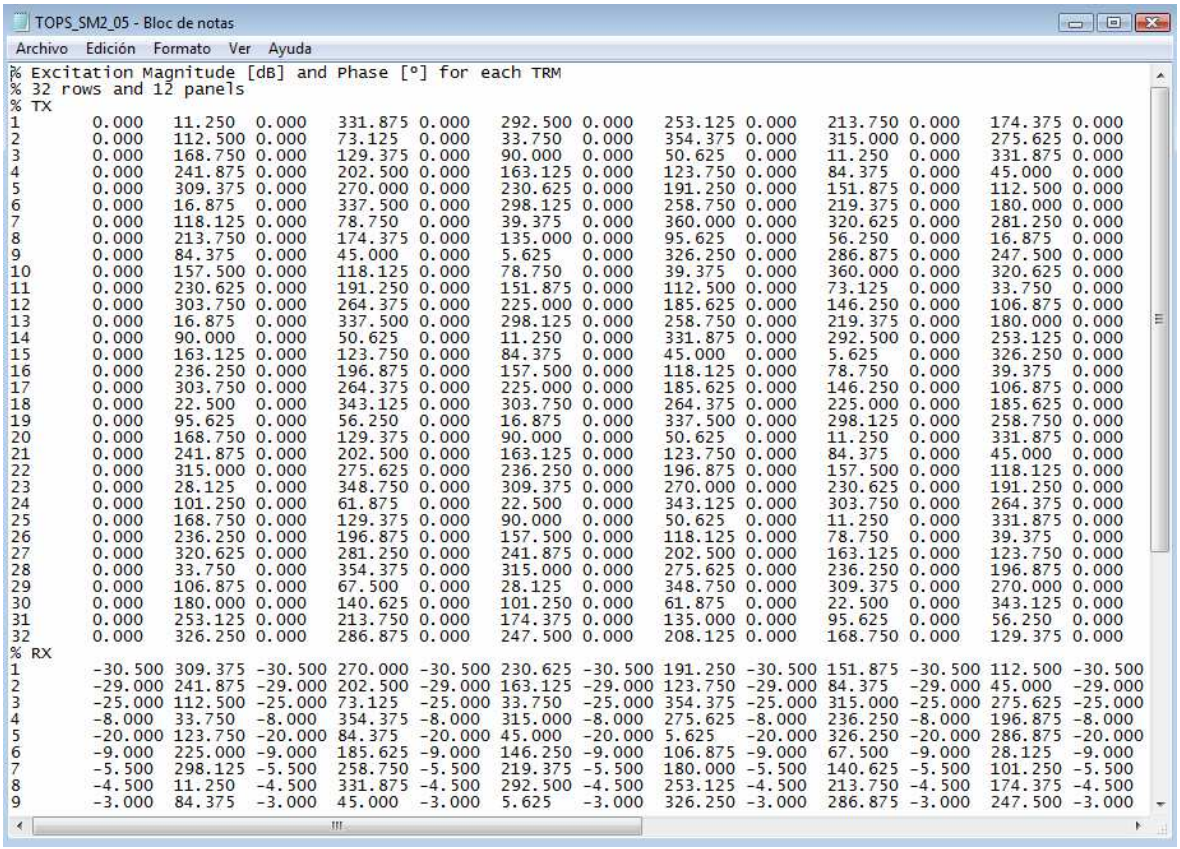

TOPS_SM2_05 - Bloc de notas

Archivo Edición Formato Ver Ayuda

```
% Excitation Magnitude [dB] and Phase [°] for each TRM
% 32 rows and 12 panels
% TX
1       0.000   11.250  0.000   331.875 0.000   292.500 0.000   253.125 0.000   213.750 0.000   174.375 0.000
2       0.000   112.500 0.000   73.125  0.000   33.750  0.000   354.375 0.000   315.000 0.000   275.625 0.000
3       0.000   168.750 0.000   129.375 0.000   90.000  0.000   50.625  0.000   11.250  0.000   331.875 0.000
4       0.000   241.875 0.000   202.500 0.000   163.125 0.000   123.750 0.000   84.375  0.000   45.000  0.000
5       0.000   309.375 0.000   270.000 0.000   230.625 0.000   191.250 0.000   151.875 0.000   112.500 0.000
6       0.000   16.875  0.000   337.500 0.000   298.125 0.000   258.750 0.000   219.375 0.000   180.000 0.000
7       0.000   118.125 0.000   78.750  0.000   39.375  0.000   360.000 0.000   320.625 0.000   281.250 0.000
8       0.000   213.750 0.000   174.375 0.000   135.000 0.000   95.625  0.000   56.250  0.000   16.875  0.000
9       0.000   84.375  0.000   45.000  0.000   5.625   0.000   326.250 0.000   286.875 0.000   247.500 0.000
10      0.000   157.500 0.000   118.125 0.000   78.750  0.000   39.375  0.000   360.000 0.000   320.625 0.000
11      0.000   230.625 0.000   191.250 0.000   151.875 0.000   112.500 0.000   73.125  0.000   33.750  0.000
12      0.000   303.750 0.000   264.375 0.000   225.000 0.000   185.625 0.000   146.250 0.000   106.875 0.000
13      0.000   16.875  0.000   337.500 0.000   298.125 0.000   258.750 0.000   219.375 0.000   180.000 0.000
14      0.000   90.000  0.000   50.625  0.000   11.250  0.000   331.875 0.000   292.500 0.000   253.125 0.000
15      0.000   163.125 0.000   123.750 0.000   84.375  0.000   45.000  0.000   5.625   0.000   326.250 0.000
16      0.000   236.250 0.000   196.875 0.000   157.500 0.000   118.125 0.000   78.750  0.000   39.375  0.000
17      0.000   303.750 0.000   264.375 0.000   225.000 0.000   185.625 0.000   146.250 0.000   106.875 0.000
18      0.000   22.500  0.000   343.125 0.000   303.750 0.000   264.375 0.000   225.000 0.000   185.625 0.000
19      0.000   95.625  0.000   56.250  0.000   16.875  0.000   337.500 0.000   298.125 0.000   258.750 0.000
20      0.000   168.750 0.000   129.375 0.000   90.000  0.000   50.625  0.000   11.250  0.000   331.875 0.000
21      0.000   241.875 0.000   202.500 0.000   163.125 0.000   123.750 0.000   84.375  0.000   45.000  0.000
22      0.000   315.000 0.000   275.625 0.000   236.250 0.000   196.875 0.000   157.500 0.000   118.125 0.000
23      0.000   28.125  0.000   348.750 0.000   309.375 0.000   270.000 0.000   230.625 0.000   191.250 0.000
24      0.000   101.250 0.000   61.875  0.000   22.500  0.000   343.125 0.000   303.750 0.000   264.375 0.000
25      0.000   168.750 0.000   129.375 0.000   90.000  0.000   50.625  0.000   11.250  0.000   331.875 0.000
26      0.000   236.250 0.000   196.875 0.000   157.500 0.000   118.125 0.000   78.750  0.000   39.375  0.000
27      0.000   320.625 0.000   281.250 0.000   241.875 0.000   202.500 0.000   163.125 0.000   123.750 0.000
28      0.000   33.750  0.000   354.375 0.000   315.000 0.000   275.625 0.000   236.250 0.000   196.875 0.000
29      0.000   106.875 0.000   67.500  0.000   28.125  0.000   348.750 0.000   309.375 0.000   270.000 0.000
30      0.000   180.000 0.000   140.625 0.000   101.250 0.000   61.875  0.000   22.500  0.000   343.125 0.000
31      0.000   253.125 0.000   213.750 0.000   174.375 0.000   135.000 0.000   95.625  0.000   56.250  0.000
32      0.000   326.250 0.000   286.875 0.000   247.500 0.000   208.125 0.000   168.750 0.000   129.375 0.000
% RX
1       -30.500 309.375 -30.500 270.000 -30.500 230.625 -30.500 191.250 -30.500 151.875 -30.500 112.500 -30.500
2       -29.000 241.875 -29.000 202.500 -29.000 163.125 -29.000 123.750 -29.000 84.375  -29.000 45.000  -29.000
3       -25.000 112.500 -25.000 73.125  -25.000 33.750  -25.000 354.375 -25.000 315.000 -25.000 275.625 -25.000
4       -8.000  33.750  -8.000  354.375 -8.000  315.000 -8.000  275.625 -8.000  236.250 -8.000  196.875 -8.000
5       -20.000 123.750 -20.000 84.375  -20.000 45.000  -20.000 5.625   -20.000 326.250 -20.000 286.875 -20.000
6       -9.000  225.000 -9.000  185.625 -9.000  146.250 -9.000  106.875 -9.000  67.500  -9.000  28.125  -9.000
7       -5.500  298.125 -5.500  258.750 -5.500  219.375 -5.500  180.000 -5.500  140.625 -5.500  101.250 -5.500
8       -4.500  11.250  -4.500  331.875 -4.500  292.500 -4.500  253.125 -4.500  213.750 -4.500  174.375 -4.500
9       -3.000  84.375  -3.000  45.000  -3.000  5.625   -3.000  326.250 -3.000  286.875 -3.000  247.500 -3.000
```

Fig. 5.30 TOPS_SM2_05.txt format with sub-array element weightings

Once the coefficients are computed, it is time to go to *Array Description* menu. In *Excitation Definition*, we are going to select *Spotlight* button and we have to select the *Spotlight File* that we want to analyse. Following with the example, Fig. 5.31 shows the necessary parameters to analyse the pattern cuts.

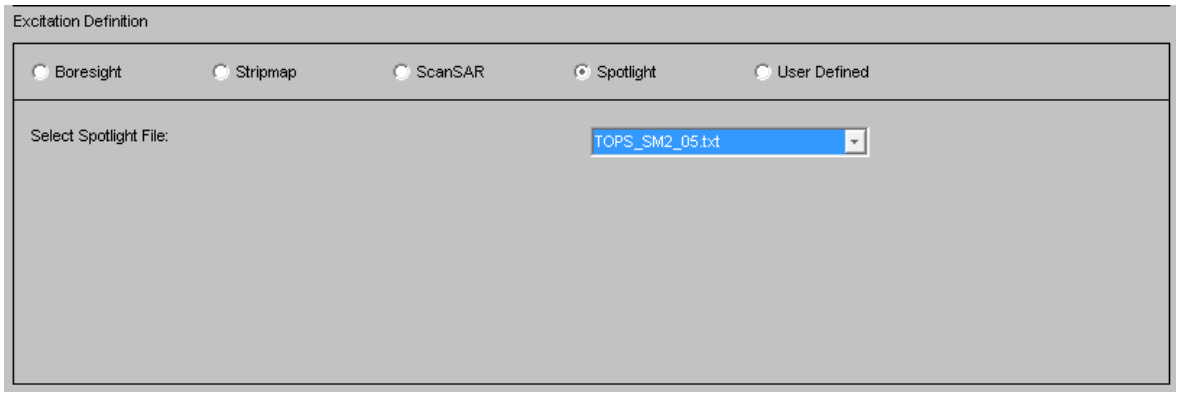

Fig. 5.31 Array Description to analysis TOPSAR mode

Finally, when the array description is loaded, we are going to obtain the pattern cuts that will be useful to do the ambiguity analysis. If we click in *Analysis* button, menu of Fig. 5.32 will appear. To compute the ambiguities, we will need the azimuth and range cuts and they can be obtained from *Directivity Pattern Cuts Computation*.

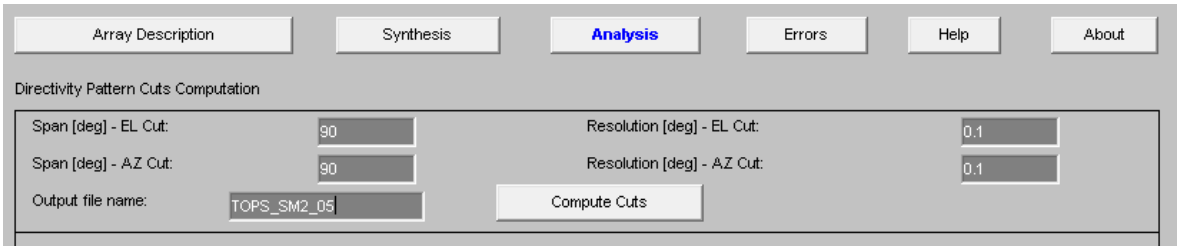

Fig. 5.32 Analysis menu to compute pattern cuts

When we click on *Compute Cuts* we are going to obtain the pattern cuts diagrams and *.txt files* with directivity patterns in azimuth and range. These files will be used in the AASR and RASR computation in the next sections. Fig. 5.33 show the azimuth and range directivity diagram obtained with pattern cuts computation.

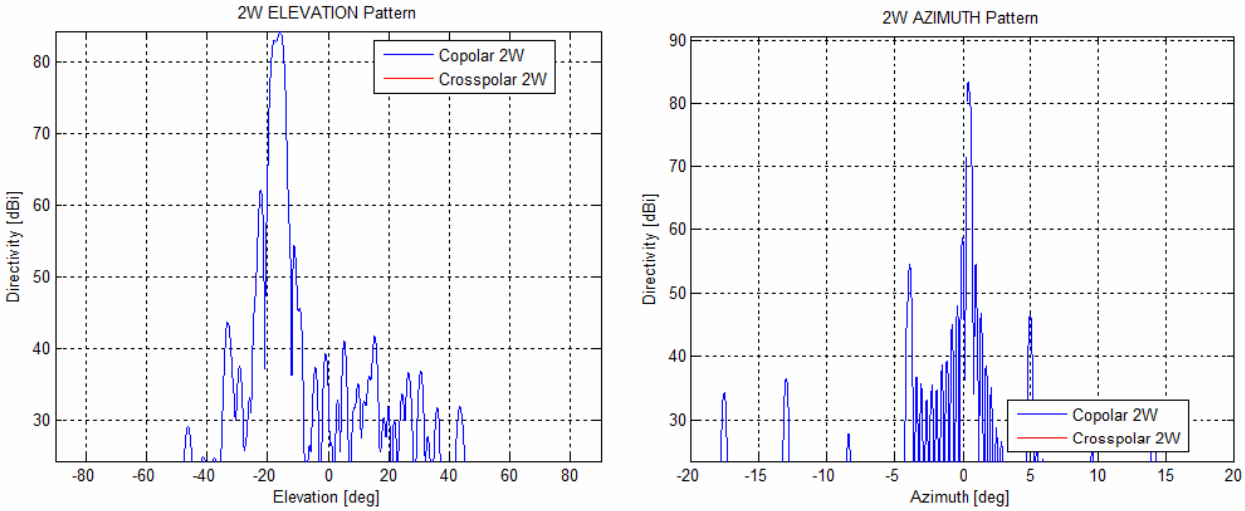

Fig. 5.33 Pattern cuts in SM2 with azimuth steering of 0.5º

5.4.3 Azimuth ambiguities for TOPSAR considering non-approximated antenna patterns

Until now, azimuth ambiguity analysis has been done using an approximated azimuth antenna pattern, modelled as a $sinc^4$ function. This model, as we will see, it was a good approximation for Stripmap mode, where the level of grating lobes is negligible since we do not use any azimuth steering. In TOPSAR case, with the azimuth steering, the grating lobes will increase, and the results obtained for azimuth ambiguities will be worse.

First of all, following a procedure similar than in section 5.2, we are going to compute the AASR for Stripmap mode. To compute these ambiguities, firstly we need to get the

azimuth antenna pattern cut of all the sub-swaths. Again, using AMOR to compute the pattern cuts, we obtain the antenna diagram that we can use instead of $sinc^4$ shape. To get the values of the radiation diagram, we will use the output file provided by AMOR which has a structure as is shown in Fig. 5.34. From this file we are going to use the last column, which contains θ angle which is related with Doppler target shifts. Besides, third column corresponds to the directivity in dBs of the antenna in the direction defined by the last column.

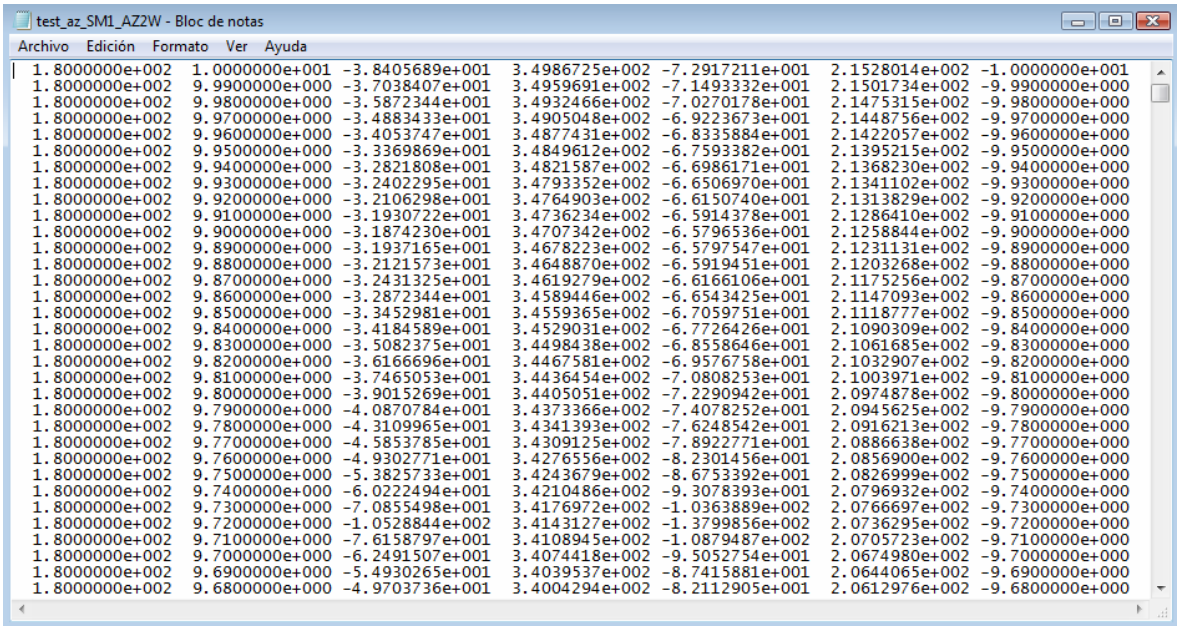

Fig. 5.34 SM1 directivity values to compute AASR

Using these values for the AAP, the values from Table 5.8 are obtained. As we can see, the values computed with the real antenna diagram and the approximated diagram are similar, a few tenth of dB different. So, we can affirm that the *sinc* shape is a good approximation for Stripmap. Now, a similar study is done for TOPSAR.

Sub-swath name	Real AASR (dB)	Aprox. AASR (dB)	Diff	Sub-swath name	Real AASR (dB)	Aprox. AASR (dB)	Diff
SM-S_1	-25.551	-25.333	0.218	SM-S_12	-25.465	-25.237	0.228
SM-S_2	-25.642	-25.443	0.199	SM-S_13	-25.728	-25.780	0.052
SM-S_3	-25.578	-25.484	0.094	SM-S_14	-22.993	-23.086	0.093
SM-S_4	-24.673	-24.569	0.104	SM-S_15	-25.906	-25.792	0.114
SM-S_5	-25.891	-25.798	0.093	SM-S_16	-23.197	-23.294	0.097
SM-S_6	-25.784	-25.681	0.103	SM-S_17	-25.907	-25.794	0.113
SM-S_7	-24.681	-24.533	0.148	SM-S_18	-23.402	-23.498	0.096
SM-S_8	-25.889	-25.804	0.085	SM-S_19	-25.900	-25.767	0.133
SM-S_9	-24.675	-24.544	0.131	SM-S_20	-23.410	-23.510	0.100
SM-S_10	-25.493	-25.267	0.226	SM-S_21	-25.779	-25.744	0.035
SM-S_11	-25.862	-25.739	0.123	SM-S_22	-23.312	-23.414	0.102

Table 5.8 AASR for Stripmap with real antenna diagram vs. approximation

To compute the ambiguities for TOPSAR mode, we will proceed in a similar way. First of all, we need to compute previously all the azimuth antenna pattern. These patterns have been synthesized with an azimuth steering of 0.5º since it is an azimuth steering that allows us to scan the scene using TOPSAR with an azimuth resolution of 18 meters, the nominal resolution for ScanSAR. Due to computation problems with AMOR, it will be possible to compute the azimuth cuts for SM1 to SM5 only, but it will be enough to establish some general conclusions.

First of all, it is interesting to see where the azimuth ambiguous zones are located in order to check if they coincide with grating lobes and, if it would be the case, if it will be possible to modify the PRF to try to avoid this coincidence. In Fig. 5.35, the AAP of sub-swaths 1, 2, 3 and 4 are plotted with an azimuth steering of 0.5º. Vertical red lines show the situation of ambiguous zones at multiples of the PRF from the desired target.

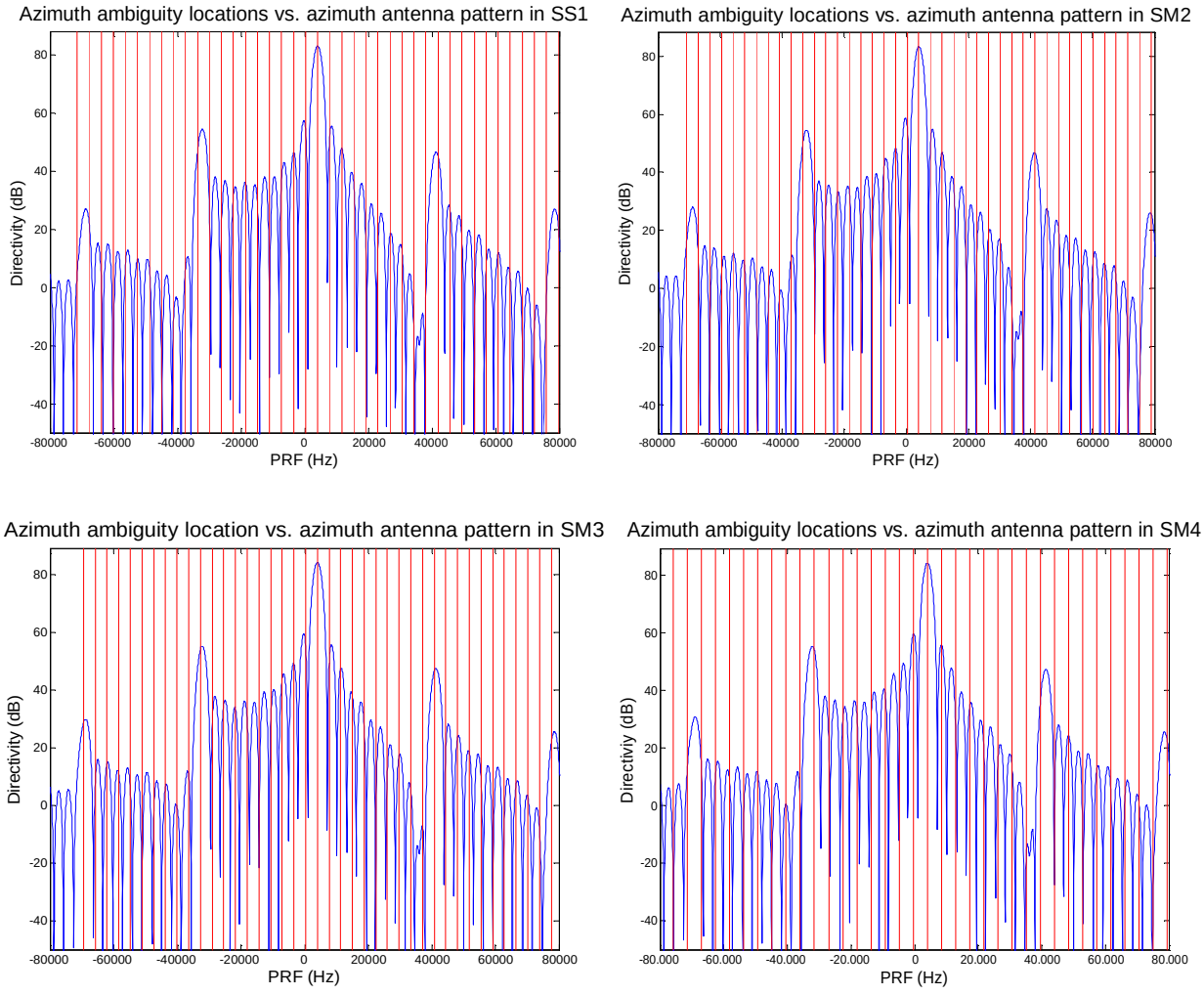

Fig. 5.35 Azimuth ambiguity locations vs. azimuth antenna patterns

As it can be observed in the figure, the density of ambiguous zones makes it difficult to avoid the coincidence of grating lobes with azimuth ambiguous frequencies. So, try to

change PRFs to avoid this coincidence is a complicated task that will not offer great results. For this reason we must compute ambiguities assuming this unavoidable effect to see if the lost of AASR is significant.

As it was explained previously, the final version of AMOR has not been delivered so it has not been possible to obtain all the azimuth pattern cuts for all the sub-swaths. On the other hand, Fig. 5.35 shows that in SS3 and SS4, there is maximum coincidence between the azimuth ambiguity location and grating lobes, so it is reasonable to conclude that we will not have so much higher deteriorations in the AASR of the other sub-swaths.

The procedure to obtain the azimuth ambiguities for TOPSAR using AMOR pattern cuts is similar to Stripmap one. Computing the AASR for the six available pattern cuts with an azimuth steering of 0.5º we obtain the results of the Fig. 5.36. As it is confirmed, the higher deterioration is in SS3, where the loss is about 2 dB. If we take the values from all sub-swaths computed with approximated antenna pattern cuts in section 5.2.3, where the worst values was around -21.5 dB, we can conclude that the worst AASR that we will obtain for TOPSAR mode will not exceed from -19 dB, which is a reasonable results to assure a correct acquisition in the radar system.

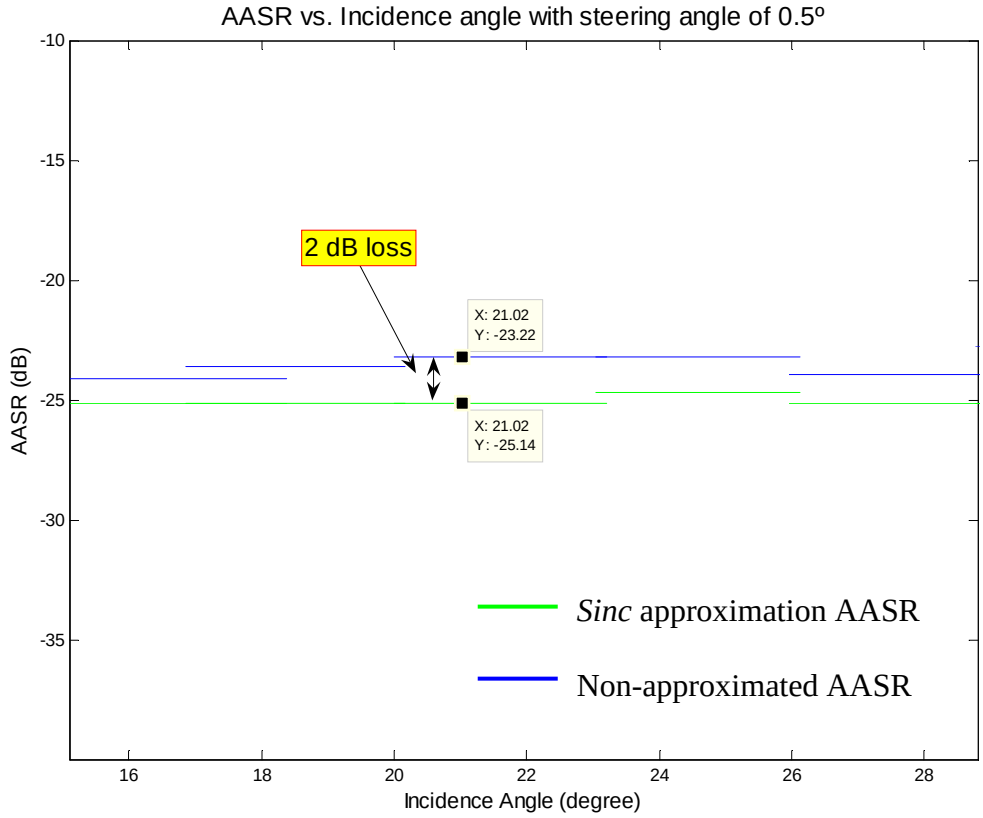

Fig. 5.36 AASR using AMOR patter cuts in SS1(16º)-SS5(28º) vs. sinc^4 approximation

5.4.4 Range ambiguities for TOPSAR considering non-approximated antenna patterns

In this section we are going to recalculate the range ambiguities using a real elevation cuts. Once again, to compute the range ambiguities, firstly we have to use AMOR to get the non-approximated range patterns. For range ambiguities, the steering in azimuth will not be really critical as in azimuth ambiguities, since it does not affect to the range pattern of the antenna. But, on the other hand, it is necessary to calculate the RASR again since the $sinc^4$ approximation is only valid for far range and it could provide wrong results when we work at near range, with low incidence angles.

To compute the RASR the elevation cuts are necessary. Although the steering angle introduce by TOPSAR mode, in Fig. 5.37 we can see that the elevation pattern of sub-swath 1 with no azimuth steering and the elevation pattern in the same sub-swath with an azimuth steering of 0.5º do not present significant differences. So, for range ambiguity analysis, we can use no steered elevation patterns. The main reason for using no-steered elevation cuts is to avoid the computation problems that AMOR presents when an azimuth steering is applied. With non-steered elevation cuts we can compute the RASR for TOPSAR in the 22 available sub-swaths.

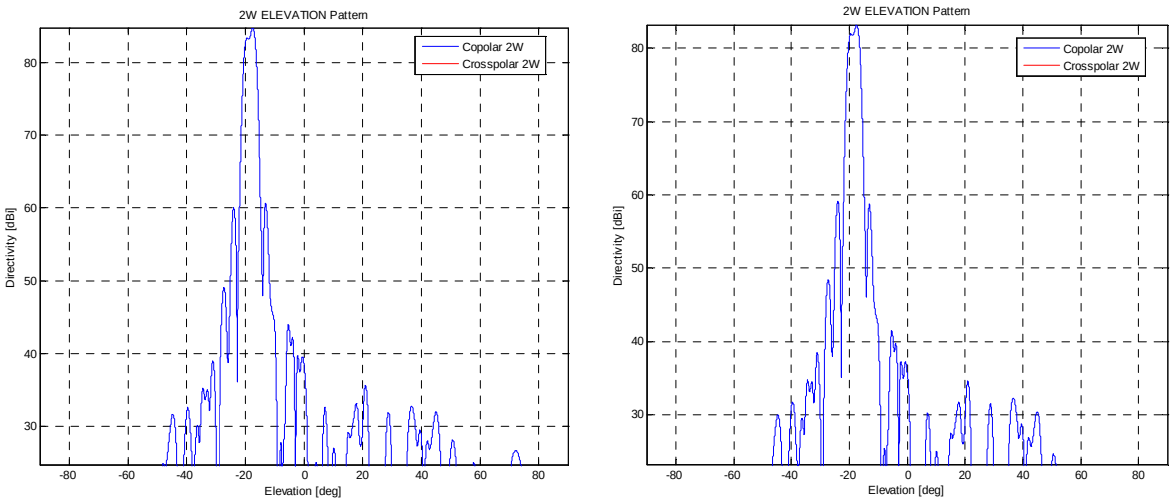

Fig. 5.37 Elevation pattern cut of SS1 with no-azimuth steering (left) vs. 0.5º azimuth steering (right)

Computing the RASR using these antenna cuts the results of Fig. 5.38 are obtained for TOPSAR mode. If we compare these values with the RASR results from Fig. 5.22, which correspond to the RASR values obtained with the $sinc^4$ approximation; for near range or low incidence angles which correspond to the first sub-swaths, the behaviour of the RASR is quite different. As we have previously explained, the reason for these variations is that it is not possible to use $sinc^4$ approximation for near range.

On the other hand, for far range which correspond to the last sub-swaths, the approximation is valid, and the results using both patterns are similar. It is coherent with the previous considerations about $sinc^4$ approximation.

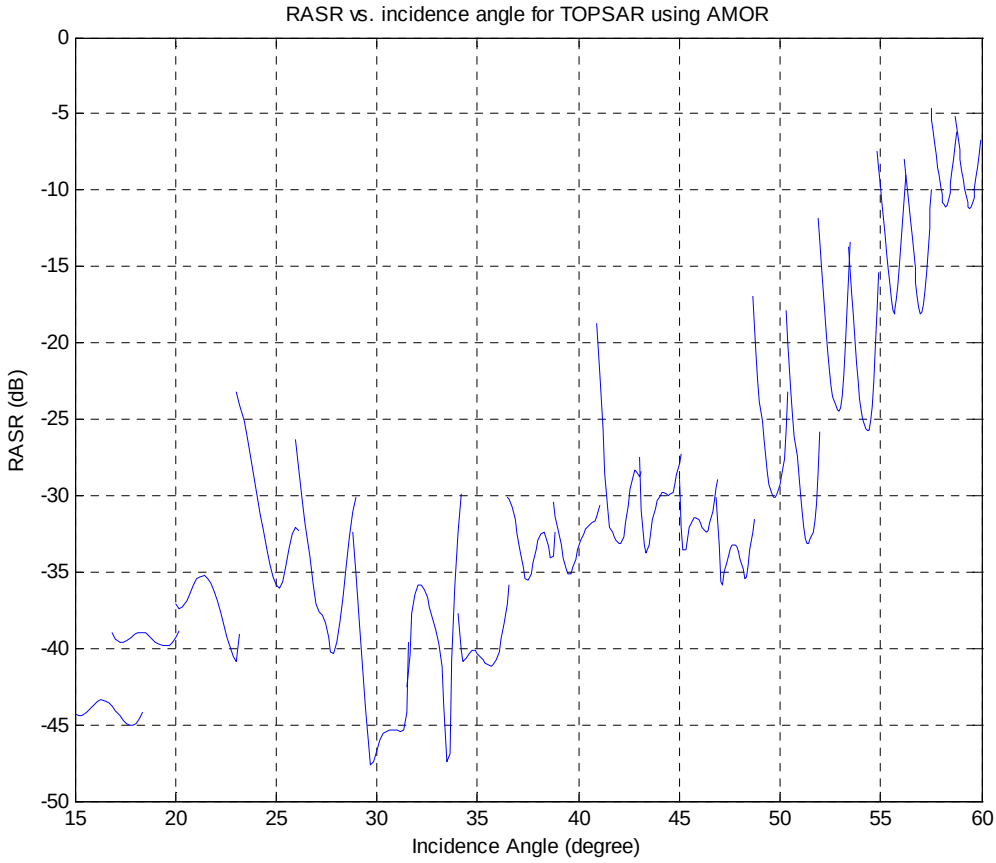

Fig. 5.38 RASR for TOPSAR using AMOR pattern cuts

The values of the RASR obtained for TOPSAR mode are in expected range. For near range, although the variations in comparison with approximated patterns analysis, the results are below the -25dB, which means the radar will not have any operation problems for these sub-swaths. On the other hand, for far range, the values of RASR get worse, increasing until -5dB for the last sub-swaths. These values of RASR are not good enough to assure the correct operation of the system.

So, we can conclude that the radar will operate with no ambiguity interference problems for incidence angle from 15 to 50 degrees (SS1-SS14) and the image reception could present some problems to higher incidence angles which correspond to the last sub-swaths (SS15-SS22).

Chapter 6 Azimuth resolution optimization for TOPSAR

Until now, the azimuth resolution for TOPSAR mode has been considered as an input and TOPSAR parameters have been chosen in order to fulfil the proposed azimuth resolution of ScanSAR mode, which is 18 meters. In this section we try to optimize the azimuth resolution selecting the steering rates and the burst times to improve this parameter. On the other hand, we must consider the unavoidable and undesired effects, such as higher quantization step or azimuth ambiguities deterioration.

6.1 Angle quantization problems. Grating lobes limitation

As it was explained in section 4, the quantization step is related to the desired azimuth resolution. If a better resolution is desired, we will need a slower steering in azimuth with more scanning time for each sub-swath. This means more directions to point and, consequently, a higher angle quantization step [36].

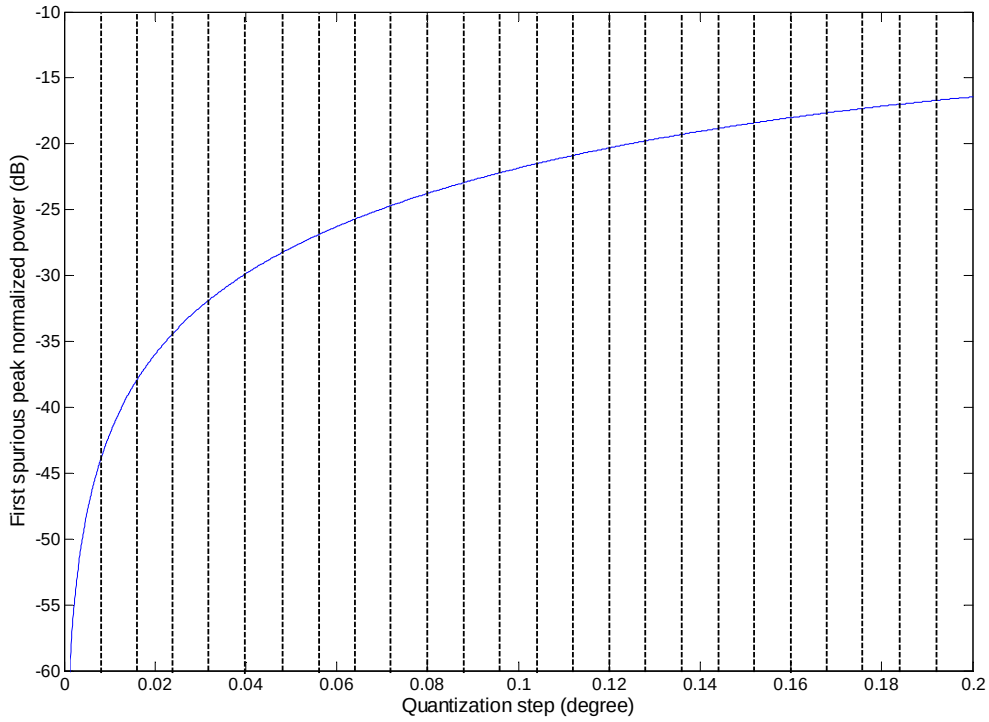

Fig. 6.1 Higher spurious peak vs. quantization step. Selectable steps, at multiples of 0.008º are marked with slashed lines

A higher quantization step means worst response to the spurious peaks of the radar. So, as the quantization step increases, the power of the first spurious peak raises too. In Fig. 6.1, the evolution of the most powerful spurious speak in function of the angle quantization step is plotted. As it can be seen, when the quantization step increases the system will have worst performance.

Besides, the stored pointing directions in the radar memory for Spotlight determine the available steps for TOPSAR, which will be multiples of 0.008º and are marked with slashed lines in the figure.

Taking the values obtained from Fig. 6.1, when the quantization step is higher than 0.064º, the normalized power of the spurious peak exceeds -25dB, degrading the ambiguity levels in azimuth due to the replicas in the spectrum. Furthermore, as it will be exposed next, taking 0.064º or 0.056º instead of 0.048º will not provide a high azimuth resolution improving.

In Fig. 6.2 we can see how the minimum angle quantization step evolves as a function of the desired azimuth resolution. Choosing a quantization step of 0.048º, the best azimuth resolutions obtained for 3 and 4 sub-swaths are 9.2 and 13 meters respectively. As it is shown in the figure, if a coarser quantization step is used, the improvement in azimuth resolution is not significant, but the quantization error increases significantly.

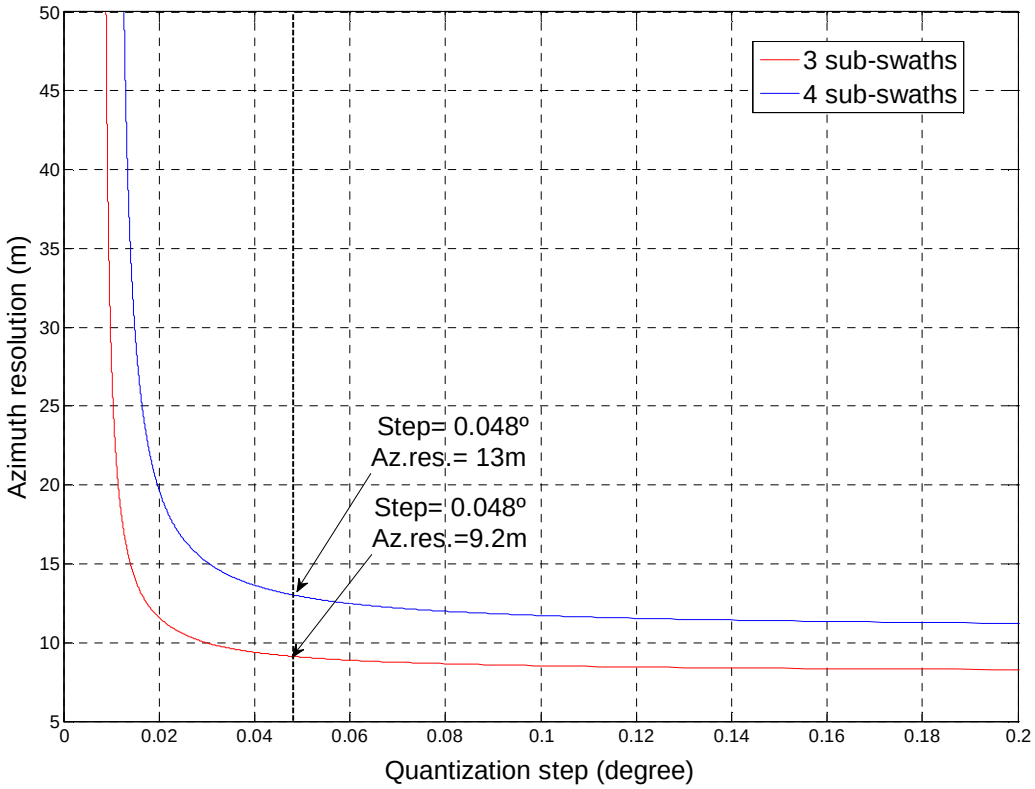

Fig. 6.2 Minimum angle quantization step vs. azimuth resolution. An step of 0.048º is chosen to calculate the parameters of TOPSAR in this section.

From now to the end, using the results obtained from Fig. 6.2, the assessment of TOPSAR mode using three and four sub-swaths will be done taking an azimuth resolution of 9.5 meters for first case and 13.5 meters in the second one in order to fulfil the requirements in all the sub-swaths. In the example, we analyse sub-swaths 5, 6 and 7 when we are working with 3 sub-swaths; and swaths 5, 6, 7 and 8 in the other case. The results using these new features can be seen in Table 6.1 and Table 6.2:

Sub-swath name	Steering angle rate (rad/s)	Steering angle rate (deg/s)	Doppler rate (Hz/s)	Burst time	Dwell time	Doppler BW	Max. steering angle
SS5	0.03241	1.8571	-6056.027	0.87926	0.14401	872	**± 0.8164**
SS6	0.03165	1.8133	-5913.292	0.88233	0.14748	872	**± 0.8000**
SS7	0.03086	1.7682	-5765.993	0.88566	0.15125	872	**± 0.7830**

Table 6.1 Optimum parameters to get an azimuth resolution of 9.5 meters using 3 sub-swaths

Sub-swath name	Steering angle rate (rad/s)	Steering angle rate (deg/s)	Doppler rate (Hz/s)	Burst time	Dwell time	Doppler BW	Max. steering angle
SS5	0.05148	2.9493	-6056.027	0.46047	0.10134	614	± 0.6790
SS6	0.05026	2.8798	-5913.292	0.46263	0.10378	614	± 0.6661
SS7	0.04901	2.8081	-5765.993	0.46497	0.10644	614	± 0.6528
SS8	0.04774	2.7351	-5616.065	0.46748	0.10928	614	± 0.6393

Table 6.2 Optimum parameters to get an azimuth resolution of 13.5 meters using 4 sub-swaths

The results coincide with what we expected. If we compare these values with results from Table 3.9 and Table 3.10 obtained with an azimuth resolution of 18 meters, the steering angle rates are slower since they are directly related to the azimuth requirements. On the other hand, the burst time dedicated to scan each sub-swath increases because a larger scanning of each sub-swath is necessary. This means more azimuth directions where the antenna needs to point to get the desired resolution. This new parameters mean higher maximum steering angles in both cases for each sub-swath. Using four sub-swaths, there are no problems in the scanning. However, taking the parameters of three sub-swaths scanning, the maximum steering angle exceeds from 0.75º which is the maximum azimuth steering angle considered to avoid an unacceptable level of grating lobes.

The limitation of the maximum steering angle comes from the grating lobes that increase when the steering in azimuth is higher. As we can see in Fig. 6.3, when an azimuth steering of 0.75º is set, the grating lobes are only 20 dB below the main signal, which could cause a noticeable deterioration in signal reception due to azimuth ambiguities. For this reason, higher steering angles in azimuth will not be allowed for scanning the scene in TOPSAR, and 0.75 will be set as the maximum steering angle that system provides a correct performance.

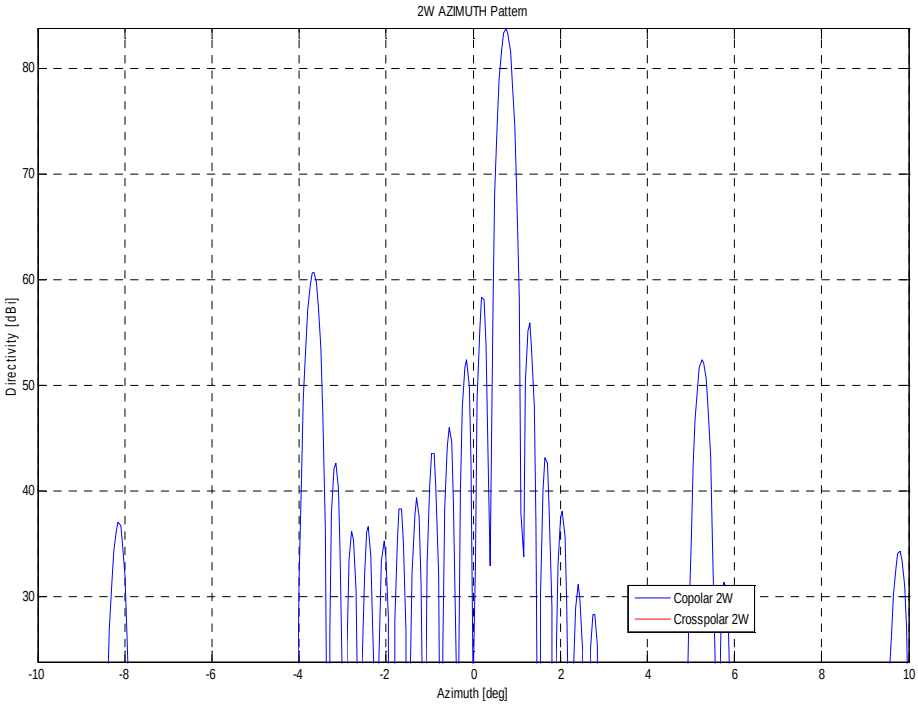

Fig. 6.3 Grating lobes of the antenna with steering of 0.75º

For this reason, we shall consider to relax slightly our azimuth resolution requirements for the 3 sub-swaths case. Therefore, an additional analysis based on a target azimuth resolution of 10 meters will be done. With this requirement the results obtained can be seen in the next table:

Sub-swath name	Steering angle rate (rad/s)	Steering angle rate (deg/s)	Doppler rate (Hz/s)	Burst time	Dwell time	Doppler BW	Max. steering angle
SS5	0.03480	1.9936	-6056.027	0.64764	0.13681	829	± 0.6456
SS6	0.03398	1.9467	-5913.292	0.65055	0.14011	829	± 0.6332
SS7	0.03313	1.8982	-5765.993	0.65371	0.14369	829	± 0.6204

Table 6.3 Optimum parameters to get an azimuth resolution of 10 meters using 3 sub-swaths

With the new azimuth resolution of 10 meters the TOPSAR parameters satisfy the PAZ specifications. Moreover, a quantization step of 0.032 can be used, as it can be seen in Fig. 6.2. Once we get the new parameters, it is time to see how the quantization error and ambiguities have changed.

Fig. 6.4 shows the Fourier transform of the error due to quantization with the azimuth resolution improvements expressed in terms of azimuth distance to the target. In case a), where we use three sub-swaths to do the scanning, the most powerful peak appears at 75 meters with a normalized power of -31.85 dB. On the other hand, in case b), the spurious peak at 74 meters has a power 28.27 dB below the useful return.

a)

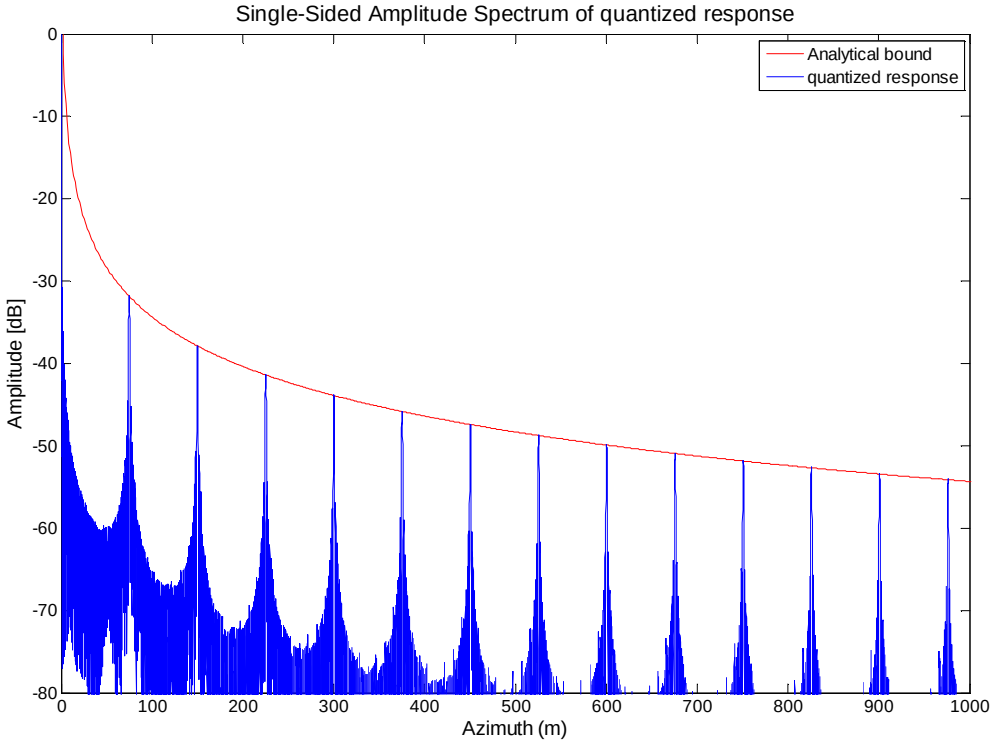

b)

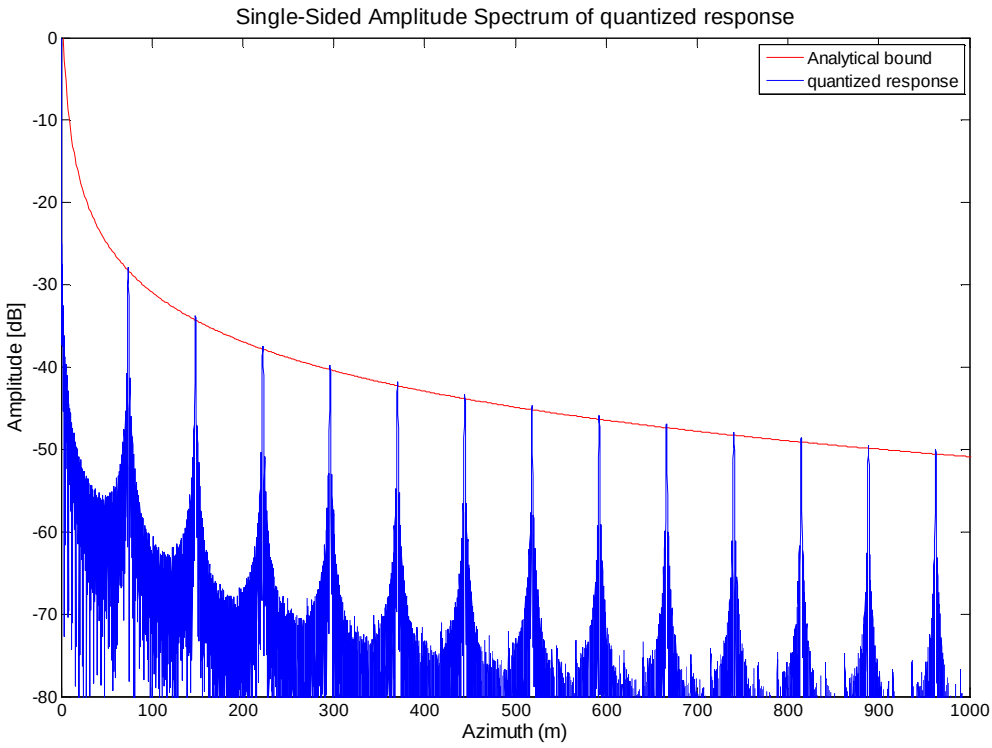

Fig. 6.4 Fourier transform of the approximated antenna azimuth sweep error a) 3 sub-swaths b) 4 sub-swaths

6.2 Azimuth ambiguities degradation

Now we are going to study how these modifications affect to the azimuth and range ambiguities. Since the azimuth resolution is improving, the Doppler bandwidth processed will change and, consequently, the azimuth ambiguities in TOPSAR mode will change too. Fig. 6.5 shows the azimuth ambiguities response using this new configuration.

Once again, due to problems with AMOR pattern cuts computation, only the analysis for the four first sub-swaths can be obtained. To compute AASR for TOPSAR with improved azimuth resolution, we need to get the azimuth pattern cuts with an azimuth steering of 0.68º approximately. This steering angle makes possible to fulfil the TOPSAR requirements with an azimuth resolution of 10 meters for 3 sub-swath case and 13.5 meters for 4 sub-swaths configuration.

Although it is only possible to compute the AASR for four first sub-swaths due to AMOR computation problems, we can obtain general results extrapolating the values obtained in these four sub-swaths to the others. As we can see in Fig. 6.5, the worst loss will be in sub-swath 3, since the azimuth ambiguity locations coincide with grating lobes of the antenna. This degradation with respect to the approximated calculation using $sinc^4$ pattern shape is about 4dB and we can conclude that it will be the maximum degradation that we will find in any sub-swath. For this reason, the poorest AASR in TOPSAR mode with azimuth resolution improved will be better than -15dB in the last sub-swaths, which present the most critical AASR levels. These results are reasonable for AASR to assure the correct

operation of the system in terms of azimuth ambiguity interferences, but the image quality can be reduced slightly.

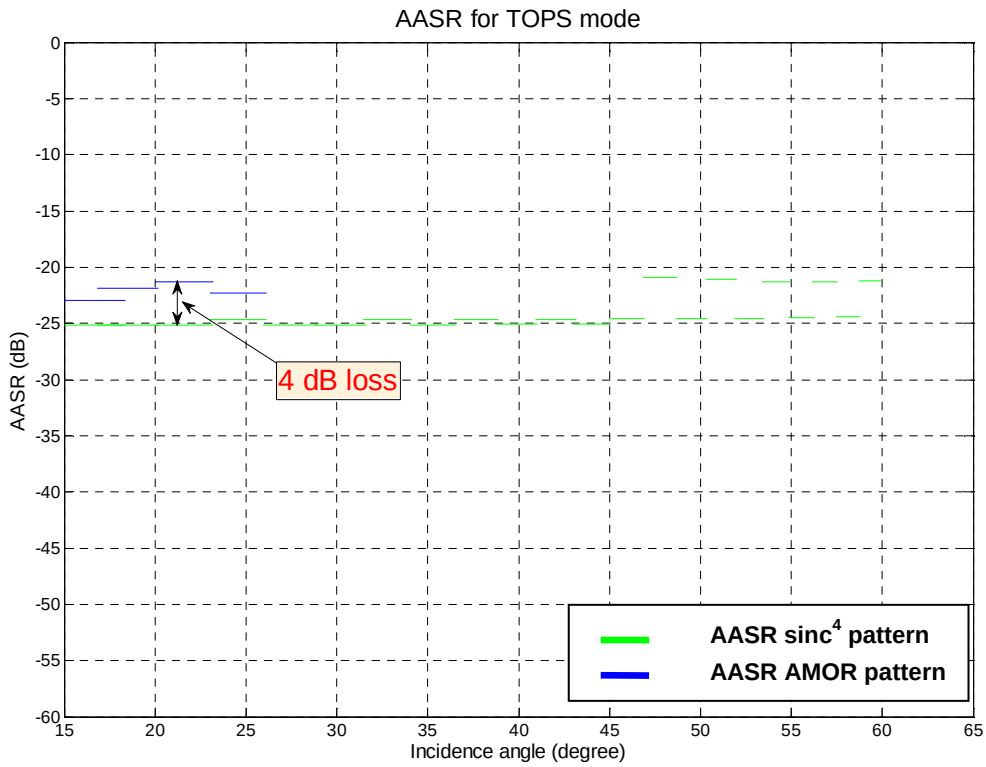

Fig. 6.5 AASR vs. Incidence angle for TOPSAR with maximum steering angle of 0.68º

On the other hand, range ambiguities do not change since they are not Doppler bandwidth or azimuth steering dependant. The only feature that would affect the range ambiguities would be the maximum steering angle, but in section 5.3.3 we saw that the differences are negligible. The range antenna cut does not change significantly when the antenna main beam is steered. Hence, the range ambiguities will not vary due to the azimuth resolution improvement.

This analysis shows another advantage of TOPSAR if it is compared with ScanSAR. The increasing in rage coverage of ScanSAR mode produce an azimuth resolution loss that can not be controlled and, consequently, the image quality will be worst. On the other hand, TOPSAR provides the same range coverage but it is possible to select the azimuth resolution changing the steering angle rates in azimuth. Obviously, the azimuth resolution will not be better than resolution in Stripmap, since the swath switching will reduce the observation time of the targets, but it will be better than in ScanSAR.

Chapter 7 TOPS AnalyseR (TOPSAR)

In order to make the computation of TOPSAR parameters easier and more comfortable, we design the TOPS AnalyserR (TOPSAR) interface. It consists on a simple MATLAB tool that provides to the user an interface to compute basic TOPSAR parameters with the input parameters of SAR system studied. The program computes the basic parameters for the analysed sub-swaths and carries out the analysis of quantization error and resulting ambiguities.

7.1 Introducing TOPSAR Interface

In this section, we are going to introduce the basic characteristics of this program and the computation options that the program offers.
When the program is executed, the interface of Fig. 7.1 is presented. This can be divided in three parts: input parameters, computation options and results text-box. In the input parameters section, user must define the parameters that characterize the system. These parameters will be the sub-swaths analysed; the number of swaths chosen to scan the scene; velocity, height and frequency of the radar system; the azimuth resolution desired and the number of ambiguities that we want to consider in the ambiguity analysis.

The computation options panel allows to the user to choose what it wants to compute. It includes TOPSAR parameters to fulfil system requirements, error due to steering angle quantization analysis, range and azimuth ambiguity analysis using theoretical antenna pattern or with real patterns computed with AMOR.

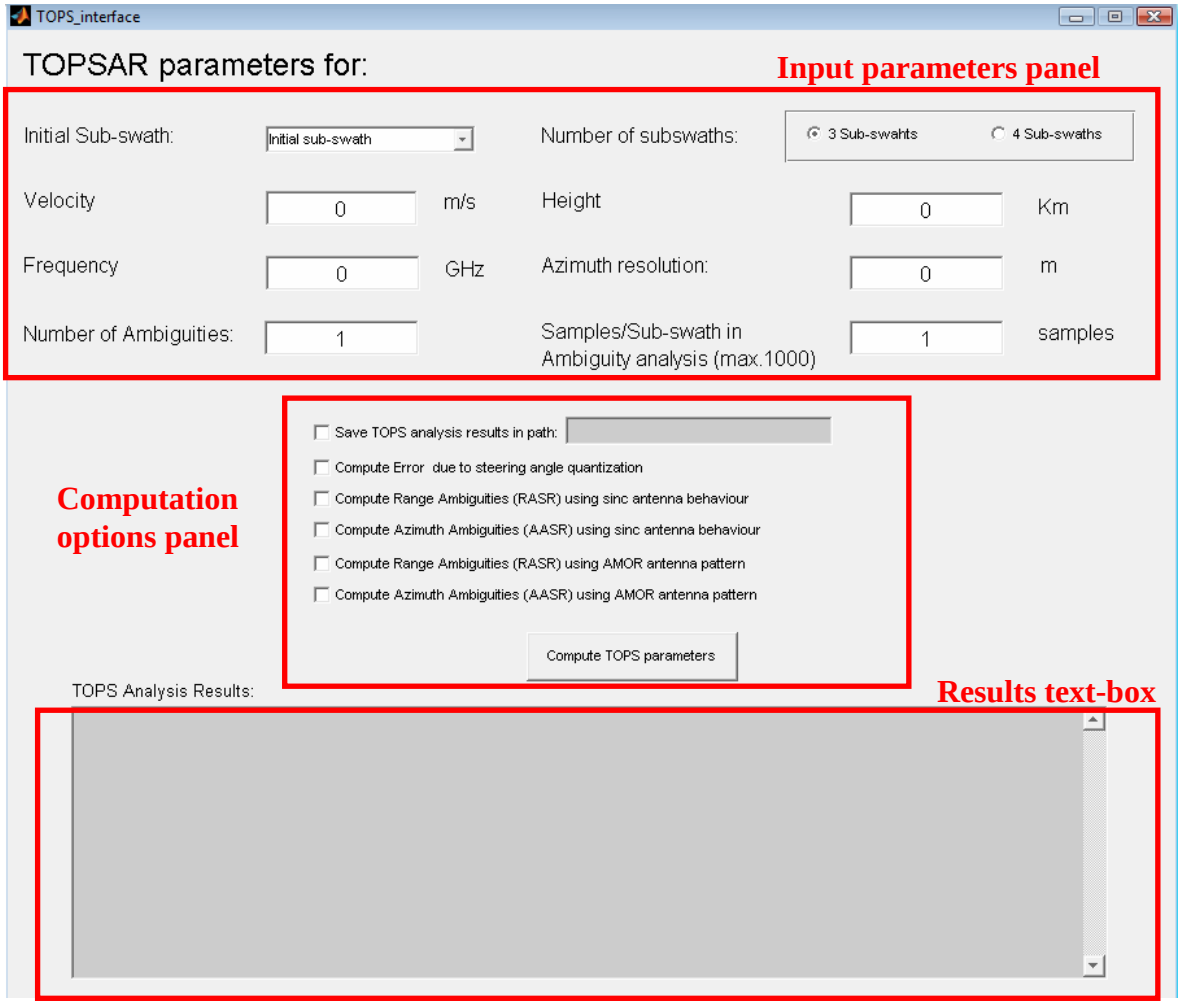

Fig. 7.1 TOPSAR front-end interface

Finally, results tool-box will provide the most significant results of the computation options that the user has chosen.

7.2 TOPSAR interface utilities

TOPSAR interface provides to the user several compute option to analyse the TOPSAR mode in any radar system. Once the input parameters are provided, when the *Compute TOPS parameters* button is pressed the basic configuration parameters for TOPSAR mode are shown in the results text-box. If the user does not choose any option, the program will provide default parameters as steering angle rates, timeline of the sub-swaths, maximum steering angles to fulfil the requirements of TOPSAR mode selected, Doppler bandwidth processed to get the desired azimuth resolution…

Fig. 7.2 shows the default parameters provided by TOPSAR interface. For this example we take as initial sub-swath the SM1 and 4 sub-swaths configuration. As system operation parameters we use PAZ flying values: a platform altitude of 510 Km, platform velocity of 7605.92 m/s, a radar operation frequency of 9.65 GHz and 18 meters of azimuth resolution. With these values we obtain the TOPSAR parameters for SS1, SS2, SS3 and SS4. The program provides antenna configuration information as well.

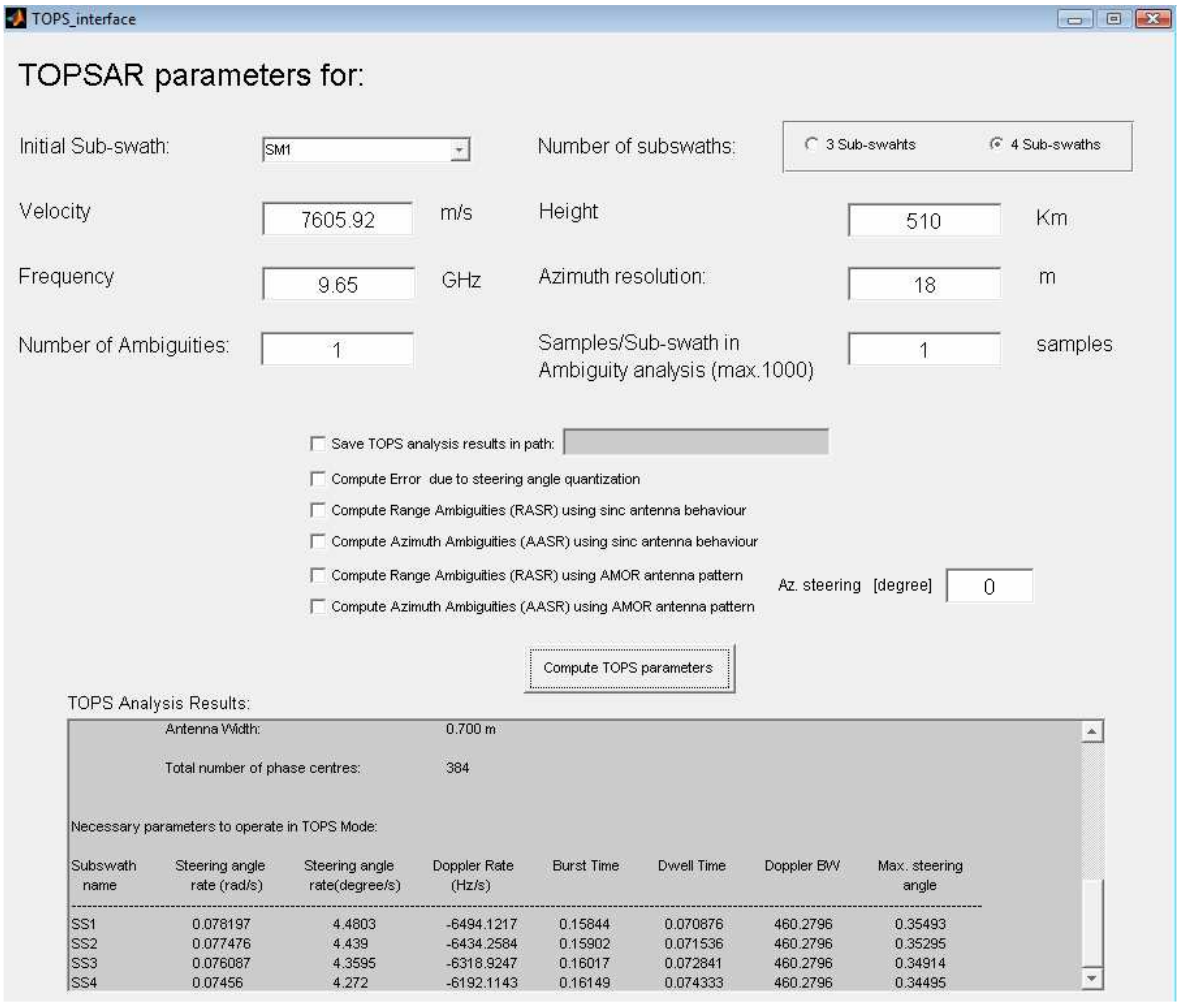

Fig. 7.2 TOPSAR front-end interface

Now we are going to explain briefly which the option that program provides to the user are. We will expose the features of each option but the results that the interface provides to the user will be explained in the next section. So, the main options of the program are the following:

- **Default results:** if any check box option is selected, the program will compute the basic parameters for TOPSAR (steering angle rates, timeline, etc.) and they will be shown in the *TOPS Analysis Results* text-box.

- **Save TOPS analysis results:** when this option is selected, the program shows the same results in the results text-box but, additionally, these parameters are stored in the path that user writes on the text-box.

- **Compute error due to steering angle quantization:** this option gives to the user a complete analysis of azimuth ambiguities that appear due to quantization of the steering angle. The results are shown with appropriate graphics showing the most interesting results including a text-box where the most significant values.

- **Ambiguity analysis with $sinc^4$ approximation:** an ambiguity analysis using the approximated antenna pattern is done when this option is chosen. This analysis is useful when we have not previously calculated the real pattern cuts.

- **Ambiguity analysis with real antenna cuts:** if the pattern cuts have been previously computed and stored, it is possible to calculate the ambiguities using them to obtain more accurate results for the AASR and RASR.

7.3 Output results provided by TOPSAR Interface

Once the basic functions of TOPSAR interface have been presented, in this section we are going to explain in detail the results obtained when we select each one. So, for each section, we are going to see which information the program gives to the user and how it can be obtained.

7.3.1 Save TOPS analysis results

This option provides to the user the possibility to save the results obtained for TOPSAR mode according to the parameters selected in the input values panel. The file is stored in the user-provided path. Furthermore, the file is stored as *TOPS_mode_heightA_azresB_numswathsC_swathiniD.txt*, where A is the altitude of the platform inserted previously by the user, B is the azimuth resolution desired, C the number of sub-swaths taken to do the TOPSAR scanning and D is the first sub-swath of the TOPSAR configuration.

Following the last example, in Fig. 7.3 the path where the file will be stored is: *C:/PFC/* . With this configuration the file name where the results will be stored will be: *TOPS_mode_height510_azres18_numswaths4_swathini1.txt* and the information that provides this file can be seen in Fig. 7.4.

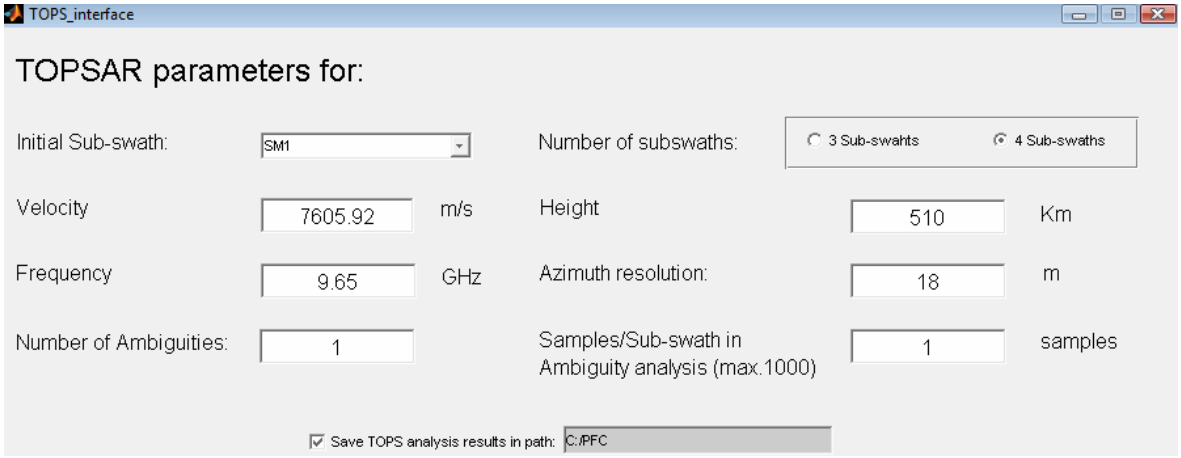

Fig. 7.3 Saving results to C:/PFC/

TOPS_mode_height510_azres18_numswaths4_swathini1 - Bloc de notas

Archivo Edición Formato Ver Ayuda

```
TOPSAR acquisition mode parameters in PAZ for sub-swaths: 1 2 3 and 4.


Input and orbital parameters:
        Planet Radius:          6378.15 Km
        Satellite altitude:     510 Km
        Platform velocity:      7605.92 m/s
        Effective velocity:     7318.93 m/s
        Radar centre Frequency: 9.650 Ghz
        Radar Wavelength:       0.031 m


Antenna configuration:
        Number of azimuth phase Centres:        12
        Radiators per azimuth phase centre:     16
        Number of radiators (azimuth):          192
        Radiating element sapcing (az):         0.8038 wavelengths
        Antenna Length:                         4.794 m

        Number of elevation Phase Centre:       32
        Radiators per Elevation Phase Centre:   1
        Number of radiators(elevation):         32
        Radiating elemet spacing (elevation):   0.7 wavelengths
        Antenna Width:                          0.700 m

        Total number of phase centres:          384


Sub-swath parameters for ScanSAR Mode:

Swath name      PRF         Incident angle near     Incident angle far      Azimuth beamwidth       Look angle near     Look angle far      Elevation beamwidth

SS1             3781.0          15.000                  18.370                  0.330               13.866              16.967              3.101
SS2             3741.4          16.850                  20.160                  0.330               15.569              18.610              3.041
SS3             3675.0          20.000                  23.200                  0.330               18.463              21.394              2.930
SS4             4440.2          23.040                  26.120                  0.330               21.247              24.058              2.810
SS5             3796.3          25.970                  28.920                  0.330               23.921              26.602              2.680
SS6             3732.1          28.780                  31.590                  0.330               26.475              29.016              2.541
SS7             4377.0          31.460                  34.140                  0.330               28.899              31.310              2.411
SS8             3782.0          34.010                  36.570                  0.330               31.193              33.483              2.290
SS9             4400.7          36.440                  38.870                  0.330               33.367              35.527              2.160
SS10            3805.0          38.750                  41.050                  0.330               35.421              37.452              2.031
SS11            4388.2          40.940                  43.130                  0.330               37.355              39.275              1.920
SS12            3816.0          43.020                  45.090                  0.330               39.179              40.979              1.800
SS13            3496.8          44.990                  46.950                  0.330               40.892              42.583              1.690
SS14            3187.7          46.850                  48.710                  0.330               42.497              44.087              1.590
SS15            3504.1          48.620                  50.380                  0.330               44.010              45.501              1.490
SS16            3200.9          50.290                  51.960                  0.330               45.425              46.825              1.400
SS17            3504.1          51.880                  53.460                  0.330               46.758              48.069              1.311
SS18            3214.0          53.390                  54.890                  0.330               48.012              49.243              1.231
SS19            3484.3          54.820                  56.240                  0.330               49.185              50.338              1.152
SS20            3214.0          56.170                  57.530                  0.330               50.281              51.371              1.090
SS21            3471.1          57.470                  58.760                  0.330               51.323              52.344              1.021
SS22            3207.0          58.700                  59.930                  0.330               52.297              53.258              0.961

Swath name      Range near      Range far   Ground range near    Ground range far    Swath width     Swath overlap   Middle look angle   Slant middle range

SS1              526.595         535.208         126.208             156.195         29.987          13.641              15.417              530.654
SS2              531.080         540.600         142.554             172.535         29.981           1.474              17.090              535.591
SS3              540.094         551.145         171.062             201.069         30.007           1.529              19.928              545.367
SS4              550.545         563.039         199.540             229.564         30.024           1.493              22.653              556.535
SS5              562.384         576.218         228.071             258.074         30.003           1.456              25.261              569.041
SS6              575.516         590.560         256.617             286.525         29.907           1.417              27.745              582.777
SS7              589.819         606.037         285.108             315.032         29.924           1.488              30.104              597.665
SS8              605.203         622.571         313.544             343.592         30.048           1.565              32.338              613.620
SS9              621.640         639.994         342.026             372.033         30.027           1.522              34.447              630.549
SS10             639.039         658.264         370.531             400.484         29.953           1.471              36.436              648.385
SS11             657.299         677.458         399.013             429.099         30.087           1.553              38.315              667.109
SS12             676.397         697.279         427.547             457.556         30.009           1.490              40.079              686.570
SS13             696.224         717.804         456.067             486.057         29.990           1.572              41.737              706.747
SS14             716.655         738.915         484.485             514.516         30.032           1.493              43.292              727.518
SS15             737.793         760.613         513.023             543.005         29.982           1.575              44.755              748.938
SS16             759.399         782.776         541.431             571.427         29.997           1.476              46.125              770.825
SS17             781.614         805.423         569.952             599.862         29.910           1.360              47.414              793.259
SS18             804.330         828.599         598.502             628.411         29.910           1.432              48.627              816.207
SS19             827.427         852.022         626.979             656.772         29.793           1.506              49.762              839.471
SS20             850.768         875.920         655.266             685.264         29.998           1.357              50.826              863.089
SS21             874.773         900.197         683.907             713.803         29.896           1.425              51.834              887.235
SS22             898.978         924.748         712.378             742.294         29.916           0.000              52.778              911.614



Necessary parameters to operate in TOPS Mode in sub-swaths: 1 2 3 4. Azimuth resolution: 18

Subswath        Steering angle  Steering angle  Doppler Rate    Burst time      Dwell time      Doppler BW      Max. steering
name             rate (rad/s)    rate (deg/s)      (Hz/s)                                                          angle

SS1             0.07820         4.4803          -6494.122       0.15844         0.07088         460             0.3549
SS2             0.07748         4.4390          -6434.258       0.15902         0.07154         460             0.3530
SS3             0.07609         4.3595          -6318.925       0.16017         0.07284         460             0.3491
SS4             0.07456         4.2720          -6192.114       0.16149         0.07433         460             0.3449
```

Fig. 7.4 Results stored at TOPS_mode_height510_azres18_numswaths4_swathini1.txt. Information about antenna and sub-swaths parameters and TOPSAR results are presented

As we can see, the saved file shows the basic antenna parameters and the radar flight and operation features. Furthermore, it provides the basic parameters of the TOPSAR operation mode and the characterization of all the sub-swaths.

7.3.2 Compute error due to angle quantization

As it was explained in Chapter 4, one of the problems that we find with TOPSAR is the impossibility of doing a continuous steering in azimuth due to limited storage capacity of the system. The quantization of the steering angle can introduce some azimuth replicas in the spectrum that have to be considered as azimuth ambiguities.

When this option is selected, the system calculates the error produced by this quantization and gives numerical and graphical information to the user. Fig. 7.5 to Fig. 7.9 are the results obtained when this command is active. When we can see, they correspond to the angle quantization analysis done in Chapter 4. Step by step, Fig. 7.5 shows the azimuth antenna pattern of the analysed sub-swaths. The $sinc^4$ approximation has been used for this analysis, since the grating lobes influence is not relevant for this error computation. In the figure, the AAP with continuous azimuth steering is plotted in blue, while in red we can see the quantized azimuth cut.

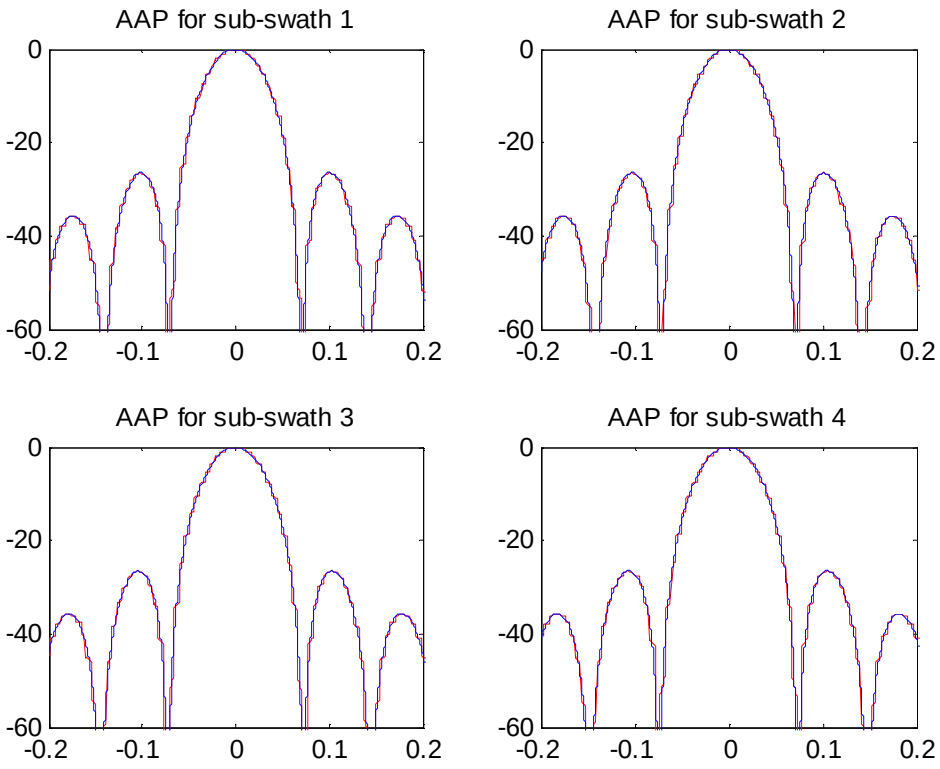

Fig. 7.5 Angle quantization error analysis for TOPSAR, a) quantized AAP versus ideal AAP

Continuing with this analysis, in Fig. 7.6, the error made due to quantization of the steering angle is plotted in function of platform movement. As we can see, it can be approximated with a sawtooth signal, Fig. 7.7 (for more precise information consult Chapter 4).

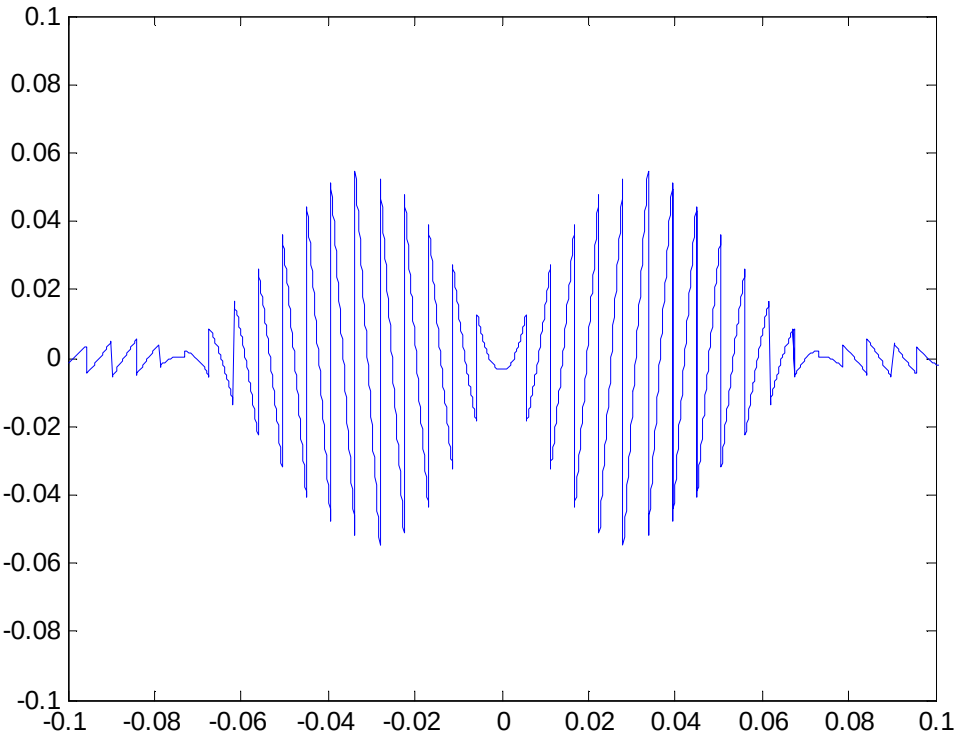

Fig. 7.6 Angle quantization error analysis for TOPSAR, b) error due to quantization

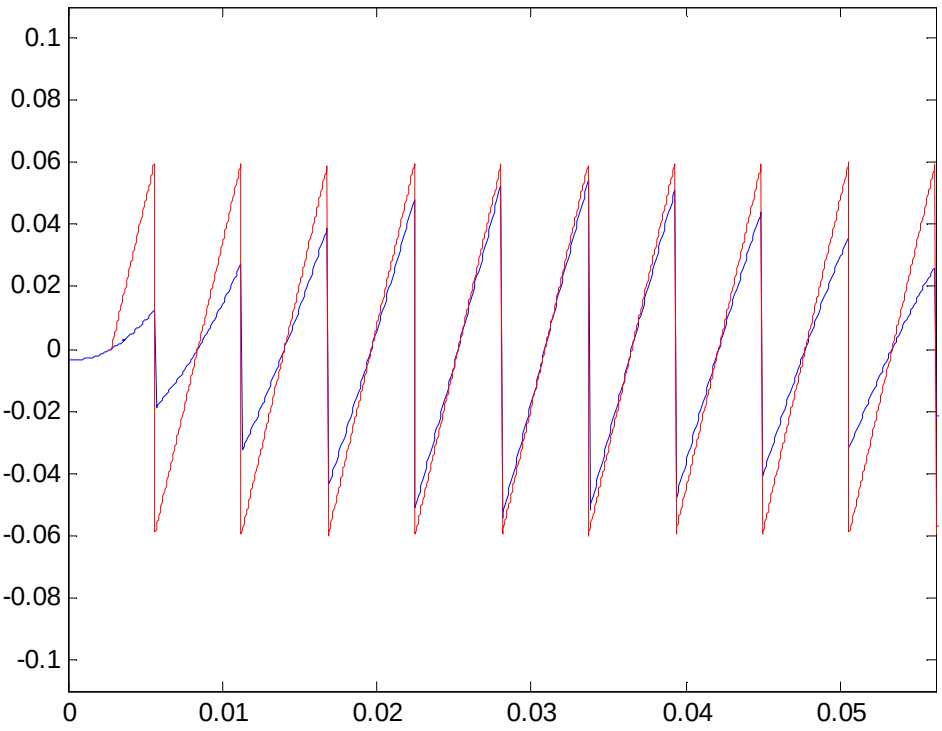

Fig. 7.7 Angle quantization error analysis for TOPSAR, c) error approximation vs. quantization error

Once we get the azimuth error, its Fourier transform can be calculated to see how this error will affect to azimuth ambiguities in reception. The Fourier transform is shown in Fig. 7.8, notice presence of azimuth periodic ambiguous signals that will interfere to signal reception.

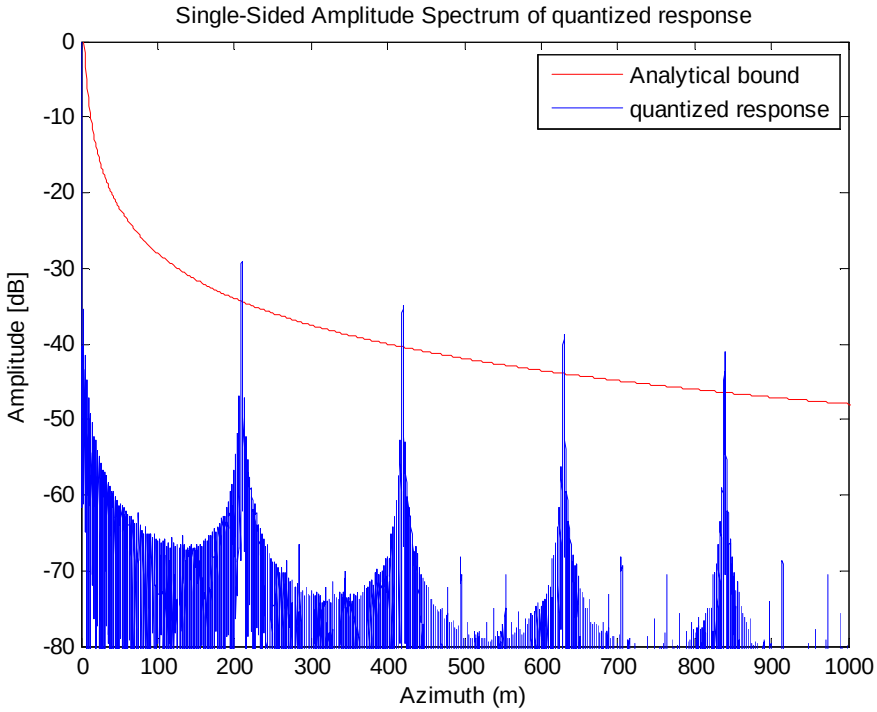

Fig. 7.8 Angle quantization error analysis for TOPSAR, d) Fourier transform of the quantization error

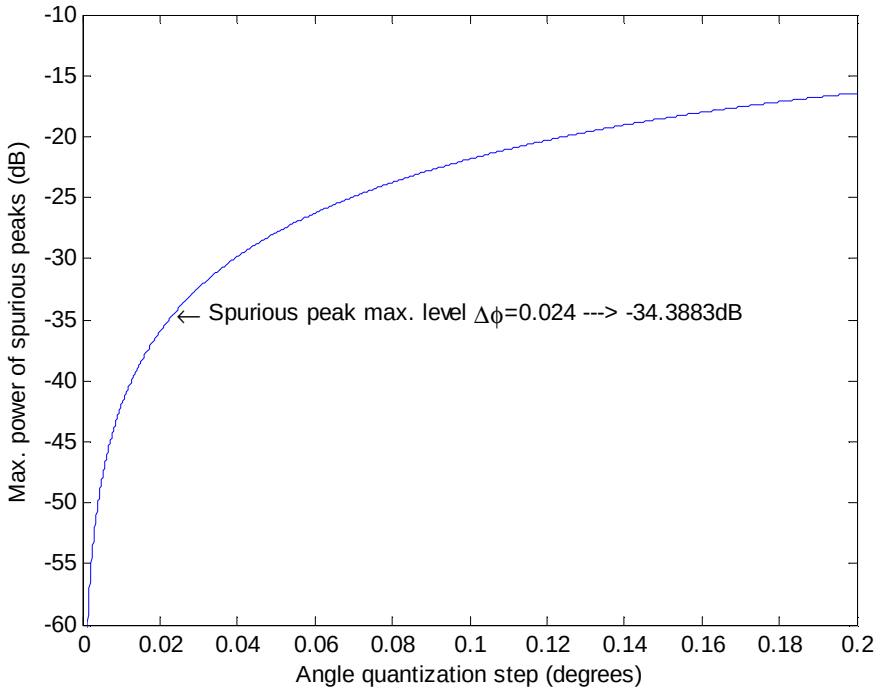

Fig. 7.9 Angle quantization error analysis for TOPSAR, e) most powerful ambiguous peak

The power of the strongest spurious peak can be obtained from Fig. 7.9. This shows the evolution of the power of this peak in function of the azimuth angle quantization step required to perform TOPSAR scanning.

Furthermore, at the same time the program gives to the user numerical information. So, when the angle quantization error analysis option is active, the results text-box shows the most relevant information of the analysis. This information will include the angle quantization step necessary for the proposed configuration, the azimuth location of spurious peaks and the power of first of these ambiguous returns. Fig. 7.10 shows the results obtained for the example used in this section.

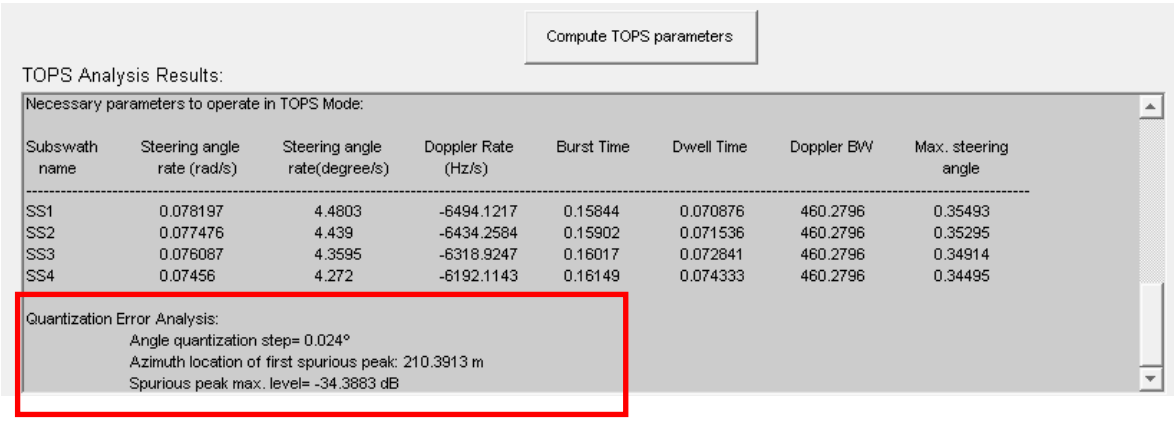

Fig. 7.10 Results from angle quantization error

7.3.3 AASR and RASR using sinc approximation

We have two options to compute the ambiguities for the radar system. The first one, which is explained in this section, computes the ambiguities using the approximated pattern cuts of the antenna. Although the results will not be as precise as we would like, it is an interesting way to get a first approximation to the real values of the AASR and RASR. It is also important when the user has not previously computed the antenna pattern cuts. With these options the user can obtain a preliminary ambiguity analysis without precise antenna information.

In ambiguity analysis two input parameters, which have not outlined until now, are very important. The first one, number of ambiguities, indicates the total ambiguous returns that the system will take into account when computing the ambiguities. In addition, the input parameter Samples/sub-swath permits to select the number of points that will be computed for each of the sub-swath analysed. The total time to compute the ambiguities will depend on these parameters. Obviously increasing the number of ambiguous zones in the analysis, the computation process will take more time. The same happens with the total points desired for each sub-swath.

In Fig. 7.11, the program is configured to compute both, azimuth and range ambiguities, using an approximated model for the antenna pattern cuts and computing 40 ambiguities giving 10 values for each sub-swath.

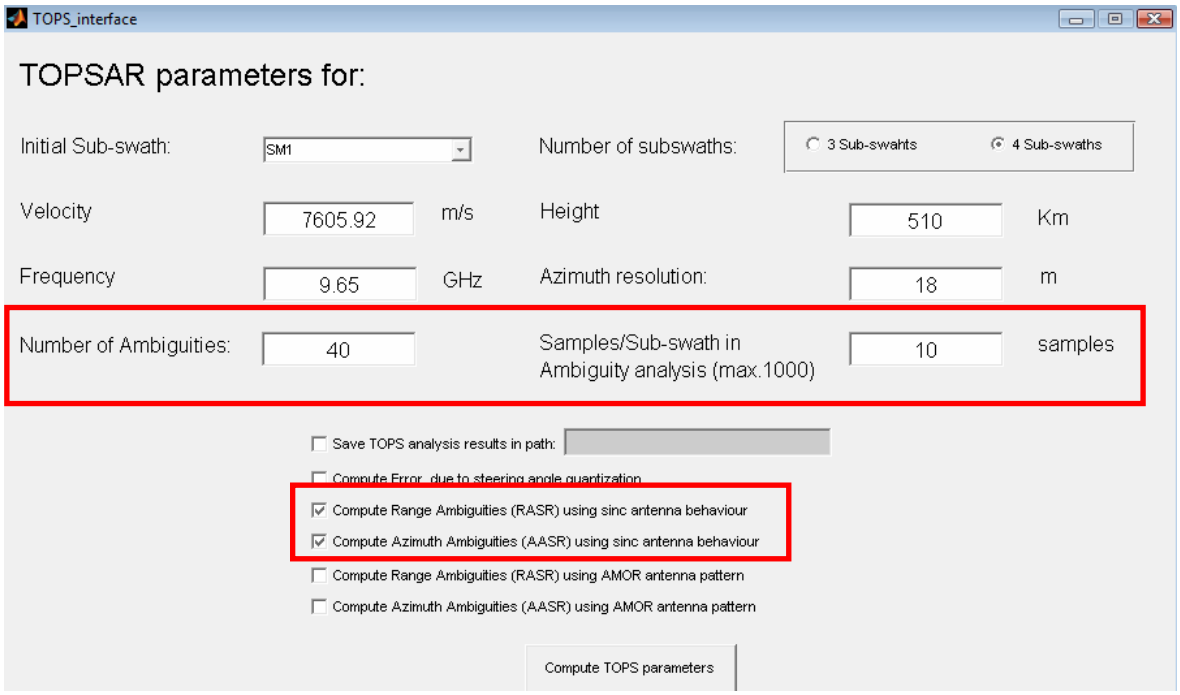

Fig. 7.11 Ambiguity analysis input parameters

With RASR and AASR check-box marked, the program will give the graphic of range and azimuth ambiguities for the studied sub-swaths. They can be seen in Fig. 7.12 and Fig. 7.13.

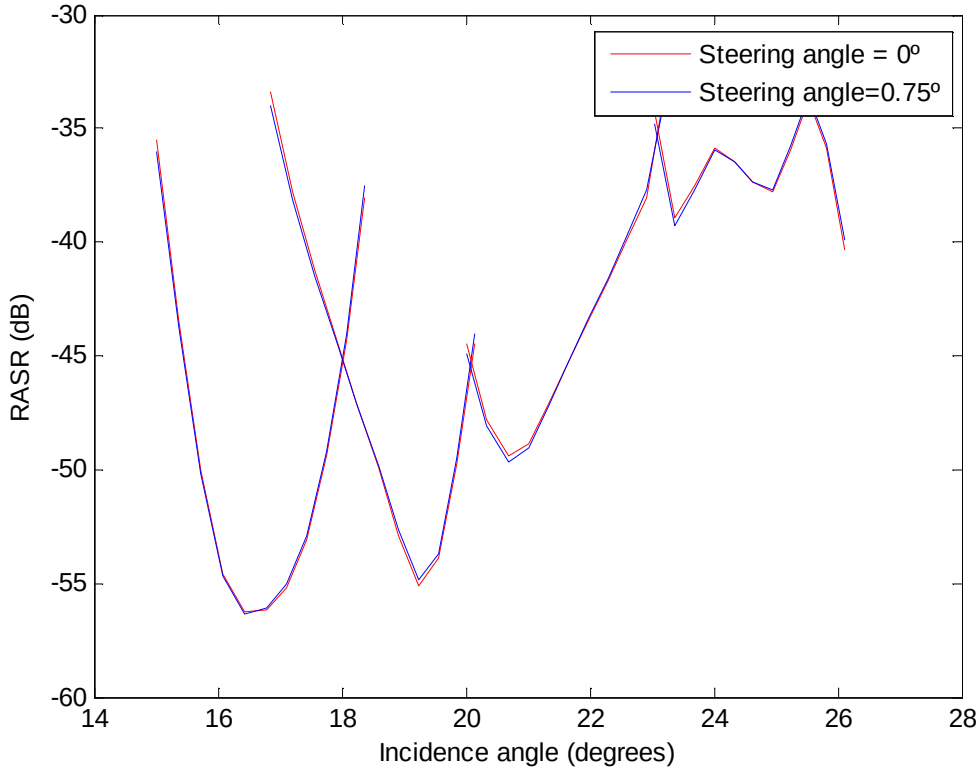

Fig. 7.12 RASR results computed with TOPSAR interface

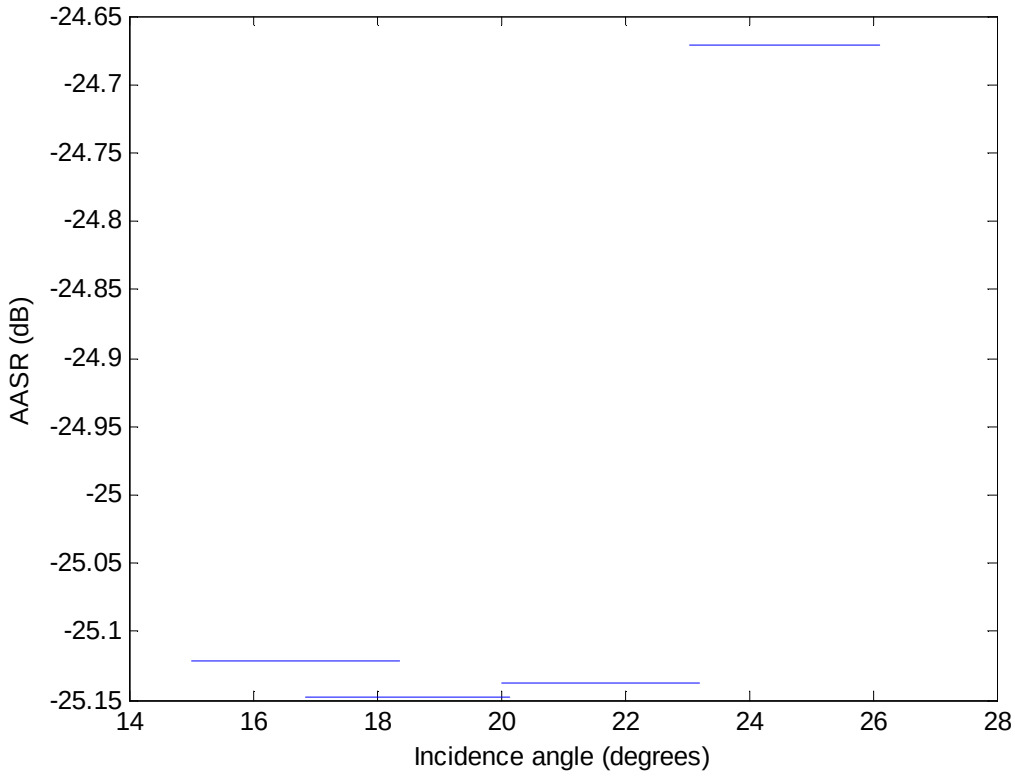

Fig. 7.13 AASR results computed with TOPSAR interface

Once again, values of the RASR and AASR of each sub-swath are shown in results text-box. The values of this example can be observed in Fig. 7.14.

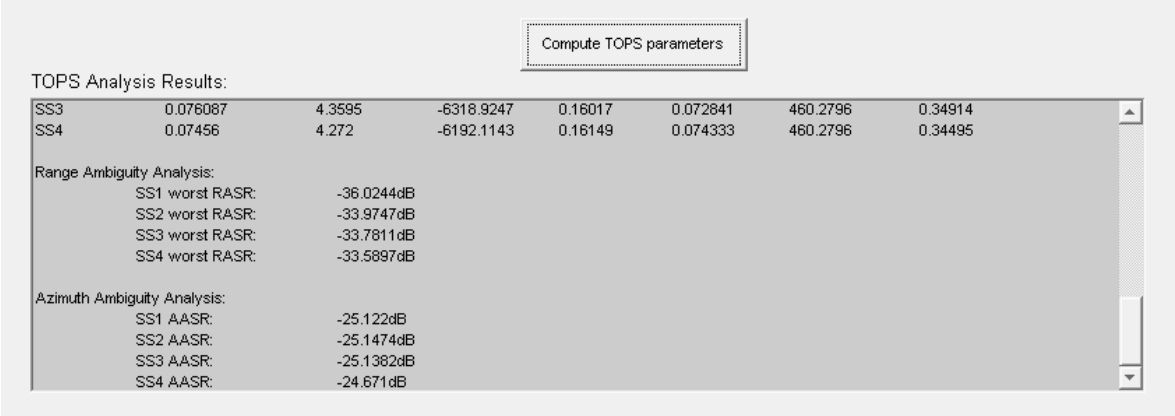

Fig. 7.14 Results for RASR and AASR in TOPSAR interface

7.3.4 AASR and RASR using real antenna patterns

It is possible to compute the AASR and RASR using real antenna pattern cuts with TOPSAR interface. To execute these options, pattern cuts has to be previously computed and saved. More precise results will be obtained with these methods since no approximation is used.

To compute range ambiguities it is not necessary to specify the azimuth steering angle since it does not affect significantly to antenna elevation cut. To calculate RASR we will need the files with antenna directivities for the analysed sub-swaths. These files must be stored as *test_el_SM*AA*_EL2W.txt* where AA is the sub-swath number. Elevation cuts files have to follow the structure shown in Fig. 7.15, where ϕ and θ coordinates are stored in the two first columns while the antenna directivity is stored in third column.

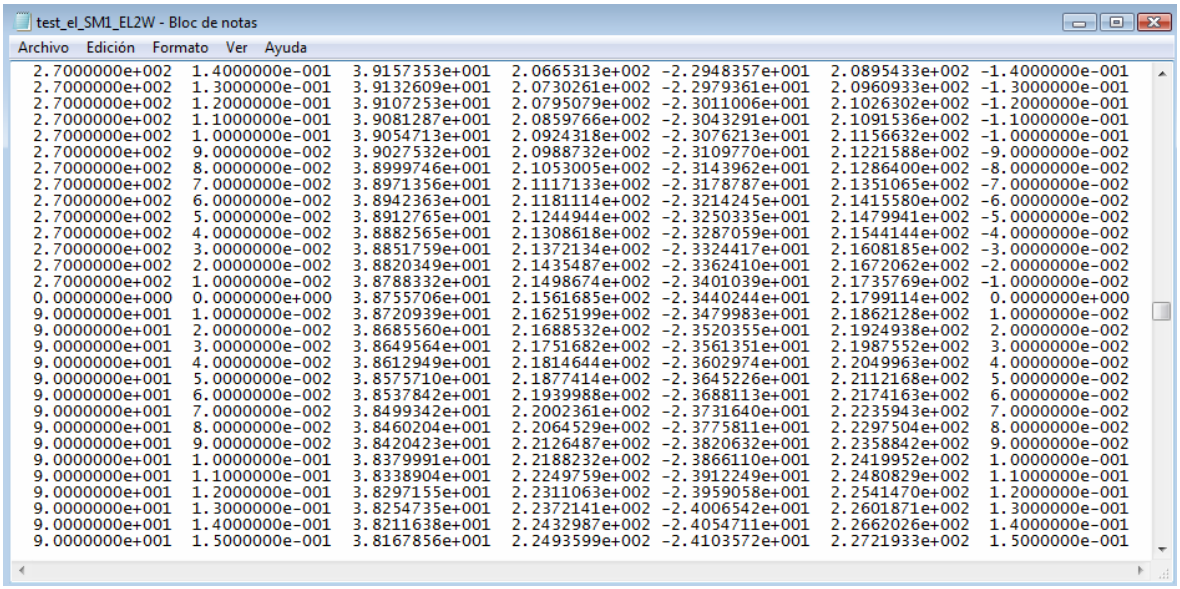

Fig. 7.15 test_el_SM1_EL2W.txt . Two first columns contain the theta and phi angles respectively. The directivity of the antenna diagram is stored in the third column

With these files, the range ambiguities can be obtained with our program. TOPSAR interface will provide the correspondent graphical results of RASR for the analysed sub-swaths and, once again, numerical information in the results text-box.

On the other hand, azimuth ambiguity calculation obtains the AASR for the azimuth steering angle chosen by the user. To get the results, we need to compute the azimuth antenna cut for this steering angle, and it must be stored as *TOPS_SMAA_BBB_HH_AZ2W.txt*, where AA is the sub-swath number and BBB is the steering angle with two decimals in degrees. In these documents, θ angle is stored in column 7, while the antenna directivity values are in third column.

Taking into account all these considerations and continuing with the same example, Fig. 7.16, Fig. 7.17 and Fig. 7.18 show the results obtained with AASR and RASR analysis using TOPSAR interface. Azimuth ambiguities have been computed for a steering angle of 0.5 degrees in this example.

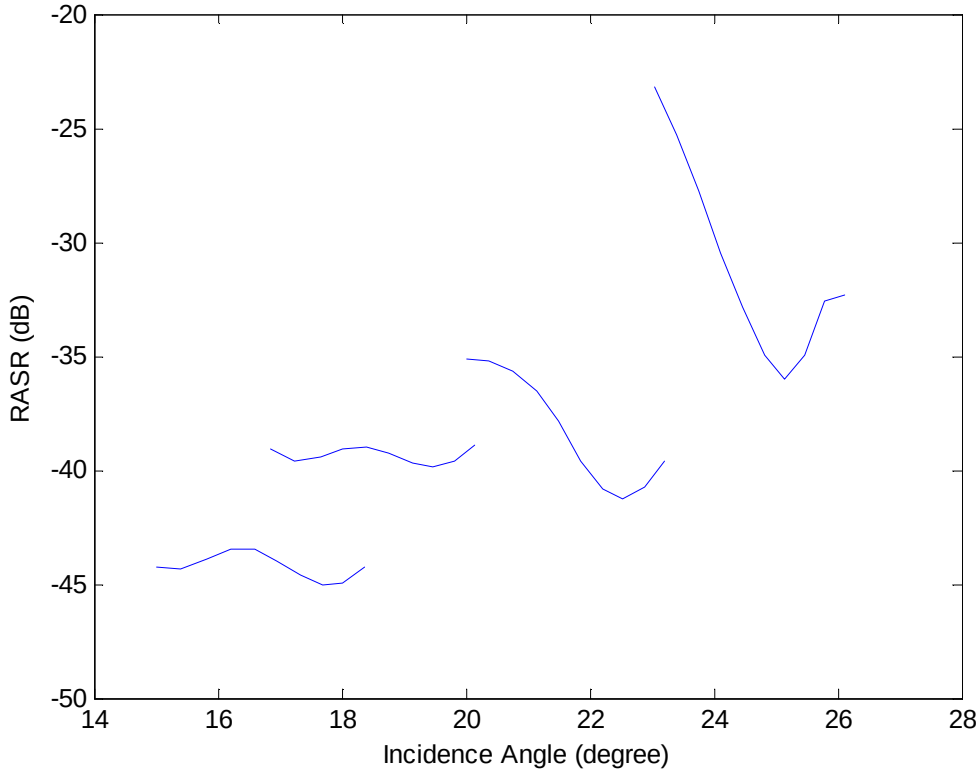

Fig. 7.16 RASR computation with TOPSAR interface

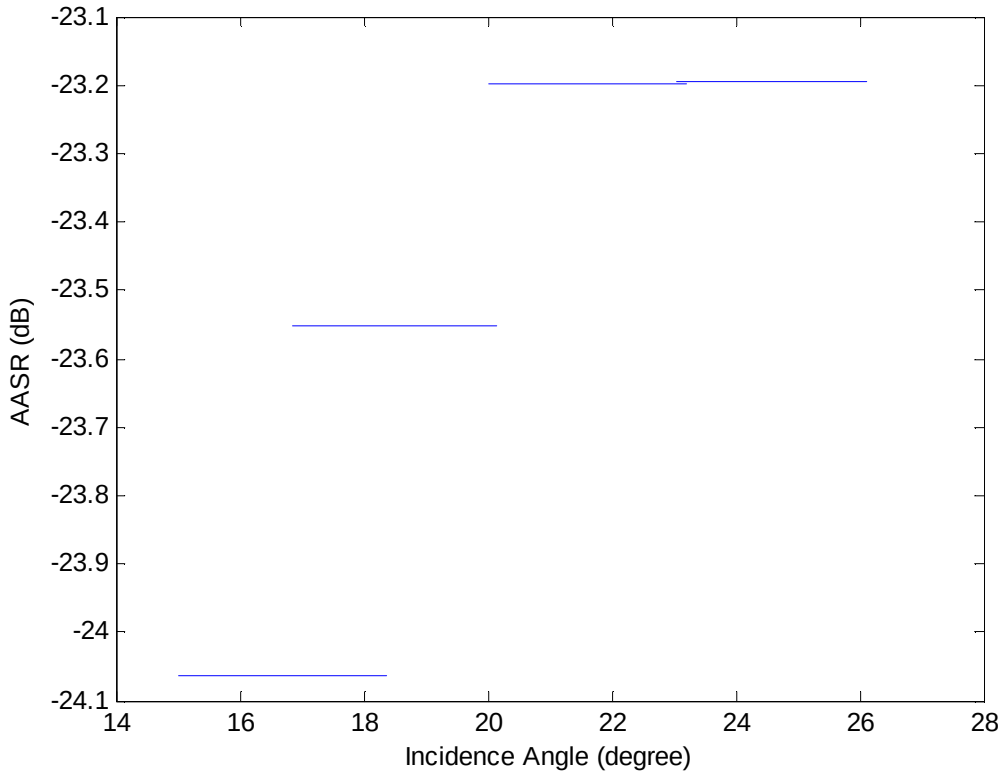

Fig. 7.17 AASR computation with TOPSAR interface

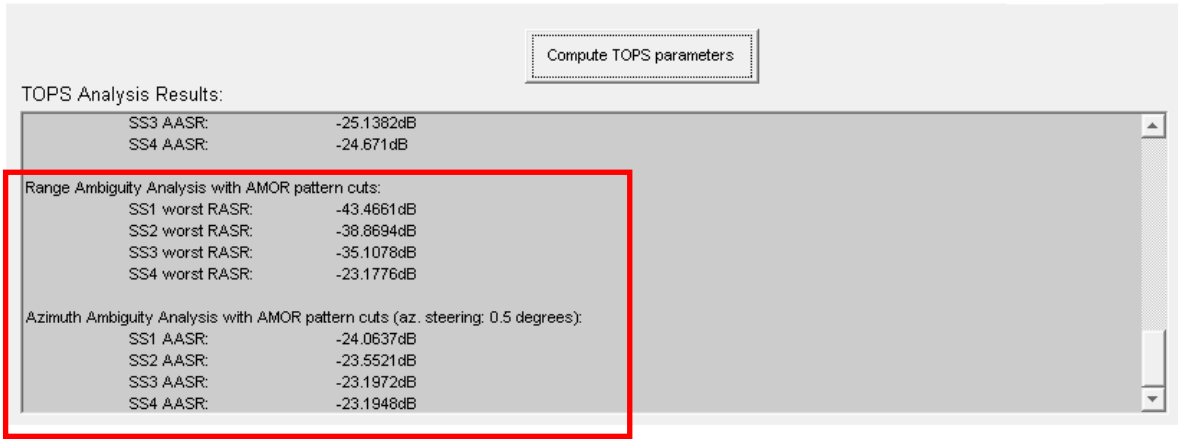

Fig. 7.18 Numerical results for RASR and AASR obtained with TOPSAR interface

Chapter 8 Conclusions and future work

In this project a new scanning mode for SAR systems, denoted as Terrain Observation by Progressive Scans (TOPSAR), has been proposed and evaluated to demonstrate its feasibility in radar imaging. TOPSAR introduces a beam steering back to forward in along-track movement of the platform. Besides, the scanning time is divided into different sub-swaths in order to get higher range coverage.

One of the new contributions of this new scanning mode is the uniform power received from all targets in azimuth direction, avoiding undesirable effects such as scalloping that appear in other high range coverage like ScanSAR. The steering in azimuth makes the uniform illumination of all targets possible.

To achieve this goal, some of the parameters of the antenna have to be modified and adapted to TOPSAR scanning. ScanSAR parameters of PAZ system have been chosen as input parameters for TOPSAR mode since their operations are similar. From them (PRFs, sub-swaths characterization, orbital parameters…), the necessary steering rates to achieve the nominal ScanSAR azimuth resolution of 18 meters have been computed for TOPSAR. Once the steering angle rates in azimuth has been obtained, the scanning time line for different sub-swaths has been calculated in order to have a uniform scanning without holes in along-track direction.

The results obtained for the nominal configuration (TOPSAR with 18 meters of azimuth resolution) are in the range of possible values for radar system. Steering angle rates around 3 or 4 degrees per second, depending on the sub-swath, are necessary. These beam steering rates can be carried out by the antenna system switching its pointing direction stored in radar memory. For TOPSAR mode, two scanning alternatives have been proposed on this project. The first one uses 3 sub-swaths commutation to scan the scene, providing range coverage of 75 Km approximately. On the other hand, the second proposal divides the scanning time in four sub-swaths which means higher range coverage (around 100 Km.) but with worst performance against ambiguities.

The burst times for each sub-swath computed in Chapter 3 to guarantee the total coverage in azimuth direction vary depending on the configuration. So, while in 3 sub-swaths alternative a burst time of 0.12 seconds is obtained, in the 4 sub-swaths case the burst time is longer, around the 0.17 seconds. Higher burst time means higher maximum steering angle in azimuth and, consequently, more directions where the antenna has to point to cover all points. This affects again to the ambiguity response of TOPSAR mode.

Once the feasibility of the TOPSAR scanning parameters has been studied for our system, the response to ambiguities and other undesired effects has been analysed to assure a right performance in the radar acquisition. First study carried out in this project is about steering angle quantization problems. Due to the limited storage capacity, it is not possible to do a continuous steering in azimuth and some positions have to be previously stored in the radar memory.

The switching between memory positions produces a quantization behaviour of the azimuth steering producing some errors compared with the ideal azimuth antenna pattern. Azimuth ambiguities will appear due to these errors. The study in Chapter 4 demonstrates that this ambiguity can be considered negligible since the most powerful spurious peak in azimuth has a power more than 30 dB below of the desired signal.

However, the angle quantization is not the only source of ambiguities. The finite sampling of the azimuth antenna pattern each T second (*T=1/PRF*) produces replicas of the received spectrum at multiples of the PRF which can not be discriminated from the useful signals. These undesirable parts of the spectrum are known as azimuth ambiguities. Furthermore, the returns of preceding and succeeding pulses that arrives at the same time that the desired return deteriorate the echo reception (range ambiguities).

The ambiguities study carried out in Chapter 5 provides a complete analysis of the ambiguity computation for Stripmap and ScanSAR which are useful to obtain the ambiguity response in TOPSAR mode. After the calculations, the right performance of TOPSAR can be guaranteed for low incidence angles (15^o – 45^o). For higher incidence angles, the range ambiguities are not rejected enough to assure the reception of the echoes and, consequently, ambiguity problems can appear in image reception.

In ScanSAR and TOPSAR scanning modes, the azimuth resolution is compromised in order to get higher range coverage. However, in TOPSAR, it is possible to improve the azimuth resolution taking slower azimuth steering angle rates. As it was exposed, it is impossible to reach the Stripmap resolution since the time is divided in different swaths and the observation time for each target is lower.

Thus, in Chapter 6, a study of the azimuth resolution optimization has been presented. Improving the azimuth resolution means lower steering angle rates and higher maximum azimuth steering angles. When the antenna is highly steered in azimuth, the grating lobes increase considerably which affects to the azimuth ambiguities. For this reason, it is not possible to achieve any azimuth resolution since the ambiguity performance gets worse rapidly.

After the study, an azimuth resolution of 10 meters has been determined as the optimum resolution when 3 sub-swaths are used. On the other hand, in 4 sub-swaths scanning, the achievable azimuth resolution that provides an acceptable response of the system is approximately 13.5 meters. It is a trade-off between range coverage and azimuth resolution for both alternatives. The most suitable configuration will depend on the user requirements for each exploration. If a high range coverage is desired the 4 sub-swath alternative will be chosen. On the other hand, if a finer azimuth resolution is required, the 3 sub-swath configuration will be better for our interests.

As it has been demonstrated in this project, the new scanning mode TOPSAR is an interesting alternative for high range coverage image acquisition. It avoids ScanSAR inherent problems, providing better acquisition results. As it was explained in Chapter 5, the ambiguity analysis demonstrates the better performance of the radar against azimuth ambiguities working with TOPSAR, since ScanSAR presents lower ratios due to non-uniformity power of the received echoes. This non-uniformity produced due to the sub-swath switching is avoided in TOPSAR thanks to the steering in azimuth of the antenna main beam. Furthermore, in TOPSAR mode, it is possible to select the azimuth resolution modifying the azimuth steering angle rates of the system which is impossible to achieve with ScanSAR mode.

In this document, the numerical analysis has been done to demonstrate the feasibility of TOPSAR mode in SAR satellites. A TOPSAR processor has to be designed to process the returns from the targets. This processor must be capable to compensate the azimuth

steering and locate correctly the targets in the scene. Simulations with this new system are the next step in TOPSAR mode analysis for radar imaging.

For a future work, once the TOPSAR mode will be simulated and their operation accepted, the mode has to be programmed in a real situation on a space-borne system to try its right performance in a real situation.

In this first approximation, it can be conclude that TOPSAR mode is an interesting proposal to be adopted as wide swath operational mode providing SAR imaging with wide range coverage with less azimuth resolution loss than ScanSAR and with better image quality.

Annex A History of SAR missions

A.1 History and principal SAR space missions

Since the SEASAT, the first civilian SAR satellite, was launched in June 1978, many other missions were sent to the space to obtain information about the Earth surface and sea. Canada, Europe, Japan and Russia have placed their own satellites in orbit for investigation in 1980s and 90s, but the origin of SAR started at 1950s. ERS-2, RADARSAT-1, ENVISAT or TerraSAR-X are some examples of SAR mission. Each mission has their own configuration in terms of frequency, polarization, orbital parameters, resolution, swath width… but the operation is similar for all of them.

In 1951, Carl A. Wiley published the basic principles of radar with synthetic aperture. C.A. Wiley, of the Goodyear Aircraft Corporation, observed that a one-to-one correspondence exists between the along-track relative position of the antenna radar and the target, and the Doppler frequency shift of the signal reflected by the targets. With this new feature, Wiley established that a frequency analysis of the echoes received, permitted by the along-track movement of the platform, could enable a finer resolution in this direction.

The Wiley's theory was used by Goodyear and University of Illinois to follow the studies in Synthetic Aperture Radar. Their major problem was implementation of a practical data processor that could analyse the Doppler history of received echoes, stored in a device, and reproduce the results for each point in the scene. The Illinois group finally carried out an experimental demonstration of Wiley's postulates using a coherent X-Band pulsed radar, a tape recorder and a frequency analyser.

Since then, other industrial and military developments with airborne platforms was carried out by Goodyear, Hughes and Westinghouse. This new technology began to be explored by the Jet Propulsion Laboratory (JPL), University of Michigan, Environmental Research Institute of Michigan (ERIM), Sandia Laboratories, and other research groups.

First SAR experiments were carried in aero-transported radar, but it was not until 1978 when the first space mission was sent by the NASA. This SAR space mission, called SEASAT, was followed by multiples missions whose main features can be seen in Table A.1.

A.2 SAR space missions

Until now, a general vision of SAR history has been exposed. In this section, the principal missions carried out in the last years are described and some results of them are presented. It is not the purpose of this thesis to have a complete analysis of other SAR systems, but it can be useful to have a first approximation to the SAR imaging.

A.2.1 SEASAT, 1978

SEASAT was the first remote sensing orbiting radar used to take pictures of Earth sea with synthetic aperture radar technique. The mission was designed to get information and monitoring oceanographic phenomena. SEASAT collected data about surface winds, sea-surface temperatures, wave heights, internal waves, atmospheric water, sea ice and ocean topography.

Satellite	Country	Year	Band	Frequency (GHz)	Wavelength (cm)	Incid. angle (deg)	Pol	Pulse Bandwidth (MHz) / Range resolution (m)	Azimuth resolution (m) / Looks
SEASAT	USA	1978	L-band	1.275	23.5	23	HH	19/7.9	6/1
SIR-A	USA	1981	L-band	1.275	23.5	50	HH	6/24.9	6.5/1
SIR-B	USA	1984	L-band	1.275	23.5	15-65	HH	12/12.5	6/1
ERS-1/2	Europe	1991/95	C-band	5.25	5.7	23	VV	15.5/9.7	25/3
ALMAZ	USSR	1991	S-band	3.0	10	30-60	HH	-/15	15/2
JERS-1	Japan	1992	L-band	1.275	23.5	39	HH	15/10	30/4
SIR-C/X-SAR	USA	1994	L-band	1.25	23.5	15-55	HH,HV, VH,VV	10/15	7.5/1
			C-band	5.3	5.7				
	Germany		X-band	9.6	3	54	VV	20/7.5	6/1
RADARSAT-1	Canada	1995	C-band	5.3	5.7	20-50	HH	11.6/12.9 17.3/8.6 30/5	28/4 50/(2-4) 100/(4-8)
SRTM	USA	2000	C-band	5.25	5.7	54	HH,VV VV	20/7.5 8/18.7	15/1 8-12/1
	Germany		X-band	9.6	3	54			
ENVISAT	Europe	2002	C-band	5.25	5.7	15-45	HH,HV, VH,VV	9/16.6	6/1 150/12 1000/(18-21)

Table A.1 Earth Orbital SAR systems parameters

SEASAT was launched at 26 June in 1978 and it flew with Earth orbit of 800 Km with an inclination of 108º. It was only operative during 105 days due to a short circuit that interrupted its operation.

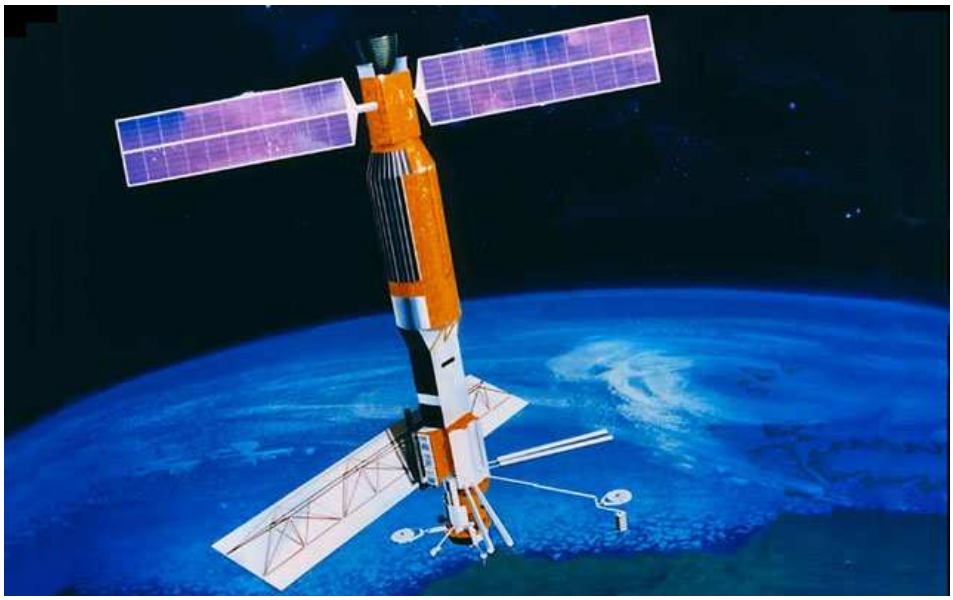

Fig. A.1 SEASAT satellite orbiting around the Earth

SEASAT was equipped with five instruments designed to obtain the maximum information about sea surface. The system was composed by a radar altimeter to measure spacecraft height above the ocean surface; a system to measure wind strength and direction; scanning radiometer to measure the ocean surface temperature; visible and infrared radiometer to identify cloud, land and water features; and the radar antenna to get high resolution images from the sea with the SAR technique. Fig. A.2 shows an image captured with SEASAT of the Los Angeles metropolitan area.

Fig. A.2 SEASAT image of Los Angeles

A.2.2 SIR-A, 1978

SIR-A was the first mission of JPL launched from Kennedy Space Center, Florida, on November 12 in 1981. It was carried into space on STS-2, the second mission carried by NASA using the Space Shuttle Columbia.

SIR-A had a orbit altitude of 259 Km with a radar frequency of 1.275 GHz, working in L-band. The antenna systems pointed with a look angle of 47 degrees and had a swath width of 50 km.

A.2.3 SIR-B, 1984

On October 5, 1984, the second Shuttle Imaging Radar (SIR-B) was launched into orbit aboard the space shuttle Challenger. A new capability that SIR-B incorporated was the possibility of working at different incidence angle form 15 to 60 degrees.

SIR-B worked with the similar basic parameters than SIR-A. That means a radar frequency of 1.275 GHz with a wavelength of 23.5 cm.

The Shuttle Imaging Radar-B experiment consisted of a several number of investigations in the earth ocean. Some of them were the study of generation and propagation of surface waves, the dynamics of internal waves, oil slick detection and properties of southern polar ice.

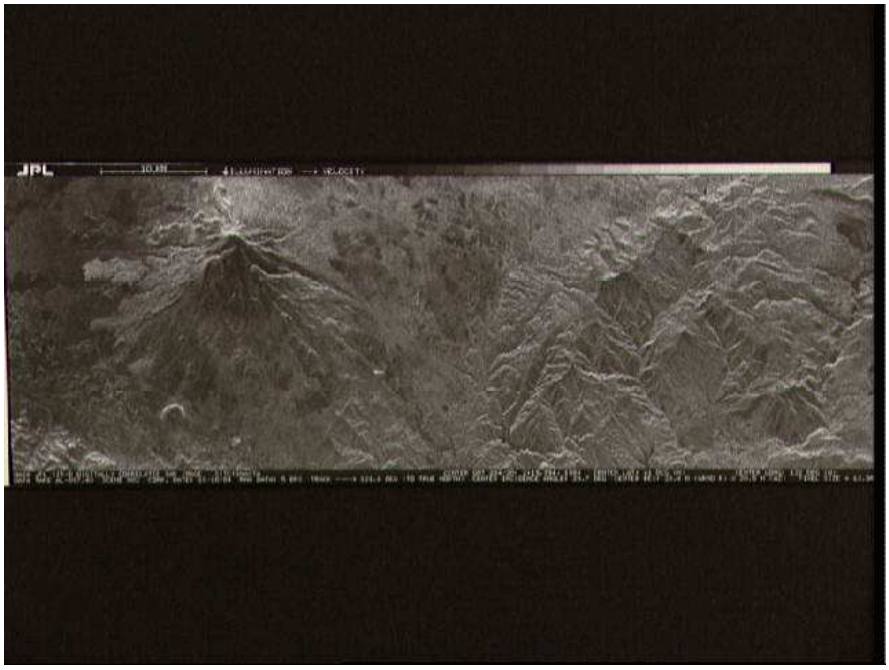

Fig. A.3 SIR-B image of Mt. Shasta Volcano

A.2.4 ERS-1/2, 1991 and 1995

The First and Second European Remote-Sensing Satellites (ERS-1 and ERS-2) were developed by the European Space Agency as an Earth Observation Satellites mission. On

17 July 1991, was launched the first European mission to the space ERS-1. The orbit of this mission has a 800 Km altitude and 98.5 degree inclination orbit. The second satellite (ERS-2) was sent to the space on 21 April in 1995. Currently, ERS-1 has finished operations while ERS-2 is still operating with a degraded attitude control.

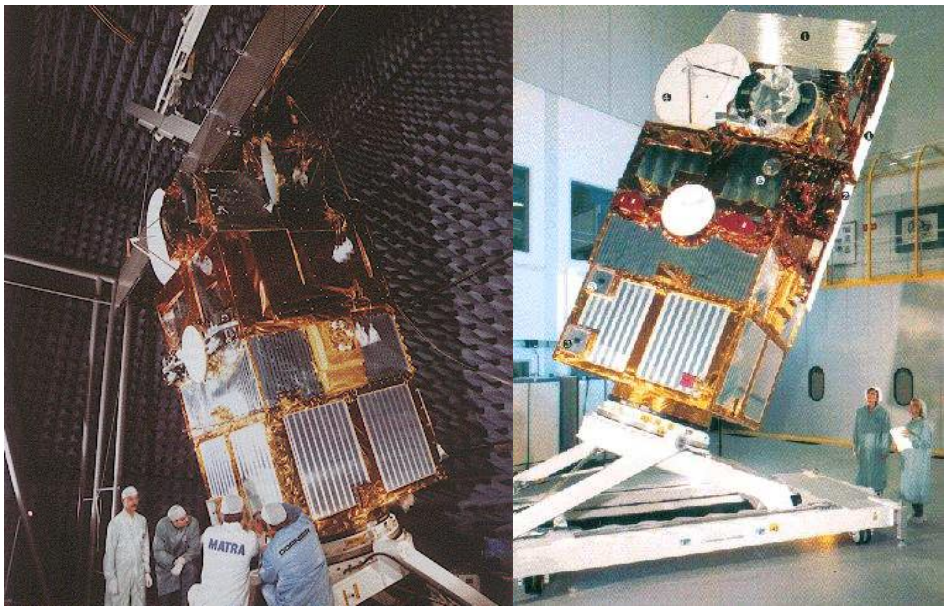

Fig. A.4 ERS-1 and ERS-2 imaging systems

The satellites incorporate a Synthetic Aperture Radar that provides cloud-free radar images of Earth's surface. Other systems that they incorporate are wind scatterometer (SCAT) to map the wind speed and direction over the ocean surface, a radar altimeter (RA), along-track Scanning Radiometer (ATSR), Microwave Sounderm Global Ozon Monitoring Experiment (GOME), precise range and range-rate equipment (PRARE) and a laser retro-reflector (LRR).

A.2.5 ALMAZ, 1991

ALMAZ mission consisted on a series of military space station launched by Soviet Union to get surface information. First missions were equipped with high resolution cameras and infrared sensors.

It was in 31 March 1991, when Almaz-1 was launched. Amaz-1 was the third satellite sent in Almaz-T mission and it was the first to incorporate high resolution radar facilities with SAR techniques. It was operative during eighteen months.

A.2.6 JERS-1, 1992

The Japan Earth Resources Satellite (JERS-1 aka Fuyo 1) started its operation in February 1992. His orbit was sun-synchronous with an altitude of 570 Km. The system consists of a net rectangular bus (0.9 m by 1.8 m by 3.2 m) with a single 2-kW solar array (3.5 m by 7 m) and an eight-segmented SAR antenna (2.4 m by 11.9 m). The spacecraft carries two Earth observation sensors: the SAR and the OPS multi-spectral imager.

Fig. A.5 Image took by JERS-1 in 1998

The SAR sub-system operates at a frequency of 1.275 GHz with a peak power of 1.3 kW, a 75 Km swath width and 18 m of azimuth resolution. The antenna works with an incidence angle of 39 degrees.

A.2.7 SIR-C/X-SAR, 1994

Spaceborne Imaging Radar-C/X-band Synthetic Aperture Radar is an imaging radar system launched by NASA Space Shuttle in 1994. The system consists of a radar antenna structure and associated radar system hardware.

SIR-C/X-SAR is a project carried out by the National Aeronautics and Space Administration (NASA), the German Space Agency (DARA) and the Italian Space Agency (ASI) together. SIR-C/X-SAR has unique contributions to Earth observation and the radar is used to make measurements about vegetation type, extend and deforestation; soil moisture content; ocean dynamics, wave and surface wind speeds and directions; volcanism and tectonic activity; and soil erosion and desertification.

SIR-C/X-SAR has an orbital altitude of 225 Km with a resolution of 30x30 m on the surface. Look angle is variable and it goes from 17 to 63 degrees from nadir. The radar instruments can work at different frequencies, so it is possible to work at L, C and X-band. Swath width change with system configuration and it is possible to select a width from 15 to 90 km.

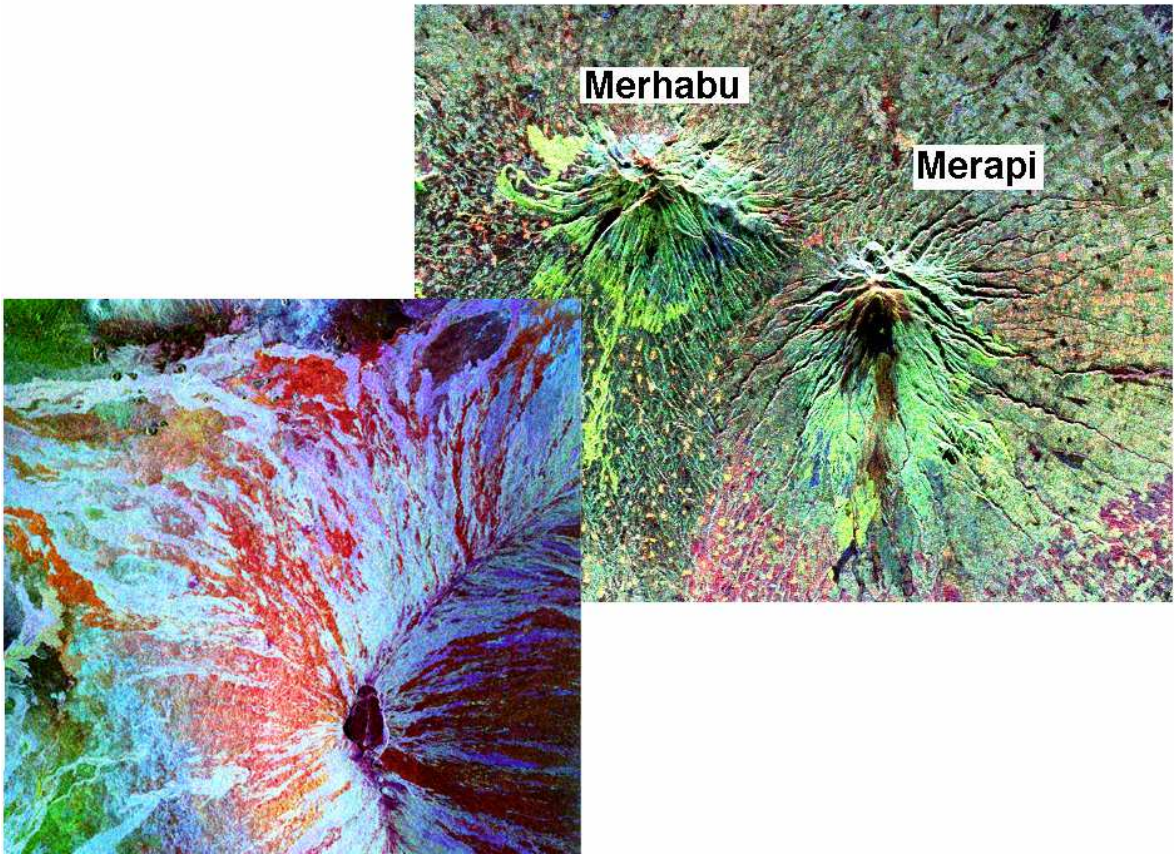

Fig. A.6 Two pictures captured with SIR-C/X-SAR system

A.2.8 RADARSAT-1, 1995

RADARSAT-1 was launched on November 4, 1995 from California. It has a sun-synchronous orbit with an altitude of 798 km and inclination of 98.6 degrees. RADARSAT-1 was developed under the management of the Canadian Space Agency (CSA) in cooperation with Canadian provincial governments and private sector. It provides images of the Earth for scientific and commercial applications. These images have been used in many fields as agriculture, cartography, hydrology, forestry, oceanography, geology, ice and ocean monitoring, artic surveillance, detecting ocean oil slicks…

RADARSAT-1 worked at C-band (5.3 GHz) and provides images with a resolution of 8-100 meters. The system can operate with an incidence angle depends on the operation mode use and it varies between 10 to 60 degree. The swath width is also commutable and it can changes from 45 Km in fine mode to 500 Km with ScanSAR wide mode.

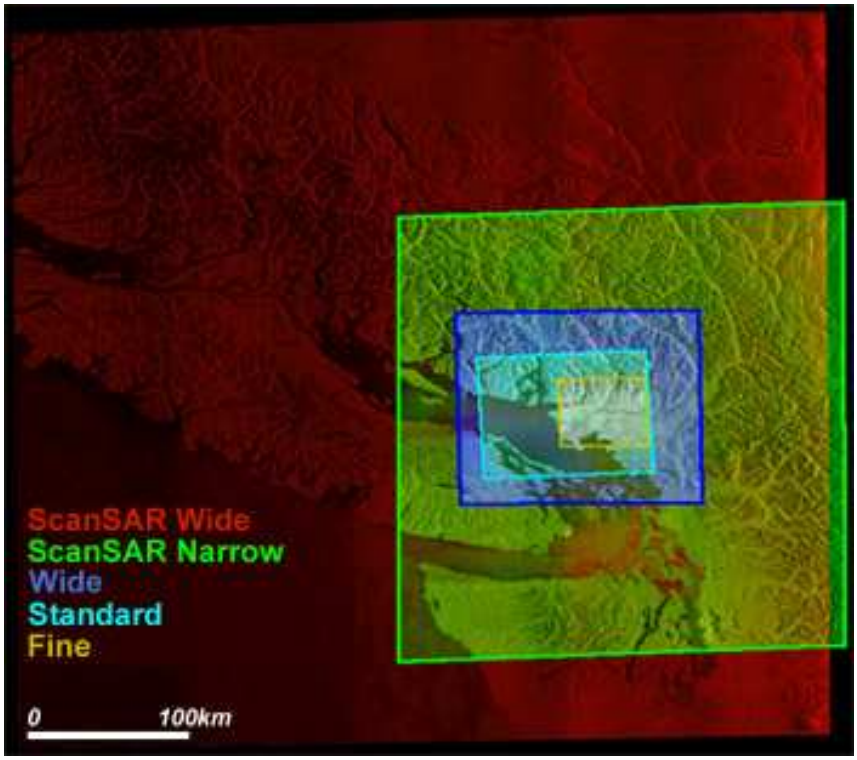

Fig. A.7 Images of RADARSAT-1 with different modes

A.2.9 ENVISAT, 2002

Envisat (Environmental Satellite) was built by the European Space Agency. This Earth-observing satellite was launched on the 1st March 2002 aboard an Ariane 5. ENVISAT orbited around the Earth with a sun-synchronous polar orbit with a height of 790 km.

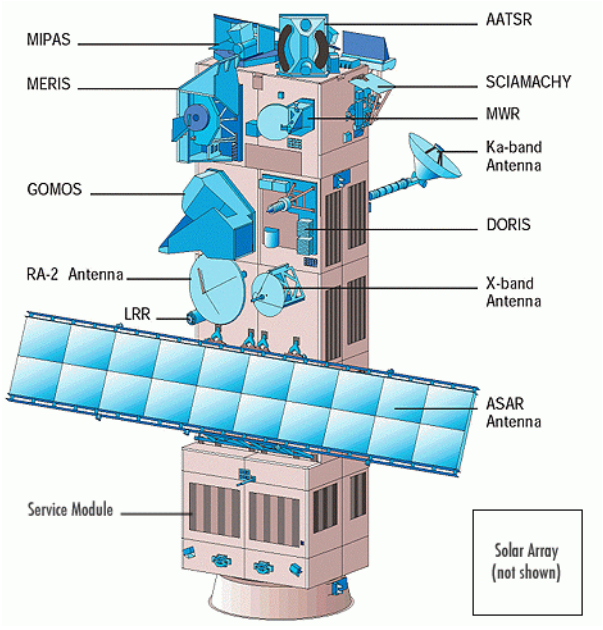

Fig. A.8 ENVISAT diagram with all equipped systems

ENVISAT flows with several instrumentation to get high resolution information of the Earth's surface. So, it was equipped with an Advanced SAR (ASAR) operating in C-band that can detect changes in surface heights with sub-millimetre precision. A Medium Resolution Imaging Spectrometer (MERIS) measures the reflectance of the surface. The temperature of the sea surface can be measured with an Advanced Along Track Scanning Radiometer (AATSR). It also carried a radar altimeter, a microwave radiometer, Doppler Orbitography and Radiopositioning Integrated by Satellite… In Fig. A.8 these and other equipped systems in ENVISAT can be seen.

A.2.10 TerraSAR-X, 2007

TerraSAR-X is a observation satellite that uses an X-band SAR to provide high-quality topographic information for commercial and scientific application. TerraSAR was launched 15 June 2007 by German Aerospace Center and EADS Astrium.

The satellite works with a frequency of 9.6 GHz (X-band) and a wavelength of 31 mm. The orbit has an altitude of 514 km. Other parameters of this satellite will be used along this document to make TOPSAR analysis since it has similar configuration than PAZ system, first Spanish Imaging satellite mission which we have been studying for the last months.

Annex B Azimuth resolution in SAR

The azimuth resolution is the shortest azimuth distance between targets that can be separated by the radar and processed separately, on a constant delay line (same range distance). If we take an antenna length in along-track direction of L_a, the radar beam has an angular spread in azimuth of $\theta_H = \lambda / L_a$, where λ is the radar operation wavelength.

Two targets on the ground separated by δx in the along track direction (azimuth), and at the same slant range R, can be detected as a two different targets if they are not both in the radar beam at the same time. From Fig. B.1, we can determine:

$$\delta x = R\theta_H = R\lambda / L_a \qquad \text{(B.1)}$$

To get the desired resolution with this system, it is necessary to increase the antenna length in along-track direction which is impossible when fine resolution is required. In a practical situation, it is difficult to obtain values of L_a / λ greater than a few hundreds.

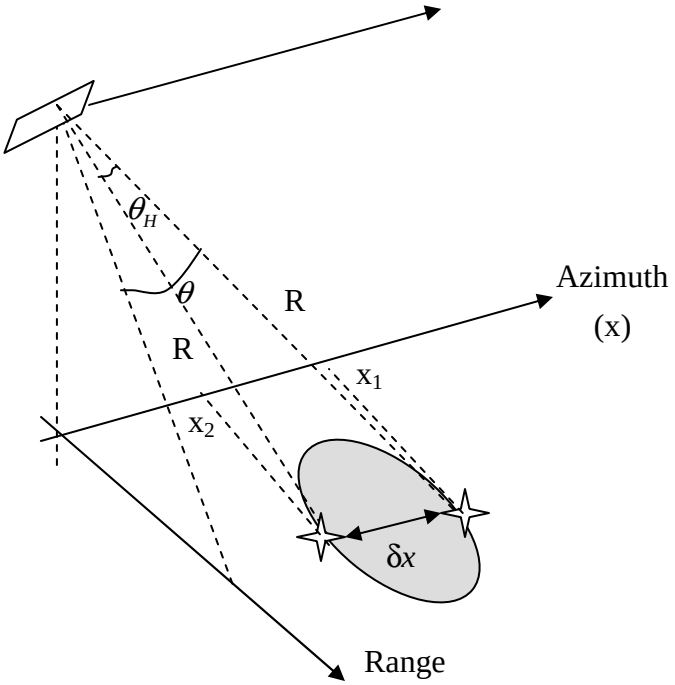

Fig. B.1 Azimuth resolution analysis for SAR

The key element of SAR is the azimuth resolution improvement that makes spaceborne imaging radars possible. It was Wiley in 1965 who observed that two point targets, at slightly different angles with respect to the track of the moving radar, have different speeds at any instant relative to the platform. The difference in relative velocity will produce distinct Doppler frequency shifts in pulses reflected from two targets that will arrive at the receiver.

For a general point target at slant range R and along-track coordinate x, azimuth relative position to the side-looking radar the Doppler shift relative to the transmitted frequency will be:

$$f_d = \frac{1}{\lambda}\frac{\partial r}{\partial t} = \frac{2}{\lambda}V_{st}\sin\theta = \frac{2V_{st}x}{\lambda R} \tag{B.2}$$

where V_{st} is the relative velocity between target and satellite, θ is the angle from the azimuth broadside direction and the factor 2 appears due to two-way travel in an active system. Therefore, if the received signal is analysed in frequency, any energy observed in the return corresponding to range R and at Doppler frequency fd_1, can be associated with a target at:

$$x_1 = \lambda R f_{d1} / 2V_{st} \tag{B.3}$$

The same analysis can be done in point x_2 which will have a Doppler frequency associated return at f_{d2}. So, although both targets are at the same range distance and illuminated by the footprint at the same time, they can be detected independently thanks to the different Doppler shift of their returns.

The Doppler frequency shift provides a second coordinate to distinguishing the targets. The two coordinates used will be the ground range Rg and the along track distance x relative to a point directly beneath the satellite. This geometry can be seen in Fig. B.2.

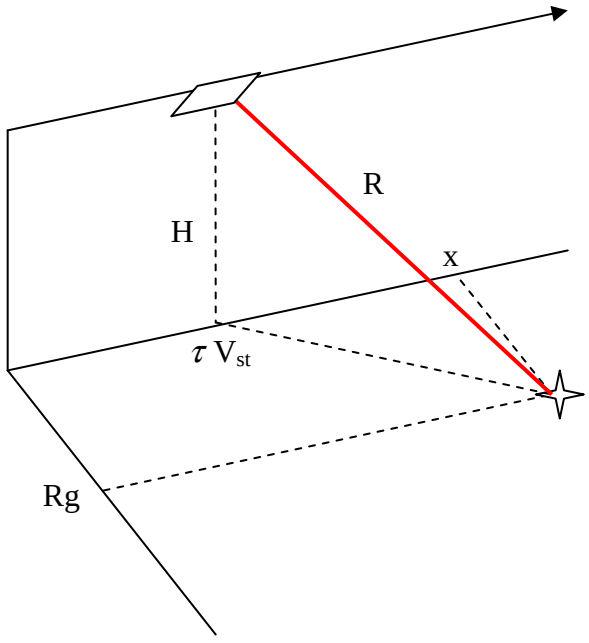

Fig. B.2 Ground range and along-track coordinates

The range distance between the target and the platform can be expressed as:

$$R^2 = \left(x - V_{st}\tau\right)^2 + R_g{}^2 + H^2 \tag{B.4}$$

where τ is the time along the flight path. The range rate is:

$$R' = \frac{\partial R}{\partial \tau} = -Vst\left(x - Vst\,\tau\right)/R \tag{B.5}$$

The time delay of received echoes is $\Delta t = 2R(0)/c$ and Doppler shift (f_{d0}) at $\tau = 0$ can be related by [31]:

$$R^2(0) = x^2 + R_g{}^2 + H^2 \tag{B.6}$$

$$f_{d0} = -\frac{2R'(0)}{\lambda} = \frac{2V_{st}x}{\lambda R(0)} \tag{B.7}$$

Combining both equations we get:

$$x^2\left[\left(\frac{2V_{st}}{\lambda f_{d0}}\right)^2 - 1\right] - R_g{}^2 = H^2 \tag{B.8}$$

which corresponds to the equation of a conic in the (Rg,x) plane. From (B.7) we can write:

$$\left|\frac{2V_{st}}{\lambda f_{d0}}\right| = \left|\frac{R(0)}{x}\right| > 1 \tag{B.9}$$

Resulting in a hyperbola as shown in Fig. B.3. The geometric location of all the returns with same delay is represented as a ellipse, while the points that cause a generic Doppler shit are represented with the hyperbolas. As we can see, only four points have the time delay and Doppler shift coincidence. The left/right ambiguity is solved by our knowledge about where the antenna beam is pointing, while the branch of the hyperbola is selected by the sign of Doppler shift received.

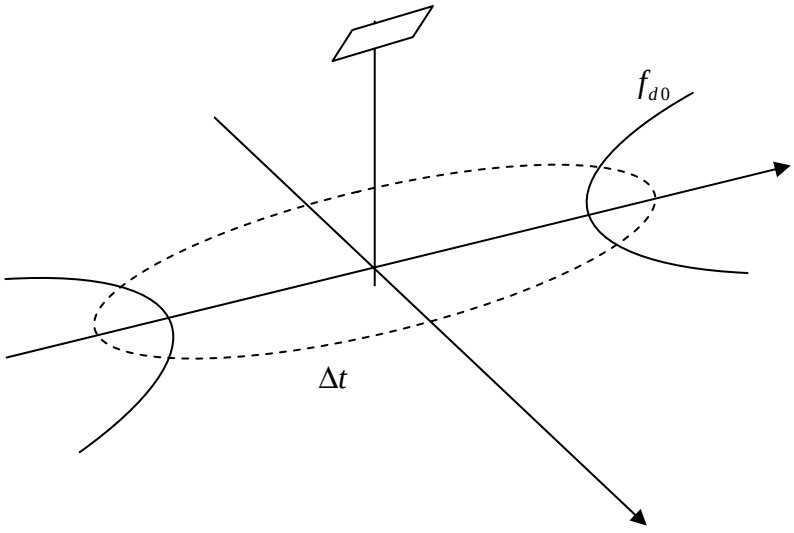

Fig. B.3 Ground range and along-track coordinates

Taking the Doppler shift of the return, the azimuth resolution is extremely related to the Doppler resolution of the receiver. So, it is possible to eliminate the antenna horizontal beamwidth dependency since it does not affect directly to the azimuth resolution. Thus, from (B.3), we can obtain:

$$\delta x = \left(\frac{\lambda R}{2V_{st}} \right) \delta f_d \tag{B.10}$$

Moreover, the frequency resolution is nominally the inverse of the time span *S* [22]. This time can be defined as the time during which any target is in view of the radar. This can be approximated as:

$$S = R\theta_H / V_{st} = R\lambda / \left(L_a V_{st} \right) \tag{B.11}$$

Which substituted in (B.10) provides an equation for azimuth resolution in SAR systems:

$$\delta x = \left(\frac{\lambda R}{2V_{st}} \right) \left(\frac{L_a V_{st}}{R\lambda} \right) = \frac{L_a}{2} \tag{B.12}$$

So, the azimuth resolution of SAR systems is directly related to the azimuth antenna length. Apparently, it could seem that it is possible to achieve any resolution using an antenna length as small as desired. Actually, it is not possible since the length of antenna will affect to the azimuth ambiguities so it is not possible to choose an arbitrary small antenna. Even so, an azimuth resolution of meters can be achieved working with a platform flying at altitudes of hundreds of kilometres, using SAR technology.

Chapter 9 REFERENCES

[1] Acker, A.E., *'Understanding Radar: The ABCs of How Radar Systems Work'* (CD) , SciTech Publishing, 2009

[2] Elachi, C., *'Spaceborne Radar Remote Sensing: Applications and Techniques'* Chapter 3: Principle and theory. New York: IEEE, 1988

[3] Sharkov, Eugene A., *'Passive Microwave Remote Sensing of the Earth'*, Physical Foundations, 2003

[4] Gibson, P., *'Introductory Remote Sensing Principles and Concepts'*, pp. 17-18 and 63, Routledge London, 2000

[5] Aerospaceweb, Radar cross section: '*http://www.aerospaceweb.org/question/electronics/q0168.shtml*'

[6] Knott, Eugene F., Shaeffer, John F., Tuley, Michael T., *``Radar Cross Section (2nd Edition)'*, pp. 7-20, SciTech Publishing, 2004

[7] Skolnik, M., *'Radar Handbook' Chapter 17 Synthetic Aperture Radar*, pp. 17.2-17.3, Front Matter, 2007

[8] SEASAT Overview: *'http://southport.jpl.nasa.gov/scienceapps/ seasat.html*'

[9] SIR-A web page: '*http://www.jpl.nasa.gov/news/features.cfm?feature=422'*

[10] SIR-B web page: '*http://www.jpl.nasa.gov/history/80s/Shuttle%20Imaging%20 Radar-B_1984.htm'*

[11] Martinson, L.W., Gaffney, B.P., Liu, B., Perry, R.P., Ruvin, A., *'Advanced digital SAR processing study'*, Final Report RCA Government System Div. Moorestown, 1982

[12] Johnson, W.T.K., *'Magellan imaging radar mission to Venus'*, Proceedings of the IEEE, June 1991

[13] ERS-1 web page: '*http://earth.esa.int/ers/satconc/*'

[14] JERS-1 web page: '*http://www.eorc.jaxa.jp/JERS-1/en/index.html*'

[15] SIR-C web page: '*http://southport.jpl.nasa.gov/sir-c/*'

[16] ERS-2 web page: '*http://www.deos.tudelft.nl/ers/ers2info.html*'

[17] RADARSAT-1 web page:
'*http://www.asc-csa.gc.ca/eng/satellites/radarsat1/default.asp*'

[18] ENVISAT web page: '*http://envisat.esa.int/*'

[19] TerraSAR-X web page: '*http://www.infoterra.de/terrasar-x.html*'

[20] RADARSAT-2 web page: '*http://www.radarsat2.info/*'

[21] Samuel W. McCandless, Jr. and Christopher R. Jackson. *'SAR Marine's User Manual' Chapter 1. Principles of Synthetic Aperture Radar*

[22] Curlander, J.C. and McDonough, R.N., *'Synthetic Aperture Radar: Systems and Signal Processing'*, New York, 1991

[23] Skolnik, M., *'Introduction to Radar Systems'*, pp. 1-7 and 30-31, McGraw-Hill Science Engineering, April 2003

[24] Elachi, C., *Spaceborne Radar Remote Sensing: Applications and Techniques'*, pp. 51-55, IEEE 1988.

[25] Balanis, C.A., *'Antenna Theory: Analysis and Design'*, pp. 151-152, John Wiley & Sons, New York, 1997

[26] Cardama, A., Jofre, Ll., Rius, J.M., Romeo, J., Blanch, S., Ferrando, M., *'Antenas'*, pp. 171-174, Edicions UPC, March 2005

[27] Harold R. Jacobs, *'Geometry. Seeing, Doing, Understanding'*, W.H. Freeman & Co Ltd; 3rd Re-issue edition, 28 April 2003

[28] Curlander, J.C. and McDonough, R.N., *'Synthetic Aperture Radar: Systems and Signal Processing'*, pp. 63-65, New York, 1991

[29] Elachi, C., *Spaceborne Radar Remote Sensing: Applications and Techniques'*, pp. 75-79, IEEE 1988.

[30] Cumming, I.G., and Wong, F. H., *'Digital Processing of Synthetic Aperture Radar Data, Algorithms and Implementation'*, Boston, Artech House, 2005

[31] Fuqing, C., Xiaoming, T., You, H., *'Research on Bi-static SAR azimuth resolution characteristics'*, APSAR 2007 IEEE, November 2007

[32] Elachi, C., *Spaceborne Radar Remote Sensing: Applications and Techniques'*, pp. 65-66, IEEE 1988.

[33] Herrmann, J., González Bottero, A., *'TerraSAR-X Mission: The New Generation in High Resolution Satellites'*, Infoterra GmbH, 88039 Friedrichshafen, Germany, April 2007

[34] PAZ ECE Team, *'Instrument Performance Analysis'*, December 2008

[35] F. D. Zan and A. M. Guarnieri. *'Topsar: terrain observation by progressive Scans'. IEEE Trans. Geosci. Remote Sensing*, vol. 44, no. 9, pp. 2352-2360, Sept. 2006.

[36] A. Meta, J. Mittermayer, U. Steinbrecher and P. Prats. *'Investigations on the TOPSAR acquisition mode with TerraSAR-X'*. German Aerospace Center, Microwave and Radar Institute.

[37] Sawtooth signal Fourier series: http://en.wikipedia.org/wiki/Sawtooth_wave

[38] Sawtooth signal Fourier series: http://mathworld.wolfram.com/FourierSeriesSawtoothWave.html

[39] Massonnet, D., Souyris, J.C., *'Imaging with Synthetic Aperture Radar'*, pp. 133-137, EPFL Press, 2008

[40] R. McHugh, S. Shaw and N. Taylor, *'Azimuth ambiguities in broadside and squint mode synthetic aperture sonar'*, IEEE 1999

[41] Delta Dirac's Train fourier analysis: *http://en.wikipedia.org/wiki/Dirac_comb*

[42] S.R. Cloude and K.P. Papathanassiou, *'Polarimetric optimization in radar interferometry'*, Electron. Lett., vol. 33, no.13, pp. 1176-1178, 1997

[43] González Arbesú, J.M., Calafell Rueda, I., Romeo Robert, J., *'Antenna Model SAR mision PAZ'*, June 2009

[44] Barton, D.K., *'Pulse compression'*, Radars - Volume 3, December 1975

[45] Paco López Dekker, Albert García Mondéjar, Toni Broquetas Ibars, *'Radiometric Budget'* SAR mission PAZ, March 2009